

UNIVERSIDAD DE GRANADA

PROGRAMA DE DOCTORADO EN QUÍMICA

FACULTAD DE CIENCIAS

DEPARTAMENTO DE QUÍMICA INORGÁNICA



UNIVERSIDAD
DE GRANADA

TESIS DOCTORAL / Ph.D. THESIS

Diseño y síntesis de electro-catalizadores
bifuncionales para procesos electro-Fenton aplicados a
la degradación de contaminantes emergentes

Design and synthesis of bifunctional electro-catalysts
for electro-Fenton processes applied to the degradation
of emerging pollutants

EDGAR FAJARDO PUERTO

Granada, Julio 2024

Editor: Universidad de Granada. Tesis Doctorales
Autor: Edgar Fajardo Puerto
ISBN: 978-84-1195-429-7
URI: <https://hdl.handle.net/10481/94953>

**DISEÑO Y SÍNTESIS DE ELECTRO-CATALIZADORES
BIFUNCIONALES PARA PROCESOS ELECTRO-FENTON
APLICADOS A LA DEGRADACIÓN DE CONTAMINANTES
EMERGENTES**

Tesis presentada para aspirar al título de Doctor
por la Universidad de Granada dentro del Programa de Doctorado en Química

EDGAR FAJARDO PUERTO

Realizada bajo la dirección de la Dra. Esther Bailón García, y el Dr. Abdelhakim Elmouwahidi, en la Facultad de Ciencias de la Universidad de Granada, y juzgada en julio de 2024, en dicha Facultad, por el siguiente Tribunal:

PRESIDENTE:

VOCALES:

SECRETARIO:

“La perfección es una pulida corrección de errores”

Mario Benedetti

“Si uno no pelea para que la vida sea feliz, ¿qué sentido tiene la vida?”

José Mujica

*A mis familias, Fajardo Puerto
y Martínez Puerto*

Agradecimientos

El Desarrollo de todo el trabajo realizado durante estos años no habría sido posible sin la supervisión de mis directores de tesis, Dra. Esther Bailón García y Dr. Abdelhakim Elmouwahidi, quienes con su dedicación, empeño y parte humana permitieron la culminación de los objetivos planteados inicialmente. Su apoyo a nivel científico y personal permitió mi crecimiento personal durante mis años predoctorales. Deseo expresarles mi más sincero y profundo agradecimiento por cada una de sus enseñanzas y la confianza depositada.

A los profesores Dr. Francisco Carrasco Marín y Dr. Agustín Francisco Pérez Cadenas, por brindarme la oportunidad de formar parte del grupo de investigación Materiales Polifuncionales Basados en Carbono (UGR-Carbon), deseo expresarles mi gratitud por tan maravillosa oportunidad y sobre todo su buen trato y calidad humana brindada.

No podría pasar por alto a la Dra. Maria Pérez Cadenas, quien ayudo no solo con la solución de dudas a nivel científico, sino que también brindo palabras de apoyo y consejos oportunos en el momento que fueron necesarios.

Durante estos años predoctorales no cabe duda de que el tiempo compartido con mis compañeros de laboratorio permitió que aquellos momentos en que las cosas no salían como se esperaban, fueran más fáciles de afrontar. Siempre una risa o alguna ayuda extra permitió mantener la fortaleza necesaria para culminar los objetivos propuestos cuando se inició esta experiencia. Quedo profundamente agradecido con todos ustedes y cada uno de los que realizaron su estancia en este periodo de tiempo, los que de alguna u otra manera llevaremos el apellido de UGR-Carbon.

En este punto no podría olvidar a los profesores Prof. Dr. Andrés Felipe Suárez Escobar y Prof. Dr. Franz Edwin López Suárez, quienes de alguna manera fueron quienes me iniciaron en el mundo de la investigación y, con su ayuda, fue posible la obtención de la financiación necesaria para el desarrollo de mis estudios doctorales.

A mis amigos de Granada con quienes pude disfrutar tiempo de calidad tanto en horas de pádel, fútbol como de tapas, solamente darles las gracias por permitirme compartir con ustedes.

A Lizz gracias por sus charlas y puntos de vista un tanto diferentes a los míos, los cuales me permitían ver las cosas desde otras perspectivas y dar con mejores soluciones, gracias.

A mi pareja Aleja, gracias por tu compañía, apoyo y paciencia durante estos años, que nos llenaron de muchas nuevas experiencias. Gratitud por siempre contigo.

Quiero agradecer a todas las personas que de cierta manera contribuyeron a la culminación de este trabajo.

Quiero agradecer a toda mi familia que han estado conmigo a lo largo de todos estos años apoyándome, paso a paso, a seguir este camino. Agradezco a mi padre por la disciplina y templanza que ha tenido conmigo, las cuales me han permitido tener la constancia necesaria para cumplir cada meta que me he propuesto. A mi madre gracias por creer y depositar todos sus esfuerzos en mí, es más fácil andar cuando se tiene un respaldo tan grande como el tuyo. A mi Padrino y mi tía Ma, gracias por brindarme todo el amor, cariño y sobre todo hacerme sentir siempre como un hijo más. A mis hermanos, quienes siempre han estado ahí. Al mayor enseñando y dando ejemplo de responsabilidad y rectitud; el menor demostrando que las mejores cosas llegan cuando los éxitos son compartidos en familia.

Finalmente, agradezco infinitamente a mis “surrónes” quienes sin saberlo me motivaron a actuar como lo hicieron sus papás en algún momento y es ser fuente de inspiración para quienes vienen detrás. Aunque quizás aun falten años para que puedan entender el trasfondo de estas palabras, espero que cuando ese momento llegue, puedan apoyarse en mí como punto de partida para que emprendan nuevas empresas y logren, uno a uno, cada uno de sus sueños, teniendo siempre en mente que venimos del mismo núcleo y que todos los logros de sus papás y míos serán migajas para los que ellos podrán conseguir. Si quien empezó en bicicleta, termino en coche; quien inicia en coche debe terminar en avión.

Edgar Fajardo Puerto

Julio 2024

Se agradece a MINCIENCIAS por la financiación otorgada para el desarrollo de los estudios de doctorado mediante la convocatoria 860. Se agradece al proyecto PID2021-127803OB-100 financiado por MICIU/AEI/10.13039/501100011033 y por FEDER Una manera de hacer Europa. Se agradece a la ayuda referencia C-EXP-247-UGR23 cofinanciado/a por Consejería de Universidad, Investigación e Innovación y por Programa FEDER Andalucía 2021-2027.



Resumen / Abstract

Esta tesis doctoral trata sobre la síntesis y caracterización de diferentes materiales basados en carbono, óxidos metálicos y materiales compuestos óxido metálico-carbono, como catalizadores activos para reacciones de reducción de oxígeno (ORR) y reacciones tipo Fenton, así como, su actividad bifuncional (generación directa de radical hidroxilo). El origen de esta investigación se debe a la necesidad de hallar nuevos procesos capaces de degradar contaminantes emergentes, como los antibióticos, que pueden causar problemas ambientales y de salud pública. Algunos materiales, que mostraron actividad ORR con alta selectividad hacia la vía de 4 electrones, fueron propuestos como prometedores catalizadores para aplicaciones en microceldas de combustible. Los resultados experimentales y su discusión se presentan en este informe en ocho capítulos.

En términos generales, se determinó que es posible obtener catalizadores bifuncionales en el proceso de electro-Fenton mediante el ajuste adecuado de una selectividad hacia los 3 electrones, con lo cual, se logra la generación directa de radicales hidroxilo capaces de degradar antibióticos como la tetraciclina.

Varias series de materiales de carbono (xerogeles y carbones activados), dopados con eco-grafeno, hierro, óxido de manganeso, nitrógeno, azufre, fósforo o boro, han sido sintetizados, caracterizados y probados en la reacción de reducción de oxígeno y en el proceso electro-Fenton. Todos los resultados obtenidos se han correlacionado con las propiedades texturales y químicas de los catalizadores sintetizados, y estos se han estructurado en los siguientes capítulos:

Capítulo I: Introducción y objetivos. Este capítulo presenta el estado del arte del proceso de electro-Fenton en el cual se enmarcan las reacciones y catalizadores involucrados en este proceso. Se presentan las ventajas y limitaciones de cada una de las variantes estudiadas como reacciones tipo Fenton, así como aquellas que pueden funcionar como catalizadores bifuncionales.

Capítulo II: Materiales y métodos. Se describen los protocolos para la síntesis, caracterización y aplicación de cada uno de los materiales y técnicas utilizados para el desarrollo de esta tesis.

Capítulo III: Síntesis fácil de tintas a base de carbono para desarrollar electrocatalizadores ORR libres de metales para la eliminación de amoxicilina mediante el proceso electro-Fenton. En este capítulo se sintetizaron tintas a base de carbono como electrocatalizadores ORR libres de metales para la eliminación de amoxicilina mediante el proceso electro-Fenton. El catalizador preparado mediante pintura con tinta (pincel) mostró los mejores resultados debido a una buena combinación de factores, como la microrrugosidad única y el alto volumen de mesoporos que resultan en los mejores parámetros ORR ($J_K=14.59 \text{ mA cm}^{-2}$, 2.03 electrones transferidos y potencial inicial de Eonset= -0.25V). Se destaca la obtención de electrodos aplicados al proceso electro-Fenton sin la necesidad de usar agentes adicionales, como aglutinantes, para la adhesión del catalizador en el electrodo.

Capítulo IV: Bio-carbones dopados (S, N, P y B) como catalizadores duales altamente eficientes para la degradación de tetraciclina mediante el proceso electro-Fenton heterogéneo. Este capítulo describe el dopaje con diferentes heteroátomos (S, N, P y B) de carbón activado obtenido a partir de un residuo de la industria del aceite de oliva (alperujo). Todas las muestras mostraron una mejora en las propiedades electroquímicas después del dopado. Sin embargo, la muestra con el mejor J_K (10.38 mA cm^{-2}) y el potencial de inicio más bajo (-0.14V) fue la dopada con N. Esto podría atribuirse a los grupos funcionales (N-piridínico y N-pirrólico), que se conocen como sitios activos para la ORR $2e^-$.

Capítulo V: Control del tamaño de las esferas de xerogel de carbono como factor clave que rige la selectividad hacia H_2O_2 en catalizadores electro-Fenton bifuncionales libres de metales para la degradación de tetraciclina. Este capítulo describe el desarrollo de esferas de xerogel de carbono dopadas con eco-grafeno, en diferentes porcentajes. Además, se evaluó el efecto del dopado en las esferas de xerogel de carbono de diferentes tamaños (micrométricas y nanométricas). Los resultados muestran que las muestras obtenidas tienen una actividad bifuncional para la generación directa de $\text{OH}\cdot$ mediante la ruta de 3 electrones. Un factor importante en la actividad catalítica es el tamaño de las esferas de xerogel de carbono, que está asociado con el efecto del dopado con N, debido a que, según los resultados de XPS, en las microsferas había una mayor cantidad de N piridínico y pirrolítico/piridónico, mientras que en las nanoesferas los principales grupos de N eran mas gráfiticos, lo cual, es más favorable para la ruta de 2 electrones.

Capítulo VI: Esferas de carbono dopadas con manganeso como catalizador eficiente para la reacción de reducción de oxígeno. En este capítulo se sintetizaron esferas de carbono mediante el método sol-gel de emulsión inversa, las cuales fueron impregnadas con manganeso (Mn) en tres porcentajes diferentes (10, 20 y 30%). Las muestras se caracterizaron textural, química y electroquímicamente. Los resultados muestran que la presencia de Mn en el material final puede aumentar la selectividad del catalizador hacia una ORR de 4 electrones; sin embargo, cuando la cantidad de manganeso es superior al 20%, la ORR tiende a 2 electrones, además de disminuir el valor de J_K . Estos resultados se atribuyen a que la presencia de manganeso en dos estados de oxidación redox (Mn^{2+} y Mn^{3+}) puede resultar en una transferencia de carga favorable al oxígeno adsorbido, mejorando la ORR. Además, la disminución en J_K se asoció con una menor cantidad de Mn^{3+} . A partir de estos resultados, es posible concluir que el dopado con Mn y la correcta sintonización de la cantidad, podría resultar en un catalizador prometedor para diferentes aplicaciones con ORR.

Capítulo VII: Degradación de antibióticos mediante el proceso Fenton asistido por una ruta de reducción de oxígeno de 3 electrones catalizada por compuestos de bio-carbón y manganeso. En este capítulo se describe la síntesis de materiales de carbono activado dopados con manganeso a partir de aguas residuales de molinos de aceite de oliva. Se probaron diferentes métodos de activación (con H_2O_2 , antes y después de la calcinación, y con CO_2). Además, con el método de activación más adecuado, se utilizaron tres porcentajes diferentes de Mn (10, 25 y 60%). Las muestras óptimas ($J_K > 8 \text{ mA cm}^{-2}$) se probaron en el proceso electro-Fenton como catalizadores bifuncionales, donde se pudo

determinar que la generación de radicales hidroxilo podría tener dos rutas: la primera es la descomposición de H_2O_2 en presencia de Mn (Fenton heterogéneo) y la segunda es la reducción de oxígeno de 3 electrones directamente. La actividad bifuncional podría atribuirse a la presencia de ciclos redox $\text{Mn}^{3+}/\text{Mn}^{2+}$ de la fase Mn_3O_4 en el compuesto.

Capítulo VIII: Conclusiones generales. En este capítulo se muestran las conclusiones generales recopiladas a partir de los capítulos presentados a lo largo de la tesis. Donde se destaca que es posible obtener catalizadores bifuncionales para procesos electro-Fenton, mediante el dopaje con heteroátomos de materiales carbonosos.

This doctoral thesis reports the synthesis and characterization of different carbon-based materials, metal oxides and metal oxide-carbon composite materials, as active catalysts for oxygen reduction reactions (ORR) and Fenton-type reactions, as well as their bifunctional activity (direct generation of hydroxyl radical), due to the need for new processes capable of degrading emerging pollutants such as antibiotics that may lead to environmental and public health problems. Some materials that showed ORR activity with high selectivity towards the 4-electron pathway were proposed as promising catalysts for applications in micro fuel cells. The experimental results and their discussion are presented in this report in eight chapters.

In general terms, it was determined that it is possible to obtain bifunctional catalysts in electro-Fenton, through the correct tuning of a selectivity towards the

3 electrons with which the direct generation of hydroxyl radicals capable of degrading antibiotics such as tetracycline is achieved.

Several series of carbon materials (xerogels and activated carbons), doped with eco-graphene, iron, manganese oxide, nitrogen, sulphur, phosphorus, or boron, have been synthesized, characterized, and tested in oxygen reduction reaction and electro-Fenton process. All the obtained results have been correlated with the textural and chemical properties of the catalysts synthesized and these have been structured in the following chapters:

Chapter I: Introduction and objectives. This chapter presents the state of the art of the electro-Fenton process, in which the reactions and catalysts involved in this process are framed. The advantages and limitations of each of the variants studied as Fenton-type reactions are presented, as well as those that can function as bifunctional catalysts.

Chapter II: Materials and methods. The protocols for the synthesis, characterization and application of each of the materials and techniques used for the development of this thesis are described.

Chapter III: Facile synthesis of carbon-based inks to develop metal-free ORR electrocatalysts for electro Fenton removal of amoxicillin. In This chapter were synthesized carbon-based inks as electrocatalysts ORR metal-free for the remotion of amoxicillin by electro-Fenton process. The catalyst prepared by ink painting (brush) showed the best results, due to a good combination of factors as,

the unique microroughness and the high volume of mesopores that result in the best ORR parameters ($J_K=14.59 \text{ mA cm}^{-2}$, 2.03 transferred electrons and initial potential of $E_{\text{onset}}=-0.25\text{V}$). The achievement of electrodes applied to the electro Fenton process without the need to use extra agents such as binders for the adhesion of the catalyst on the electrode is highlighted.

Chapter IV: Doped Bio-Carbons (S, N, P and B) as highly efficient dual catalysts for the degradation of tetracycline through heterogeneous electro-Fenton process. This Chapter describes the doped with different heteroatoms (S, N, P and B) of activated carbon obtained from a waste of the olive industry (alperujo). All samples showed improvement in the electrochemical properties later of doped, which indicates, however, the sample with the best J_K (10.38 mA cm^{-2}) and E° onset lowest (-0.14V) was the doped with N. This could be attributed to the functional groups (N-pyridinic and N-pyrrolic) that are known as active sites for the ORR $2e^-$.

Chapter V: Size control of carbon xerogel spheres as key factor governing the H_2O_2 selectivity in metal-free bifunctional electro-Fenton catalysts for tetracycline degradation. This Chapter describes the development of carbon xerogel spheres doped with eco-graphene, in different percentages. In addition, was tested the effect of doped in the carbon xerogel spheres of different size (micro and nanometric). The results show that the samples obtained have a bifunctional activity for generation direct of $\text{OH}\cdot$ for way 3 electrons. The size of the carbon xerogel spheres, result important in the catalytic activity, principally associated with the effect of N doped, due to that conform to the XPS results, in the micro spheres had

higher amount of N pyridinic and pyrrolic/pyridonic, meanwhile that in the nano spheres the principal N groups N graphitic, which is most favourable for the way of 2 electrons.

Chapter VI: Manganese doped carbon spheres as an efficient catalyst for Oxygen Reduction Reaction. In this Chapter were synthesized carbon spheres by inverse emulsion sol-gel method, which were impregnated with manganese (Mn) in three different percentage (10, 20 and 30%). The samples were characterized textural, chemical, and electrochemically. The results show that the presence of Mn in the final material can increase the selectivity of catalyst to an ORR 4 electrons, however, when the amount of manganese is higher than 20%, the ORR tends to 2 electrons, in addition to the value of J_K decrease. These results are attributed to that the presence of manganese in two redox oxidation states (Mn^{2+} and Mn^{3+}) can result in a favourable charge-transfer to adsorbed oxygen, improving the ORR. Also, the decrease in J_K was associated with a lower amount of Mn^{3+} . From these results, it's possible conclude that the doped with Mn and the correct syntonise of the amount, could give as result a promising catalyst for different applications with ORR.

Chapter VII: Antibiotic degradation via Fenton process assisted by a 3-electron oxygen reduction reaction pathway catalyzed by bio-carbon-manganese composites. In this Chapter described the synthesis of manganese-doped activated carbon materials from olive mill wastewater. In this chapter, were tested different methods of activation (with H_2O_2 pre and post calcination, and CO_2 method). In addition, with the optimal activation method, were tested three different percentage of Mn (10, 25 and 60%). The optimal samples ($J_K > 8 \text{ mA cm}^{-2}$), were

tested in electro-Fenton process as bifunctional catalysts, where was possible determinate that the generation of hydroxyl radical could have two routes, the first is the decomposition of H₂O₂ in presence of Mn (heterogeneous Fenton) and the second, the ORR 3 electrons directly. The bifunctional activity could be attributed to the presence of redox cycles Mn³⁺/Mn²⁺ from Mn₃O₄ phase in the composite.

Chapter VIII: General conclusions. In this chapter, the general conclusions gathered from the chapters presented throughout the thesis are highlighted. It emphasizes that it is possible to obtain bifunctional catalysts for electro-Fenton processes through the doping of carbonaceous materials with heteroatoms.

Algunos de los resultados de este trabajo han sido publicados en las siguientes revistas y han sido presentados en varios congresos internacionales y nacionales / Some of the results of this work have been already published in the following Journal, and presented in several International and National Conferences:

Lista de publicaciones / List of papers

- A. Barranco-López, A. I. Moral-Rodríguez, E. Fajardo-Puerto, A. Elmouwahidi, E. Bailón-García., *Highly graphitic Fe-doped carbon xerogels as dual-functional electro-Fenton catalysts for the degradation of tetracycline in wastewater.* Environmental Research, 2023. 115757.
- Valencia-Valero LC, Fajardo-Puerto E, Elmouwahidi A, Bailón-García E, Carrasco-Marín F, Pérez-Cadenas AF., *Facile synthesis of carbon-based*

inks to develop metal-free ORR electrocatalysts for electro-Fenton removal of Amoxicillin. Gels, 2024. 10(1). 53.

Lista de congresos / List of conferences

- **XV Reunión del Grupo Español del Carbón (GEC)**, Granada, Spain, April, 2022.
- **XXXVIII Reunión Bienal de la Sociedad Española de Química**, Granada, Spain, June, 2022.
- **Congreso Colombiano del Carbono 2022**, Villavicencio, Colombia, November, 2022.
- **XLII Reunión Ibérica de Adsorción**, Valencia, Spain, September, 2022.
- **SECAT 2023**, Malaga-Torremolinos, Spain, June, 2023.
- **XVI Reunión del Grupo Español del Carbón (GEC)**, Gijon, Spain, October, 2023.

Otros trabajos realizados en colaboración con miembros del grupo de investigación “Materiales Polifuncionales Basados en Carbono (UGR-Carbon)” que actualmente están en proceso, se enumeran a continuación / Other works made in collaboration with members of research group “Materiales Polifuncionales Basados en Carbono (UGR-Carbon)” that actually is in process are listed below

- Fajardo-Puerto E, Bailón-García E, Moral-Rodríguez A. I, Elmouwahidi A, Carrasco-Marín F, Pérez-Cadenas AF. *Carbonization temperature and its*

effect on the chemical structure and Fenton-type catalytic activity of magnetite coated with carbon xerogel.

- Fajardo-Puerto E, Bailón-García E, Moral-Rodríguez A. I, Elmouwahidi A, Carrasco-Marín F, Pérez-Cadenas AF. *Spinel ferrites with excellent catalytic activity for application in Fenton, photo-Fenton and electro-Fenton.*
- Elmouwahidi A, Fajardo-Puerto E, Pérez-Cadenas M, Amaro-Gahete J, Bailón-García E, Carrasco-Marín F, Pérez-Cadenas AF. *Carbon microspheres coated with manganese as bifunctional catalysts in electro Fenton processes.*

CONTENTS

CHAPTER I: INTRODUCTION AND OBJECTIVES	41
1.1.-FROM FENTON AND ORR 2E--TYPE CATALYSTS TO BIFUNCTIONAL ELECTRODES FOR ENVIRONMENTAL REMEDIATION USING THE ELECTRO-FENTON PROCESS.....	43
<i>1.1.1.- Environmental Problems.....</i>	<i>43</i>
<i>1.1.2.- Fenton Reaction</i>	<i>45</i>
<i>1.1.3.- Electro-Fenton Process</i>	<i>57</i>
<i>1.1.4.- Promising New Fenton Catalysts: Spinel Ferrites and Perovskites</i>	<i>70</i>
<i>1.1.5.- Oxygen Reduction Reaction through Two Electrons (ORR 2 e⁻).....</i>	<i>79</i>
<i>1.1.6.-Bifunctional Electro-Fenton Catalyst for Direct OH• Formation</i>	<i>92</i>
<i>1.1.7.- CONCLUSIONS.....</i>	<i>97</i>
BIBLIOGRAPHY	98
OBJECTIVES	151
CHAPTER II: MATERIALES Y METODOS	155
2.1.- MATERIALES	157
<i>Preparación de los materiales empleados como catalizadores.....</i>	<i>157</i>
<i>2.1.1.- Xerogel de carbono.....</i>	<i>157</i>
<i>2.1.2.- Oxido de grafeno</i>	<i>158</i>
<i>2.1.3.- Carbones activados.....</i>	<i>158</i>

2.1.4.- Magnetita	158
2.2.- TECNICAS DE CARACTERIZACIÓN.....	159
<i>Caracterización química y textural</i>	<i>159</i>
2.2.1.- <i>Isotermas de adsorción</i>	<i>159</i>
2.2.2.- <i>Modelo Brünauer, Emmett y Teller (B.E.T).....</i>	<i>160</i>
2.2.3.- <i>Modelo Dubinin-Radushkevich y Stoeckli</i>	<i>161</i>
2.2.4.- <i>Modelo B.J.H.....</i>	<i>162</i>
2.2.5.- <i>Teoría de la Densidad Funcional</i>	<i>163</i>
2.2.6.- <i>Microscopia Electrónica de Barrido (SEM).....</i>	<i>164</i>
2.2.7.- <i>Microscopia Electrónica de transmisión (TEM).....</i>	<i>164</i>
2.2.8.- <i>Espectroscopía de fotoemisión de rayos X (XPS).....</i>	<i>165</i>
2.2.9.- <i>Espectroscopía RAMAN.....</i>	<i>166</i>
2.2.10.- <i>Difracción de rayos X (DRX)</i>	<i>166</i>
2.2.11.- <i>Espectroscopía infrarroja por transformada de Fourier (FTIR)</i>	<i>167</i>
<i>Caracterización electro-química</i>	<i>167</i>
2.2.12.- <i>Preparación electrodo RRDE.....</i>	<i>167</i>
2.2.13.- <i>Preparación electrodo para electro-Fenton.....</i>	<i>167</i>
2.2.14.- <i>Voltametría Cíclica (CV)</i>	<i>168</i>
2.2.15.- <i>Voltametría de Barrido Lineal (LSV)</i>	<i>169</i>
2.2.16.- <i>Electro-Fenton.....</i>	<i>170</i>
BIBLIOGRAPHY	171

CHAPTER III: FACILE SYNTHESIS OF CARBON-BASED INKS TO DEVELOP METAL-FREE ORR ELECTROCATALYSTS FOR ELECTRO FENTON REMOVAL OF AMOXICILLIN.....	179
3.1.-INTRODUCTION	181
3.2.-EXPERIMENTAL	183
3.2.1.- <i>Graphene Oxide (OG)</i>	183
3.2.2.- <i>Magnetite (Fe₃O₄)</i>	184
3.2.3.- <i>Preparation of the Xerogel/OG ink</i>	185
<i>Deposition methods</i>	185
3.2.4.- <i>Conventional catalyst (sample C)</i>	185
3.2.5.- <i>Painted catalyst (sample P)</i>	186
3.2.6.- <i>Screen printed catalyst (sample S)</i>	186
<i>Characterization</i>	186
3.2.7.- <i>Chemical and textural characterization</i>	186
3.2.8.- <i>Electrochemical characterization</i>	187
3.2.9.- <i>Electro-Fenton processes</i>	188
3.3.-RESULTS AND DISCUSSION.....	188
<i>Catalysts ORR</i>	188
3.3.1.- <i>Porosity and surface area determination</i>	188
3.3.2.- <i>Raman Characterization</i>	190
3.3.3.- <i>XPS Characterization</i>	191
3.3.4.- <i>Morphology</i>	192
3.3.5.- <i>Electrochemical Characterization</i>	194
<i>Catalyst Fenton</i>	197

3.3.6.- <i>X-ray diffraction</i>	197
3.3.7.- <i>Morphology</i>	198
3.3.8.- <i>Electro-Fenton experiments</i>	199
3.4.-CONCLUSIONS	203
BIBLIOGRAPHY	204
CHAPTER IV: DOPED BIO-CARBON (S, N, P OR B) AS HIGHLY EFFICIENT DUAL CATALYSTS FOR THE DEGRADATION OF TETRACYCLINE THROUGH HETEROGENEOUS ELECTRO-FENTON PROCESS	217
4.1.- INTRODUCTION	219
4.2.- EXPERIMENTAL	221
4.2.1.- <i>Preparation of carbon materials</i>	221
4.2.2.- <i>Textural and Chemical characterization</i>	222
4.2.3.- <i>Electrochemical characterization: Oxygen electro reduction</i>	222
4.2.4.- <i>Electro Fenton process</i>	224
4.3.- RESULTS AND DISUSSIONS	225
4.3.1.- <i>Morphological characterization</i>	225
4.3.2.- <i>Textural characterization</i>	226
4.3.3.- <i>Chemical characterization</i>	228
4.3.4.- <i>Electrochemical characterization</i>	234
4.3.5.- <i>Electro-Fenton process</i>	239

4.4.- CONCLUSIONS.....	241
BIBLIOGRAPHY	242
CHAPTER V: SIZE CONTROL OF CARBON XEROGEL SPHERES AS KEYFACTOR GOVERNING THE H₂O₂ SELECTIVITY IN METAL- FREE BIFUNCTIONAL ELECTRO-FENTON CATALYSTS FOR TETRACYCLINE	255
5.1.- INTRODUCTION	257
5.2.- EXPERIMENTAL	262
5.2.1.- Eco-graphene (EG).....	262
5.2.2.- Carbon xerogel spheres (CS)	262
5.2.3.- N-doped Carbon xerogel spheres (N-CS)	264
5.2.4.- Chemical and textural characterization	264
5.2.5.- Electrochemical characterization	265
5.2.6.- Electro-Fenton Processes	266
5.3.- RESULTS AND DISCUSSION.....	267
5.3.1.- Morphological characterization.....	267
5.3.2.- Textural characterization	271
5.3.3.- Raman characterization	272
5.3.4.- Elemental analysis and XPS	274
5.3.5.- Electrochemical characterization	280
5.3.6.- Electro-Fenton experiments	288
5.4.- CONCLUSIONS.....	292

BIBLIOGRAPHY	293
---------------------------	------------

CHAPTER VI: MANGANESE DOPED CARBON SPHERES AS AN EFFICIENT CATALYST FOR OXYGEN REDUCTION REACTION.....305

6.1.- INTRODUCTION	307
---------------------------------	------------

6.2.- EXPERIMENTAL	310
---------------------------------	------------

<i>6.2.1.- Synthesis of carbon spheres doped with manganese.....</i>	<i>310</i>
--	------------

<i>6.2.2.- Textural and chemical characterization of carbon spheres.....</i>	<i>311</i>
--	------------

<i>6.2.3.- Electrochemical measurements</i>	<i>312</i>
---	------------

6.3.- RESULTS AND DISCUSSION.....	314
--	------------

<i>6.3.1.- Textural and chemical characterizations</i>	<i>314</i>
--	------------

<i>6.3.2.- Electrochemical characterization</i>	<i>323</i>
---	------------

6.4.- CONCLUSIONS.....	330
-------------------------------	------------

BIBLIOGRAPHY	331
---------------------------	------------

CHAPTER VII: ANTIBIOTIC DEGRADATION VIA FENTON PROCESS ASSISTED BY A 3-ELECTRON OXYGEN REDUCTION REACTION PATHWAY CATALYZED BY BIO-CARBON-MANGANESE COMPOSITES.....343

7.1.- INTRODUCTION	345
---------------------------------	------------

7.2.- EXPERIMENTAL	347
---------------------------------	------------

<i>7.2.1.- Synthesis of bio-carbon-manganese composites</i>	<i>347</i>
---	------------

7.2.2.- <i>Textural and chemical characterization</i>	348
7.2.3.- <i>Electrochemical characterization</i>	349
7.2.4.- <i>Electro Fenton processes</i>	350
7.3.- RESULTS AND DISCUSSIONS	351
7.3.1.- <i>Porosity and surface area of bio-carbon-manganese composites</i>	351
7.3.2.- <i>X-ray diffraction of the composites</i>	354
7.3.3.- <i>XPS spectra</i>	355
7.3.4.- <i>Electrochemical characterization</i>	360
7.3.5.- <i>Electro-Fenton</i>	365
7.4.- CONCLUSIONS	369
BIBLIOGRAPHY	370
CHAPTER VIII: CONCLUSIONES GENERALES	385

CHAPTER I: INTRODUCTION AND OBJECTIVES

Abstract

Currently, the presence of emerging contaminants in water sources has raised concerns worldwide due to low rates of mineralization, and in some cases, zero levels of degradation through conventional treatment methods. For these reasons, researchers in the field are focused on the use of advanced oxidation processes (AOPs) as a powerful tool for the degradation of persistent pollutants. These AOPs are based mainly on the in-situ production of hydroxyl radicals ($\text{OH}\cdot$) generated from an oxidizing agent (H_2O_2 or O_2) in the presence of a catalyst. Among the most studied AOPs, the Fenton reaction stands out due to its operational simplicity and good levels of degradation for a wide range of emerging contaminants. However, it has some limitations such as the storage and handling of H_2O_2 . Therefore, the use of the electro-Fenton (EF) process has been proposed in which H_2O_2 is generated in situ by the action of the oxygen reduction reaction (ORR). However, it is important to mention that the ORR is given by two routes, by two or four electrons, which results in the products of H_2O_2 and H_2O , respectively. For this reason, current efforts seek to increase the selectivity of ORR catalysts toward the $2e^-$ route and thus improve the performance of the EF process. This work reviews catalysts for the Fenton reaction, ORR $2e^-$ catalysts, and presents a short review of some proposed catalysts with bifunctional activity for ORR $2e^-$ and Fenton processes. Finally, the most important factors for electro-Fenton dual catalysts to obtain high catalytic activity in both Fenton and ORR $2e^-$ processes are summarized.

1.1.-FROM FENTON AND ORR $2E^-$ -TYPE CATALYSTS TO BIFUNCTIONAL ELECTRODES FOR ENVIRONMENTAL REMEDIATION USING THE ELECTRO-FENTON PROCESS

1.1.1.- Environmental Problems

One of the largest problems facing society today is water pollution, so special interest has been aroused in knowing the main pollutants that affect it and their subsequent treatment. Currently, some pollutants considered conventional (metals, fats and oils, nitrates, etc.) are controlled and monitored; however, more and more attention has been paid in recent years to those termed today as emerging [1-3]. Emerging contaminants can be defined as substances and/or chemical compounds that are not normally monitored but nevertheless remain continuous and remain present in water bodies despite being treated by conventional wastewater treatment plants [4-7].

Pharmaceuticals, along with their metabolites and degradation products, are considered emerging contaminants [8]. Their continuous discharge, together with their toxic and harmful levels, makes them highly dangerous for human and aquatic organisms [9,10]; therefore, it explains the importance of exercising controls and monitoring the concentrations of these pollutants both in the ecosystem and in effluents [11,12]. Currently, the global pharmaceutical market exceeds one trillion US dollars [13], which demonstrates the strong growth of this industry and its impact on the environment.

Among pharmaceutical products, antibiotics are of special interest because they are made to affect microorganisms, so they are prone to affect microbial communities in aquatic systems, causing a possible disappearance of them, which

may have key functions in the ecosystem [14]. An antibiotic is defined as a chemotherapeutic agent capable of stopping the growth of microorganisms through cell destruction [15]. Antibiotic use has grown steadily globally, mostly in low- and middle-income countries [16]. It has been found that the presence of antibiotics in the environment favors the proliferation of microorganisms resistant to this type of drug [17].

Aquatic environments have been considered large deposits of antibiotics since this type of contaminant can arrive through two main ways, wastewater discharge and agricultural activity [18]. An example of this was a study conducted in 165 rivers in 72 countries, where researchers detected the presence of antibiotics in more than 60% of the 711 sampling sites [19]. In addition to these bodies of water, groundwater has also been susceptible to contamination with antibiotics mainly through the leaching of soils fertilized with manure from livestock, since it contains high concentrations of veterinary drugs [20].

Currently, wastewater treatment processes are composed of three phases in a general way:

1. Primary treatment by physicochemical operations.
2. Secondary treatment by biological processes.
3. Tertiary treatment by additional processes.

However, these treatment technologies only achieve moderate to significant elimination of some antibiotics [21]. For this reason, other types of treatments have been explored to achieve almost total elimination of the antibiotics present in water. Currently, in this study, advanced oxidation processes (AOP's) are explored [22-24], such as Fenton, electro-Fenton, ozonation, photocatalysis, and electrocoagulation, among others [25-29], which are based on the in-situ production

of hydroxyl radicals ($\text{OH}\cdot$) generated from an oxidizing agent (H_2O_2 , O_2) in the presence of a catalyst. $\text{OH}\cdot$ has strong oxidizing power and thus, a high capacity to degrade organic compounds to simpler and less toxic biodegradable substances, and in some cases, even reaching complete mineralization [30].

1.1.2.- Fenton Reaction

The first report on the Fenton reaction dates from 1876, where a mixture of H_2O_2 and Fe^{2+} salt (Fenton reagent) was used to achieve the oxidation of tartaric acid [31]; from there, various investigations have been carried out to apply this reaction in multiple applications. It is currently mainly used in environmental remediation [32-36].

The Fenton reaction can be considered an AOP, where it is based on a mixture of ferrous ion (Fe^{2+}) (usually in a liquid state) with hydrogen peroxide (H_2O_2) [37], which, under the right reaction conditions, results in the formation of hydroxyl radicals [38] with high oxidative potential capable of degrading a wide range of contaminants (figure 1.1) [39].



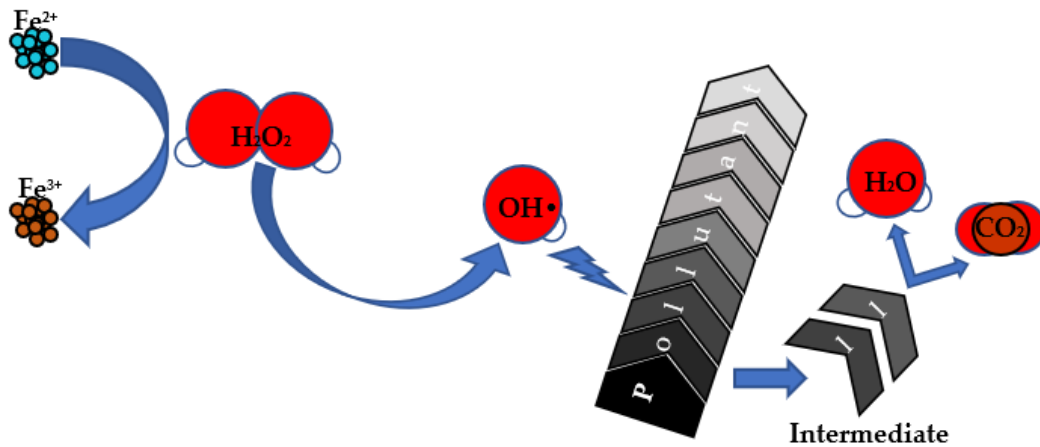


Figure 1.1. Scheme of the Fenton process. In general, the multiple reactions involved can be summarized by Equations (1.1) and (1.2) [40,41].

The Fenton reactions are based on the oxidation of Fe^{2+} to Fe^{3+} , which simultaneously generates the hydroxyl radical (equation 1.1), followed by the reduction of Fe^{3+} to Fe^{2+} (equation 1.2), which allows the regeneration of the catalyst. However, the reaction in which $\text{OH}\cdot$ is produced is much faster than that of catalyst regeneration [42], leading to the accumulation of Fe^{3+} and therefore decreasing catalytic efficiency.

Among its main advantages are its operational simplicity, zero toxicity, mild reaction conditions (ambient temperature and atmospheric pressures), and high degradation efficiency [43-46]. However, there are still some important limitations to overcome such as the slow reduction rate of Fe^{3+} to Fe^{2+} resulting in high levels of sludge generation with iron content, the deactivation of the catalyst, and a narrow pH working range [47-51].

The pH level is one of the most important parameters because it limits degradation efficiency. At pH values below 3, H₂O₂ goes on to form oxonium ions (H₃O₂⁺), which have less oxidative power than OH•, while as the pH rises above 3, colloidal ferric species such as ferric hydroxide are formed from dissolved iron, which produces high amounts of sludge [52].

Recently, numerous investigations have been carried out (see table 1.1) focused on the optimization of Fenton conditions. Variables such as catalyst pollutant and H₂O₂ concentration have been evaluated, as well as the pH of the solution, to determine under what conditions the highest percentage of pollutant molecule degradation is reached.

Typically, the pH is a crucial factor in the Fenton process, hardly affecting catalyst stability and pollutant degradation. From this, numerous investigations have been carried out with different pH values found at important degradation levels of pollutants such as antibiotics, colorants, and industrial wastewater. It is known that the pH optimal value for the Fenton reaction is closer to 3 due to the stability of H₂O₂, OH•, and Fe³⁺. In this sense, Rao et al. [53] treated complex recalcitrant wastewater using FeSO₄·7H₂O as a catalyst (typical Fenton catalyst) in a concentration of 50 mg L⁻¹ and a pH value of 3 obtaining a degradation of 72% of DQO. On the other hand, Zhao et al. [54] removed a polymer quaternary ammonium salt using the same catalyst but using a pH of 2 and a Fenton catalyst concentration slightly lower (40 mg L⁻¹), achieving a percentage of elimination closer to 70%. Liu et al. [55] degraded a reference colorant for degradation tests, methylene blue, and analyzed the activation of the Fenton reaction under visible light irradiation using MoS₂-Fe (150 mg L⁻¹) as the Fenton catalyst at a pH value of 3, reaching a degradation of 65%. In turn, Qin et al. [56] achieved a 99.1% degradation level for

a widely used antibiotic, amoxicillin, using 1 g L^{-1} of a core-shell structured $\text{MnFe}_2\text{O}_4@\text{C-NH}_2$ at a pH of 3 (Figure 1.2).

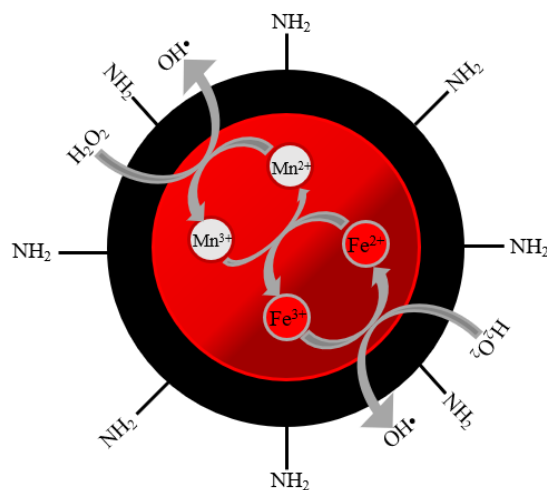


Figure 1.2. Schematic of the OH^\bullet generation by $\text{MnFe}_2\text{O}_4@\text{C-NH}_2$. Adapted from [56].

Other antibiotics tested at pH 3 have been sulfamerazine (40 mg L^{-1}), sulfathiazole (0.5 mg L^{-1}), azithromycin (0.1 mg L^{-1}), norfloxacin (50 mg L^{-1}), and sulfamethoxazole (0.01 mg L^{-1}), with removal percentages $>65\%$, using as Fenton catalysts, CNTs- Fe_3O_4 (0.5 mg L^{-1}), dissolved iron from zero-valent iron nanoparticles (9 mg L^{-1}), $\text{MnFe}_3\text{O}_4\text{-HS}$ (1000 mg L^{-1}), $\text{Fe}_3\text{O}_4/\text{Schwertmannita}/\text{carbon}$ (50 mg L^{-1}) (figure 1.3) and fresh powder from Fe^0 , respectively [57-61]. On the other hand, Hommem et al. [62] studied a range of pHs from 3.5 to 4.5, for the degradation of amoxicillin (0.45 mg L^{-1}) using $\text{FeSO}_4 \cdot 7\text{H}_2\text{O}$ (0.095 mg L^{-1}) as catalysts, obtaining 100% degradation in all cases.

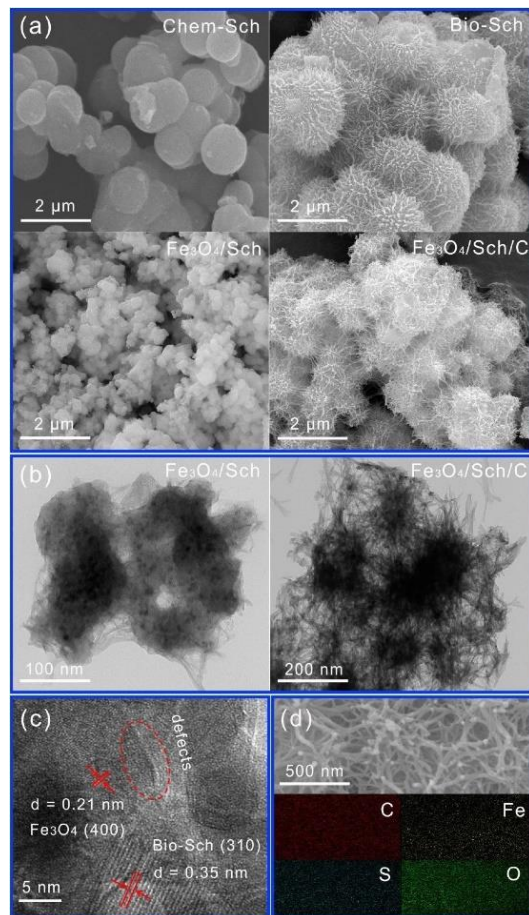


Figure 1.3. (a) SEM images of Chem-Sch, Bio-Sch, Fe₃O₄/Sch, Fe₃O₄/Sch/C, (b) TEM of Fe₃O₄/Sch and Fe₃O₄/Sch/C, (c) HRTEM of Fe₃O₄/Sch/C, and (d) elemental mapping of different elements C, Fe, S, and O recorded from Fe₃O₄/Sch/C [60].

Other authors tried to increase the operating pH to facilitate the use of the Fenton process in a real application. Cheng et al. achieved a tetracycline hydrochloride degradation of 91.3% at a pH value of 4 using magnetic pullulan

hydrogel as a Fenton catalyst (1250 mg L^{-1}) [63]. Similarly, Wang et al. [64] obtained a good tetracycline degradation (83%) at a pH value of 4.3 using iron loaded in graphitic carbon derived from microplastics. The highest pH values (5 to 5.5) tested also obtained good results: 100% degradation of carbamazepine and norfloxacin and 86.9% for ciprofloxacin using $\text{LaCu}_{0.5}\text{Mn}_{0.5}\text{O}_3$, $\text{FeSO}_4 \cdot 7\text{H}_2\text{O}$ with hydroxylamine ($10 \text{ }\mu\text{M}$ of Fe^{2+}), and $\delta\text{-Fe}_3\text{OOH/MWCNTs}$ as Fenton catalysts, respectively [65-67]. However, neutralization of the final effluent is still required, so the search for catalysts and conditions that allow the development of this process at a neutral pH value is preferred. In this way, several researchers have studied the degradation of different pollutants such as amoxicillin, sulfadiazine, tetracycline, sulfadiazine, and rifampicin metronidazole, among others, working at pHs of 6 to 7.5, and obtaining degradation higher than 90% using goethite, $\text{Fe}_2(\text{SO}_4)_3 \cdot \text{H}_2\text{O}$, single-atom iron fixed in porous carbon, copper-modified MgFe-CO_3 double-layered hydroxide, $\text{rGO}@n\text{Fe/Pd}$, magnetic biocarbon, $\text{CoFe}_2\text{O}_4\text{-S}$, and $\text{LaCu}_{0.8}\text{Mn}_{0.2}\text{O}_3$ [68-75] as Fenton catalysts. Guo et al. [76] also achieved the total degradation of ofloxacin at the widest pH using $\text{GO-Fe}_3\text{O}_4$ in a discharge plasma system. Wang et al. [77] also obtained the total degradation of ofloxacin using $\text{Fe}_3\text{O}_4@\text{S-doped ZnO}$ at a pH of 5.2 to 9.0. For their part, Sun et al. [78] worked in a wide range of pH values from 3 to 9, degrading 99% of sodium sulfadiazine with FeCO_3 [6000 mg L^{-1}].

Table 1.1. Operating conditions for some Fenton processes.

Catalyst	[Catalyst]	[H ₂ O ₂]	Pollutant	[Pollutant]	pH	Elimination	Ref.
LaCu _{0.5} Mn _{0.5} O ₃	0.6 g L ⁻¹	0.7 g L ⁻¹	Carbamazepine (CZP)	15 mg L ⁻¹	5.5	100%	[65]
ZnO doped Fe ₃ O ₄ @S	0.25 g L ⁻¹	5 mL L ⁻¹	Ofloxacin (OFX)	10 mg L ⁻¹	5.2–9.0	100%	[77]
FeSO ₄ ·7H ₂ O	50 mg L ⁻¹	26.4 mM	Industrial wastewater (DQO)	850 mg L ⁻¹ (DQO)	3	72%	[53]
FeSO ₄ ·7H ₂ O	40 mg L ⁻¹	23 mL L ⁻¹	Hydroxyethylpolydiallyldimethylammoniumacrylamide-acrylic-acrylate (PDM)	200 mg L ⁻¹	2	69.3%	[54]
Siderite (FeCO ₃)	6 g L ⁻¹	100 mMol L ⁻¹	sodium sulfadiazine	50 mg L ⁻¹	9	99%	[78]
Goethite	-	460 mg L ⁻¹	Amoxicillin	105 mg L ⁻¹	6.5–7	83%	[68]
MnFe ₂ O ₄ @C-NH ₂	1 g L ⁻¹	3 mL L ⁻¹	Amoxicillin	30 mg L ⁻¹	3.0	99.1%	[56]
Fe ₂ (SO ₄) ₃ ·xH ₂ O	30 mg L ⁻¹	-	Tetracycline	50 mg L ⁻¹	6.0	90%	[69]
Fe ₂ (SO ₄) ₃ ·7H ₂ O	0.095 mg L ⁻¹	2.35 mg L ⁻¹	Amoxicillin	0.45 mg L ⁻¹	3.5–4.5	100%	[62]
rGO-Fe ₃ O ₄	0.23 g L ⁻¹	-	Ofloxacin	20 mg L ⁻¹	7.0–4.0	99.9%	[76]
MoS ₂ -Fe	150 mg L ⁻¹	10 mMol L ⁻¹	Methylene blue	25 mg L ⁻¹	3	65%	[55]
CNTs-Fe ₃ O ₄	0.5 g L ⁻¹	24.5 mM	Sulfamerazine	40 mg L ⁻¹	3	70%	[57]
Dissolved iron from zero valence iron nanoparticles (nZVI)	9 mg L ⁻¹	34 mg L ⁻¹	Sulfathiazole	0.5 mg L ⁻¹	3	>96%	[58]
Fe ₂ (SO ₄) ₃ ·7H ₂ O with hydroxylamine	10 μM de Fe ²⁺	1.0 mM	Norfloxacin	10 mg L ⁻¹	5	100%	[66]
CuS@Fe ₃ O ₄ /Pt	-	-	Tetracycline	40 mg L ⁻¹	-	78%	[79]
Single-atom iron fixed in porous carbon (Fe-ISA@CN)	100 mg L ⁻¹	10 mM	Sulfadiazine	2 mg L ⁻¹	6.5	96%	[70]
LDH-CuMgFe-CO ₃	0.5 g L ⁻¹	4 mMol L ⁻¹	Sulfathiazole	0.15 mg L ⁻¹	7.5	100%	[71]
rGO@nFe/Pd	200 mg L ⁻¹	167 mMol	Rifampicin	50 mg L ⁻¹	6.14	94.6%	[72]
MnFe ₂ O ₄ -HS	1 g L ⁻¹	29.4 mM	Azithromycin	0.1 mg L ⁻¹	3.0	92.6%	[59]
MagFePC (Hybrid)	250 mg L ⁻¹	5 mL L ⁻¹	Tetracycline	-	6.0	100%	[80]
Magnetic pullulan hydrogels	1.25 g L ⁻¹	1.25 mL L ⁻¹	Tetracycline hydrochloride	20 mg L ⁻¹	4.0	91.3%	[63]
Magnetic biocarbon	0.2 g L ⁻¹	50 mM	Metronidazole	20 mg L ⁻¹	6.0	97.4%	[73]
CoFe ₂ O ₄ -S	500 mg L ⁻¹	5 mMol L ⁻¹	Tetracycline	0.1 M	7.0	90%	[74]
COF (Photo-Fenton)	167 mg L ⁻¹	50 mL L ⁻¹	Rhodamine B	150 mg L ⁻¹	4.4	41.2%	[81]
Fe ₃ O ₄ /Schwettmann/Carbon	50 mg	45 μL	Norfloxacin	50 mg L ⁻¹	3.0	100%	[60]
δ-Fe ₃ OOH/MWCNTs	235 mg L ⁻¹	20.6 mMol	Ciprofloxacin	10 mg L ⁻¹	5.3	86.9%	[67]
Fe ²⁺	5.0 mMol L ⁻¹ de Fe ²⁺	10 mmol L ⁻¹	Antibiotic resistance gene (ARG)	11.53 Log ₁₀ (copies) g ⁻¹ dry sludge	3	66.86%	[82]
Fe-MPC	0.02 g L ⁻¹	1.0 mM	Tetracycline	40 mg L ⁻¹	4.3	83%	[64]
Fresh powder from Fe ⁰	-	-	Sulfamethoxazole	10 μg L ⁻¹	3	100%	[61]
LaCu _{0.8} Mn _{0.2} O ₃	0.2 g L ⁻¹	13.8 × 10 ⁻³ mol L ⁻¹	Paracetamol	50 mg L ⁻¹	6.7	90%	[75]

Apart from the commonly mentioned conditions, relevance has been found in some unusual factors, such as the slow and continuous addition of diluted H_2O_2 , which improved the stoichiometric efficacy of the reaction compared to the concentrated reagent being added only once [83]. Similarly, a high concentration of H_2O_2 causes an unfavorable effect on the reaction by bringing $\text{OH}\cdot$ to H_2O [84], which decreases the efficiency of the process.

Although high percentages of elimination have been achieved for some pollutants, it is important to note that those tests in which dissolved iron has been used in solution (conventional process) have an optimal pH value close to 3, which maintains the previously mentioned limitations.

In order to overcome its limitations, one of the variations in the conventional process is the use of chelating agents, which can allow the reaction to happen at a pH close to neutral; however, the possible harmful effects such as toxicity and contribution to total organic carbon remain to limit its use [85]. Therefore, the use of heterogeneous catalysts is proposed, where the reactive species are generated mainly on the surface of the catalyst [86], and not, as in the homogeneous process, where the reaction happens in the solution. This makes the recovery and reuse of the heterogeneous catalyst easier [87] and decreases the leaching of Fe^{3+} and, therefore, the generation of sludge. However, some heterogeneous catalysts, although they present minor leaching, behave as if they were homogeneous [88].

An ideal Fenton heterogeneous catalyst must have high catalytic activity and stability, and be easy to recover and reuse [89,90]. To supply this, different materials have been evaluated with iron in different oxidation states. Fe^0 has been reported as a possible heterogeneous Fenton catalyst when maintained in acidic conditions and

in the presence of dissolved O_2 [91,92]. In the presence of oxygen, the in-situ generation of H_2O_2 in zero-valent materials is possible, since the surface of the material can reduce O_2 using two electrons, accompanied by the generation of Fe^{2+} [93]. Iron oxides, possessing Fe in different oxidation states and being the most abundant minerals in the earth's crust, have been evaluated in the Fenton process. Among these, goethite [94], hematite [95], and magnetite [96] have been investigated. Among the mentioned iron oxides, Fe_3O_4 has aroused greater interest, due to its zero toxicity, effective catalytic activity (thanks to its Fe^{2+} species in its crystal structure), as well as its easy recovery and reuse due to its magnetic properties [97-100]. However, Fe_3O_4 presents a low catalytic activity, mainly due to the slow speed of the Fe^{3+}/Fe^{2+} cycle. Therefore, several strategies have been proposed to overcome this limitation, such as coating, use of materials as supports, adjuvants, etc. [101].

It has been found that the addition of different carbon materials can enhance the Fenton reaction because the presence of carboxyl, carbonyl, and quinone groups present in the carbon material surface accelerates the reduction of Fe^{3+} to Fe^{2+} (figure 1.4) [102-106]. On the other hand, carbon materials have been also used as support of the Fenton catalyst. Sun et al. [107] prepared ferric hydroxyquinoline supported on active carbon fiber, which enhanced the Fe^{3+}/Fe^{2+} cycle through the free electrons presents in the carbon material. Yao et al. [108] supported copper ferrite on reduced graphene oxide finding that the presence of two metal ions improved the redox cycle of both ions Cu and Fe together, with a synergistic effect between the nanocube structure of the copper ferrite and the mesoporosity of the support. Kuśmierk et al. [109] and Cruz et al. [110] used organic xerogel as support for Fe/N and $CoFe_2O_4$ and, in both investigations, a catalytic improvement was

observed and ascribed to a higher activation of H_2O_2 due to the coexistence of two different atoms (Fe and N or Co and Fe) in a same matrix.

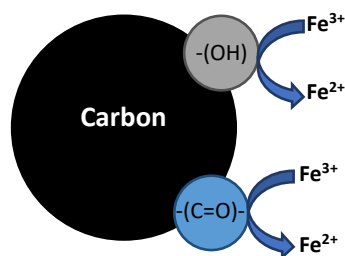


Figure 1.4. Effect of the addition of carbon in the promoted reduction of Fe^{3+} to Fe^{2+} [104].

This bimetallic synergism and the effect of the support were also observed by other authors. Zhang et al. [111] prepared Fe/Cu bimetallic-phase-supported montmorillonite using a two-step strategy of impregnation and calcination and found excellent efficiency in the removal of rhodamine B in comparison to single-metal-loaded montmorillonite. These results were ascribed to (i) the expansion of the montmorillonite pore size due to the insertion of Cu and Fe atoms making this clay more suitable as a Fenton catalyst, (ii) the electrons involved in the redox reaction of bimetallic active sites promote the rate of mutual oxidation reactions by enhancing the H_2O_2 conversion into oxidant radicals, and (iii) the leaching of the pure metal ions decreases due to the good stability of support. Li et al. [112] synthesized Fe–Mn/SAPO-18 zeolite catalysts by ion exchange, maintaining the zeolite structure. The author observed an enhanced degradation efficiency of methyl orange compared to the single-metal catalysts (Fe and Mn), which was also

attributed to the synergistic effect of bimetal that improves $\text{OH}\cdot$ radical generation and also promotes the formation of another active species, $\text{HO}_2\cdot$. Similarly, Xu et al. [113] used sepiolite as support for Fe_3O_4 dispersion to be used as catalysts for the Fenton degradation of bisphenol A (BPA). The high surface area of the catalyst and the electron transfer and π - π interactions are responsible for the good BPA adsorption properties. Thus, the preconcentration of BFA by adsorption near the active site centers and the generation of hydroxyl radicals in the reaction of H_2O_2 and active sites make the Fenton degradation easier on the surface of Fe_3O_4 -Sep. Ferroudj et al. [114] tried to analyze the catalyst's structure-activity relationships and the effect of Fe^{3+} doping in the Fenton degradation of methyl orange (MO) and reactive back 5 (RB5) by the synthesis of Fe^{3+} doped and undoped maghemite/silica microporous and mesoporous microspheres (γ - $\text{Fe}_2\text{O}_3/\text{SiO}_2$ MS). For that study, the authors concluded that porosity and Fe dispersion play an important role in the Fenton reaction. The creation of mesoporosity in the support enhances the reactants and products diffusion allowing a faster degradation of the tested dyes regarding its microporous counterpart, mainly for the RG5 molecule due to the biggest size. This degradation activity was improved after the doping of the silica framework with Fe^{3+} . Thus, the best results were obtained for the Fe-doped γ - $\text{Fe}_2\text{O}_3/\text{SiO}_2$ MS mesoporous catalyst. This material allows an almost complete degradation of MO in 25 min in contrast to the doped microporous catalyst, which achieved 92% of MO degradation in 1 h, and the undoped materials, which produces a much low degradation efficiency (63%) in 1 h. Similar results were obtained in the degradation of RB5. The above-commented strategies to enhance the Fenton active-phase performances and the improvements achieved are collected and summarized in Table 1.2.

Table 1.2. Strategies and improvements in the development of electro-Fenton Catalysts.

Catalyst	Strategy	Improvement	Ref
Fe (NO ₃) ₃ ·9H ₂ O	Addition of MWCNT and complexation on the surface of the MWCNT through the surface groups.	<ul style="list-style-type: none"> Faster Fe³⁺/Fe²⁺ cycle (Demonstrated by the generation of OH[•] and HO₂[•], combined with an accelerated decomposition of the contaminant). Better catalytic activity by MWCNT carboxylates groups. Accelerating the intermediate step from Fe-OOH to Fe²⁺. 	[102]
FeCl ₃ ·6H ₂ O	Addition of carbon materials (powdered activated carbon and carbon nanotubes).	<ul style="list-style-type: none"> The reduction from Fe³⁺ to Fe²⁺ was accelerated. Due to the reducing power of carbon materials. 	[103]
Fe (NO ₃) ₃ ·9H ₂ O	Addition of hydrothermally prepared carbon.	<ul style="list-style-type: none"> Promoted the Fe³⁺/Fe²⁺ cycle through the transfer of electrons from carbonaceous material to Fe³⁺. Hydroxyl groups on the surface of hydrothermal carbon strongly affect the reduction of Fe³⁺. 	[104]
Fe ₂ O ₃ @FeB	FeB coating to Fe ₂ O ₃ core.	<ul style="list-style-type: none"> An efficient Fe³⁺/Fe²⁺ cycle was achieved, thanks to the oxidizing and constantly ceding electrons to Fe³⁺. The Fe²⁺ could also generate H₂O₂ in situ by the activation pathway of a single electron of O₂. 	[115]
FeCl ₃ ·6H ₂ O	Addition of granular activated carbon.	<ul style="list-style-type: none"> The formation of Fe²⁺ was accelerated, which improved the catalytic oxidation of the target contaminant. 	[105]
Ferrihydrite	Addition of biocarbon and <i>S. oneidensis</i> .	<ul style="list-style-type: none"> Faster Fe³⁺ reduction rate. 	[106]
Montmorillonite (Fe/Cu-MMT)	Preparation of Fe–Cu bimetallic active sites.	<ul style="list-style-type: none"> The bleaching efficiency higher, by the electrons involved in the redox reaction of the metals, promoting the mutual oxidation. A decrease in the leaching of pure metal ions of Fe and Cu. 	[111]
Fe–Mn/SAPO-18	Fe–Mn bimetallic active sites supported on SAPO-18.	<ul style="list-style-type: none"> Improved degradation efficiency of the contaminant. 	[112]
Fe ₃ O ₄ –Sep	Sepiolite support for Fe ₃ O ₄ nanoparticles.	<ul style="list-style-type: none"> Improved adsorption of the catalyst and, therefore, the in-situ degradation of the contaminant on the surface of Fe₃O₄–Sep. 	[113]
γ-Fe ₂ O ₃ –SiO ₂	Mesoporosity creation.	<ul style="list-style-type: none"> The substitution of microporosity or mesoporosity led to a greater discoloration of the effluent to be treated. 	[114]
QuFe@ACF	Active carbon fiber support.	<ul style="list-style-type: none"> Free electrons in the carbon fibers were able to drive electron transfer to ferric 8-hydroxyquinoline to promote the Fe³⁺/Fe²⁺ cycle faster. 	[107]
Fe-C	Fe-doped carbon xerogel.	<ul style="list-style-type: none"> Improved dispersion of Fe⁰ species. 	[116]
CF/rGO	Reduced graphene oxide support for copper ferrite.	<ul style="list-style-type: none"> The redox efficiency improved due to the two metal ions (Cu²⁺/Cu⁺ and Fe³⁺/Fe²⁺). Synergistic effect between the nanotube structure of the copper ferrite together with the mesoporosity of the support. 	[108]
Fe–N/C	Carbon xerogel support for heteroatoms (Fe, N).	<ul style="list-style-type: none"> Improved mass transfer to catalytic active sites. Increased activation of H₂O₂ due to the coexistence of Fe and N. 	[109]
CoFe ₂ O ₄ /NOM	Xerogel support from the natural organic matrix (NOM) for CoFe ₂ O ₄ .	<ul style="list-style-type: none"> Increased surface area, increasing exposure to catalytically active sites. 	[110]

As evidenced in the literature, supporting Fenton heterogeneous catalysts is an effective method to increase the speed of the $\text{Fe}^{3+}/\text{Fe}^{2+}$ cycle, making it possible to enhance the efficiency of the process. In the same way, an interesting option is the use of metal-doped (e.g., N-Cu) or bimetallic active phases (e.g., Fe-Mn or Fe-Cu), which not only favor redox or Fenton reactions but also more complex reactions such as the oxygen reduction reaction (ORR) (e.g., nitrogen), which is very important for the electro-Fenton process, another variable of conventional Fenton that is addressed below.

1.1.3.- Electro-Fenton Process

Heterogeneous Fenton has been proven to be a process with considerable potential for treating a wide range of pollutants. However, the storage, transport, and handling of H_2O_2 , as well as the high costs associated with the excess consumption of the reagent are a limitation of the process [117]. To overcome these problems, the heterogeneous electro-Fenton (HEF) has been proposed, where the main contributions are the in situ production of H_2O_2 through the ORR at the cathode, the reduction of Fe^{3+} in the same electrode to supply Fe^{2+} again and the improved generation of $\text{OH}\cdot$ by the applied electricity [118-120].

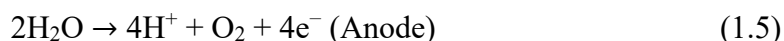
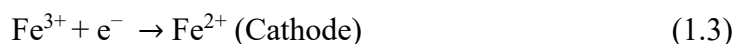
This process has been successfully used for the degradation of different recalcitrant pollutants such as drugs, dyes, petroleum derivatives, etc. [121-124]. The mechanism of the electro-Fenton process is given by several stages, summarized in [125]:

1. Electrogeneration of H_2O_2 (cathodic reduction of O_2).
2. Production of $\text{OH}\cdot$ (Fenton reaction).

3. Promotion of the formation of OH• physisorbed on the surface of the electrode.

4. Regeneration of Fe²⁺ through the direct reduction of Fe³⁺ at the cathode.

In general, the reactions involved in the process can be summarized in Equations (1.3)-(1.6) [126-128]. However, it is necessary to pay special attention to the possible side reactions associated with the electrolysis of water that can decrease the performance of the catalytic activity of the process [129].



One of the most important benefits of this process to highlight is the expansion of the working pH range with the removal of contaminants at a pH close to neutral as well as its improvement in levels of biodegradability and toxicity [130,131]. However, as evidenced by equations (1.4) and (1.6), ORR is the limiting step of the process, so it is important to pay attention to the cathode used [132-134].

Traditionally, carbon materials have been used as cathodes due to their good conductivity, stability, and low cost. Thus, these carbon materials are presented as excellent candidates as high-performance cathode electrodes for electro-Fenton reactions for several reasons that are described in the following. Sun et al. [135] synthesized a family of porous biochars by the chemical activation of cellulose powder with ZnCl₂ and demonstrated that the carbonization temperature plays an

important role in the catalytic performance in the EF oxidation of organic contaminants. While a high carbonization temperature favors the generation of water via the 4-electron pathway, a mild temperature of carbonization (400 °C) improved the generation of H₂O₂ via the 2-electron pathway. This different behavior is attributed to the surface chemistry of the carbon surface; mild carbonization temperatures provide an oxygen-functional-group-rich surface with a high C-O/C=O ratio, which enhances the H₂O₂ selectivity. In contrast, the use of higher carbonization temperatures (700 °C) guarantees a highly graphitic structure and created a carbon defect-rich porous structure highly selective to the 4-electron route. As a consequence, the biochar prepared at 550 °C presents a better catalytic performance as the cathode material for the EF degradation of several organic pollutants in presence of Fe (II), presenting a high H₂O₂ production rate (796.1 mg/g/h at -0.25 V vs. RHE at pH of 1) and achieving an almost complete removal (99%) of phenol after 1 h (at -0.25 V vs. RHE, pH = 3, [Fe (II)] = 0.5 mM, electrolyte: ([Na₂SO₄] = 0.1 M). Ergan et al. [136] also analyzed the effect of the thermal activation of activated carbon fibers in the H₂O₂ electrogeneration and EF efficiency. In this case, the effect of the carbonization time (from 1 h to 10 h) at 900 °C and also the carbonization atmosphere (CO₂ or N₂) was analyzed, observing that the best H₂O₂ production and dye (acid orange 7) degradation (92.9%) was obtained when the fibers were activated in an N₂ atmosphere for 5 h due to a superior hydrophobicity, crystallite size, and larger electroactive surface area. Ramírez-Pereda et al. [137] compared two types of carbon materials: carbon fibers (CF) and vitreous carbon (VC) as electrodes for the electrogeneration of H₂O₂. The authors found that the generation of H₂O₂ is enhanced using CF (96% of H₂O₂ production efficiency) in comparison to VC (54% of H₂O₂ production efficiency), which was

attributed to possible competitive reactions. Xia et al. [138,139] analyzed the performance of a polyacrylonitrile-based carbon fiber brush (PAN-CFB) as a cathode electrode for ORR reduction to H_2O_2 and studied the effect of the electrochemical modification of its surface. For the unmodified PAN-CFB, the highest production of H_2O_2 (current efficiency > 90%) was observed at a potential of -0.9 V in an acidic medium, whereas for electrochemically modified PAN-CFB, it was obtained at -0.4 V. However, in a neutral medium (pH = 7), an electrochemically modified PAN-CFB cathode inefficiently generated H_2O_2 (41.2% of current efficiency) in comparison with unmodified PAN-CFB, which still retains the high current efficiency (>90%). This was explained based on the surface chemistry modification after the electrochemical modification treatment, which converts the N-containing groups from pyridinic-N to 2-pyridone—these newly ORR active sites were influenced by solution pH, leading to different pathways in acidic or neutral media. Gao et al. [140] synthesized porous carbon felt modified with polypyrrole (Ppy) and anthraquinone 2-sulfonate, which had a higher specific surface area with more active sites for ORR; in addition, the modification with Ppy decreases the charge transfer resistance. In turn, Chen et al. [141] showed that the adsorption capacity of the carbon-based cathode plays an important role in the EF degradation of tetracycline. For that, they activated carbon felt with KOH at different temperatures, finding that the surface area and the oxygen-containing functional groups on the surface increased in the KOH activation, which significantly enhanced the drug adsorption capacity (being the sample carbonized at 900 °C, which presents the highest adsorption capacity) and also produced the best tetracycline degradation. This highest degree of pollutant degradation (tetracycline 80% removal) was explained based on the 3D structure and good

adsorption capacity of activated carbon felt, which creates a space where the organic pollutant is adsorbed and preconcentrated near the active sites in charge of generating the H_2O_2 , and, consequently, exposed to a high concentration of hydroxyl radicals in the system of homogeneous catalysis. Wang et al. [142] obtained a complete degradation of dimethyl phthalate using KOH-activated graphite felt at 900 °C. This high performance was attributed to the high surface area, the presence of oxygenated functional groups, and the more hydrophilic surface generated by the activation of the KOH.

Want et al. [143] pointed out the importance of electrode conductivity on its EF performance. For that, CNT and graphene-modified carbon felt were synthesized and the effect of this modification was analyzed in the degradation of azo-dye (RB5) by EF reaction. The modification of the carbon felt with CNT and graphene increases the degradation rate by 1.2 and 1.5 times than with the original carbon felt, respectively, giving degradation rates of 55.3% and 70.1%, respectively, which was attributed to the improved roughening of the smooth carbon felt fiber (specific surface area), conductivity, and corrosion resistance.

Since the ORR reaction is crucial for the H_2O_2 production, the improvement in the O_2 supply to the active sites seems to be a key factor for the improvement in the EF efficiency, together with, as described above, the preconcentration of the pollutant near the H_2O_2 -producing active sites. In this sense, Özcan et al. [144] compared carbon felt with carbon sponge as cathode materials for the degradation of basic blue 3 (BB3) by EF process finding a faster BB3 degradation using the carbon sponge-based electrode, which was associated with the major H_2O_2 production. Sopaj et al. [145] also evaluated the performance of carbon sponges in comparison with carbon felt and stainless steel in sulfamethazine degradation. The

highest production of H_2O_2 , and, consequently, the highest degradation, was obtained using the carbon sponge instead of carbon felt, the classical cathode for the electro-Fenton process, and stainless steel. This improved catalytic performance of carbon sponge is attributed to the high specific surface area and porosity, which results in inadequate conditions for the mass transport of species of interest (O_2 and H_2O_2) throughout its 3D structure. Ganiyu et al. [146] also synthesized a carbon foam with high performance (total degradation and high mineralization) in the EF degradation of sulfanilamide, which was also attributed to the interconnected spherical cells' porous structure (Figure 1.5), with high-area B.E.T. that improved the diffusion of substances and gaseous oxygen in the pores and active sites of the cathode, together with an excellent hydrophobicity and conductivity. Nonetheless, it exhibited poor performance in the electro-regeneration of Fe^{2+} from the reduction of Fe^{3+} . This poor Fe^{2+} electro-regeneration of "gas diffuser materials" was also observed by Brillas et al. [147]. They demonstrated that H_2O_2 generation is important; however, it is not a uniquely important factor in the degradation of pollutants by EF. They analyzed the Fe(III)–EDDS-assisted EF degradation of butylated hydroxyanisole (BHA) using a carbon felt or an air-diffusion electrode as a cathode. They observed a much higher Fe(III) reduction efficiency in the novel Fe(III)–EDDS-assisted EF process in comparison with conventional EF. Moreover, the carbon felt resulted in a higher butylate hydroxyanisole degradation despite having an H_2O_2 generation lower than the air-diffusion cathode, which was attributed to the greater regeneration of Fe^{2+} observed using the carbon felt. To overcome this limitation, Chu et al. [148] used a dual cathode system: a gas diffusion electrode (GDE) to generate H_2O_2 by O_2 reduction and a graphite electrode for the regeneration of Fe^{2+} from Fe^{3+} and analyzed its performance as a

conventional single-cathode system in the degradation of 4-nitrophenol. They observed that the dual cathode system led to a more effective degradation of 4-nitrophenol, even with a lower initial Fe^{2+} concentration attributed to the rapid change between the $\text{Fe}^{3+}/\text{Fe}^{2+}$ couple in the dual cathode system. Since the main function of GDE is the electrogeneration of H_2O_2 , the regeneration of Fe^{2+} by the cathodic reduction in the single-cathode system is very weak, whereas this regeneration was enhanced by the reduction at the graphite cathode in the dual-cathode system. Chu et al. [149] have also improved the reduction of Fe^{3+} of graphite by its modification with acidified carbon nanotubes, obtaining a degradation of 94.7% of p-nitrophenol. The acidification of the carbon nanotube enhanced the performance in the Fe^{3+} reduction in comparison with the unmodified graphite cathode.

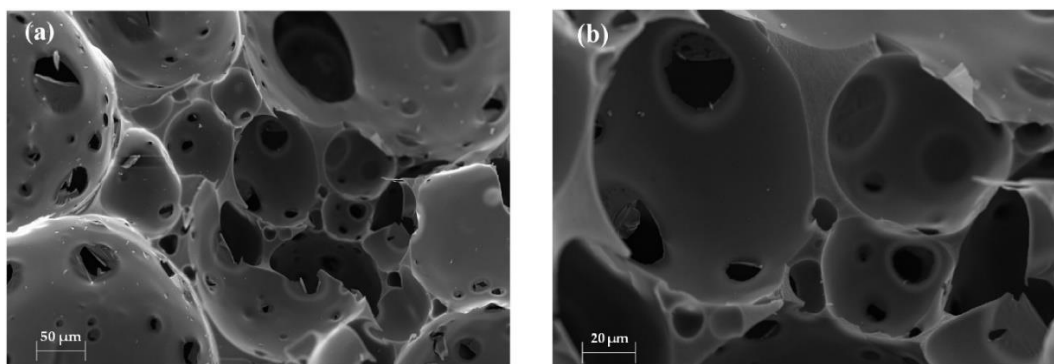


Figure 1.5. SEM images of carbon foam with low (a) and high magnification (b) [146].

Other advanced electrodes that improve the O_2 -supply are gas diffusion electrodes (GDE) evaluated by different researchers. Zarei et al. [150] synthesized

a three-dimensional graphene (3DG)-based carbon paper GDE for the removal of nalidixic acid. The nalidixic acid removal was 90%, which was attributed to a higher surface area with more irregularities and roughness than graphene oxide, allowing rapid diffusion of O_2 to achieve higher H_2O_2 production. On the other hand, Zhou et al. [151] used graphite felt, but in this case, as a floating cathode in which one side of a porous cathode is open to the air, and the other side is submerged in the aqueous solution instead of the traditionally submerged cathode. This novel strategy allows the creation of a three-phase boundary (O_2 gas, electrolyte, and cathode) allowing the usage of O_2 from both air and the electrolyte. This disposition is more energy-efficient and cost-effective in comparison with a GDE because avoids hydrophobic gas diffusion layer formation and the use of an air or O_2 pump. An ibuprofen degradation of 78.3%, with only 25.4% obtained in the conventional position. Liu et al. [152] used a GDE of graphene doped with N-doped carbon nanotubes as the cathode in the dimethyl phthalate removal (100%), finding that the graphene-nanotubes interaction significantly improves the ORR activity.

The hydrophobicity of the cathodes also so important in the EF reaction. Chu et al. [153] managed to completely degrade cefepime with a sandwich-like superhydrophobic carbon cathode composed of graphite, carbon nanotubes, and PTFE observing that the hydrophobicity of the electrode significantly affects the ORR to H_2O_2 (figure 1.6). Moreover, the prepared superhydrophobic carbon cathode resulted in an excellent reduction of O_2 to H_2O_2 , and, consequently, an excellent cefepime degradation, which is mainly dependent on the $OH\cdot$ production via Fenton reactions. Karatas et al. [154] also attributed the excellent performance of a carbon black electrode for the full degradation of atrazine to the superhydrophobic character of the electrode obtained because this high

hydrophobicity provides high H_2O_2 yield by supporting the mass transfer of oxygen molecules.

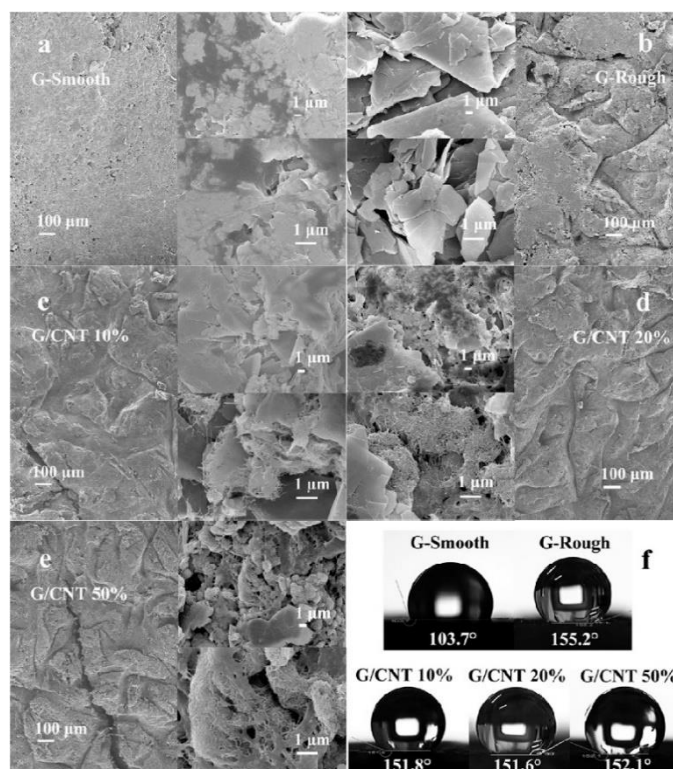


Figure 1.6. SEM images of “G-Smooth” cathode (a), “G-Rough” cathode (b), “G/CNT 10%” cathode (c), “G/CNT 20%” cathode (d), and “G/CNT 50%” cathode (e); Water contact angle images of the cathodes (f) [153].

Another strategy to improve EF performance is the use of metallic-doped electrode materials. Huang et al. [155] prepared a graphite felt-based cathode by first doping the graphite felt with Fe-Mn, then with active carbon, carbon black, and PTFE, and used it for the degradation of ciprofloxacin (figure 1.7). This modified

graphite felt-based cathode showed a higher degradation efficiency (95.4%) and wider operational pH range than their unmodified counterpart, which was principally associated with the larger surface area and volume pore as well as more active sites. Various researchers have also proposed doping carbon materials for improving EF efficiency. Ma et al. [156] doped multiwalled carbon nanotubes with Ag and Cu foam and noted that the high Ag dispersion improves the ORR and Fe^{2+} regeneration. Dung et al. [157] synthesized cobalt ferrite-coated carbon felt for the degradation of tartrazine (97%), where it is noted that the presence of $\text{Co}^{3+}/\text{Co}^{2+}$ and $\text{Fe}^{3+}/\text{Fe}^{2+}$ pairs improve the pollutant degradation; additionally, an additional Fenton catalyst was not needed in this test because the cathode fulfilled both functions. Paz et al. [158] used doped Vulcan XC72 with tungsten oxide nanoparticles and showed an improvement in the H_2O_2 production due to the surface being more acidic and hydrophilic. Fdez-Sanromán et al. [159] degraded 100% of pymetrozine with a cathode based on carbon felt and modified with carbon nanofibers doped with iron; the improvement was explained by the porous structure that was enhanced with the incorporated nanofibers, and it was also explained that the catalytic activity of a typical Fenton catalyst is more effective in the presence of iron.

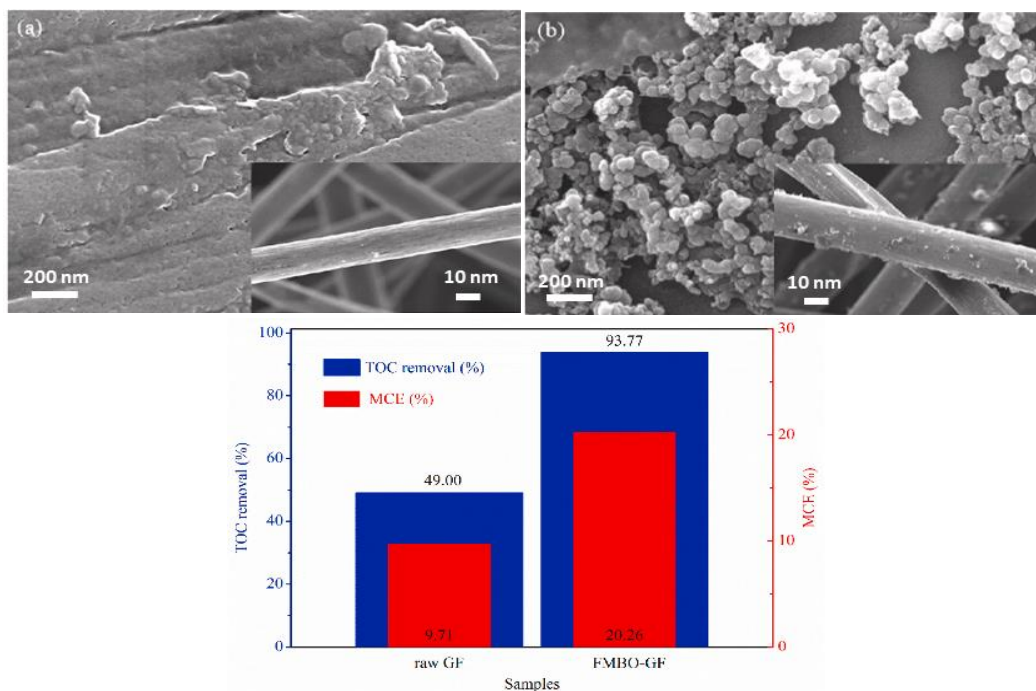


Figure 1.7. SEM images of (a) the unmodified graphite felt (raw GF) cathode, (b) the unmodified graphite felt (FMBO-GF) cathode, and (c) TOC removal efficiency and the mineralization current efficiency (MCE) of raw GF and FMBO-GF in 2 h under 25 mg L^{-1} initial pollutant concentration, pH 7, and 2 mA cm^{-2} current density [155].

In general, it could be summarized that the important parameters to take into account in the cathode preparation are the mesoporous structure that translates into the high surface area, the hydrophobicity that plays an important role in terms of the diffusivity of O_2 inside and outside of the electrode, as well as the regeneration of Fe^{2+} that happens in the electrode, and finally, the composition of the cathode, especially the presence of efficient nitrogenous groups toward ORR [160,161].

However, more in-depth research should be conducted, despite the extensive literature that supports the above. In this regard, Cordeiro stressed that graphite within a series of carbonaceous materials presented the smallest B.E.T. area and zero existence of oxygenated groups on the surface, and still showed the best efficiency of H_2O_2 , which was associated with its lamellar structure and low hydrophobicity leading to the faster release of H_2O_2 compared to more porous materials [162].

Another important parameter to consider in the cathode environment is the balance between the three reactants (oxygen, proton, and electron), which must have a molar rate of 2:1:2, respectively [163]. For this, it is important to start studying how to supply air/ O_2 , which is based on two types of aeration specifically.

1. Direct aeration in solution.
2. Aeration through a gas diffusing electrode (GDE).

Direct aeration in solution through bubbling is the traditional method; on the other hand, GDEs have the advantage that thanks to their porous structure and coexistence of the limits of three phases, they have solved the problems of low solubility and mass transfer of O_2 [164], which can accelerate ORR kinetics and gas-use efficiency, summarizing even better energy use. In general, GDEs can improve ORR mainly due to two main mechanisms [165].

1. The increase in the mass transfer of O_2 improves the contact of the gas with the catalyst and, therefore, the active sites for the ORR.

2. The increase in the mass transfer is not only in reference to O_2 but also between the catalyst and electrolyte, which promotes the release of H_2O_2 and active sites, improving the formation of the oxidizing species.

GDEs can be defined as porous electrodes in which the solid part is in contact with the gas phase, and then with the solution to be treated [166], which generates a three-phase interface in which the reactions of interest will happen. GDEs are mainly composed of a catalyst layer (in contact with the solution) and a diffuser (in contact with air or oxygen) (figure 1.8) [167]. At this point, it is important to clarify that a very thick layer of catalyst can decrease the output rate of H_2O_2 to the solution, which can cause it to degrade on the surface of the material. An alternative to adjusting the thickness of the layer or avoiding its limitation is to adjust the hydrophobicity of the catalyst [168].

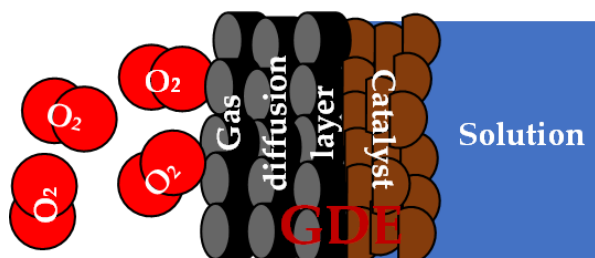


Figure 1.8. Schematic of a gas diffusion electrode adapted from [166].

As it has been pointed out, good results have been obtained in the EF degradation of a huge variety of emerging pollutants. However, since H_2O_2 production by the O_2 reduction at the cathode seems to be the limiting step, a deeper

investigation into ORR is necessary to better understand how cathode variations benefit or affect the efficiency of the EF process.

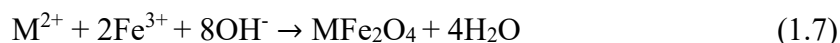
1.1.4.- Promising New Fenton Catalysts: Spinel Ferrites and Perovskites

Fenton catalysts with higher reaction rates are currently being sought to increase their overall efficiencies. Among these, spinel ferrites have attracted increasing interest in recent years due to their low cost, excellent catalytic activity, and magnetic properties that allow a facile separation and reutilization. In this section, the synthesis routes, advantages, and applications of spinel ferrites will be described.

There are different methods of synthesis within which the following stand out:

I. Chemical coprecipitation

Chemical coprecipitation is one of the most promising methods thanks to its ease of realization, as well as the possibility of mass production. It is mainly based on the co-precipitation of materials by a pH change. In general, this method consists of a mixture of precursors with the species of M^{2+} and M^{3+} (metal), to later precipitate the particles by the addition of a base (KOH, NaOH, or NH_4OH). It can be summarized in Equation (1.7) [169-172].



II. Sol-Gel Method

This method is one of the most used for the synthesis of nanoparticles due to its relatively low cost, operational simplicity, and high homogeneity of the material obtained. It is based on a series of reactions, summarized in the hydrolysis of a

metal alkoxide and the subsequent polycondensation of the hydroxyl groups formed, which produces a three-dimensional matrix [173-175], which must subsequently be subjected to thermal processes to improve the crystallinity of the nanoparticles.

III. Hydrothermal/Solvothermal

This process can be defined as a series of chemical reactions that occur in a closed system with one or more precursors in the presence of the solvent (water for the hydrothermal case), at a temperature above the boiling point of this [176]. This process has several advantages such as its operational simplicity, versatility, and low cost, among others [177,178]. An important advantage to highlight is the well-controlled diffusivity within the system [179], which allows good control of the structure and morphology of the synthesized particles.

From these synthesis methods, it has been possible to obtain different new Fenton-type catalysts at the nanometer scale, with different coatings and supports [180-182] in order to improve the efficiency of the hetero-Fenton process. It has been established that in the hetero-Fenton process, having a catalyst with a higher amount of transition-metal ions and a higher specific area leads to better Fenton activity [183,184]. Fe_3O_4 is currently being extensively investigated as a Fenton catalyst [185-187] due to its relatively high activity and easy magnetic separation. An essential advantage is the presence of Fe^{2+} and Fe^{3+} in a single material, due to its cubic structure where half of the Fe^{3+} ions occupied all of the tetrahedral sites and the Fe^{2+} ions are founded in the octahedral, allowing the presence of the two important species in Fenton processes. It has been reported in the literature that transition-metal ions occupying tetrahedral sites are catalytically inert, while those

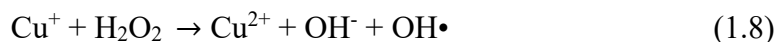
located at octahedral sites tend to determine catalytic activity, which is due to effect that the metal cations in these positions are found exclusively on the surface of the solid and thus take part in reactions to generate $\text{OH}\cdot$ radicals [188]. It has been suggested that the activation of H_2O_2 in the presence of magnetite takes place on the surface of the solid, i.e., the $\text{Fe}^{+3}\text{-OH}$ [189].

According to crystalline field theory, common metal cations have the following order of preference to occupy octahedral sites, $\text{Cr}^{3+} > \text{Ni}^{3+} > \text{Cu}^{3+} > \text{Al}^{3+} > \text{Mg}^{2+} > \text{Fe}^{2+} > \text{Co}^{2+} > \text{Fe}^{3+} > \text{Mn}^{2+} > \text{Zn}^{2+}$ [190]. The most studied are Fe, Mn, Cu, Ni, Zn, and Co [191,192].

Spinel ferrites have a general formula of $\text{A}^{+2}\text{B}^{+3}_2\text{O}^{-2}_4$ and a cubic lattice structure, where positions A and B are occupied by divalent and trivalent metal cations, according to the distribution of cations in the lattice, and the spinels can be normal, random, or inverse. In a normal spinel, tetrahedral sites are related to position A and octahedral sites to B. In a reverse spinel, tetrahedral sites are occupied by half of the B cations and the octahedral sites by all of the A cations. This distribution of cations is responsible for determining the magnetic properties of ferrites [193]. There are different types of spinel-structured materials; however, in this work, we will focus specifically on three of them: copper and cobalt ferrites and iron cobaltite.

Copper ferrite (CuFe_2O_4) is a well-known material with a reverse-spinel structure, which has a stable structure that reduces metals leaching, together with unique magnetic, electrical, physical, and chemical properties [194-197]. These properties make them a promising Fenton-type catalyst. Cu^+ ions have been

reported to have the ability to generate OH• radicals by a mechanism similar to that of Fe²⁺ according to Equations (1.8)–(1.10) [198].



Feng et al. [199] synthesized CuFe₂O₄ nanoparticles to be used as a Fenton catalyst in the degradation of sulfanilamide. They suggest that CuO is more reactive and effective than Fe³⁺ for the activation of H₂O₂ and, which is more important, can work in a higher pH range than conventional iron oxides. Moreover, Zhang et al. [200] observed that the leaching of Cu⁺² is 30 times lower in CuFe₂O₄ than with CuO. The promising performance of the copper spinel ferrite as a Fenton catalyst was pointed out by several authors. Suraj et al. [201] synthesized CuFe₂O₄ by the chemical coprecipitation method and used it as a heterogeneous Fenton catalyst for the treatment of pulp and paper wastewater, obtaining a 78% elimination of the chemical oxygen demand. Ding et al. [202] demonstrated that the morphology of the spinel is also very important. They synthesized hollow CuFe₂O₄ spheres with oxygen vacancies (figure 1.9), which demonstrated greater degradation of ciprofloxacin than normal CuFe₂O₄ particles. This better performance of hollow spheres was attributed, among other factors, to the synergistic oxygen vacancies and confinement effects on the catalyst surface. The oxygen vacancies produce highly active electron rich Cu⁺ species, which enhanced the H₂O₂ activation and, thus, the hydroxyl radical generation. In turn, the hollow structure is responsible for concentrating the organic pollutants near the •OH-generator active sites, improving the organic pollutant molecules/•OH radicals contact, and accelerating the

degradation. According to Deyou et al. [203], the particle size and surface area are more important factors than a crystalline structure for improving the catalytic efficiency of CuFe_2O_4 . López-Ramón et al. [204] evaluated the effect of calcination temperature on the catalytic activity of CuFe_2O_4 synthesized by the sol-gel method, finding that the calcination temperature has two opposite effects: the activity decreases with increasing temperature due to the increase in crystalline size and cubic to tetragonal transformation of ferrite and appearance of hematite; however, the metal leaching decreases with increasing calcination temperatures.

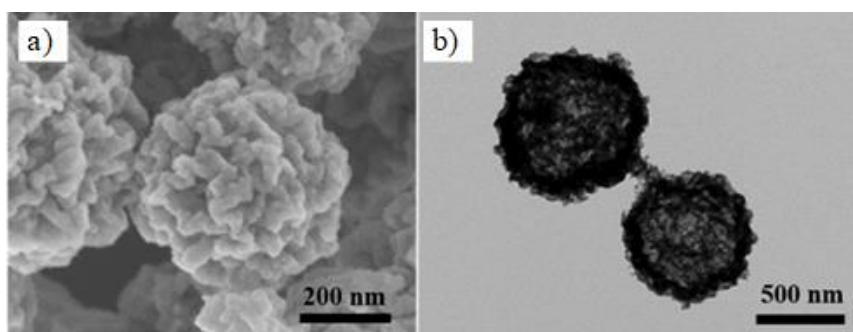
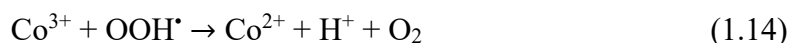
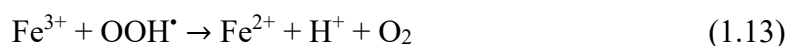
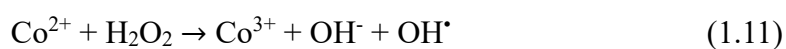


Figure 1.9. SEM (a) and TEM (b) of CuFe_2O_4 hollow spheres [202].

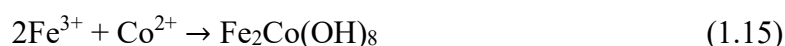
Cobalt ferrite (CoFe_2O_4), like other ferrites, has a high catalytic activity, stable crystal structure, low solubility, magnetic properties, as well as the ease of controlling the leaching of cobalt due to the strong interactions between metals, and the strong redox activity of Co with catalytic properties similar to those of noble metals (Pt, Ir, and Au) [205–208], which make it a promising material as a Fenton-like catalyst.

Feng et al. [209] synthesized monodispersed CoFe_2O_4 nanoparticles by a solvothermal method to evaluate them as a Fenton catalyst in the degradation of methylene blue, reaching a concentration decrease of 96.8%. The authors highlighted that the existence of Co^{2+} ions could favor the decomposition of H_2O_2 to $\text{OH}\cdot$ and subsequently give way to different reactions, as evidenced in Equations (1.11)–(1.14).



Sing and Singhal [210] demonstrated that the transition-metal doping of cobalt ferrites is a promising method for tuning the physical characteristics of catalysts and thus, enhancing their catalytic and magnetic properties. For that, the authors synthesized a series of Ru-doped cobalt ferrite nanoparticles by the sol-gel method for the photo-Fenton degradation of red Remazol textile dye, achieving a degradation of approximately 90% within 120 min. The mechanism proposed is based on the photocatalytic and Fenton character of the Ru-modified ferrite. An electron-hole pair is created by the irradiation of cobalt ferrite nanoparticles with visible light. The photogenerated electrons are responsible for the $\text{OH}\cdot$ generation from H_2O_2 and also the reduction of the Fe^{3+} cation on cobalt ferrite to Fe^{2+} , which further generates $\text{OH}\cdot$ radicals in the reaction with hydrogen peroxide. Vinosha et al. [211] also analyzed the photo-Fenton performance of CoFe_2O_4 nanoparticles obtained by means of chemical coprecipitation, achieving almost total degradation

of methylene blue (~99.3% in 75 min) under visible light irradiation. As an outstanding result, they proposed that the pH used in the synthesis was not an impact parameter that affected the morphology of the catalyst; however, it significantly affects the particle size (a more alkaline (pH > 9) medium, larger crystallite size). It has been proposed that the reactions that lead to the formation of CoFe₂O₄ by the chemical coprecipitation method in an aqueous medium, are those presented in equations (1.15) and (1.16) [212].



In turn, Iron cobaltite (FeCo₂O₄) has been also studied in environmental remediation and energy storage, thanks to its electrical properties and electrochemical performance [213]. In the energy storage field, Mohamed et al. demonstrated that iron cobaltite nanorods show a better capacity and lower overpotential as the cathode of lithium–O₂ batteries than other metal cobaltites (Mn, Ni, and Zn) [214] because the FeCo₂O₄ surface has the highest number of electropositive Co³⁺ active sites that improve the oxygen adsorption and Fe²⁺ in the tetrahedral site that favors the release of electrons to reduce oxygen. Yadav et al. [215] demonstrated that iron cobaltites are also efficient for supercapacitive and photocatalytic applications due to the valence states of the Fe³⁺/Fe²⁺ and Co³⁺/Co²⁺ species, which are considered active catalytic sites. These nanoflake-like iron cobaltites present a capacitance as high as 1230 F g⁻¹ (5 mV s⁻¹) with a good rate capability and superior cycling stability and also show a good photocatalytic performance achieving up to 94.19% degradation of crystal violet dye under sunlight illumination. However, despite this, very little work has been carried out

with reference to their evaluation as a Fenton-like catalyst. Zhang et al. [216] synthesized nitrogen-containing carbon/FeCo₂O₄ composites and analyzed their performances as Fenton catalysts for the degradation of methylene blue obtaining almost 100% removal in 10 min without pH adjustment, which was attributed to the uniform distribution of bimetals and nitrogen doping, which ensured the exposure of sites with high catalytic activity. Zhao et al. [217] analyzed the behavior of FeCo₂O₄/g-C₃N₄ as a photo-Fenton catalyst in the degradation of rhodamine B (RhB), obtaining 98% degradation in 45 min, which was attributed to a synergetic interaction between photocatalytic and Fenton-like reactions and the effective separation of the photogenerated charges. Therefore, it is proposed that the use of iron cobaltite as a pristine catalyst (without doping or support) in the Fenton reaction may be promising for future applications.

In general, spinel ferrites turn out to be attractive materials for catalytic activities in Fenton processes, mainly because they manage to improve the generation reaction of Fe²⁺ and achieve a synergistic effect between metal ions with valences similar to those of iron involved in the process (M²⁺, M³⁺, M: Metal).

Perovskites are other types of materials with promising catalytic activity that can be synthesized by the abovementioned methods (Chemical coprecipitation, sol-gel, and hydro/solvothermal) [218–221]. Perovskites can be defined as a type of mixed oxide with different formulations, binary (ABO), ternary (AA'BO or ABB'O), and quaternary (AA'BB'O), where A and B are cations sites occupied by alkali metals, alkaline-earth metals or rare-earth metals and transition metals, respectively [222].

Some perovskites have been studied in different Fenton-type reactions, for example, Carrasco-Díaz et al. [75] removed paracetamol by Fenton reaction using $\text{LaCu}_{1-x}\text{M}_x\text{O}_3$ ($\text{M} = \text{Mn}, \text{Ti}$) as the catalyst and determined that the most active catalyst was the one that contained the highest amount of Cu^{2+} at the surface. Moreover, they found that the titanium and manganese species seem not to be responsible for the improvement of activity with respect to the sample LaCuO_3 . Li et al. [223] synthesized a $\text{Ca}_{1-x}\text{FeO}_{3-\delta}$ perovskite and determined that the A-site cation can distort the FeO_6 octahedra in the perovskite and regulate the oxygen vacancies (OV) concentration; in this way, an A-site cation deficient of $\text{Ca}_{0.9}\text{FeO}_{3-\delta}$ results in an improved H_2O_2 activation for the degradation of tetracycline by a Fenton-like process. Similarly, Xie et al. [224] found that the copper incorporation in LaCoO_3 perovskite improved the electro-Fenton activity due to the enhancement of redox activity and oxygen vacancies, but in this case, by the substitution of B-site elements, which synergistically promoted the activation of hydrogen peroxide to a hydroxyl radical ($\text{OH}\cdot$). On the other hand, Rusevova et al. [225] degraded phenol via heterogeneous Fenton-like reactions using iron-containing LaFeO_3 , and BiFeO_3 perovskites, and made a comparison with data reported in the literature using, as a catalyst, nano-sized Fe(II, III) oxide particles, determining that the perovskites synthesized in this work had a higher catalytic activity. Zhao et al. [226] determined that BiFeO_3 supported in carbon aerogel (BFO/CA) with a three-dimensional (3D) structure improves the catalytic activity and stability of BiFeO_3 , resulting in an interesting strategy for the development of advanced catalysts for its possible application in Fenton processes.

In summary, perovskites are materials similar to spinel ferrites, and the contribution of two different metal species (formation of OVs) can be of interest to the Fenton process.

1.1.5.- Oxygen Reduction Reaction through Two Electrons (ORR $2e^-$)

The oxygen reduction reaction (ORR) has attracted attention in recent years due to its applicability in various fields of industry, both in energy storage and water treatment processes [227-229]. However, this review is focused on ORR as a route for the electrogeneration of H_2O_2 , a product that controls the efficiency of the electro-Fenton oxidation reaction.

In general, ORR involves two types of reactions [230]:

- I. Oxygen molecules that are converted directly into water ($4e^-$);
- II. Oxygen molecules that are initially reduced to peroxide and later to water ($2e^-$).

Analyzing the mechanism, it has been established that ORR $2e^-$ takes place in two steps involving two single proton-coupled electron transfers; in the first, there is the transfer of electrons and generation of the HOO intermediate linked to the active site (*), while in the second, H_2O_2 is produced (equations (1.17) and 1.18)).



However, H_2O_2 types formed at the cathode can react in three ways [231]:

- I. Being electro-reduced to H_2O at the cathode (usually at porous cathodes).

- II. Being oxidized to O_2 at the anode via $HO_2\cdot$ as an intermediate.
- III. Disproportionate to O_2 and H_2O in a non-electrochemical reaction.

Therefore, the objective in the design of catalysts for the electroproduction of H_2O_2 by ORR is to synthesize materials capable of binding the OOH^* intermediate with the appropriate strength; this is neither very strong nor weak to avoid the $4e^-$ pathway predominating [232].

The most studied way of improving the performance of the ORR $2e^-$ is the synthesis and optimization of the cathode materials, since, together with the generation of H_2O_2 , the current efficiency and, therefore, the energy consumption needs can also be taken into account [233]. In general, an optimal catalyst for ORR $2e^-$ must have good electrical conductivity, stability, and resistance to acid corrosion [234], properties associated with carbon-based materials [235]. Carbon materials have proven to have excellent properties for use as a cathode due to their high electrical conductivity, zero toxicity, low cost, high stability, and high catalytic activity [236-238]. However, although carbonaceous materials exhibit high selectivity toward H_2O_2 production, they have a slow kinetic toward this reaction, resulting in poor performance.

Different strategies to improve the electrochemical production of H_2O_2 have been recently studied and one of them consists of the deposition of other catalysts or metal oxides (MnO_2 , V_2O_5 , and CeO_2) on the surface of carbonaceous materials [155]. On the other hand, doping with heteroatoms such as oxygen (O), sulfur (S), nitrogen (N), and fluorine (F) is another strategy developed to increase the electrocatalytic performance of carbon materials. The carbon lattice doping with heteroatoms introduces defects to the carbon structure, modifying their atomic and

electronic structure and, thus, resulting in new promising materials for several energetic applications such as energy production and storage. However, the improvement mechanism of the introduction of these heteroatoms is still under debate by researchers worldwide. Some authors [239-243] found that the introduction of some oxygen functional groups can induce greater electrical conductivity and electrocatalytic activity thanks to the formation of a hydrophilic surface. Recently, different carbonaceous materials have been evaluated as ORR $2e^-$ catalysts, where the importance of the amount and type of oxygenated functional groups present on the surface of these has been evidenced, finding that a greater amount of carboxyl group translates into greater efficiency in H_2O_2 generation because it facilitates the displacement of the electron density of the active site, allowing a better interaction in the adsorption of O_2 [162,244]. In the same way, it has also been established that the higher the ratio of I_D/I_G in carbonaceous materials, the greater the production of H_2O_2 [245].

Zahoor et al. [246] indicated that the sp^2 electron configuration of graphite, graphene, and nanotubes are rich in π electrons which can be transferred without resistance in ORR; however, this electron flow is not enough to promote ORR. Thus, the heteroatom introduction (e.g., N) within its network induces π electron activation by bonding with the solitary electron pairs of N and providing negative charges. The carbon atoms adjacent to nitrogen have a high positive charge density, which increases the adsorption of oxygen and reactive intermediates, which results in enhanced ORR activity. Okamoto et al. [247] found by density-functional calculations that the adsorption of O_2 is more energetically favorable with the increase in the number of N around a C=C bond. Lagarreta-Mendoza et al. [248] proposed quantum phenomena for the explication of the ORR mechanism on N-

doped carbon-based electrocatalysts, which consists of the hybridization change in carbon atoms in the graphene lattice, from sp^2 to sp^3 . Nitrogen doping could induce a quantum tunnel phenomenon called nitrogen inversion, which consists of a process in which the lone pair of a sp^3 nitrogen atom migrates from one face of the atom, travels through the nucleus (quantum tunneling), and reappears on the other side. This inversion of nitrogen (due to network defects) allows the N atom to act as a “switch” that activates or stops the flow of electrons, generating active sites for ORR. The heteroatom–carbon interaction induces the activation of the electron π when joining with the lone pairs of N so that later, the O_2 molecules are reduced into the carbons positively charged by the neighboring N. Additionally, it has been observed that the insertion of a single atom of N does not, apparently, have enough influence to alter the carbon, so a minimum of three atoms are necessary to cause small differences in the length of the C and N bonds [248]. As reported in the literature, N-pyrrolic is more likely to promote ORR $4e^-$ by increasing electron donation capacity, while N-pyridinic has more tendency for ORR $2e^-$ [249]. Wang et al. [250] investigated the ORR $2e^-$ activity of multiwalled carbon nanotubes (MWCNT) with different degrees of oxidation by oxidation with concentrated sulfate and potassium permanganate at 20 to 60 °C for 1 h. They observed that the presence of oxygen groups created after the oxidation treatment enhances the H_2O_2 generation, with the MWCNT always being oxidized and more active than the nonoxidized counterpart. Among the oxidized MWCNT, the sample prepared at middle conditions (40 °C and 1 h) present the best H_2O_2 selectivity which was explained by the composition of its outer and inner structure. After the oxidation treatment, the outer surface is damaged by the creation of a large number of defects together with the introduction of oxygen functional groups such as COOH and C-

O-C that act as excellent active sites for the ORR $2e^-$, while the inner structure is maintained, ensuring its good electrical conductivity.

Similarly, it is reported that carbon doping with heteroatoms and transition metals can energetically optimize the charge and rotation density of carbon, helping to promote the activation and reduction of O_2 by weakening the O-O bond in the ORR process [251]. Some studies have found that N can change the mode of adsorption of O_2 , while sulfur (S) affects the binding capacity of the OOH intermediate by varying the spin density [252,253]. Ting Soo et al. [254] reviewed the electrochemical performance of modified graphene as an ORR electrocatalyst, and the spin density, charge, and energy gap were evaluated, finding that the microstructural properties of heteroatom-doped graphene and the high spin density or atomic charge density on adjacent carbon atoms are the key factors that contribute to the enhanced electrocatalytic activity. However, an over-dose of heteroatom doping has negative effects due to the formation of high-sized clusters that make electron transfer difficult. Zhang et al. [255] explained that any chemical species that is substituted for graphene can lead to a high asymmetry spin density and atomic charge density, which promotes ORR. However, by applying DFT calculations they demonstrated that ORR on N-doped graphene is a four-electron pathway. Conversely, Pei Su et al. [256] prepared N-doped graphene showing high H_2O_2 yield, selectivity, and low EEC. They also observed that the C=C and N-pyridinic bonds in N-graphene have the ability to enhance the onset potential, while the N-graphitic groups are responsible for the current disk obtained. Moreover, in EF reaction, they demonstrated that N-graphitic are responsible for the H_2O_2 generation, and N-pyridinic groups catalyze the $OH\cdot$ radical productions from H_2O_2 (figure 1.10). To further investigate the effect of the N-group amount and nature,

Pei Su et al. [257] controlled the N-surface chemistry of N-doped graphene (N-GE) via pyrolysis temperatures (200, 300, 400, 550, 750, and 950 °C) in the catalytic activity, observing that the value of electrons transferred in the ORR was in the range of 2 to 2.5 for temperatures of 200 to 400 °C, and from 2.5 to 2.7 for further temperature increases. Thus, the sample pyrolyzed at 400 °C presented the highest active N content and H₂O₂ selectivity and achieved the highest phenol degradation (93.58%). They proposed that the conversion of graphite N and pyridinic-N in N-GE plays an important role in the oxygen reduction reaction (ORR) and OH• conversion, while the conversion of pyridinic-N-oxide to pyridinic-N is critical for catalyst stability and sustainability.

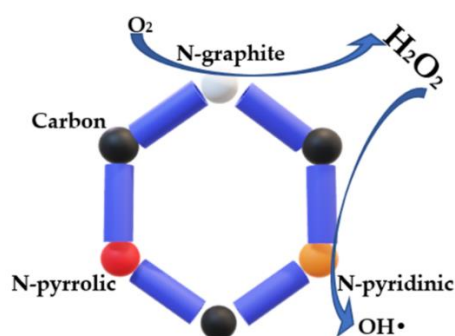


Figure 1.10. Schematic illustration of the effect of N-contained surface groups in the generation and activation of H₂O₂. Adapted from [256].

Qin et al. [258] and Xie et al. [259] evaluated N and O co-doped carbon material, highlighting the synergistic effect of the different species composed of the two atoms in question on the generation of H₂O₂. The pyridine-N groups combined with ether (C-O-C)/carboxyl (COOH) were highlighted, which presented lower adsorption energy of the intermediate *OOH, facilitating protonation toward H₂O₂.

Some studies [260] have also pointed out that the COOH and carbonyl ($-C=O$) groups are active for ORR $2e^-$, and mainly the COOH group.

Iglesias et al. [261] synthesized N-doped graphitized carbon nanohorns (N-CNH) via coating and controlled annealing of polydopamine (PDA) (figure 1.11) and analyzed its use as an electrode material for OEE $2e^-$. The excellent catalytic performance of N-CNH to perform ORR $2e^-$ is explained based on the high surface area and accessible porosity of the CNH scaffold, a good distribution of different N-contained surface groups, and improved conductivity and easy electron transfer. The authors also highlight that the microporosity and the specific pyridinic/pyrrolic ratio are crucial factors affecting the ORR route. The microporosity decreases the residence time of H_2O_2 on the material avoiding further reduction to H_2O . The relative types of N atoms also affect the electrocatalytic performance. However, the influence is dependent on the pH. At an acidic pH, protonation of the N-pyridinic occurs which compromises the ability to weaken the O-O bond producing H_2O_2 as the main product while at a neutral or alkaline pH, a reduction in selectivity toward H_2O_2 is observed because the formation of H_2O by the O-O breaking becomes progressively more available.

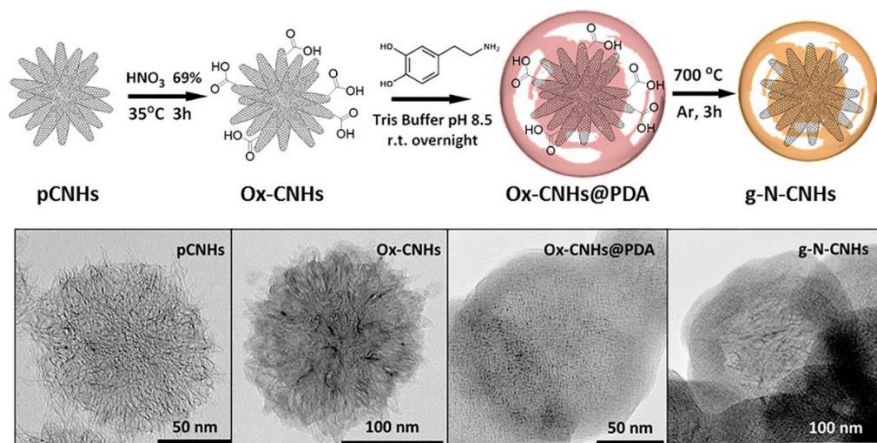


Figure 1.11. Synthesis of N-doped graphitized carbon nanohorns and TEM images at each stage of the synthesis [261].

Chen et al. [262] also demonstrated that porosity is so important in controlling the selectivity of the process. Chen et al. determined that activated carbon with abundant micropores and a high surface area is better for high ORR activity via $4e^-$, while carbon and graphite black with a smaller specific area tend to catalyze ORR via $2e^-$. Granules with more micropores facilitated the ORR process and caused a further reduction of H₂O₂, leading to less H₂O₂ generation. Similarly, Wenhui He et al. [263] analyzed the effect of the 3D hierarchical porosity on N-doped carbon on the catalytic performance. For that, they prepared N-doped carbon with hierarchical micro-, meso-, and macroporosity by the use of 3D macroporous templates and endogenous pore-generating agents with the assistance of KOH activation. It was concluded that the catalytic efficiency of nitrogen-doped species in ORR highly depends on their degree of exposure to the carbon matrix and that the hierarchical structure can strongly influence the rate of diffusion of O₂ and rapid release of H₂O₂.

In general, it can be concluded that there are some important requirements to obtain carbonaceous materials with high catalytic activity for ORR $2e^-$ such as high porosity (subject to further investigation), large surface area, presence of oxygenated groups, bonds C=C, N-pyridinic, and a greater amount of C atoms sp^3 hybridization.

Zhang et al. [264] synthesized interface atomic domains (IAD) of C/N/O atoms (pyridine-N, C=O), from biomass tar by pyrolysis, oxidation, and doping. With this assured an ordered structure (by pyrolysis), with functional groups C=O (oxidation), which results as a host for the generation of N-pyridinic (doping). As a result, it was found that the material obtained had high selectivity for ORR $2e^-$ (N-pyridinic) and an excellent mass transfer of O_2 (C=O and ordered structure).

Another strategy is the doping of porous carbon materials with transition metals which can accelerate the redox reaction by the action of metal ions, thereby increasing the rate of electron transfer. Similarly, nonprecious metals have proven to have an excellent capacity for ORR [265]. It has been shown that compared to bare carbon, metal/carbon compounds have a noticeable improvement toward ORR [266]. Metal/carbon catalysts can adsorb O_2 in two ways, which translates into a greater or lesser efficiency toward reduction via 2 or 4 electrons [267-270].

- I. Lateral adsorption leads to a longer bond length and therefore weakens the O=O bond, giving as a product, H_2O (figure 1.12).
- II. Adsorption at the end, where oxygen is adsorbed in the form of OOH, which can produce H_2O_2 and H_2O (Figure 1.12).

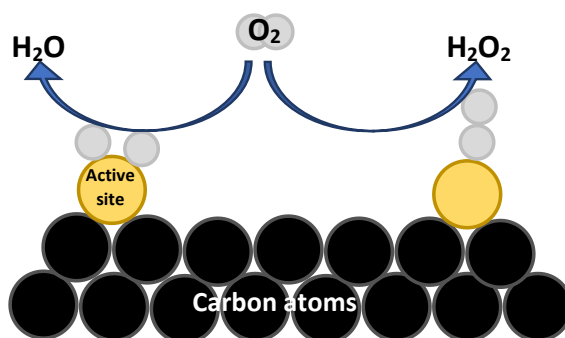


Figure 1.12. ORR pathways depend on the geometric structure of catalysts. Adapted from [271].

Thus, to obtain metal-doped materials selective to the electrogeneration of H_2O_2 , the end-on adsorption of O_2 molecules on the catalyst surfaces need to be promoted. One strategy is the isolation of the active atomic metal sites [271]. For that, three pathways have been developed: (i) alloying an active metal with an inert metal that can induce geometric isolation of the active metal where the O_2 is end-on adsorbed; (ii) the partial poisoning of the active metal surface with an inert phase or molecules, e.g., the coating of Pt nanoparticles with amorphous carbon by CVD (figure 1.13); and (iii) the synthesis of atomically dispersed catalysts.

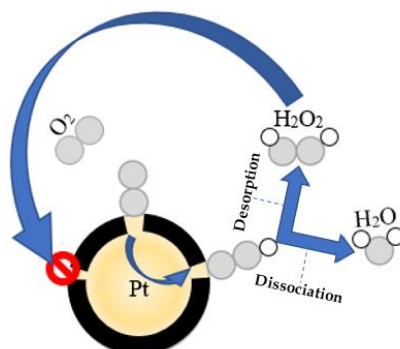


Figure 1.13. Effect of a carbon coating on Pt/C catalysts surface by acetylene CVD, and H₂O₂ selectivity depending on the CVD operation time for Pt/C catalysts. Adapted from [272].

Some nonprecious metals, used as a doping material in carbonaceous matrices, despite increasing costs, are offset by high dispersion in the matrix, which favors the production of H₂O₂ [273]. In general, although iron may be an ideal metal to regulate the binding energy of the intermediate *OOH with the carbon matrix, it has been shown that it has a strong tendency toward the route of 4e⁻ [274,275]. Co is one of the metals studied for ORR, demonstrating greater selectivity toward two electrons compared to Fe [276]. On the other hand, Chen et al. [277] investigated the incorporation of Cu atoms in mesoporous N/O-codoped graphitic carbon catalysts with a tailored mesoporosity concluding that the H₂O₂ production depends on the number of C atoms bound to the O atom, which increases by doping with a tiny amount of N. However, the inclusion of copper significantly decreased the selectivity toward H₂O₂. Cu, having a strong binding with oxygen, quickly generates blockages of the active sites due to the O and OH species generated in the reaction [278]. In other studies, Zhang et al. [279] synthesized Au@Cu_{2-x}S-CNTs

core-shell deficient in Cu and determined that the catalysts exhibited higher ORR activity and selectivity toward H_2O_2 , associated with the Cu defects, which (from theoretical calculations) decreases the energy of reaction of OOH^* . Wang et al. [280] probed that the nanostructure of the Cu active site is the key to the success of the catalyst; if the active site and host effect are optimally coordinated, it will certainly show considerable potential in the catalytic performance. For that, the authors designed electron-deficient and electron-rich Cu active sites by the regulation of nitrogenous ligand solvents and analyzed the effect in the capture and activation of the $\text{C}\equiv\text{C}$ bond of acetylene. The results showed that the Cu sites, stabilized by N-pyrrolic, generate electron-deficient states that improve the activation capacity of acetylene and, thus, the catalytic activity (hydrochlorination). In turn, Hyo-Noh et al. [281] determined that Cu can strongly increase the chemical bonding with O (unfavorable for ORR $2e^-$) and thus bare Cu particles cannot catalyze the ORR at all, but this energy can be easily controlled by the coating with N-doped carbon shells (regulated through CO_2 treatment), resulting in ORR activity comparable to the Pt (111) surface.

Therefore, recently, the investigate into other types of metals has begun. Lenarda et al. [282] investigated different metal (Fe, Ni, Mn, and Co) nanoparticles embedded with an N-doped graphitic carbon and determined that the nature of the metal dictates the type of final surface N-group by obtaining different N-pyridinic/N-pyrrolic ratios, which is essential for H_2O_2 selectivity. The optimal ratio was obtained when Co was used.

Thus, Co is presented as a promising metal to increase the ORR activity without losing H_2O_2 selectivity. In a recent study, Gao et al. [283] prepared single-atom transition metals anchored in nitrogen-doped graphene citing that Co could be an

active site for the ORR $2e^-$ pathway since the bond with the OOH^* intermediate has optimized adsorption energy, neither too strong nor too weak, in addition to presenting a higher OOH^* to O^* reduction barrier than that achieved with iron and magnesium atoms. However, Cao et al. [284] evaluated Co nanoparticles supported on N-doped holey graphene aerogel in ORR, determining that the reaction pathway was given by a 4-electron process. Collman et al. [285] studied the geometric effect of cobalt on two different porphyrin structures (monomeric and dicobalt), where the monomeric consists of a Co atom surrounded by N, with which they were able to determine that the selectivity toward H_2O_2 is favored mainly by the isolated site above the electronic effects, since in both cases, the union of the OOH^* is the same. In turn, Ferrara et al. [286] studied the effect of pyrolysis temperature against the selectivity of H_2O_2 in Co-encapsulated nanoparticles on a nitrogen-doped carbon matrix, determining those higher temperatures ($>800\text{ }^\circ\text{C}$) lead to greater H_2O_2 selectivity, attributed to a larger degree of graphitization and pyrrolic N content. However, the N and O content progressively decreases with increasing pyrolysis temperature, leading to a lower ORR current density.

However, some of the problems of catalysts doped with nonprecious metals are related to their instability in selectivity toward H_2O_2 with pH. At acidic pHs, the $2e^-$ route is favored; however, at basic pHs, the $4e^-$ route is given. Therefore, the use of metal oxides such as magnetite has been proposed to improve the ORR $2e^-$ activity of catalysts based on carbonaceous materials [287].

With the above, and considering the other limitations associated with both the ORR $2e^-$ and Fenton reactions, the doping of carbonaceous materials with structures of the spinel ferrite type is proposed as a viable solution, where the desired bifunctionality is achieved, both for obtaining H_2O_2 and its subsequent

decomposition (Fenton) to $\bullet\text{OH}$. This fact, together with the metal active site control and the spontaneous radical $\bullet\text{OH}$ production in controlled N-doped carbons, opens the gate to the design of new bifunctional catalysts for the simultaneous production of H_2O_2 and its conversion to $\bullet\text{OH}$ radicals for the electro-Fenton oxidation of organic pollutants in the water.

1.1.6.-Bifunctional Electro-Fenton Catalyst for Direct $\text{OH}\bullet$ Formation

Despite the advances achieved in EF and ORR for the on-site production of H_2O_2 , there are still some problems to overcome such as the secondary pollution related to the Fenton catalysts [288,289] and the requirement of two catalysts: one selective to the reduction of oxygen to H_2O_2 and another Fenton-type catalyst for the transformation of H_2O_2 to hydroxyl radicals. Recent efforts are being made to develop materials with dual functionality for the electroreduction of oxygen to H_2O_2 and Fenton catalysis. However, the preparation of heterogeneous EF catalysts with high selectivity and activity toward ORR via the two-electron pathway is challenging since the active sites for Fenton catalysis are mainly transition metals that usually catalyze oxygen reduction via the $4e^-$ route without the production of H_2O_2 .

One strategy to develop bifunctional catalysts capable of generating and activating H_2O_2 is the doping of carbon materials with different heteroatoms or carbon structures. Li et al. [290] demonstrated that heteroatom-doped carbon materials can convert H_2O_2 to $\bullet\text{OH}$ radicals without the need for a Fenton metal catalyst. For that, the authors synthesized an O, F-codoped carbon bifunctional catalyst by the carbonization of polyvinylidene fluoride and proposed that the H_2O_2 generation depends principally on the ratio C-O/C=O (optimal value in 4), while

the activation to $\text{OH}\cdot$ occurs on the semi-ionic C-F bonds obtaining a sulfamerazine degradation of 90.1% in 3 h during the metal-free EF process. A similar fact was observed by Yang et al. [291] using N-doped graphene. They found that the bifunctional effect is attributed to the presence of N-graphite, which influences the H_2O_2 generation and N-pyrrolic responsible for H_2O_2 activation. Similarly, Haider et al. [292] synthesized, in situ, an electrode from polyaniline-derived N-doped carbon nanofibers with bifunctional activity in EF, which was attributed to the content of C=C, oxygen groups, and N-graphitic, which enhanced the H_2O_2 generation and which can be further activated by N-pyridinic to generate the $\text{OH}\cdot$ radicals. In turn, Qin et al. [293] used it as a bifunctional metal-free cathode based on O-doped carbon nanotubes. They attributed the excellent metal-free EF behavior of this catalyst to the defects and the C-sp³ that enhances the oxygen adsorption promoting the H_2O_2 production and to the -C=O active sites that are associated with the $\text{OH}\cdot$ production. Chen et al. [294] found that groups BC₃ and BC₂O present in a boride-activated carbon enhanced the oxygen adsorption and facilitated the desorption of $\cdot\text{OOH}$, improving the H_2O_2 generation but also promoting the in situ conversion to $\text{OH}\cdot$. Xie et al. [295] showed that the reduced graphene oxide could improve the H_2O_2 generation, while the MOF (MIL-88A) and carbon felt (MIL-88A/CF) could activate the H_2O_2 to $\text{OH}\cdot$; thus the cathode rGO/MIL-88A/CF resulted in an excellent bifunctional catalyst.

The introduction of different metals in the carbon matrix for use as bifunctional catalysts has also been studied from simple immobilization to more complex structures such as core-shell. Zhang et al. [296] immobilized Fe₃O₄ in a gas diffusion electrode (GDE) and used it as a rotating cathode for the EF removal of tetracycline. They concluded that the rotating disk gas diffuser greatly enhanced the

mass transfer providing a high efficiency in the H_2O_2 generation, whereas the Fe_3O_4 active phase was capable of dissociating the H_2O_2 to $\text{OH}\cdot$. Cui et al. [297] also developed a $\text{Fe}_3\text{O}_4/\text{MWCNTs}/\text{CB}$ (carbon black) GDE, which has high performance in the production and activation of H_2O_2 . The presence of CB enhanced the H_2O_2 production, whereas its activation to $\text{OH}\cdot$ was ascribed to $\equiv\text{Fe}(\text{II})$ on the surface of $\text{Fe}_3\text{O}_4/\text{MWCNTs}$. Moreover, an improvement in the regeneration of Fe^{2+} was observed due to the high-speed charge channel of MWCNT (figure 1.14). On the other hand, Hu et al. [298] synthesized a bifunctional catalyst based on Fe_3C and FeN nanoparticles encapsulated by porous graphitic layers and determined by density function calculations that the active sites for H_2O_2 generation were the Fe_3C , and the activation to $\text{OH}\cdot$ depend on FeN_x sites. Cao et al. [299] designed and synthesized FeO_x nanoparticles embedded into N-doped hierarchically porous carbon for its use as a bifunctional catalyst against phenol, sulfamethoxazole, atrazine, rhodamine B, and 2,4-dichlorophenol in neutral water solution. They found that the presence of N pyridinic and N-pyrrolic increased the H_2O_2 selectivity, and the FeO_x nanoparticles could enhance the electron transfer to improve the $\text{OH}\cdot$ production. Moreover, the $\text{Fe}^{3+}/\text{Fe}^{2+}$ cycle could be enhanced by the strong interaction between N-doped porous carbon and FeO_x NPs.

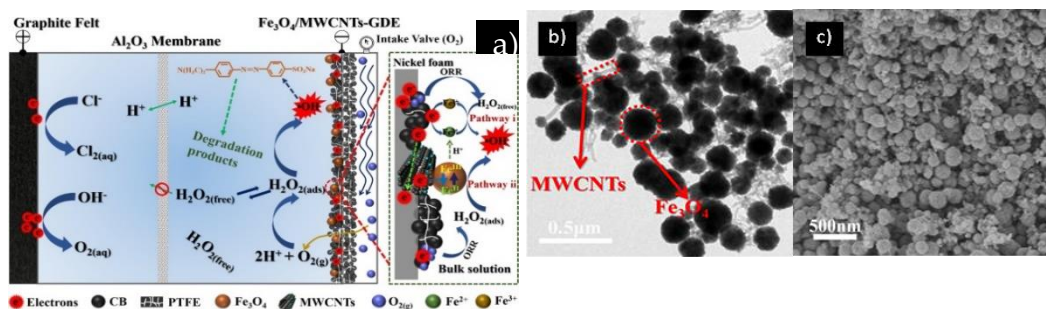


Figure 1.14. (a) Possible heterogeneous EF catalytic mechanisms using $\text{Fe}_3\text{O}_4/\text{MWCNTs}/\text{CB}$ GDE dual-composite. (b) TEM and (c) SEM images of $\text{Fe}_3\text{O}_4/\text{MWCNTs}/\text{CB}$ composite [297].

Another proposal to improve the production and activation of H_2O_2 has been the use of catalysts with the presence of two or more different metal or metallic species that can moderate the activity of alone metals and thereby obtain better bifunctional activity. Ghasemi et al. [300] prepared a cathode with carbon nanotubes (CNTs) and CuFe nano-layered double hydroxide showing that the incorporation of CNTs improves the H_2O_2 generation, and the atoms of Cu and Fe were responsible for the generation of $\text{OH}\cdot$. Cui et al. [301] used $\text{Cu}/\text{CuFe}_2\text{O}_4$ integrated graphite felt as a bifunctional cathode and attributed the H_2O_2 generation to Cu^0 and the $\text{OH}\cdot$ production to primary Fe^{2+} ions. Moreover, the $\text{Fe}^{3+}/\text{Fe}^{2+}$ redox cycles could be accelerated by the electron donation of Cu^0 and Fe^0 , and even Cu^+ . Similarly, Luo et al. [302] degraded 98.1% of tetracycline in 2 h using Cu-doped $\text{Fe}@\text{Fe}_2\text{O}_3$ core-shell nanoparticles loaded on nickel foam as a cathode, and determined that Cu^0 and Fe^0 react with O_2 producing H_2O_2 ; Fe^{2+} and Cu^+ are responsible for the $\text{OH}\cdot$ generation from the in situ generated H_2O_2 . Moreover, they proposed that Fe^{2+} and Cu^{2+} additional EF active sites could be generated from the

redox process between Cu^+ and Fe^{3+} and the replacement reaction between Cu^{2+} and Fe^0 . Sun et al. [303] synthesized a nickel foam cathode co-modified with core-shell CoFe alloy/N-doped carbon (CoFe@NC) and carbon nanotubes (CNTs), where the production of H_2O_2 was attributed to CNTs and the activation to $\text{OH}\cdot$ to CoFe@NC through Fe^{2+} and Co^{2+} oxidation to Fe^{3+} and Co^{3+} , which are again reduced by Co^0/Fe^0 and the electric field. Similarly, Yu et al. [304] determined that the carbon felt was the ORR catalyst selective to H_2O_2 , and the Co and Fe atoms generated the OH (Co > Fe) in the cathode of CoFe-layered double hydroxide/carbon felt with bifunctional activity. Li et al. [305] prepared an electrode doped with Fe and Mn oxides coated with a carbon layer and determined that the carbon material was responsible for H_2O_2 generation, and the metals for $\text{OH}\cdot$ production. It was also noted that the presence of Mn considerably improves the regeneration of $\text{Fe}^{3+}/\text{Fe}^{2+}$ due to Mn that could transfer an electron to Fe to accelerate the cycle.

Bifunctional catalysts using a 3-electron ORR pathway have also been recently proposed as an improved alternative. Xiao et al. [306] reported a catalyst capable of directly generating $\text{OH}\cdot$ via a 3-electron pathway with FeCo alloy encapsulated by carbon aerogel. This performance was principally associated with the generation of H_2O_2 by the 2 electron ORR of the COOH group present in the graphite shell, followed by the reduction by one electron toward $\text{OH}\cdot$. This 3-electron pathway can be regulated by the electrons from the encapsulated metals.

1.1.7.- CONCLUSIONS

This chapter summarizes the different strategies for the design of catalysts with high performance toward Fenton processes and the ORR by the $2e^-$ route as a mechanism to improve the efficiency of the electro-Fenton process, finally focusing on the design of bifunctional electro-Fenton catalysts for the production and activation of H_2O_2 .

The key to obtaining high efficiency of ORR $2e^-$ is the proper use of structures that allow the end-on adsorption of O_2 , oxygenated functional groups on the surface of the catalyst, as well as the inclusion of doping atoms that allow synergistic effects toward the selectivity of H_2O_2 . Although the strategies developed have been based on the amount of H_2O_2 produced and the ORR pathway, some research has opened a gate to the possibility that the morphology of the surface of the catalyst has a much greater impact than expected. Therefore, it is necessary to evaluate, in detail, not only the chemical composition but also other factors such as hydrophobicity, roughness, and/or porosity of the catalyst surface. In general, there are several parameters to consider in the search for an ideal catalyst for ORR $2e^-$, but the amount of N-pyridinic, hydrophobicity, roughness, and doping metal, are so far the most crucial.

As Fenton catalysts, different Fenton-type metals and bimetallic-based materials have been reviewed, raising spinel ferrites as an alternative of interest to provide the bifunctionality for carbonaceous materials, by improving selectivity toward ORR $2e^-$, maintaining the metal ions necessary for Fenton-type catalytic activity suitable for generating $OH\cdot$ obtained from the H_2O_2 generated in the same structure of the catalyst.

Finally, bifunctional electro-Fenton catalysts are described for the production and activation of H₂O₂. The main strategies are focused on the use of heteroatom-doped carbon materials or carbon-encapsulated Fenton-type metals/carbon composites that moderate the metal's activity and provide an active site for H₂O₂ generation by the ORR 2e⁻ route, presenting metal sites for the activation of in situ generated H₂O₂ to OH• radicals required for the degradation of organic pollutants.

BIBLIOGRAPHY

- [1] Li, L.; Zhao, X.; Liu, D.; Song, K.; Liu, Q.; He, Y. Occurrence and ecological risk assessment of PPCPs in typical inflow rivers of Taihu lake, China. *J. Environ. Manag.* 2021, 285, 112176. <https://doi.org/10.1016/j.jenvman.2021.112176>.
- [2] Archana, G.; Dhodapkar, R.; Kumar, A. Ecotoxicological risk assessment and seasonal variation of some pharmaceuticals and personal care products in the sewage treatment plant and surface water bodies (lakes). *Environ. Monit. Assess.* 2017, 189, 446. <https://doi.org/10.1007/s10661-017-6148-3>.
- [3] Luo, Y.; Guo, W.; Ngo, H.H.; Nghiem, L.D.; Hai, F.I.; Zhang, J.; Liang, S.; Wang, X.C. A review on the occurrence of micropollutants in the aquatic environment and their fate and removal during wastewater treatment. *Sci. Total Environ.* 2014, 473–474, 619–641. <https://doi.org/10.1016/j.scitotenv.2013.12.065>.
- [4] UNESCO. Emerging Pollutants in Water and Wastewater. 2020. Available online: <https://en.unesco.org/emergingpollutantsinwaterandwastewater> (accessed on 1 July 2022).
- [5] Molina, C.B.; Sanz-Santos, E.; Boukhemkhem, A.; Bedia, J.; Belver, C.;

- Rodriguez, J.J. Removal of emerging pollutants in aqueous phase by heterogeneous Fenton and photo-Fenton with Fe₂O₃-TiO₂-clay heterostructures. *Environ. Sci. Pollut. Res.* 2020, 27, 38434–38445. <https://doi.org/10.1007/s11356-020-09236-8>.
- [6] Mailler, R.; Gasperi, J.; Coquet, Y.; Buleté, A.; Vulliet, E.; Deshayes, S.; Zedek, S.; Mirande-Bret, C.; Eudes, V.; Bressy, A.; et al. Removal of a wide range of emerging pollutants from wastewater treatment plant discharges by micro-grain activated carbon in fluidized bed as tertiary treatment at large pilot scale. *Sci. Total Environ.* 2016, 542, 983–996. <https://doi.org/10.1016/j.scitotenv.2015.10.153>.
- [7] González-Mira, A.; Torreblanca, A.; Hontoria, F.; Navarro, J.C.; Mañanós, E.; Varó, I. Effects of ibuprofen and carbamazepine on the ion transport system and fatty acid metabolism of temperature conditioned juveniles of *Solea senegalensis*. *Ecotoxicol. Environ. Saf.* 2018, 148, 693–701. <https://doi.org/10.1016/j.ecoenv.2017.11.023>.
- [8] Kazakova, J.; Villar-Navarro, M.; Ramos-Payán, M.; Aranda-Merino, N.; Román-Hidalgo, C.; Bello-López, M.Á.; Fernán-dez-Torres, R. Monitoring of pharmaceuticals in aquatic biota (*Procambarus clarkii*) of the Doñana National Park (Spain). *J. Environ. Manag.* 2021, 297, 113314. <https://doi.org/10.1016/j.jenvman.2021.113314>.
- [9] Majumder, A.; Gupta, B.; Gupta, A.K. Pharmaceutically active compounds in aqueous environment: A status, toxicity and insights of remediation. *Environ. Res.* 2019, 176, 108542. <https://doi.org/10.1016/j.envres.2019.108542>.
- [10] Rashid, S.S.; Liu, Y.Q. Comparison of life cycle toxicity assessment

- methods for municipal wastewater treatment with the inclusion of direct emissions of metals, PPCPs and EDCs. *Sci. Total Environ.* 2021, 756, 143849. <https://doi.org/10.1016/j.scitotenv.2020.143849>.
- [11] Chaturvedi, P.; Shukla, P.; Giri, B.S.; Chowdhary, P.; Chandra, R.; Gupta, P.; Pandey, A. Prevalence and hazardous impact of pharmaceutical and personal care products and antibiotics in environment: A review on emerging contaminants. *Environ. Res.* 2021, 194, 110664. <https://doi.org/10.1016/j.envres.2020.110664>.
- [12] Rodil, R.; Quintana, J.B.; Concha-Graña, E.; López-Mahía, P.; Muniategui-Lorenzo, S.; Prada-Rodríguez, D. Emerging pollutants in sewage, surface and drinking water in Galicia (NW Spain). *Chemosphere* 2012, 86, 1040–1049. <https://doi.org/10.1016/j.chemosphere.2011.11.053>.
- [13] An, W.; Duan, L.; Zhang, Y.; Zhou, Y.; Wang, B.; Yu, G. Pollution characterization of pharmaceutically active compounds (PhACs) in the northwest of Tai Lake Basin, China: Occurrence, temporal changes, riverine flux and risk assessment. *J. Hazard. Mater.* 2022, 422, 126889. <https://doi.org/10.1016/j.jhazmat.2021.126889>.
- [14] Rodriguez-Mozaz, S.; Vaz-Moreira, I.; Varela Della Giustina, S.; Llorca, M.; Barceló, D.; Schubert, S.; Berendonk, T.U.; Michael-Kordatou, I.; Fatta-Kassinos, D.; Martinez, J.L.; et al. Antibiotic residues in final effluents of European wastewater treatment plants and their impact on the aquatic environment. *Environ. Int.* 2020, 140, 105733. <https://doi.org/10.1016/j.envint.2020.105733>.
- [15] Kümmerer, K. Antibiotics in the aquatic environment—A review—Part I. *Chemosphere* 2009, 75, 417–434.

- <https://doi.org/10.1016/j.chemosphere.2008.11.086>.
- [16] Gelband, H.; Miller-Petrie, M.; Pant, S.; Gandra, S.; Levinson, J.; Barter, D.; White, A.; Laxminarayan, R. The State of the World's Antibiotics 2015. In *Justice A Distance*; Center for Disease Dynamics, Economics & Policy 2015; pp. 1–30. <https://doi.org/10.1017/cbo9781316336267.001>.
- [17] Bengtsson-Palme, J.; Kristiansson, E.; Larsson, D.G.J. Environmental factors influencing the development and spread of antibiotic resistance. *FEMS Microbiol. Rev.* 2018, 42, 68–80. <https://doi.org/10.1093/femsre/fux053>.
- [18] Dong, J.; Yan, D.; Mo, K.; Chen, Q.; Zhang, J.; Chen, Y.; Wang, Z. Antibiotics along an alpine river and in the receiving lake with a catchment dominated by grazing husbandry. *J. Environ. Sci.* 2022, 115, 374–382. <https://doi.org/10.1016/j.jes.2021.08.007>.
- [19] Wilke, C. Many of the World's Rivers are Flush with Dangerous Levels of Antibiotics 2019. *Science News*, 14 June 2019.
- [20] Gros, M.; Catalán, N.; Mas-Pla, J.; Čelić, M.; Petrović, M.; Farré, M.J. Groundwater antibiotic pollution and its relationship with dissolved organic matter: Identification and environmental implications. *Environ. Pollut.* 2021, 289, 117927. <https://doi.org/10.1016/j.envpol.2021.117927>.
- [21] Wang, K.; Zhuang, T.; Su, Z.; Chi, M.; Wang, H. Antibiotic residues in wastewaters from sewage treatment plants and pharmaceutical industries: Occurrence, removal and environmental impacts. *Sci. Total Environ.* 2021, 788, 147811. <https://doi.org/10.1016/j.scitotenv.2021.147811>.
- [22] Qian, M.; Yang, L.; Chen, X.; Li, K.; Xue, W.; Li, Y.; Zhao, H.; Cao, G.; Guan, X.; Shen, G. The treatment of veterinary antibiotics in swine

- wastewater by biodegradation and Fenton-like oxidation. *Sci. Total Environ.* 2020, 710, 136299. <https://doi.org/10.1016/j.scitotenv.2019.136299>.
- [23] Jafarisani, M.; Cheshme Khavar, A.H.; Mahjoub, A.R.; Luque, R.; Rodríguez-Padrón, D.; Satari, M.; Gharravi, A.M.; Khastar, H.; Kazemi, S.S.; Masoumikarimi, M. Enhanced visible-light-driven photocatalytic degradation of emerging water contaminants by a modified zinc oxide-based photocatalyst; In-vivo and in-vitro toxicity evaluation of wastewater and PCO-treated water. *Sep. Purif. Technol.* 2020, 243, 116430. <https://doi.org/10.1016/j.seppur.2019.116430>.
- [24] Ata, R.; Yıldız Töre, G. Characterization and removal of antibiotic residues by NFC-doped photocatalytic oxidation from domestic and industrial secondary treated wastewaters in Meric-Ergene Basin and reuse assessment for irrigation. *J. Environ. Manag.* 2019, 233, 673–680. <https://doi.org/10.1016/j.jenvman.2018.11.095>.
- [25] Zha, S.; Cheng, Y.; Gao, Y.; Chen, Z.; Megharaj, M.; Naidu, R. Nanoscale zero-valent iron as a catalyst for heterogeneous Fenton oxidation of amoxicillin. *Chem. Eng. J.* 2014, 255, 141–148. <https://doi.org/10.1016/j.cej.2014.06.057>.
- [26] Wang, A.; Zhang, Y.; Han, S.; Guo, C.; Wen, Z.; Tian, X.; Li, J. Electro-Fenton oxidation of a β -lactam antibiotic cefoperazone: Mineralization, biodegradability and degradation mechanism. *Chemosphere* 2021, 270, 129486. <https://doi.org/10.1016/j.chemosphere.2020.129486>.
- [27] Wang, C.; Lin, C.Y.; Liao, G.Y. Degradation of antibiotic tetracycline by ultrafine-bubble ozonation process. *J. Water Process Eng.* 2020, 37, 101463. <https://doi.org/10.1016/j.jwpe.2020.101463>.

- [28] Baaloudj, O.; Assadi, I.; Nasrallah, N.; El Jery, A.; Khezami, L.; Assadi, A.A. Simultaneous removal of antibiotics and inactivation of antibiotic-resistant bacteria by photocatalysis: A review. *J. Water Process Eng.* 2021, 42, 102089. <https://doi.org/10.1016/j.jwpe.2021.102089>.
- [29] Baran, W.; Adamek, E.; Jajko, M.; Sobczak, A. Removal of veterinary antibiotics from wastewater by electrocoagulation. *Chemosphere* 2018, 194, 381–389. <https://doi.org/10.1016/j.chemosphere.2017.11.165>.
- [30] Salas, G. Tratamiento por Oxidación Avanzada (Reacción Fenton) de Aguas Residuales de la Industria Textil. *Rev. Peru. Quim. e Ing. Quim.* 2010, 12, 30–38.
- [31] Fenton, H.J. Oxidation of Tartaric Acid in presence of Iron. *J. Chem. Soc. Trans.* 1894, 65, 899–910. <https://doi.org/10.1039/CT8946500899>.
- [32] Huang, Y.; Liu, H.; Liu, S.; Li, C.; Yuan, S. Glucose oxidase modified Fenton reactions for in-situ ROS generation and potential application in groundwater remediation. *Chemosphere* 2020, 253, 126648. <https://doi.org/10.1016/j.chemosphere.2020.126648>.
- [33] Ramos, J.M.P.; Pereira-Queiroz, N.M.; Santos, D.H.S.; Nascimento, J.R.; de Carvalho, C.M.; Tonholo, J.; Zanta, C.L.P.S. Printing ink effluent remediation: A comparison between electrochemical and Fenton treatments. *J. Water Process Eng.* 2019, 31, 100803. <https://doi.org/10.1016/j.jwpe.2019.100803>.
- [34] Usman, M.; Ho, Y.S. A bibliometric study of the Fenton oxidation for soil and water remediation. *J. Environ. Manag.* 2020, 270, 110886. <https://doi.org/10.1016/j.jenvman.2020.110886>.
- [35] Wong, K.T.; Jang, S.B.; Choong, C.E.; won Kang, C.; Lee, G.C.; Song, J.Y.;

- Yoon, Y.; Jang, M. In situ Fenton remediation for diesel contaminated clayey zone assisted by thermal plasma blasting: Synergism and cost estimation. *Chemosphere* 2022, 286, 131574. <https://doi.org/10.1016/j.chemosphere.2021.131574>.
- [36] Jain, B.; Singh, A.K.; Kim, H.; Lichtfouse, E.; Sharma, V.K. Treatment of organic pollutants by homogeneous and heterogeneous Fenton reaction processes. *Environ. Chem. Lett.* 2018, 16, 947–967. <https://doi.org/10.1007/s10311-018-0738-3>.
- [37] Sharma, M.; Mohapatra, T.; Ghosh, P. Hydrodynamics, mass and heat transfer study for emerging heterogeneous Fenton process in multiphase fluidized-bed reactor system for wastewater treatment—A review. *Chem. Eng. Res. Des.* 2021, 171, 48–62. <https://doi.org/10.1016/j.cherd.2021.04.019>.
- [38] Yu, G.H.; Kuzyakov, Y. Fenton chemistry and reactive oxygen species in soil: Abiotic mechanisms of biotic processes, controls and consequences for carbon and nutrient cycling. *Earth-Sci. Rev.* 2021, 214, 103525. <https://doi.org/10.1016/j.earscirev.2021.103525>.
- [39] Gligorovski, S.; Streckowski, R.; Barbati, S.; Vione, D. Environmental Implications of Hydroxyl Radicals ($\bullet\text{OH}$). *Chem. Rev.* 2015, 115, 13051–13092. <https://doi.org/10.1021/cr500310b>.
- [40] Amir, J.; Rojas, A.; Fernando, L.; Giraldo, G.; Trujillo, J.M. Empleo del reactivo de Fenton para la degradación del colorante Tartrazina *. *Lasallista Investig.* 2009, 6, 27–34.
- [41] Zhang, X.; Zhang, Y.; Yu, Z.; Wei, X.; Wu, W.D.; Wang, X.; Wu, Z. Facile synthesis of mesoporous anatase/rutile/hematite triple heterojunctions for

- superior heterogeneous photo-Fenton catalysis. *Appl. Catal. B Environ.* 2020, 263, 118335. <https://doi.org/10.1016/j.apcatb.2019.118335>.
- [42] Song, W.; Cheng, M.; Ma, J.; Ma, W.; Chen, C.; Zhao, J. Decomposition of hydrogen peroxide driven by photochemical cycling of iron species in clay. *Environ. Sci. Technol.* 2006, 40, 4782–4787. <https://doi.org/10.1021/es060624q>.
- [43] Wang, N.; Zheng, T.; Zhang, G.; Wang, P. A review on Fenton-like processes for organic wastewater treatment. *J. Environ. Chem. Eng.* 2016, 4, 762–787. <https://doi.org/10.1016/j.jece.2015.12.016>.
- [44] Ochando-Pulido, J.M.; Pimentel-Moral, S.; Verardo, V.; Martinez-Ferez, A. A focus on advanced physico-chemical processes for olive mill wastewater treatment. *Sep. Purif. Technol.* 2017, 179, 161–174. <https://doi.org/10.1016/j.seppur.2017.02.004>.
- [45] Babuponnusami, A.; Muthukumar, K. A review on Fenton and improvements to the Fenton process for wastewater treatment. *J. Environ. Chem. Eng.* 2014, 2, 557–572. <https://doi.org/10.1016/j.jece.2013.10.011>.
- [46] Bokare, A.D.; Choi, W. Review of iron-free Fenton-like systems for activating H₂O₂ in advanced oxidation processes. *J. Hazard. Mater.* 2014, 275, 121–135. <https://doi.org/10.1016/j.jhazmat.2014.04.054>.
- [47] Fernández, L.; González-Rodríguez, J.; Gamallo, M.; Vargas-Osorio, Z.; Vázquez-Vázquez, C.; Piñeiro, Y.; Rivas, J.; Feijoo, G.; Moreira, M.T. Iron oxide-mediated photo-Fenton catalysis in the inactivation of enteric bacteria present in wastewater effluents at neutral pH. *Environ. Pollut.* 2020, 266, 115181. <https://doi.org/10.1016/j.envpol.2020.115181>.
- [48] Wang, L.; Zhang, Y.; Qian, J. Graphene aerogel-based catalysts in Fenton-

- like reactions for water decontamination: A short review. *Chem. Eng. J. Adv.* 2021, 8, 100171. <https://doi.org/10.1016/j.ceja.2021.100171>.
- [49] Dinçer, A.R.; Çifçi, D.İ.; Cinkaya, D.D.; Dülger, E.; Karaca, F. Treatment of organic peroxide containing wastewater and water recovery by fenton-adsorption and fenton-nanofiltration processes. *J. Environ. Manag.* 2021, 299, 113557. <https://doi.org/10.1016/j.jenvman.2021.113557>.
- [50] Hu, C.; Huang, D.; Zeng, G.; Cheng, M.; Gong, X.; Wang, R.; Xue, W.; Hu, Z.; Liu, Y. The combination of Fenton process and *Phanerochaete chrysosporium* for the removal of bisphenol A in river sediments: Mechanism related to extracellular enzyme, organic acid and iron. *Chem. Eng. J.* 2018, 338, 432–439. <https://doi.org/10.1016/j.cej.2018.01.068>.
- [51] Soufi, A.; Hajjaoui, H.; Elmoubarki, R.; Abdennouri, M.; Qourzal, S.; Barka, N. Spinel ferrites nanoparticles: Synthesis methods and application in heterogeneous Fenton oxidation of organic pollutants—A review. *Appl. Surf. Sci. Adv.* 2021, 6, 100145. <https://doi.org/10.1016/j.apsadv.2021.100145>.
- [52] Cheng, M.; Zeng, G.; Huang, D.; Lai, C.; Xu, P.; Zhang, C.; Liu, Y. Hydroxyl radicals based advanced oxidation processes (AOPs) for remediation of soils contaminated with organic compounds: A review. *Chem. Eng. J.* 2016, 284, 582–598. <https://doi.org/10.1016/j.cej.2015.09.001>.
- [53] Rao, S.N.; Shrivastava, S. Treatment of complex recalcitrant wastewater using Fenton process. *Mater. Today Proc.* 2020, 29, 1161–1165. <https://doi.org/10.1016/j.matpr.2020.05.399>.
- [54] L Zhao, X.; Chen, L.; Ma, H.; Ma, J.; Gao, D. Effective removal of polymer

- quaternary ammonium salt by biodegradation and a subsequent Fenton oxidation process. *Ecotoxicol. Environ. Saf.* 2020, 188, 109919. <https://doi.org/10.1016/j.ecoenv.2019.109919>.
- [55] Liu, C.; Yi, H.; Yang, B.; Jia, F.; Song, S. Activation of Fenton reaction by controllable oxygen incorporation in MoS₂-Fe under visible light irradiation. *Appl. Surf. Sci.* 2021, 566, 150674. <https://doi.org/10.1016/j.apsusc.2021.150674>.
- [56] Qin, H.; Cheng, H.; Li, H.; Wang, Y. Degradation of ofloxacin, amoxicillin and tetracycline antibiotics using magnetic core-shell MnFe₂O₄@C-NH₂ as a heterogeneous Fenton catalyst. *Chem. Eng. J.* 2020, 396, 125304. <https://doi.org/10.1016/j.cej.2020.125304>.
- [57] Liu, Y.; Zhang, X.; Deng, J.; Liu, Y. A novel CNTs-Fe₃O₄ synthesized via a ball-milling strategy as efficient fenton-like catalyst for degradation of sulfonamides. *Chemosphere* 2021, 277, 130305. <https://doi.org/10.1016/j.chemosphere.2021.130305>.
- [58] Fornazaria, A.L.; Labriola, V.F.; Da Silva, B.F.; Castro, L.F.; Perussi, J.R.; Vieira, E.M.; Azevedo, E.B. Coupling Zero-Valent Iron and Fenton processes for degrading sulfamethazine, sulfathiazole, and norfloxacin. *J. Environ. Chem. Eng.* 2021, 9, 105761. <https://doi.org/10.1016/j.jece.2021.105761>.
- [59] Qin, H.; Yang, Y.; Shi, W.; She, Y.; Wu, S. Heterogeneous Fenton degradation of azithromycin antibiotic in water catalyzed by amino/thiol-functionalized MnFe₂O₄ magnetic nanocatalysts. *J. Environ. Chem. Eng.* 2021, 9, 106184. <https://doi.org/10.1016/j.jece.2021.106184>.
- [60] Li, T.; Chen, Y.; Wang, X.; Liang, J.; Zhou, L. Modifying organic carbon in

- Fe₃O₄-loaded schwertmannite to improve hetero-geneous Fenton activity through accelerating Fe(II) generation. *Appl. Catal. B Environ.* 2021, 285, 119830. <https://doi.org/10.1016/j.apcatb.2020.119830>.
- [61] Goswami, A.; Jiang, J.Q.; Petri, M. Treatability of five micro-pollutants using modified Fenton reaction catalysed by ze-ro-valent iron powder (Fe(0)). *J. Environ. Chem. Eng.* 2021, 9, 105393. <https://doi.org/10.1016/j.jece.2021.105393>.
- [62] Homem, V.; Alves, A.; Santos, L. Amoxicillin degradation at ppb levels by Fenton's oxidation using design of experiments. *Sci. Total Environ.* 2010, 408, 6272–6280. <https://doi.org/10.1016/j.scitotenv.2010.08.058>.
- [63] Cheng, S.; Zhang, C.; Li, J.; Pan, X.; Zhai, X.; Jiao, Y.; Li, Y.; Dong, W.; Qi, X. Highly efficient removal of antibiotic from biomedical wastewater using Fenton-like catalyst magnetic pullulan hydrogels. *Carbohydr. Polym.* 2021, 262, 117951. <https://doi.org/10.1016/j.carbpol.2021.117951>.
- [64] Wang, C.; Sun, R.; Huang, R.; Wang, H. Superior fenton-like degradation of tetracycline by iron loaded graphitic carbon derived from microplastics: Synthesis, catalytic performance, and mechanism. *Sep. Purif. Technol.* 2021, 270, 118773. <https://doi.org/10.1016/j.seppur.2021.118773>.
- [65] Del Álamo, A.C.; González, C.; Pariente, M.I.; Molina, R.; Martínez, F. Fenton-like catalyst based on a reticulated porous perovskite material: Activity and stability for the on-site removal of pharmaceutical micropollutans in a hospital wastewater. *Chem. Eng. J.* 2020, 401, 126113. <https://doi.org/10.1016/j.cej.2020.126113>.
- [66] Wang, C.; Yu, G.; Chen, H.; Wang, J. Degradation of norfloxacin by hydroxylamine enhanced fenton system: Kinetics, mechanism and

- degradation pathway. *Chemosphere* 2021, 270, 129408. <https://doi.org/10.1016/j.chemosphere.2020.129408>.
- [67] L Salari, M.; Rakhshandehroo, G.R.; Nikoo, M.R.; Zerafat, M.M.; Mooselu, M.G. Optimal degradation of Ciprofloxacin in a heterogeneous Fenton-like process using (δ -FeOOH)/MWCNTs nanocomposite. *Environ. Technol. Innov.* 2021, 23, 101625. <https://doi.org/10.1016/j.eti.2021.101625>.
- [68] Karimnezhad, H.; Navarchian, A.H.; Tavakoli Gheinani, T.; Zinadini, S. Amoxicillin removal by Fe-based nanoparticles immobilized on polyacrylonitrile membrane: Individual nanofiltration or Fenton reaction, vs. engineered combined process. *Chem. Eng. Res. Des.* 2020, 153, 187–200. <https://doi.org/10.1016/j.cherd.2019.10.031>.
- [69] Chen, P.; Sun, F.; Wang, W.; Tan, F.; Wang, X.; Qiao, X. Facile one-pot fabrication of ZnO₂ particles for the efficient Fenton-like degradation of tetracycline. *J. Alloys Compd.* 2020, 834, 155220. <https://doi.org/10.1016/j.jallcom.2020.155220>.
- [70] Yang, W.; Hong, P.; Yang, D.; Yang, Y.; Wu, Z.; Xie, C.; He, J.; Zhang, K.; Kong, L.; Liu, J. Enhanced Fenton-like degradation of sulfadiazine by single atom iron materials fixed on nitrogen-doped porous carbon. *J. Colloid Interface Sci.* 2021, 597, 56–65. <https://doi.org/10.1016/j.jcis.2021.03.168>.
- [71] de Melo Costa-Serge, N.; Gonçalves, R.G.L.; Rojas-Mantilla, H.D.; Santilli, C.V.; Hammer, P.; Nogueira, R.F.P. Fenton-like degradation of sulfathiazole using copper-modified MgFe-CO₃ layered double hydroxide. *J. Hazard. Mater.* 2021, 413, 125388. <https://doi.org/10.1016/j.jhazmat.2021.125388>.
- [72] Liu, L.; Xu, Q.; Owens, G.; Chen, Z. Fenton-oxidation of rifampicin via a green synthesized rGO@nFe/Pd nanocomposite. *J. Hazard. Mater.* 2021,

- 402, 123544. <https://doi.org/10.1016/j.jhazmat.2020.123544>.
- [73] Yi, Y.; Luo, J.; Fang, Z. Magnetic biochar derived from *Eichhornia crassipes* for highly efficient Fenton-like degradation of antibiotics: Mechanism and contributions. *J. Environ. Chem. Eng.* 2021, 9, 106258. <https://doi.org/10.1016/j.jece.2021.106258>.
- [74] Gao, Y.; Zhu, W.; Liu, J.; Lin, P.; Zhang, J.; Huang, T.; Liu, K. Mesoporous sulfur-doped CoFe₂O₄ as a new Fenton catalyst for the highly efficient pollutants removal. *Appl. Catal. B Environ.* 2021, 295, 120273. <https://doi.org/10.1016/j.apcatb.2021.120273>.
- [75] Carrasco-Díaz, M.R.; Castillejos-López, E.; Cerpa-Naranjo, A.; Rojas-Cervantes, M.L. Efficient removal of paracetamol using LaCu_{1-x}M_xO₃ (M = Mn, Ti) perovskites as heterogeneous Fenton-like catalysts. *Chem. Eng. J.* 2016, 304, 408–418. <https://doi.org/10.1016/j.cej.2016.06.054>.
- [76] Guo, H.; Li, Z.; Xie, Z.; Song, J.; Xiang, L.; Zhou, L.; Li, C.; Liuni Liao; Li, J.; Wang, H. Accelerated Fenton reaction for antibiotic ofloxacin degradation in discharge plasma system based on graphene-Fe₃O₄ nanocomposites. *Vacuum* 2021, 185, 110022. <https://doi.org/10.1016/j.vacuum.2020.110022>.
- [77] Wang, X.; Jin, H.; Wu, D.; Nie, Y.; Tian, X.; Yang, C.; Zhou, Z.; Li, Y. Fe₃O₄@S-doped ZnO: A magnetic, recoverable, and reusable Fenton-like catalyst for efficient degradation of ofloxacin under alkaline conditions. *Environ. Res.* 2020, 186, 109626. <https://doi.org/10.1016/j.envres.2020.109626>.
- [78] Sun, F.; Liu, H.; Wang, H.; Shu, D.; Chen, T.; Zou, X.; Huang, F.; Chen, D. A novel discovery of a heterogeneous Fenton-like system based on natural

- siderite: A wide range of pH values from 3 to 9. *Sci. Total Environ.* 2020, 698, 134293. <https://doi.org/10.1016/j.scitotenv.2019.134293>.
- [79] Ma, E.; Wang, K.; Hu, Z.; Wang, H. Dual-stimuli-responsive CuS-based micromotors for efficient photo-Fenton degradation of antibiotics. *J. Colloid Interface Sci.* 2021, 603, 685–694. <https://doi.org/10.1016/j.jcis.2021.06.142>.
- [80] Gu, W.; Huang, X.; Tian, Y.; Cao, M.; Zhou, L.; Zhou, Y.; Lu, J.; Lei, J.; Zhou, Y.; Wang, L.; et al. High-efficiency adsorption of tetracycline by cooperation of carbon and iron in a magnetic Fe/porous carbon hybrid with effective Fenton regeneration. *Appl. Surf. Sci.* 2021, 538, 147813. <https://doi.org/10.1016/j.apsusc.2020.147813>.
- [81] Liao, Q.; Wang, D.; Ke, C.; Zhang, Y.; Han, Q.; Zhang, Y.; Xi, K. Metal-free Fenton-like photocatalysts based on covalent organic frameworks. *Appl. Catal. B Environ.* 2021, 298, 120548. <https://doi.org/10.1016/j.apcatb.2021.120548>.
- [82] Luo, L.; Wang, G.; Wang, Z.; Ma, J.; He, Y.; He, J.; Wang, L.; Liu, Y.; Xiao, H.; Xiao, Y.; et al. Optimization of Fenton process on removing antibiotic resistance genes from excess sludge by single-factor experiment and response surface methodology. *Sci. Total Environ.* 2021, 788, 147889. <https://doi.org/10.1016/j.scitotenv.2021.147889>.
- [83] Teel, A.L.; Warberg, C.R.; Atkinson, D.A.; Watts, R.J. Comparison of mineral and soluble iron Fenton's catalysts for the treatment of trichloroethylene. *Water Res.* 2001, 35, 977–984. [https://doi.org/10.1016/S0043-1354\(00\)00332-8](https://doi.org/10.1016/S0043-1354(00)00332-8).
- [84] Lewis, S.; Lynch, A.; Bachas, L.; Hampson, S.; Ormsbee, L.; Bhattacharyya,

- D. Chelate-modified fenton reaction for the degradation of trichloroethylene in aqueous and two-phase systems. *Environ. Eng. Sci.* 2009, 26, 849–859. <https://doi.org/10.1089/ees.2008.0277>.
- [85] Bello, M.M.; Abdul Raman, A.A.; Asghar, A. A review on approaches for addressing the limitations of Fenton oxidation for recalcitrant wastewater treatment. *Process Saf. Environ. Prot.* 2019, 126, 119–140. <https://doi.org/10.1016/j.psep.2019.03.028>.
- [86] Huang, C.; Zhang, C.; Huang, D.; Wang, D.; Tian, S.; Wang, R.; Yang, Y.; Wang, W.; Qin, F. Influence of surface functionalities of pyrogenic carbonaceous materials on the generation of reactive species towards organic contaminants: A review. *Chem. Eng. J.* 2021, 404, 127066. <https://doi.org/10.1016/j.cej.2020.127066>.
- [87] Dumesic, J.A.; Huber, G.W.; Boudart, M. Principles of Heterogeneous Catalysis. *Handbook of Heterogeneous Catalysis* (eds G. Ertl, H. Knözinger, F. Schüth and J. Weitkamp). 2008 ; <https://doi.org/10.1002/9783527610044.hetcat0001>.
- [88] Expósito, E.; Sánchez-Sánchez, C.M.; Montiel, V. Mineral Iron Oxides as Iron Source in Electro-Fenton and Photoelectro-Fenton Mineralization Processes. *J. Electrochem. Soc.* 2007, 154, E116. <https://doi.org/10.1149/1.2744134>.
- [89] Bai, Z.; Yang, Q.; Wang, J. Degradation of sulfamethazine antibiotics in Fenton-like system using Fe₃O₄ magnetic nanoparticles as catalyst. *Environ. Prog. Sustain. Energy* 2017, 36, 1743–1753. <https://doi.org/10.1002/ep.12639>.
- [90] Xie, W.; Huang, Z.; Zhou, F.; Li, Y.; Bi, X.; Bian, Q.; Sun, S. Heterogeneous

- fenton-like degradation of amoxicillin using MOF-derived Fe₀ embedded in mesoporous carbon as an effective catalyst. *J. Clean. Prod.* 2021, 313, 127754. <https://doi.org/10.1016/j.jclepro.2021.127754>.
- [91] Furia, F.; Minella, M.; Gosetti, F.; Turci, F.; Sabatino, R.; Di Cesare, A.; Corno, G.; Vione, D. Elimination from wastewater of antibiotics reserved for hospital settings, with a Fenton process based on zero-valent iron. *Chemosphere* 2021, 283, 131170. <https://doi.org/10.1016/j.chemosphere.2021.131170>.
- [92] Rodriguez-Rodriguez, J.; Ochando-Pulido, J.M.; Martinez-Ferez, A. The effect of pH in tannery wastewater by Fenton vs. Heterogeneous Fenton process. *Chem. Eng. Trans.* 2019, 73, 205–210. <https://doi.org/10.3303/CET1973035>.
- [93] He, J.; Yang, X.; Men, B.; Wang, D. Interfacial mechanisms of heterogeneous Fenton reactions catalyzed by iron-based materials: A review. *J. Environ. Sci.* 2016, 39, 97–109. <https://doi.org/10.1016/j.jes.2015.12.003>.
- [94] Liu, G.; Zhang, Y.; Yu, H.; Jin, R.; Zhou, J. Acceleration of goethite-catalyzed Fenton-like oxidation of ofloxacin by biochar. *J. Hazard. Mater.* 2020, 397, 122783. <https://doi.org/10.1016/j.jhazmat.2020.122783>.
- [95] Huang, X.; Hou, X.; Zhao, J.; Zhang, L. Hematite facet confined ferrous ions as high efficient Fenton catalysts to degrade organic contaminants by lowering H₂O₂ decomposition energetic span. *Appl. Catal. B Environ.* 2016, 181, 127–137. <https://doi.org/10.1016/j.apcatb.2015.06.061>.
- [96] Yang, S.; Xiong, Y.; Ge, Y.; Zhang, S. Heterogeneous Fenton oxidation of nitric oxide by magnetite: Kinetics and mechanism. *Mater. Lett.* 2018, 218,

- 257–261. <https://doi.org/10.1016/j.matlet.2018.01.171>.
- [97] Liu, W.; Zhou, J.; Liu, D.; Liu, S.; Liu, X.; Xiao, S. Enhancing electronic transfer by magnetic iron materials and metal-organic framework via heterogeneous Fenton-like process and photocatalysis. *Mater. Sci. Semicond. Process* 2021, 135, 106096. <https://doi.org/10.1016/j.mssp.2021.106096>.
- [98] Hassani, A.; Karaca, M.; Karaca, S.; Khataee, A.; Açışlı, Ö.; Yılmaz, B. Preparation of magnetite nanoparticles by high-energy planetary ball mill and its application for ciprofloxacin degradation through heterogeneous Fenton process. *J. Environ. Manag.* 2018, 211, 53–62. <https://doi.org/10.1016/j.jenvman.2018.01.014>.
- [99] Gholizadeh, A.M.; Zarei, M.; Ebratkhahan, M.; Hasanzadeh, A. Phenazopyridine degradation by electro-Fenton process with magnetite nanoparticles-activated carbon cathode, artificial neural networks modeling. *J. Environ. Chem. Eng.* 2021, 9, 104999. <https://doi.org/10.1016/j.jece.2020.104999>.
- [100] Gonçalves, R.G.L.; Lopes, P.A.; Resende, J.A.; Pinto, F.G.; Tronto, J.; Guerreiro, M.C.; de Oliveira, L.C.A.; de Castro Nunes, W.; Neto, J.L. Performance of magnetite/layered double hydroxide composite for dye removal via adsorption, Fenton and photo-Fenton processes. *Appl. Clay Sci.* 2019, 179, 105152. <https://doi.org/10.1016/j.clay.2019.105152>.
- [101] Rial, J.B.; Ferreira, M.L. Challenges of dye removal treatments based on IONzymes: Beyond heterogeneous Fenton. *J. Water Process Eng.* 2021, 41, 102065. <https://doi.org/10.1016/j.jwpe.2021.102065>.
- [102] Yang, Z.; Yu, A.; Shan, C.; Gao, G.; Pan, B. Enhanced Fe(III)-mediated

- Fenton oxidation of atrazine in the presence of functionalized multi-walled carbon nanotubes. *Water Res.* 2018, 137, 37–46. <https://doi.org/10.1016/j.watres.2018.03.006>.
- [103] Seo, J.; Lee, H.J.; Lee, H.; Kim, H.E.; Lee, J.Y.; Kim, H.S.; Lee, C. Enhanced production of reactive oxidants by Fenton-like reactions in the presence of carbon materials. *Chem. Eng. J.* 2015, 273, 502–508. <https://doi.org/10.1016/j.cej.2015.03.114>.
- [104] Qin, Y.; Zhang, L.; An, T. Hydrothermal Carbon-Mediated Fenton-Like Reaction Mechanism in the Degradation of Alachlor: Direct Electron Transfer from Hydrothermal Carbon to Fe(III). *ACS Appl. Mater. Interfaces* 2017, 9, 17115–17124. <https://doi.org/10.1021/acsami.7b03310>.
- [105] Bach, A.; Semiat, R. The role of activated carbon as a catalyst in GAC/iron oxide/H₂O₂ oxidation process. *Desalination* 2011, 273, 57–63. <https://doi.org/10.1016/j.desal.2010.04.020>.
- [106] Kappler, A.; Wuestner, M.L.; Ruecker, A.; Harter, J.; Halama, M.; Behrens, S. Biochar as an Electron Shuttle between Bacteria and Fe(III) Minerals. *Environ. Sci. Technol. Lett.* 2014, 1, 339–344. <https://doi.org/10.1021/ez5002209>.
- [107] Sun, L.; Yao, Y.; Wang, L.; Mao, Y.; Huang, Z.; Yao, D.; Lu, W.; Chen, W. Efficient removal of dyes using activated carbon fibers coupled with 8-hydroxyquinoline ferric as a reusable Fenton-like catalyst. *Chem. Eng. J.* 2014, 240, 413–419. <https://doi.org/10.1016/j.cej.2013.12.009>.
- [108] Yao, T.; Qi, Y.; Mei, Y.; Yang, Y.; Aleisa, R.; Tong, X.; Wu, J. One-step preparation of reduced graphene oxide aerogel loaded with mesoporous copper ferrite nanocubes: A highly efficient catalyst in microwave-assisted

- Fenton reaction. *J. Hazard. Mater.* 2019, 378, 105. <https://doi.org/10.1016/j.jhazmat.2019.05.105>.
- [109] Kuśmierk, K.; Kiciński, W.; Norek, M.; Polański, M.; Budner, B. Oxidative and adsorptive removal of chlorophenols over Fe-, N- and S-multi-doped carbon xerogels. *J. Environ. Chem. Eng.* 2021, 9, 105568. <https://doi.org/10.1016/j.jece.2021.105568>.
- [110] Cruz, D.R.S.; de Jesus, G.K.; Santos, C.A.; Silva, W.R.; Wisniewski, A.; Cunha, G.C.; Romão, L.P.C. Magnetic nanostructured material as heterogeneous catalyst for degradation of AB210 dye in tannery wastewater by electro-Fenton process. *Chemosphere* 2021, 280, 130675. <https://doi.org/10.1016/j.chemosphere.2021.130675>.
- [111] Zhang, X.; Guo, Y.; Shi, S.; Liu, E.; Li, T.; Wei, S.; Li, Y.; Li, Y.; Sun, G.; Zhao, Z. Efficient and stable iron-copper montmorillonite heterogeneous Fenton catalyst for removing Rhodamine B. *Chem. Phys. Lett.* 2021, 776, 138673. <https://doi.org/10.1016/j.cplett.2021.138673>.
- [112] Li, X.; Tian, Z.; Liang, K.; Wang, Y. Enhanced photo-Fenton degradation performance over multi-metal co-supported SAPO-18 zeolites by promoted active species yield. *J. Photochem. Photobiol. A Chem.* 2019, 379, 79–87. <https://doi.org/10.1016/j.jphotochem.2019.04.032>.
- [113] Xu, X.; Chen, W.; Zong, S.; Ren, X.; Liu, D. Magnetic clay as catalyst applied to organics degradation in a combined adsorption and Fenton-like process. *Chem. Eng. J.* 2019, 373, 140–149. <https://doi.org/10.1016/j.cej.2019.05.030>.
- [114] Ferroudj, N.; Beaunier, P.; Davidson, A.; Abramson, S. Fe³⁺-doped ordered mesoporous γ -Fe₂O₃/SiO₂ microspheres as a highly efficient magnetically

- separable heterogeneous Fenton catalyst. *Microporous Mesoporous Mater.* 2021, 326, 111373. <https://doi.org/10.1016/j.micromeso.2021.111373>.
- [115] Wei, K.; Liu, X.; Cao, S.; Cui, H.; Zhang, Y.; Ai, Z. Fe₂O₃@FeB composites facilitate heterogeneous Fenton process by efficient Fe(III)/Fe(II) cycle and in-situ H₂O₂ generation. *Chem. Eng. J. Adv.* 2021, 8, 100165. <https://doi.org/10.1016/j.cej.2021.100165>.
- [116] Carrasco-Díaz, M.R.; Castillejos-López, E.; Cerpa-Naranjo, A.; Rojas-Cervantes, M.L. On the textural and crystalline properties of Fe-carbon xerogels. Application as Fenton-like catalysts in the oxidation of paracetamol by H₂O₂. *Microporous Mesoporous Mater.* 2017, 237, 282–293. <https://doi.org/10.1016/j.micromeso.2016.09.035>.
- [117] Asghar, A.; Raman, A.A.A.; Daud, W.M.A.W. Advanced oxidation processes for in-situ production of hydrogen peroxide/hydroxyl radical for textile wastewater treatment: A review. *J. Clean. Prod.* 2015, 87, 826–838. <https://doi.org/10.1016/j.jclepro.2014.09.010>.
- [118] Yazici Guvenc, S.; Dincer, K.; Varank, G. Performance of electrocoagulation and electro-Fenton processes for treatment of nanofiltration concentrate of biologically stabilized landfill leachate. *J. Water Process Eng.* 2019, 31, 100863. <https://doi.org/10.1016/j.jwpe.2019.100863>.
- [119] Tian, Y.; Zhou, M.; Pan, Y.; Cai, J.; Ren, G. Pre-magnetized Fe₀ as heterogeneous electro-Fenton catalyst for the degradation of p-nitrophenol at neutral pH. *Chemosphere* 2020, 240, 124962. <https://doi.org/10.1016/j.chemosphere.2019.124962>.
- [120] Huang, L.Z.; Zhu, M.; Liu, Z.; Wang, Z.; Hansen, H.C.B. Single sheet iron

- oxide: An efficient heterogeneous electro-Fenton catalyst at neutral pH. *J. Hazard. Mater.* 2019, 364, 39–47. <https://doi.org/10.1016/j.jhazmat.2018.10.026>.
- [121] Midassi, S.; Bedoui, A.; Bensalah, N. Efficient degradation of chloroquine drug by electro-Fenton oxidation: Effects of operating conditions and degradation mechanism. *Chemosphere* 2020, 260, 127558. <https://doi.org/10.1016/j.chemosphere.2020.127558>.
- [122] Elbatea, A.A.; Nosier, S.A.; Zatout, A.A.; Hassan, I.; Sedahmed, G.H.; Abdel-Aziz, M.H.; El-Naggar, M.A. Removal of reactive red 195 from dyeing wastewater using electro-Fenton process in a cell with oxygen sparged fixed bed electrodes. *J. Water Process Eng.* 2021, 41, 102042. <https://doi.org/10.1016/j.jwpe.2021.102042>.
- [123] Senthilnathan, J.; Younis, S.A.; Kwon, E.E.; Surejan, A.; Kim, K.H.; Yoshimura, M. An efficient system for electro-Fenton oxidation of pesticide by a reduced graphene oxide-aminopyrazine@3D Ni foam gas diffusion electrode. *J. Hazard. Mater.* 2020, 400, 123323. <https://doi.org/10.1016/j.jhazmat.2020.123323>.
- [124] McQuillan, R.V.; Stevens, G.W.; Mumford, K.A. Assessment of the electro-Fenton pathway for the removal of naphthalene from contaminated waters in remote regions. *Sci. Total Environ.* 2021, 762, 143155. <https://doi.org/10.1016/j.scitotenv.2020.143155>.
- [125] Poza-Nogueiras, V.; Rosales, E.; Pazos, M.; Sanromán, M.Á. Current advances and trends in electro-Fenton process using heterogeneous catalysts—A review. *Chemosphere* 2018, 201, 399–416. <https://doi.org/10.1016/j.chemosphere.2018.03.002>.

- [126] Matyszczyk, G.; Krzyczkowska, K.; Fidler, A. A novel, two-electron catalysts for the electro-Fenton process. *J. Water Process Eng.* 2020, 36, 101242. <https://doi.org/10.1016/j.jwpe.2020.101242>.
- [127] Liang, J.; Xiang, Q.; Lei, W.; Zhang, Y.; Sun, J.; Zhu, H.; Wang, S. Ferric iron reduction reaction electro-Fenton with gas diffusion device: A novel strategy for improvement of comprehensive efficiency in electro-Fenton. *J. Hazard. Mater.* 2021, 412, 125195. <https://doi.org/10.1016/j.jhazmat.2021.125195>.
- [128] Zhang, C.; Zhou, M.; Yu, X.; Ma, L.; Yu, F. Modified iron-carbon as heterogeneous electro-Fenton catalyst for organic pollutant degradation in near neutral pH condition: Characterization, degradation activity and stability. *Electrochim. Acta* 2015, 160, 254–262. <https://doi.org/10.1016/j.electacta.2015.01.092>.
- [129] Zhu, W.; Li, Y.; Gao, Y.; Wang, C.; Zhang, J.; Bai, H.; Huang, T. A new method to fabricate the cathode by cyclic voltammetric electrodeposition for electro-Fenton application. *Electrochim. Acta* 2020, 349, 136415. <https://doi.org/10.1016/j.electacta.2020.136415>.
- [130] Ganzenko, O.; Trelu, C.; Oturan, N.; Huguenot, D.; Péchaud, Y.; van Hullebusch, E.D.; Oturan, M.A. Electro-Fenton treatment of a complex pharmaceutical mixture: Mineralization efficiency and biodegradability enhancement. *Chemosphere* 2020, 253, 126659. <https://doi.org/10.1016/j.chemosphere.2020.126659>.
- [131] Robles, I.; Becerra, E.; Barrios, J.A.; Maya, C.; Jiménez, B.; Rodríguez-Valadez, F.J.; Rivera, F.; García-Espinoza, J.D.; Godínez, L.A. Inactivation of helminth eggs in an electro-Fenton reactor: Towards full electrochemical

- disinfection of human waste using activated carbon. *Chemosphere* 2020, 250, 126260. <https://doi.org/10.1016/j.chemosphere.2020.126260>.
- [132] Wang, Y.; Liu, Y.; Liu, T.; Song, S.; Gui, X.; Liu, H.; Tsiakaras, P. Dimethyl phthalate degradation at novel and efficient electro-Fenton cathode. *Appl. Catal. B Environ.* 2014, 156–157, 1–7. <https://doi.org/10.1016/j.apcatb.2014.02.041>.
- [133] Zhao, K.; Quan, X.; Chen, S.; Yu, H.; Zhang, Y.; Zhao, H. Enhanced electro-Fenton performance by fluorine-doped porous carbon for removal of organic pollutants in wastewater. *Chem. Eng. J.* 2018, 354, 606–615. <https://doi.org/10.1016/j.cej.2018.08.051>.
- [134] Liu, Y.; Chen, S.; Quan, X.; Yu, H.; Zhao, H.; Zhang, Y. Efficient Mineralization of Perfluorooctanoate by Electro-Fenton with H₂O₂ Electro-generated on hierarchically Porous Carbon. *Environ. Sci. Technol.* 2015, 49, 13528–12533. <https://doi.org/10.1021/acs.est.5b03147>.
- [135] Sun, C.; Chen, T.; Huang, Q.; Duan, X.; Zhan, M.; Ji, L.; Li, X.; Wang, S.; Yan, J. Biochar cathode: Reinforcing electro-Fenton pathway against four-electron reduction by controlled carbonization and surface chemistry. *Sci. Total Environ.* 2021, 754, 142136. <https://doi.org/10.1016/j.scitotenv.2020.142136>.
- [136] Ergen, B.T.; Gengec, E. Dye degradation and kinetics of online Electro-Fenton system with thermally activated carbon fiber cathodes. *J. Environ. Chem. Eng.* 2020, 8, 104217. <https://doi.org/10.1016/j.jece.2020.104217>.
- [137] Ramírez-Pereda, B.; Álvarez-Gallegos, A.; Rangel-Peraza, J.G.; Bustos-Terrones, Y.A. Kinetics of Acid Orange 7 oxidation by using carbon fiber and reticulated vitreous carbon in an electro-Fenton process. *J. Environ.*

- Manag. 2018, 213, 279–287.
<https://doi.org/10.1016/j.jenvman.2018.01.022>.
- [138] Xia, G.; Lu, Y.; Xu, H. An energy-saving production of hydrogen peroxide via oxygen reduction for electro-Fenton using electrochemically modified polyacrylonitrile-based carbon fiber brush cathode. *Sep. Purif. Technol.* 2015, 156, 553–560. <https://doi.org/10.1016/j.seppur.2015.10.048>.
- [139] Xia, G.; Lu, Y.; Xu, G.; Gao, C.; Xu, H. Electro-Fenton Degradation of Methylene Blue Using Polyacrylonitrile-Based Carbon Fiber Brush Cathode. *CLEAN Soil Air Water* 2014, 43, 229–236. <https://doi.org/10.1002/clen.201300931>.
- [140] Gao, Y.; Zhu, W.; Li, Y.; Li, J.; Yun, S.; Huang, T. Novel porous carbon felt cathode modified by cyclic voltammetric electro-deposited polypyrrole and anthraquinone 2-sulfonate for an efficient electro-Fenton process. *Int. J. Hydrog. Energy* 2021, 46, 9707–9717. <https://doi.org/10.1016/j.ijhydene.2020.04.197>.
- [141] Chen, S.; Tang, L.; Feng, H.; Zhou, Y.; Zeng, G.; Lu, Y.; Yu, J.; Ren, X.; Peng, B.; Liu, X. Carbon felt cathodes for electro-Fenton process to remove tetracycline via synergistic adsorption and degradation. *Sci. Total Environ.* 2019, 670, 921–931. <https://doi.org/10.1016/j.scitotenv.2019.03.086>.
- [142] Wang, Y.; Liu, Y.; Wang, K.; Song, S.; Tsiakaras, P.; Liu, H. Preparation and characterization of a novel KOH activated graphite felt cathode for the electro-Fenton process. *Appl. Catal. B Environ.* 2015, 165, 360–368. <https://doi.org/10.1016/j.apcatb.2014.09.074>.
- [143] Wang, Y.-T.; Tu, C.-H.; Lin, Y.-S. Application of Graphene and Carbon Nanotubes on Carbon Felt Electrodes for the Electro-Fenton System.

- Materials 2019, 12, 1698. <https://doi.org/10.3390/ma12101698>.
- [144] Özcan, A.; Şahin, Y.; Savaş Kopalal, A.; Oturan, M.A. Carbon sponge as a new cathode material for the electro-Fenton process: Comparison with carbon felt cathode and application to degradation of synthetic dye basic blue 3 in aqueous medium. *J. Electroanal. Chem.* 2008, 616, 71–78. <https://doi.org/10.1016/j.jelechem.2008.01.002>.
- [145] Sopaj, F.; Oturan, N.; Pinson, J.; Podvorica, F.I.; Oturan, M.A. Effect of cathode material on electro-Fenton process efficiency for electrocatalytic mineralization of the antibiotic sulfamethazine. *Chem. Eng. J.* 2020, 384, 123249. <https://doi.org/10.1016/j.cej.2019.123249>.
- [146] Ganiyu, S.O.; de Araújo, M.J.G.; de Araújo Costa, E.C.T.; Santos, J.E.L.; dos Santos, E.V.; Martínez-Huitle, C.A.; Pergher, S.B.C. Design of highly efficient porous carbon foam cathode for electro-Fenton degradation of antimicrobial sulfanilamide. *Appl. Catal. B Environ.* 2021, 283, 119652. <https://doi.org/10.1016/j.apcatb.2020.119652>.
- [147] Ye, Z.; Brillas, E.; Centellas, F.; Cabot, P.L.; Sirés, I. Electro-Fenton process at mild pH using Fe(III)-EDDS as soluble catalyst and carbon felt as cathode. *Appl. Catal. B Environ.* 2019, 257, 117907. <https://doi.org/10.1016/j.apcatb.2019.117907>.
- [148] Chu, Y.Y.; Qian, Y.; Wang, W.J.; Deng, X.L. A dual-cathode electro-Fenton oxidation coupled with anodic oxidation system used for 4-nitrophenol degradation. *J. Hazard. Mater.* 2012, 199–200, 179–185. <https://doi.org/10.1016/j.jhazmat.2011.10.079>.
- [149] Chu, Y.; Su, H.; Lv, R.; Zhang, X. Enhanced electro-reduction of Fe^{3+} to Fe^{2+} by acidified carbon nanotube-modified graphite cathode and its

- application in a novel Fenton process for p-nitrophenol degradation. *J. Water Process Eng.* 2021, 40, 101912. <https://doi.org/10.1016/j.jwpe.2020.101912>.
- [150] Zarei, M.; Beheshti Nahand, F.; Khataee, A.; Hasanzadeh, A. Removal of nalidixic acid from aqueous solutions using a cathode containing three-dimensional graphene. *J. Water Process Eng.* 2019, 32, 100978. <https://doi.org/10.1016/j.jwpe.2019.100978>.
- [151] Zhou, W.; Meng, X.; Rajic, L.; Xue, Y.; Chen, S.; Ding, Y.; Kou, K.; Wang, Y.; Gao, J.; Qin, Y.; et al. “Floating” cathode for efficient H₂O₂ electrogeneration applied to degradation of ibuprofen as a model pollutant. *Electrochem. Commun.* 2018, 96, 37–41. <https://doi.org/10.1016/j.elecom.2018.09.007>.
- [152] Liu, T.; Wang, K.; Song, S.; Brouzgou, A.; Tsiakaras, P.; Wang, Y. New Electro-Fenton Gas Diffusion Cathode based on Nitrogen-doped Graphene@Carbon Nanotube Composite Materials. *Electrochim. Acta* 2016, 194, 228–238. <https://doi.org/10.1016/j.electacta.2015.12.185>.
- [153] Chu, Y.; Su, H.; Liu, C.; Zheng, X. Fabrication of sandwich-like superhydrophobic cathode for the electro-Fenton degradation of cefepime: H₂O₂ electro-generation, degradation performance, pathway and biodegradability improvement. *Chemosphere* 2022, 286, 131669. <https://doi.org/10.1016/j.chemosphere.2021.131669>.
- [154] Karatas, O.; Gengec, N.A.; Gengec, E.; Khataee, A.; Kobya, M. High-performance carbon black electrode for oxygen reduction reaction and oxidation of atrazine by electro-Fenton process. *Chemosphere* 2021, 287, 132370. <https://doi.org/10.1016/j.chemosphere.2021.132370>.
- [155] Huang, A.; Zhi, D.; Zhou, Y. A novel modified Fe–Mn binary oxide graphite

- felt (FMBO-GF) cathode in a neutral electro-Fenton system for ciprofloxacin degradation. *Environ. Pollut.* 2021, 286, 117310. <https://doi.org/10.1016/j.envpol.2021.117310>.
- [156] Ma, B.; Lv, W.; Li, J.; Yang, C.; Tang, Q.; Wang, D. Promotion removal of aniline with electro-Fenton processes utilizing carbon nanotube 3D morphology modification of an Ag-loaded copper foam cathode. *J. Water Process Eng.* 2021, 43, 102295. <https://doi.org/10.1016/j.jwpe.2021.102295>.
- [157] Dung, N.T.; Duong, L.T.; Hoa, N.T.; Thao, V.D.; Ngan, L.V.; Huy, N.N. A comprehensive study on the heterogeneous electro-Fenton degradation of tartrazine in water using CoFe₂O₄/carbon felt cathode. *Chemosphere* 2022, 287, 132141. <https://doi.org/10.1016/j.chemosphere.2021.132141>.
- [158] Paz, E.C.; Aveiro, L.R.; Pinheiro, V.S.; Souza, F.M.; Lima, V.B.; Silva, F.L.; Hammer, P.; Lanza, M.R.V.; Santos, M.C. Evaluation of H₂O₂ electrogeneration and decolorization of Orange II azo dye using tungsten oxide nanoparticle-modified carbon. *Appl. Catal. B Environ.* 2018, 232, 436–445. <https://doi.org/10.1016/j.apcatb.2018.03.082>.
- [159] Fdez-Sanromán, A.; Acevedo-García, V.; Pazos, M.; Sanromán, M.Á.; Rosales, E. Iron-doped cathodes for electro-Fenton implementation: Application for pymetrozine degradation. *Electrochim. Acta* 2020, 338, 135768. <https://doi.org/10.1016/j.electacta.2020.135768>.
- [160] Li, L.; Hu, H.; Teng, X.; Yu, Y.; Zhu, Y.; Su, X. Electrogeneration of H₂O₂ using a porous hydrophobic acetylene black cathode for electro-Fenton process. *Chem. Eng. Process. Process Intensif.* 2018, 133, 34–39. <https://doi.org/10.1016/j.cep.2018.09.013>.
- [161] Yu, F.; Tao, L.; Cao, T. High yield of hydrogen peroxide on modified

- graphite felt electrode with nitrogen-doped porous carbon carbonized by zeolitic imidazolate framework-8 (ZIF-8) nanocrystals. *Environ. Pollut.* 2019, 255, 113119. <https://doi.org/10.1016/j.envpol.2019.113119>.
- [162] Cordeiro-Junior, P.J.; Kronka, M.S.; Goulart, L.A.; Veríssimo, N.C.; Mascaro, L.H.; dos Santos, M.C.; Bertazzoli, R.; de Vasconcelos Lanza, M.R. Catalysis of oxygen reduction reaction for H₂O₂ electrogeneration: The impact of different conductive carbon matrices and their physicochemical properties. *J. Catal.* 2020, 392, 56–68. <https://doi.org/10.1016/j.jcat.2020.09.020>.
- [163] An, J.; Li, N.; Zhao, Q.; Qiao, Y.; Wang, S.; Liao, C.; Zhou, L.; Li, T.; Wang, X.; Feng, Y. Highly efficient electro-generation of H₂O₂ by adjusting liquid-gas-solid three phase interfaces of porous carbonaceous cathode during oxygen reduction reaction. *Water Res.* 2019, 164, 114933. <https://doi.org/10.1016/j.watres.2019.114933>.
- [164] Ridruejo, C.; Alcaide, F.; Álvarez, G.; Brillas, E.; Sirés, I. On-site H₂O₂ electrogeneration at a CoS₂-based air-diffusion cathode for the electrochemical degradation of organic pollutants. *J. Electroanal. Chem.* 2018, 808, 364–371. <https://doi.org/10.1016/j.jelechem.2017.09.010>.
- [165] Li, D.; Zheng, T.; Liu, Y.; Hou, D.; Yao, K.K.; Zhang, W.; Song, H.; He, H.; Shi, W.; Wang, L.; et al. A novel Electro-Fenton process characterized by aeration from inside a graphite felt electrode with enhanced electrogeneration of H₂O₂ and cycle of Fe³⁺/Fe²⁺. *J. Hazard. Mater.* 2020, 396, 122591. <https://doi.org/10.1016/j.jhazmat.2020.122591>.
- [166] Kubanek, F.; Turek, T.; Krewer, U. Modeling Oxygen Gas Diffusion Electrodes for Various Technical Applications. *Chem. Ing. Tech.* 2019, 91,

- 720–733. <https://doi.org/10.1002/cite.201800181>.
- [167] Wang, J.; Li, C.; Rauf, M.; Luo, H.; Sun, X.; Jiang, Y. Gas diffusion electrodes for H₂O₂ production and their applications for electrochemical degradation of organic pollutants in water: A review. *Sci. Total Environ.* 2021, 759, 143459. <https://doi.org/10.1016/j.scitotenv.2020.143459>.
- [168] Murawski, E.; Kananizadeh, N.; Lindsay, S.; Rao, A.M.; Popat, S.C. Decreased gas-diffusion electrode porosity due to increased electrocatalyst loading leads to diffusional limitations in cathodic H₂O₂ electrosynthesis. *J. Power Sources* 2021, 481, 228992. <https://doi.org/10.1016/j.jpowsour.2020.228992>.
- [169] Jiang, W.; Yang, H.C.; Yang, S.Y.; Horng, H.E.; Hung, J.C.; Chen, Y.C.; Hong, C.Y. Preparation and properties of superpara-magnetic nanoparticles with narrow size distribution and biocompatible. *J. Magn. Mater.* 2004, 283, 210–214. <https://doi.org/10.1016/j.jmmm.2004.05.022>.
- [170] Lin, C.-C.; Lai, Y.-P.; Wu, K.-Y. A high-productivity process for mass-producing Fe₃O₄ nanoparticles by co-precipitation in a rotating packed bed. *Powder Technol.* 2021, 395, 369–376. <https://doi.org/10.1016/j.powtec.2021.09.036>.
- [171] Lin, C.C.; Lee, C.Y. Adsorption of ciprofloxacin in water using Fe₃O₄ nanoparticles formed at low temperature and high reactant concentrations in a rotating packed bed with co-precipitation. *Mater. Chem. Phys.* 2020, 240, 122049. <https://doi.org/10.1016/j.matchemphys.2019.122049>.
- [172] Rao, M.N.; Sultana, R.; Kota, S.H. Hazardous Waste. *Solid Hazard. Waste Manag.* 2017, 1, 159–207. <https://doi.org/10.1016/B978-0-12-809734-2.00005-5>.

- [173] Praveen, P.; Viruthagiri, G.; Mugundan, S.; Shanmugam, N. Structural , optical and morphological analyses of pristine titanium di-oxide nanoparticles—Synthesized via sol—gel route. *Spectrochim. Acta Part A Mol. Biomol. Spectrosc.* 2014, 117, 622–629. <https://doi.org/10.1016/j.saa.2013.09.037>.
- [174] Dubey, R.S. Temperature-dependent phase transformation of TiO₂ nanoparticles synthesized by sol-gel method. *Mater. Lett.* 2018, 215, 312–317. <https://doi.org/10.1016/j.matlet.2017.12.120>.
- [175] Zanurin, A.; Johari, N.A.; Alias, J.; Ayu, H.M.; Redzuan, N.; Izman, S. Research progress of sol-gel ceramic coating: A review. *Mater. Today Proc.* 2021, 48, 1849–1854. <https://doi.org/10.1016/j.matpr.2021.09.203>.
- [176] Demazeau, G. Solvothermal and hydrothermal processes: The main physico-chemical factors involved and new trends. *Res. Chem. Intermed.* 2010, 37, 107–123. <https://doi.org/10.1007/s11164-011-0240-z>.
- [177] Krajian, H.; Abdallah, B.; Kakhia, M.; Alkafri, N. Hydrothermal growth method for the deposition of ZnO films: Structural, chemical and optical studies. *Microelectron. Reliab.* 2021, 125, 114352. <https://doi.org/10.1016/j.microrel.2021.114352>.
- [178] Dem, L.N.; Lyutin, V.I. Status of hydrothermal growth of bulk ZnO: Latest issues and advantages. *J. Cryst. Growth* 2008, 310, 993–999. <https://doi.org/10.1016/j.jcrysgr.2007.11.145>.
- [179] Yadav, S.; Sharma, A. Importance and challenges of hydrothermal technique for synthesis of transition metal oxides and composites as supercapacitor electrode materials. *J. Energy Storage* 2021, 44, 103295. <https://doi.org/10.1016/j.est.2021.103295>.

- [180] Guo, X.; Wang, K.; Xu, Y. Tartaric acid enhanced CuFe₂O₄-catalyzed heterogeneous photo-Fenton-like degradation of methylene blue. *Mater. Sci. Eng. B* 2019, 245, 75–84. <https://doi.org/10.1016/j.mseb.2019.05.015>.
- [181] He, H.; Lu, J. Highly photocatalytic activities of magnetically separable reduced graphene oxide-CoFe₂O₄ hybrid nanostructures in dye photodegradation. *Sep. Purif. Technol.* 2017, 172, 374–381. <https://doi.org/10.1016/j.seppur.2016.08.040>.
- [182] Boepple, M.; Zhu, Z.; Hu, X.; Weimar, U.; Barsan, N. Impact of heterostructures on hydrogen sulfide sensing: Example of core-shell CuO/CuFe₂O₄ nanostructures. *Sens. Actuators B Chem.* 2020, 321, 128523. <https://doi.org/10.1016/j.snb.2020.128523>.
- [183] Liu, X.; Li, S.; Akinwolemiwa, B.; Hu, D.; Wu, T.; Peng, C. Low-crystalline transition metal oxide / hydroxide on MWCNT by Fenton-reaction-inspired green synthesis for lithium ion battery and OER electrocatalysis. *Electrochim. Acta* 2021, 387, 138559. <https://doi.org/10.1016/j.electacta.2021.138559>.
- [184] Cheng, Z.; Li, S.; Thang, T.; Gao, X.; Luo, S.; Guo, M. Biochar loaded on MnFe₂O₄ as Fenton catalyst for Rhodamine B removal: Characterizations, catalytic performance, process optimization and mechanism. *Colloids Surfaces A Physicochem. Eng. Asp.* 2021, 631, 127651. <https://doi.org/10.1016/j.colsurfa.2021.127651>.
- [185] Zhou, T.; Huang, X.; Zhai, T.; Ma, K.; Zhang, H. Fabrication of novel three-dimensional Fe₃O₄-based particles electrodes with enhanced electrocatalytic activity for Berberine removal. *Chemosphere* 2022, 287, 132397. <https://doi.org/10.1016/j.chemosphere.2021.132397>.

- [186] Yang, R.; Peng, Q.; Yu, B.; Shen, Y.; Cong, H. Yolk-shell Fe₃O₄@MOF-5 nanocomposites as a heterogeneous Fenton-like catalyst for organic dye removal. *Sep. Purif. Technol.* 2021, 267, 118620. <https://doi.org/10.1016/j.seppur.2021.118620>.
- [187] Zhu, X.; Zhang, L.; Zou, G.; Chen, Q.; Guo, Y.; Liang, S.; Hu, L.; North, M.; Xie, H. Carboxylcellulose hydrogel confined-Fe₃O₄ nanoparticles catalyst for Fenton-like degradation of Rhodamine B. *Int. J. Biol. Macromol.* 2021, 180, 792–803. <https://doi.org/10.1016/j.ijbiomac.2021.04.067>.
- [188] Jacobs, J.P.; Maltha, A.; Reinjtjes, J.; Drimal, J.; Ponec, V. Brongersm The surface of catalytically active spinels. *Catalysis* 1994, 147, 294–300. <https://doi.org/10.1006/jcat.1994.1140>.
- [189] So, H.L.; Lin, K.Y.; Chu, W. Triclosan removal by heterogeneous Fenton-like process: Studying the kinetics and surface chemistry of Fe₃O₄ as catalyst. *J. Environ. Chem. Eng.* 2019, 7, 103432. <https://doi.org/10.1016/j.jece.2019.103432>.
- [190] Miller, A. Distribution of Cations in Spinels. *Appl. Phys.* 1959, 30, S24–S25. <https://doi.org/10.1063/1.2185913>.
- [191] Han, X.; Liu, S.; Huo, X.; Cheng, F.; Zhang, M.; Guo, M. Facile and large-scale fabrication of (Mg,Ni)(Fe,Al)₂O₄ heterogeneous photo-Fenton-like catalyst from saprolite laterite ore for effective removal of organic contaminants. *J. Hazard. Mater.* 2020, 392, 122295. <https://doi.org/10.1016/j.jhazmat.2020.122295>.
- [192] Wang, Y.; Tian, D.; Chu, W.; Li, M.; Lu, X. Nanoscaled magnetic CuFe₂O₄ as an activator of peroxymonosulfate for the degradation of antibiotics norfloxacin. *Sep. Purif. Technol.* 2019, 212, 536–544.

- <https://doi.org/10.1016/j.seppur.2018.11.051>.
- [193] Amulya, M.A.S.; Nagaswarupa, H.P.; Kumar, M.R.A.; Ravikumar, C.R.; Kusuma, K.B.; Prashantha, S.C. Evaluation of bifunctional applications of CuFe_2O_4 nanoparticles synthesized by a sonochemical method. *J. Phys. Chem. Solids* 2021, 148, 109756. <https://doi.org/10.1016/j.jpics.2020.109756>.
- [194] Gao, J.; Wu, S.; Han, Y.; Tan, F.; Shi, Y.; Liu, M.; Li, X. 3D mesoporous CuFe_2O_4 as a catalyst for photo-Fenton removal of sulfonamide antibiotics at near neutral pH. *J. Colloid Interface Sci.* 2018, 524, 409–416. <https://doi.org/10.1016/j.jcis.2018.03.112>.
- [195] Saravanakumar, B.; Ramachandran, S.P.; Ravi, G.; Ganesh, V.; Guduru, R.K.; Yuvakkumar, R. Electrochemical performances of monodispersed spherical CuFe_2O_4 nanoparticles for pseudocapacitive applications. *Vacuum* 2019, 168, 108798. <https://doi.org/10.1016/j.vacuum.2019.108798>.
- [196] Wu, X.; Xia, F.; Nan, Z. Facile synthesis of double-mesoporous-shelled hollow spheres of $\text{Cu-CuFe}_2\text{O}_4/\text{SiO}_2$ composite as excellent Fenton catalyst. *Mater. Chem. Phys.* 2020, 242, 122490. <https://doi.org/10.1016/j.matchemphys.2019.122490>.
- [197] Li, J.; Ren, Y.; Ji, F.; Lai, B. Heterogeneous catalytic oxidation for the degradation of p-nitrophenol in aqueous solution by persulfate activated with CuFe_2O_4 magnetic nano-particles. *Chem. Eng. J.* 2017, 324, 63–73. <https://doi.org/10.1016/j.cej.2017.04.104>.
- [198] Fontecha-Cámara, M.A.; Moreno-Castilla, C.; López-Ramón, M.V.; Álvarez, M.A. Mixed iron oxides as Fenton catalysts for gallic acid removal from aqueous solutions. *Appl. Catal. B Environ.* 2016, 196, 207–215.

- <https://doi.org/10.1016/j.apcatb.2016.05.032>.
- [199] Feng, Y.; Liao, C.; Shih, K. Copper-promoted circumneutral activation of H₂O₂ by magnetic CuFe₂O₄ spinel nanoparticles: Mechanism, stoichiometric efficiency, and pathway of degrading sulfanilamide. *Chemosphere* 2016, 154, 573–582. <https://doi.org/10.1016/j.chemosphere.2016.04.019>.
- [200] Zhang, T.; Zhu, H.; Croue, J. Production of Sulfate Radical from Peroxymonosulfate Induced by a Magnetically Separable CuFe₂O₄ Spinel in Water: Efficiency, Stability, and Mechanism. *Environ. Sci. Technol.* 2013, 47, 2784–2791. <https://doi.org/10.1021/es304721g>.
- [201] Suraj, P.; Kumar, V.; Thakur, C.; Ghosh, P. Taguchi optimization of COD removal by heterogeneous Fenton process using copper ferro spinel catalyst in a fixed bed reactor—RTD, kinetic and thermodynamic study. *J. Environ. Chem. Eng.* 2019, 7, 102859. <https://doi.org/10.1016/j.jece.2018.102859>.
- [202] Ding, R.; Li, W.; He, C.; Wang, Y.; Liu, X.; Zhou, G.; Mu, Y. Oxygen vacancy on hollow sphere CuFe₂O₄ as an efficient Fenton-like catalysis for organic pollutant degradation over a wide pH range. *Appl. Catal. B Environ.* 2021, 291, 120069. <https://doi.org/10.1016/j.apcatb.2021.120069>.
- [203] Yu, D.; Ni, H.; Wang, L.; Wu, M.; Yang, X. Nanoscale-confined precursor of CuFe₂O₄ mediated by hyperbranched polyamide as an unusual heterogeneous Fenton catalyst for efficient dye degradation. *J. Clean. Prod.* 2018, 186, 146–154. <https://doi.org/10.1016/j.jclepro.2018.03.134>.
- [204] López-Ramón, M.V.; Álvarez, M.A.; Moreno-Castilla, C.; Fontecha-Cámara, M.A.; Yebra-Rodríguez, Á.; Bailón-García, E. Effect of calcination temperature of a copper ferrite synthesized by a sol-gel method on its

- structural characteristics and performance as Fenton catalyst to remove gallic acid from water. *J. Colloid Interface Sci.* 2018, 511, 193–202. <https://doi.org/10.1016/j.jcis.2017.09.117>.
- [205] Xu, M.; Li, J.; Yan, Y.; Zhao, X.; Yan, J.; Zhang, Y.; Lai, B. Catalytic degradation of sulfamethoxazole through peroxy monosulfate activated with expanded graphite loaded CoFe_2O_4 particles. *Chem. Eng. J.* 2019, 369, 403–413. <https://doi.org/10.1016/j.cej.2019.03.075>.
- [206] Guo, X.; Li, H.; Zhao, S. Fast degradation of Acid Orange II by bicarbonate-activated hydrogen peroxide with a magnetic S-modified CoFe_2O_4 catalyst. *Taiwan Inst. Chem. Eng.* 2015, 55, 90–100. <https://doi.org/10.1016/j.jtice.2015.03.039>.
- [207] Yao, Y.; Yang, Z.; Zhang, D.; Peng, W.; Sun, H.; Wang, S. Magnetic CoFe_2O_4 -Graphene Hybrids: Facile Synthesis, Characterization, and Catalytic Properties. *Ind. Eng. Chem. Res.* 2012, 51, 6044–6051. <https://doi.org/10.1021/ie300271p>.
- [208] Hong, P.; Li, Y.; He, J.; Saeed, A.; Zhang, K. Rapid degradation of aqueous doxycycline by surface $\text{CoFe}_2\text{O}_4/\text{H}_2\text{O}_2$ system: Behaviors, mechanisms, pathways and DFT calculation. *Appl. Surf. Sci.* 2020, 526, 146557. <https://doi.org/10.1016/j.apsusc.2020.146557>.
- [209] Feng, X.; Mao, G.Y.; Bu, F.X.; Cheng, X.L.; Jiang, D.M.; Jiang, J.S. Controlled synthesis of monodisperse CoFe_2O_4 nanoparticles by the phase transfer method and their catalytic activity on methylene blue discoloration with H_2O_2 . *Magn. Mater.* 2013, 343, 126–132. <https://doi.org/10.1016/j.jmmm.2013.05.001>.
- [210] Singh, S.; Singhal, S. Transition metal doped cobalt ferrite nanoparticles:

- Efficient photocatalyst for photodegradation of textile dye. *Mater. Today Proc.* 2019, 14, 453–460. <https://doi.org/10.1016/j.matpr.2019.04.168>.
- [211] Vinosha, P.A.; Das, S.J. Investigation on the role of pH for the structural, optical and magnetic properties of cobalt ferrite nanoparticles and its effect on the photo-fenton activity. *Mater. Today Proc.* 2018, 5, 8662–8671. <https://doi.org/10.1016/j.matpr.2017.12.291>.
- [212] Kachi, W.; Al-Shammari, A.M.; Zainal, I.G. Cobalt Ferrite Nanoparticles: Preparation, characterization and salinized with 3-aminopropyl triethoxysilane. *Energy Procedia* 2019, 157, 1353–1365. <https://doi.org/10.1016/j.egypro.2018.11.300>.
- [213] Sun, Z.; Liu, X.; Dong, X.; Zhang, X.; Tan, Y.; Yuan, F.; Zheng, S.; Li, C. Synergistic activation of peroxymonosulfate via in situ growth FeCo₂O₄ nanoparticles on natural rectorite: Role of transition metal ions and hydroxyl groups. *Chemosphere* 2021, 263, 127965. <https://doi.org/10.1016/j.chemosphere.2020.127965>.
- [214] Mohamed, S.G.; Tsai, Y.Q.; Chen, C.J.; Tsai, Y.T.; Hung, T.F.; Chang, W.S.; Liu, R.S. Ternary Spinel MCo₂O₄ (M = Mn, Fe, Ni, and Zn) Porous Nanorods as Bifunctional Cathode Materials for Lithium-O₂ Batteries. *Appl. Mater. Interfaces* 2015, 7, 12038–12046. <https://doi.org/10.1021/acsami.5b02180>.
- [215] Yadav, A.A.; Hunge, Y.M.; Kulkarni, S.B. Synthesis of multifunctional FeCo₂O₄ electrode using ultrasonic treatment for photocatalysis and energy storage applications. *Ultrason. Sonochem.* 2019, 58, 104663. <https://doi.org/10.1016/j.ultsonch.2019.104663>.
- [216] Zhang, T.; Ma, Q.; Zhou, M.; Li, C.; Sun, J.; Shi, W.; Ai, S. Degradation of

- methylene blue by a heterogeneous Fenton reaction catalyzed by FeCo₂O₄-N-C nanocomposites derived by ZIFs. *Powder Technol.* 2021, 383, 212–219. <https://doi.org/10.1016/j.powtec.2021.01.051>.
- [217] Zhao, L.; Yang, D.; Ma, L.; Feng, X.; Ding, H. An efficient heterogeneous catalyst of FeCo₂O₄/g-C₃N₄ composite for catalytic peroxymonosulfate oxidation of organic pollutants under visible light. *Colloids Surfaces A* 2021, 610, 125725. <https://doi.org/10.1016/j.colsurfa.2020.125725>.
- [218] Shan, Z.; Ma, F.; You, S.; Shan, L.; Kong, D.; Guo, H.; Cui, C. Enhanced visible light photo-Fenton catalysis by lanthanum-doping BiFeO₃ for norfloxacin degradation. *Environ. Res.* 2023, 216, 114588. <https://doi.org/10.1016/j.envres.2022.114588>.
- [219] Chen, X.; Qiao, J.; Wang, Z.; Sun, W.; Sun, K. Layered perovskites with exsolved Co-Fe nanoalloy as highly active and stable anodes for direct carbon solid oxide fuel cells. *J. Alloys Compd.* 2023, 940, 168872. <https://doi.org/10.1016/j.jallcom.2023.168872>.
- [220] Torregrosa-Rivero, V.; Sánchez-Adsuar, M.-S.; Illán-Gómez, M.J. Exploring the effect of using carbon black in the sol-gel synthesis of BaMnO₃ and BaMn_{0.7}Cu_{0.3}O₃ perovskite catalysts for CO oxidation. *Catal. Today* 2023, in press. <https://doi.org/10.1016/j.cattod.2023.02.005>.
- [221] Nguyen, A.T.; Phung, V.D.; Mittova, V.O.; Ngo, H.D.; Vo, T.N.; Le Thi, M.L.; Nguyen, V.H.; Mittova, I.Y.; Le, M.L.P.; Ahn, Y.N.; et al. Fabricating nanostructured HoFeO₃ perovskite for lithium-ion battery anodes via coprecipitation. *Scr. Mater.* 2022, 207, 114259. <https://doi.org/10.1016/j.scriptamat.2021.114259>.
- [222] Alrozi, R.; Zubir, N.A.; Bakar, N.F.A.; Ladewig, B.P.; Motuzas, J.; Bakar,

- N.H.H.A.; Wang, D.K.; da Costa, J.C.D. Functional role of B-site substitution on the reactivity of CaMFeO_3 (M = Cu, Mo, Co) perovskite catalysts in heterogeneous Fenton-like degradation of organic pollutant. *J. Taiwan Inst. Chem. Eng.* 2023, 143, 104675. <https://doi.org/10.1016/j.jtice.2023.104675>.
- [223] Li, J.; Ma, W.; Zhong, D.; Li, K.; Ma, J.; Zhang, S.; Du, X. Oxygen vacancy concentration modulation of perovskite-based heterogeneous catalysts for Fenton-like oxidation of tetracycline. *J. Clean. Prod.* 2022, 362, 132469. <https://doi.org/10.1016/j.jclepro.2022.132469>.
- [224] Xie, L.; Liu, X.; Chang, J.; Zhang, C.; Li, Y.; Zhang, H.; Zhan, S.; Hu, W. Enhanced redox activity and oxygen vacancies of perovskite triggered by copper incorporation for the improvement of electro-Fenton activity. *Chem. Eng. J.* 2022, 428, 131352. <https://doi.org/10.1016/j.cej.2021.131352>.
- [225] Rusevova, K.; Köferstein, R.; Rosell, M.; Richnow, H.H.; Kopinke, F.D.; Georgi, A. LaFeO_3 and BiFeO_3 perovskites as nano-catalysts for contaminant degradation in heterogeneous Fenton-like reactions. *Chem. Eng. J.* 2014, 239, 322–331. <https://doi.org/10.1016/j.cej.2013.11.025>.
- [226] Zhao, H.; Cao, J.; Lv, H.; Wang, Y.; Zhao, G. 3D nano-scale perovskite-based composite as Fenton-like system for efficient oxidative degradation of ketoprofen. *Catal. Commun.* 2013, 41, 87–90. <https://doi.org/10.1016/j.catcom.2013.07.017>.
- [227] Ho, J.H.; Li, Y.; Dai, Y.; Kim, T.; Wang, J.; Ren, J.; Yun, H.S.; Liu, X. Ionothermal synthesis of N-doped carbon supported CoMn_2O_4 nanoparticles as ORR catalyst in direct glucose alkaline fuel cell. *Int. J. Hydrog. Energy* 2021, 46, 20503–20515. <https://doi.org/10.1016/j.ijhydene.2021.03.145>.

- [228] Estrada-Arriaga, E.B.; Guadarrama-Pérez, O.; Silva-Martínez, S.; Cuevas-Arteaga, C.; Guadarrama-Pérez, V.H. Oxygen re-duction reaction (ORR) electrocatalysts in constructed wetland-microbial fuel cells: Effect of different carbon-based catalyst biocathode during bioelectricity production. *Electrochim. Acta* 2021, 370, 137745. <https://doi.org/10.1016/j.electacta.2021.137745>.
- [229] Gao, X.; He, L.; Yu, H.; Xie, F.; Yang, Y.; Shao, Z. The non-precious metal ORR catalysts for the anion exchange membrane fuel cells application: A numerical simulation and experimental study. *Int. J. Hydrog. Energy* 2020, 45, 23353–23367. <https://doi.org/10.1016/j.ijhydene.2020.06.066>.
- [230] Liu, H.; Yang, D.H.; Wang, X.Y.; Zhang, J.; Han, B.H. N-doped graphitic carbon shell-encapsulated FeCo alloy derived from metal–polyphenol network and melamine sponge for oxygen reduction, oxygen evolution, and hydrogen evolution reactions in alkaline media. *J. Colloid Interface Sci.* 2021, 581, 362–373. <https://doi.org/10.1016/j.jcis.2020.07.055>.
- [231] Zhou, W.; Meng, X.; Gao, J.; Alshwabkeh, A.N. Hydrogen peroxide generation from O₂ electroreduction for environmental remediation: A state-of-the-art review. *Chemosphere* 2019, 225, 588–607. <https://doi.org/10.1016/j.chemosphere.2019.03.042>.
- [232] Melchionna, M.; Fornasiero, P.; Prato, M. The Rise of Hydrogen Peroxide as the Main Product by Metal-Free Catalysis in Oxygen Reductions. *Adv. Mater.* 2019, 31, 1802920. <https://doi.org/10.1002/adma.201802920>.
- [233] Yu, F.; Wang, Y.; Ma, H. Enhancing the yield of H₂O₂ from oxygen reduction reaction performance by hierarchically porous carbon modified active carbon fiber as an effective cathode used in electro-Fenton. *J.*

- Electroanal. Chem. 2019, 838, 57–65.
<https://doi.org/10.1016/j.jelechem.2019.02.036>.
- [234] Zhao, Q.; An, J.; Wang, X.; Li, N. In-situ hydrogen peroxide synthesis with environmental applications in bioelectrochemical systems: A state-of-the-art review. *Int. J. Hydrog. Energy* 2020, 46, 3204–3219.
<https://doi.org/10.1016/j.ijhydene.2020.05.227>.
- [235] Candia-Onfray, C.; Bollo, S.; Yáñez, C.; Escalona, N.; Marco, J.F.; Menéndez, N.; Salazar, R.; Recio, F.J. Nanostructured Fe-N-C pyrolyzed catalyst for the H₂O₂ electrochemical sensing. *Electrochim. Acta* 2021, 387, 138468. <https://doi.org/10.1016/j.electacta.2021.138468>.
- [236] Liu, Y.; Quan, X.; Fan, X.; Wang, H.; Chen, S. High-yield electrosynthesis of hydrogen peroxide from oxygen reduction by hierarchically porous carbon. *Angew. Chem. Int. Ed.* 2015, 54, 6837–6841.
<https://doi.org/10.1002/anie.201502396>.
- [237] Qiu, Z.; Ge, X.; Huang, N.; Zhou, S.; Zhang, J.; Xuan, J. Polyethylene oxide-polypropylene oxide -polyethylene oxide derived porous carbon materials with different molecular weights as ORR catalyst in alkaline electrolytes. *Int. J. Hydrog. Energy* 2021, 46, 2952–2959.
<https://doi.org/10.1016/j.ijhydene.2020.07.175>.
- [238] Inozemtseva, A.I.; Kataev, E.Y.; Frolov, A.S.; Amati, M.; Gregoratti, L.; Beranová, K.; Dieste, V.P.; Escudero, C.; Fedorov, A.; Tarasov, A.V.; et al. On the catalytic and degradative role of oxygen-containing groups on carbon electrode in non-aqueous ORR. *Carbon N. Y.* 2021, 176, 632–641.
<https://doi.org/10.1016/j.carbon.2020.12.008>.
- [239] Wang, X.; Sun, G.; Routh, P.; Kim, D.H.; Huang, W.; Chen, P. Heteroatom-

- doped graphene materials: Syntheses, properties and applications. *Chem. Soc. Rev.* 2014, 43, 7067–7098. <https://doi.org/10.1039/c4cs00141a>.
- [240] Eisenberg, D.; Stroek, W.; Geels, N.J.; Tanase, S.; Ferbinteanu, M.; Teat, S.J.; Mettraux, P.; Yan, N.; Rothenberg, G. A rational synthesis of hierarchically porous, N-doped carbon from Mg-based MOFs: Understanding the link between nitrogen content and oxygen reduction electrocatalysis. *Phys. Chem. Chem. Phys.* 2016, 18, 20778–20783. <https://doi.org/10.1039/c6cp04132a>.
- [241] Shibuya, R.; Kondo, T.; Nakamura, J. Active sites in nitrogen-doped carbon materials for oxygen reduction reaction. *Carbon-Based Met. Catal. Des. Appl.* 2018, 1–2, 227–249. <https://doi.org/10.1002/9783527811458.vol1-ch8>.
- [242] Zhou, W.; Rajic, L.; Meng, X.; Nazari, R.; Zhao, Y.; Wang, Y.; Gao, J.; Qin, Y.; Alshawabkeh, A.N. Efficient H₂O₂ electrogeneration at graphite felt modified via electrode polarity reversal: Utilization for organic pollutants degradation. *Chem. Eng. J.* 2019, 364, 428–439. <https://doi.org/10.1016/j.cej.2019.01.175>.
- [243] Zhu, J.; Xiao, X.; Zheng, K.; Li, F.; Ma, G.; Yao, H.; Wang, X.; Chen, Y. KOH-treated reduced graphene oxide: 100% selectivity for H₂O₂ electroproduction. *Carbon* 2019, 153, 6–11. <https://doi.org/10.1016/j.carbon.2019.07.009>.
- [244] Wu, K.H.; Wang, D.; Lu, X.; Zhang, X.; Xie, Z.; Liu, Y.; Su, B.J.; Chen, J.M.; Su, D.S.; Qi, W.; et al. Highly Selective Hydrogen Peroxide Electrosynthesis on Carbon: In Situ Interface Engineering with Surfactants. *Chem* 2020, 6, 1443–1458. <https://doi.org/10.1016/j.chempr.2020.04.002>.

- [245] Xu, H.; Guo, H.; Chai, C.; Li, N.; Lin, X.; Xu, W. Anodized graphite felt as an efficient cathode for in-situ hydrogen peroxide production and Electro-Fenton degradation of rhodamine B. *Chemosphere* 2022, 286, 131936. <https://doi.org/10.1016/j.chemosphere.2021.131936>.
- [246] Zahoor, A.; Christy, M.; Hwang, Y.J.; Lim, Y.R.; Kim, P.; Nahm, K.S. Improved electrocatalytic activity of carbon materials by nitrogen doping. *Appl. Catal. B Environ.* 2014, 147, 633–641. <https://doi.org/10.1016/j.apcatb.2013.09.043>.
- [247] Okamoto, Y. First-principles molecular dynamics simulation of O₂ reduction on nitrogen-doped carbon. *Appl. Surf. Sci.* 2009, 256, 335–341. <https://doi.org/10.1016/j.apsusc.2009.08.027>.
- [248] Legarreta-Mendoza, A.; Flores-Holguín, N.; Lardizabal-Gutiérrez, D. A proposal based on quantum phenomena for the ORR mechanism on nitrogen-doped carbon-based electrocatalysts. *Int. J. Hydrog. Energy* 2019, 44, 12374–12380. <https://doi.org/10.1016/j.ijhydene.2018.10.232>.
- [249] Zhu, Y.; Qiu, S.; Deng, F.; Ma, F.; Zheng, Y. Degradation of sulfathiazole by electro-Fenton using a nitrogen-doped cathode and a BDD anode: Insight into the H₂O₂ generation and radical oxidation. *Sci. Total Environ.* 2020, 722, 137853. <https://doi.org/10.1016/j.scitotenv.2020.137853>.
- [250] Wang, Y.; Yi, M.; Wang, K.; Song, S. Enhanced electrocatalytic activity for H₂O₂ production by the oxygen reduction reaction: Rational control of the structure and composition of multi-walled carbon nanotubes. *Chin. J. Catal.* 2019, 40, 523–533. [https://doi.org/10.1016/S1872-2067\(19\)63314-0](https://doi.org/10.1016/S1872-2067(19)63314-0).
- [251] Yu, Y.; You, S.; Du, J.; Zhang, P.; Dai, Y.; Liu, M.; Jiang, B.; Ren, N.; Zou, J. Ti³⁺-self-doped TiO₂ with multiple crystal-phases anchored on acid-

- pickled ZIF-67-derived Co_3O_4 @N-doped graphitized-carbon as a durable catalyst for oxygen reduction in alkaline and acid media. *Chem. Eng. J.* 2021, 403, 126441. <https://doi.org/10.1016/j.cej.2020.126441>.
- [252] Li, Z.; Wang, W.; Zhou, M.; He, B.; Ren, W.; Chen, L.; Xu, W.; Hou, Z.; Chen, Y. In-situ self-templated preparation of porous core-shell $\text{Fe}_{1-x}\text{S}@N, S$ co-doped carbon architecture for highly efficient oxygen reduction reaction. *J. Energy Chem.* 2021, 54, 310–317. <https://doi.org/10.1016/j.jechem.2020.06.010>.
- [253] Zhu, Y.; Deng, F.; Qiu, S.; Ma, F.; Zheng, Y.; Lian, R. Enhanced electro-Fenton degradation of sulfonamides using the N, S co-doped cathode: Mechanism for H_2O_2 formation and pollutants decay. *J. Hazard. Mater.* 2021, 403, 123950. <https://doi.org/10.1016/j.jhazmat.2020.123950>.
- [254] Soo, L.T.; Loh, K.S.; Mohamad, A.B.; Daud, W.R.W.; Wong, W.Y. An overview of the electrochemical performance of modified graphene used as an electrocatalyst and as a catalyst support in fuel cells. *Appl. Catal. A Gen.* 2015, 497, 198–210. <https://doi.org/10.1016/j.apcata.2015.03.008>.
- [255] Zhang, L.; Xia, Z. Mechanisms of oxygen reduction reaction on nitrogen-doped graphene for fuel cells. *J. Phys. Chem. C* 2011, 115, 11170–11176. <https://doi.org/10.1021/jp201991j>.
- [256] Su, P.; Zhou, M.; Lu, X.; Yang, W.; Ren, G.; Cai, J. Electrochemical catalytic mechanism of N-doped graphene for enhanced H_2O_2 yield and in-situ degradation of organic pollutant. *Appl. Catal. B Environ.* 2019, 245, 583–595. <https://doi.org/10.1016/j.apcatb.2018.12.075>.
- [257] Su, P.; Zhou, M.; Song, G.; Du, X.; Lu, X. Efficient H_2O_2 generation and spontaneous $\bullet\text{OH}$ conversion for in-situ phenol degradation on nitrogen-

- doped graphene: Pyrolysis temperature regulation and catalyst regeneration mechanism. *J. Hazard. Mater.* 2020, 397, 122681. <https://doi.org/10.1016/j.jhazmat.2020.122681>.
- [258] Qin, M.; Fan, S.; Wang, L.; Gan, G.; Wang, X.; Cheng, J.; Hao, Z.; Li, X. Oxygen and nitrogen co-doped ordered mesoporous carbon materials enhanced the electrochemical selectivity of O₂ reduction to H₂O₂. *J. Colloid Interface Sci.* 2020, 562, 540–549. <https://doi.org/10.1016/j.jcis.2019.11.080>.
- [259] Xie, Y.; Li, Y.; Huang, Z.; Zhang, J.; Jia, X.; Wang, X.S.; Ye, J. Two types of cooperative nitrogen vacancies in polymeric carbon nitride for efficient solar-driven H₂O₂ evolution. *Appl. Catal. B Environ.* 2020, 265, 118581. <https://doi.org/10.1016/j.apcatb.2019.118581>.
- [260] Zhou, W.; Xie, L.; Gao, J.; Nazari, R.; Zhao, H.; Meng, X.; Sun, F.; Zhao, G.; Ma, J. Selective H₂O₂ electrosynthesis by O-doped and transition-metal-O-doped carbon cathodes via O₂ electroreduction: A critical review. *Chem. Eng. J.* 2021, 410, 128368. <https://doi.org/10.1016/j.cej.2020.128368>.
- [261] Iglesias, D.; Giuliani, A.; Melchionna, M.; Marchesan, S.; Criado, A.; Nasi, L.; Bevilacqua, M.; Tavagnacco, C.; Vizza, F.; Prato, M.; et al. N-Doped Graphitized Carbon Nanohorns as a Forefront Electrocatalyst in Highly Selective O₂ Reduction to H₂O₂. *Chem* 2018, 4, 106–123. <https://doi.org/10.1016/j.chempr.2017.10.013>.
- [262] Chen, J.Y.; Li, N.; Zhao, L. Three-dimensional electrode microbial fuel cell for hydrogen peroxide synthesis coupled to wastewater treatment. *J. Power Sources* 2014, 254, 316–322. <https://doi.org/10.1016/j.jpowsour.2013.12.114>.

- [263] He, W.; Jiang, C.; Wang, J.; Lu, L. High-Rate Oxygen Electroreduction over Graphitic-N Species Exposed on 3D Hierarchically Porous Nitrogen-Doped Carbons. *Angew. Chem.* 2014, 53, 9503–9507. <https://doi.org/10.1002/anie.201404333>.
- [264] Zhang, T.; Wu, J.; Wang, Z.; Wei, Z.; Liu, J.; Gong, X. Transfer of molecular oxygen and electrons improved by the regulation of C-N/C = O for highly efficient $2e^-$ ORR. *Chem. Eng. J.* 2022, 433, 133591. <https://doi.org/10.1016/j.cej.2021.133591>.
- [265] Chen, D.; Zhu, J.; Mu, X.; Cheng, R.; Li, W.; Liu, S.; Pu, Z.; Lin, C.; Mu, S. Nitrogen-Doped carbon coupled FeNi₃ intermetallic compound as advanced bifunctional electrocatalyst for OER, ORR and zn-air batteries. *Appl. Catal. B Environ.* 2020, 268, 118729. <https://doi.org/10.1016/j.apcatb.2020.118729>.
- [266] Gao, Y.; Zhu, W.; Wang, C.; Zhao, X.; Shu, M.; Zhang, J.; Bai, H. Enhancement of oxygen reduction on a newly fabricated cathode and its application in the electro-Fenton process. *Electrochim. Acta* 2020, 330, 135206. <https://doi.org/10.1016/j.electacta.2019.135206>.
- [267] Teng, Z.; Cai, W.; Sim, W.; Zhang, Q.; Wang, C.; Su, C.; Ohno, T. Applied Catalysis B: Environmental Photoexcited single metal atom catalysts for heterogeneous photocatalytic H₂O₂ production: Pragmatic guidelines for predicting charge separation. *Appl. Catal. B Environ.* 2021, 282, 119589. <https://doi.org/10.1016/j.apcatb.2020.119589>.
- [268] Yeager, E. Dioxygen electrocatalysis: Mechanisms in relation to catalyst structure. *J. Mol. Catal.* 1986, 38, 5–25. [https://doi.org/10.1016/0304-5102\(86\)87045-6](https://doi.org/10.1016/0304-5102(86)87045-6).

- [269] Chan, A.W.; Hoffmann, R.; Ho, W. Theoretical aspects of photoinitiated chemisorption, dissociation, and desorption of O₂ on Pt(111). *Langmuir* 1992, 8, 1111–1119. <https://doi.org/10.1021/la00040a017>.
- [270] Viswanathan, V.; Hansen, H.A.; Rossmeisl, J.; Norskov, J. Unifying the 2e⁻ and 4e⁻ reduction of oxygen on metal surfaces. *J. Phys. Chem. Lett.* 2012, 3, 2948–2951. <https://doi.org/10.1021/jz301476w>.
- [271] Kim, J.H.; Kim, Y.T.; Joo, S.H. Electrocatalyst design for promoting two-electron oxygen reduction reaction: Isolation of active site atoms. *Curr. Opin. Electrochem.* 2020, 21, 109–116. <https://doi.org/10.1016/j.coelec.2020.01.007>.
- [272] Choi, C.H.; Kwon, H.C.; Yook, S.; Shin, H.; Kim, H.; Choi, M. Hydrogen peroxide synthesis via enhanced two-electron oxygen reduction pathway on carbon-coated pt surface. *J. Phys. Chem. C* 2014, 118, 30063–30070. <https://doi.org/10.1021/jp5113894>.
- [273] Perry, S.C.; Mavrikis, S.; Wang, L.; León, C.P. De Future perspectives for the advancement of electrochemical hydrogen peroxide production. *Curr. Opin. Electrochem.* 2021, 30, 100792. <https://doi.org/10.1016/j.coelec.2021.100792>.
- [274] Huang, Y.; Liu, W.; Kan, S.; Liu, P.; Hao, R.; Hu, H.; Zhang, J.; Liu, H.; Liu, M.; Liu, K. Tuning morphology and structure of Fe–N–C catalyst for ultra-high oxygen reduction reaction activity. *Int. J. Hydrog. Energy* 2020, 45, 6380–6390. <https://doi.org/10.1016/j.ijhydene.2019.12.130>.
- [275] Daniel, G.; Kosmala, T.; Dalconi, M.C.; Nodari, L.; Badocco, D.; Pastore, P.; Lorenzetti, A.; Granozzi, G.; Durante, C. Upcycling of polyurethane into iron-nitrogen-carbon electrocatalysts active for oxygen reduction reaction.

- Electrochim. Acta 2020, 362, 137200.
<https://doi.org/10.1016/j.electacta.2020.137200>.
- [276] Zhang, J.; Song, L.H.; Zhao, C.F.; Yin, X.P.; Zhao, Y.F. Co, N co-doped porous carbons as high-performance oxygen reduction electrocatalysts. *Xinxing Tan Cailiao/New Carbon Mater.* 2021, 36, 209–218.
[https://doi.org/10.1016/S1872-5805\(21\)60016-1](https://doi.org/10.1016/S1872-5805(21)60016-1).
- [277] Chen, E.; Bevilacqua, M.; Tavagnacco, C.; Montini, T.; Yang, C.M.; Fornasiero, P. High surface area N/O co-doped carbon materials: Selective electrocatalysts for O₂ reduction to H₂O₂. *Catal. Today* 2020, 356, 132–140.
<https://doi.org/10.1016/j.cattod.2019.06.034>.
- [278] Chen, J.; Wang, Z.; Mao, J.; Liu, C.; Chen, Y.; Lu, Z.; Feng, S.P. Bimetallic Ag–Cu nanosheets assembled flower-like structure for oxygen reduction reaction. *J. Alloys Compd.* 2021, 856, 157379.
<https://doi.org/10.1016/j.jallcom.2020.157379>.
- [279] Zhang, A.; Liu, Y.; Wu, J.; Zhu, J.; Cheng, S.; Wang, Y.; Hao, Y.; Zeng, S. Electrocatalytic selectivity to H₂O₂ enabled by two-electron pathway on Cu-deficient Au@Cu_{2-x}S-CNTs electrocatalysts. *Chem. Eng. J.* 2023, 454, 140317. <https://doi.org/10.1016/j.cej.2022.140317>.
- [280] Wang, B.; Jin, C.; Shao, S.; Yue, Y.; Zhang, Y.; Wang, S.; Chang, R.; Zhang, H.; Zhao, J.; Li, X. Electron-deficient Cu site catalyzed acetylene hydrochlorination. *Green Energy Environ.* 2022, 1–13, in press.
<https://doi.org/10.1016/j.gee.2022.01.005>.
- [281] Noh, S.H.; Seo, M.H.; Ye, X.; Makinose, Y.; Okajima, T.; Matsushita, N.; Han, B.; Ohsaka, T. Design of an active and durable catalyst for oxygen reduction reactions using encapsulated Cu with N-doped carbon shells

- (Cu@N-C) activated by CO₂ treatment. *J. Mater. Chem. A* 2015, 3, 22031–22034. <https://doi.org/10.1039/c5ta06108c>.
- [282] Lenarda, A.; Bevilacqua, M.; Tavagnacco, C.; Nasi, L.; Criado, A.; Vizza, F.; Melchionna, M.; Prato, M.; Fornasiero, P. Selective Electrocatalytic H₂O₂ Generation by Cobalt@N-Doped Graphitic Carbon Core–Shell Nanohybrids. *ChemSusChem* 2019, 12, 1664–1672. <https://doi.org/10.1002/cssc.201900238>.
- [283] Gao, J.; Yang, H.; Gao, J.; Yang, H.; Huang, X.; Hung, S.; Cai, W.; Jia, C. Enabling Direct H₂O₂ Production in Acidic Media through Rational Design of Transition Metal Single Atom Catalyst Enabling Direct H₂O₂ Production in Acidic Media through Rational Design of Transition Metal Single Atom Catalyst. *Chem* 2019, 6, 658–674. <https://doi.org/10.1016/j.chempr.2019.12.008>.
- [284] Cao, K.W.; Huang, H.; Li, F.M.; Yao, H.C.; Bai, J.; Chen, P.; Jin, P.J.; Deng, Z.W.; Zeng, J.H.; Chen, Y. Co nanoparticles supported on three-dimensionally N-doped holey graphene aerogels for electrocatalytic oxygen reduction. *J. Colloid Interface Sci.* 2020, 559, 143–151. <https://doi.org/10.1016/j.jcis.2019.10.025>.
- [285] Coliman, J.P.; Denisevich, P.; Konai, Y.; Marrocco, M.; Koval, C.; Anson, F.C. Electrode Catalysis of the Four-Electron Reduction of Oxygen to Water by Dicobalt Face-to-Face Porphyrins. *J. Am. Chem. Soc.* 1980, 102, 6027–6036. <https://doi.org/10.1021/ja00539a009>.
- [286] Ferrara, M.; Bevilacqua, M.; Melchionna, M.; Criado, A.; Crosera, M.; Tavagnacco, C.; Vizza, F.; Fornasiero, P. Exploration of cobalt@N-doped carbon nanocomposites toward hydrogen peroxide (H₂O₂) electrosynthesis:

- A two level investigation through the RRDE analysis and a polymer-based electrolyzer implementation. *Electrochim. Acta* 2020, 364, 137287. <https://doi.org/10.1016/j.electacta.2020.137287>.
- [287] Cheng, X.; Dou, S.; Qin, G.; Wang, B.; Yan, P.; Taylor, T.; Yang, X. Rational design of highly selective nitrogen-doped Fe₂O₃-CNTs catalyst towards H₂O₂ generation in alkaline media. *Int. J. Hydrog. Energy* 2020, 45, 6128–6137. <https://doi.org/10.1016/j.ijhydene.2019.12.187>.
- [288] Yue, D.; Qian, X.; Kan, M.; Fang, M.; Jia, J.; Yang, X.; Zhao, Y. A metal-free visible light active photo-electro-Fenton-like cell for organic pollutants degradation. *Appl. Catal. B Environ.* 2018, 229, 211–217. <https://doi.org/10.1016/j.apcatb.2018.02.033>.
- [289] Hartmann, M.; Kullmann, S.; Keller, H. Wastewater treatment with heterogeneous Fenton-type catalysts based on porous materials. *J. Mater. Chem.* 2010, 20, 9002–9017. <https://doi.org/10.1039/c0jm00577k>.
- [290] Li, Y.; Cao, W.X.; Zuo, X.J. O- and F-doped porous carbon bifunctional catalyst derived from polyvinylidene fluoride for sulfamerazine removal in the metal-free electro-Fenton process. *Environ. Res.* 2022, 212, 113508. <https://doi.org/10.1016/j.envres.2022.113508>.
- [291] Yang, W.; Zhou, M.; Oturan, N.; Li, Y.; Su, P.; Oturan, M.A. Enhanced activation of hydrogen peroxide using nitrogen doped graphene for effective removal of herbicide 2,4-D from water by iron-free electrochemical advanced oxidation. *Electrochim. Acta* 2019, 297, 582–592. <https://doi.org/10.1016/j.electacta.2018.11.196>.
- [292] Haider, M.R.; Jiang, W.L.; Han, J.L.; Sharif, H.M.A.; Ding, Y.C.; Cheng, H.Y.; Wang, A.J. In-situ electrode fabrication from polyaniline derived N-

- doped carbon nanofibers for metal-free electro-Fenton degradation of organic contaminants. *Appl. Catal. B Environ.* 2019, 256, 117774. <https://doi.org/10.1016/j.apcatb.2019.117774>.
- [293] Qin, X.; Zhao, K.; Quan, X.; Cao, P.; Chen, S.; Yu, H. Highly efficient metal-free electro-Fenton degradation of organic contaminants on a bifunctional catalyst. *J. Hazard. Mater.* 2021, 416, 125859. <https://doi.org/10.1016/j.jhazmat.2021.125859>.
- [294] Chen, X.; Wang, L.; Sun, W.; Yang, Z.; Jin, J.; You, D.; Liu, G. Enhanced electrochemical advanced oxidation on boride activated carbon: The influences of boron groups. *Electrochim. Acta* 2021, 400, 139462. <https://doi.org/10.1016/j.electacta.2021.139462>.
- [295] Xie, F.; Gao, Y.; Zhang, J.; Bai, H.; Zhang, J.; Li, Z.; Zhu, W. A novel bifunctional cathode for the generation and activation of H₂O₂ in electro-Fenton: Characteristics and mechanism. *Electrochim. Acta* 2022, 430, 141099. <https://doi.org/10.1016/j.electacta.2022.141099>.
- [296] Zhang, Y.; Gao, M.; Wang, S.G.; Zhou, W.; Sang, Y.; Wang, X.H. Integrated electro-Fenton process enabled by a rotating Fe₃O₄/gas diffusion cathode for simultaneous generation and activation of H₂O₂. *Electrochim. Acta* 2017, 231, 694–704. <https://doi.org/10.1016/j.electacta.2017.02.091>.
- [297] Cui, L.; Huang, H.; Ding, P.; Zhu, S.; Jing, W.; Gu, X. Cogeneration of H₂O₂ and •OH via a novel Fe₃O₄/MWCNTs composite cathode in a dual-compartment electro-Fenton membrane reactor. *Sep. Purif. Technol.* 2020, 237, 116380. <https://doi.org/10.1016/j.seppur.2019.116380>.
- [298] Hu, J.; Wang, S.; Yu, J.; Nie, W.; Sun, J.; Wang, S. Duet Fe₃C and FeN_xSites for H₂O₂ Generation and Activation toward Enhanced Electro-Fenton

- Performance in Wastewater Treatment. *Environ. Sci. Technol.* 2021, 55, 1260–1269. <https://doi.org/10.1021/acs.est.0c06825>.
- [299] Cao, P.; Quan, X.; Zhao, K.; Chen, S.; Yu, H.; Niu, J. Selective electrochemical H₂O₂ generation and activation on a bifunctional catalyst for heterogeneous electro-Fenton catalysis. *J. Hazard. Mater.* 2020, 382, 121102. <https://doi.org/10.1016/j.jhazmat.2019.121102>.
- [300] Ghasemi, M.; Khataee, A.; Gholami, P.; Soltani, R.D.C.; Hassani, A.; Orooji, Y. In-situ electro-generation and activation of hydrogen peroxide using a CuFeNLDH-CNTs modified graphite cathode for degradation of cefazolin. *J. Environ. Manag.* 2020, 267, 110629. <https://doi.org/10.1016/j.jenvman.2020.110629>.
- [301] Cui, L.; Li, Z.; Li, Q.; Chen, M.; Jing, W.; Gu, X. Cu/CuFe₂O₄ integrated graphite felt as a stable bifunctional cathode for high-performance heterogeneous electro-Fenton oxidation. *Chem. Eng. J.* 2020, 127666. <https://doi.org/10.1016/j.cej.2020.127666>.
- [302] Luo, T.; Feng, H.; Tang, L.; Lu, Y.; Tang, W.; Chen, S.; Yu, J.; Xie, Q.; Ouyang, X.; Chen, Z. Efficient degradation of tetracycline by heterogeneous electro-Fenton process using Cu-doped Fe@Fe₂O₃: Mechanism and degradation pathway. *Chem. Eng. J.* 2020, 382, 122970. <https://doi.org/10.1016/j.cej.2019.122970>.
- [303] Sun, X.; Qi, H.; Sun, Z. Bifunctional nickel foam composite cathode co-modified with CoFe@NC and CNTs for electrocatalytic degradation of atrazine over wide pH range. *Chemosphere* 2022, 286, 131972. <https://doi.org/10.1016/j.chemosphere.2021.131972>.
- [304] Yu, D.; He, J.; Wang, Z.; Pang, H.; Li, L.; Zheng, Y.; Chen, Y.; Zhang, J.

- Mineralization of norfloxacin in a CoFe-LDH/CF cathode-based heterogeneous electro-fenton system: Preparation parameter optimization of the cathode and conversion mechanisms of H₂O₂ to ·OH. *Chem. Eng. J.* 2021, 417. <https://doi.org/10.1016/j.cej.2021.129240>.
- [305] Li, Y.; Wang, C.; Pan, S.; Zhao, X.; Liu, N. Mn doping improves in-situ H₂O₂ generation and activation in electro-Fenton process by Fe/Mn@CC cathode using high-temperature shock technique. *Chemosphere* 2022, 307, 136074. <https://doi.org/10.1016/j.chemosphere.2022.136074>.
- [306] Xiao, F.; Wang, Z.; Fan, J.; Majima, T.; Zhao, H.; Zhao, G. Selective Electrocatalytic Reduction of Oxygen to Hydroxyl Radicals via 3-Electron Pathway with FeCo Alloy Encapsulated Carbon Aerogel for Fast and Complete Removing Pollutants. *Angew. Chem. Int. Ed.* 2021, 60, 10375–10383. <https://doi.org/10.1002/anie.202101804>.

OBJECTIVES

The general objective of this work is the development of different materials based on carbon doped with heteroatoms, transition metals or metal oxides and to study their catalytic activity as electro-catalysts for the electro-Fenton process general. Based on this, the carbon materials (xerogels and bio-carbons activated) were doped with different atoms or structures, these materials were characterized and tested in electro-Fenton process in a bifunctional activity. The results were correlated with the chemical, electrochemical, textural, and morphological properties.

The oxygen reduction reaction (ORR) plays a fundamental role in the electro-Fenton process, making its thorough study and understanding crucial for overcoming current limitations. In the development of ORR catalysts applied to electro-Fenton, achieving maximum selectivity towards the two-electron pathway is sought. However, many studies to date have overlooked the potential direct generation of hydroxyl radicals through a three-electron pathway. Therefore, it is necessary to determine possible correlations between material properties that lead to greater selectivity towards the three-electron pathway.

Finally, considering the progress in the use of carbon-based materials in ORR applications, the objective in this case was to optimize the selectivity towards the two or three-electron pathway of the carbonaceous materials developed in this doctoral thesis, through doping with different dopants.

CHAPTER II: MATERIALES Y METODOS DE CARACTERIZACION

2.1.- MATERIALES

Preparación de los materiales empleados como catalizadores

En la presenta tesis se han sintetizado, caracterizado y evaluado diferentes materiales para sus aplicaciones como catalizadores ORR, electro-Fenton y/o bifuncionales. Estos materiales pueden ser enlistados como:

- I. Xerogeles de carbón dopado con oxido de grafeno.
- II. Esferas de xerogeles de carbono impregnadas con manganeso.
- III. Carbones activados dopados con heteroátomos (S, N, P y B).
- IV. Carbones activados dopados con manganeso (Mn).
- V. Magnetita recubierta con xerogeles de carbono.

La síntesis de cada material será explicada al detalle en cada capítulo. Sin embargo, a continuación, se explicarán teóricamente el fundamento y la ruta de síntesis para la obtención de dichos materiales.

2.1.1.- Xerogeles de carbono

Los xerogeles de carbono son sólidos porosos sintetizados principalmente mediante la policondensación de precursores de carbono. Al formarse, el gel, este es sometido a un proceso de secado, mediante el aumento de la temperatura o la reducción de la presión [1]. En este proceso de secado se podría producir un colapso parcial de la estructura interna del gel, lo que podría resultar en una disminución de la estructura porosa.

2.1.2.- Oxido de grafeno

El óxido de grafeno es un compuesto estructuralmente similar al grafeno, pero con la adición de grupos oxigenados tales como hidroxilo, alcoxi, carbonilo, entre otros. Estos grupos funcionales confieren al óxido de grafeno mejoras significativas sobre el grafeno puro, como una mayor solubilidad y la capacidad de funcionalizar su superficie [2]. Como resultado, el óxido de grafeno tiene una amplia gama de aplicaciones en diversos campos. Actualmente, el método más común para su obtención implica el uso de agentes oxidantes en contacto con grafito, conocido principalmente como el método de Hummers [3].

2.1.3.- Carbones activados

El carbón activado es un material poroso obtenido mediante la carbonización y activación de un precursor de carbono. La activación puede ser realizada mediante tratamientos físicos o químicos y, en la actualidad, se están realizando modificaciones superficiales para mejorar las propiedades del carbón activado y así ampliar sus aplicaciones en otros campos como la catálisis [4]. Por otra parte, se puede producir carbón activado partiendo de bioresiduos (madera, cascara de coco, etc), con lo cual se disminuye el impacto ambiental y mejora la economía de los diferentes procesos industriales generadores de dichos residuos [5].

2.1.4.- Magnetita

La magnetita es un óxido de hierro (Fe_3O_4) que presenta en su estructura el hierro en dos estados de valencia (Fe^{2+} y Fe^{3+}) lo que le confiere propiedades interesantes para su aplicación como catalizador Fenton. La magnetita puede ser sintetizada por diferentes métodos, sin embargo, uno de los más empleados actualmente es la coprecipitación química, debido a su simplicidad operacional.

Este método se basa en la mezcla de dos sales precursoras de hierro con los iones metálicos de interés, los cuales, al entrar en contacto con una solución básica, dan paso a la nucleación y posterior transformación a magnetita como producto final [6].

2.2.- TECNICAS DE CARACTERIZACIÓN

Caracterización química y textural

2.2.1.- Isotermas de adsorción

Se realizó la adsorción física de gases N₂ a -196°C y de CO₂ a 0°C, las cuales fueron realizadas con los equipos QUADRASORB-SI y AUTOSORB-1C, respectivamente, de la casa comercial Quantachrome Instruments. Se siguió un procedimiento típico, en el cual se pesan aproximadamente 0.05 g para posteriormente ser desgasificados a vacío dinámico de 10⁻⁶ Bar a 110°C durante 12 horas.

Con los datos obtenidos de las isotermas de adsorción de N₂, fueron calculados los parámetros de superficie específica (S_{B.E.T}) haciendo uso del modelo Brünauer, Emmett y Teller, volumen de microporos (W₀) determinado por el método de Dubinin-Radushkevich, la anchura media de microporos (L₀) con la ecuación de Stoeckli y el volumen de mesoporos calculado a partir del método de Barret, Joyner y Halenda (B.J.H). A partir de los datos obtenidos de las isotermas de CO₂, también fueron calculados el volumen y anchura media de microporos más estrechos, usando los mismos modelos. Las ecuaciones mencionadas son descritas a continuación.

2.2.2.- Modelo Brünauer, Emmett y Teller (B.E.T)

El modelo B.E.T se basa en 5 principales supuestos los cuales son [7]:

- I. Superficie de adsorción uniforme
- II. La molécula adsorbida en una capa se considera un potencial sitio de adsorción para la siguiente capa
- III. Nula limitación en cuanto al espesor de la multicapa
- IV. No existen interacciones entre moléculas de la misma capa
- V. Mayor energía de adsorción en la primera capa

Teniendo en cuenta estos supuestos, se plantea la ecuación 2.1:

$$\frac{V}{V_m} = \frac{C\left(\frac{P}{P_0}\right)}{\left[1+(C-1)\left(\frac{P}{P_0}\right)\right]\left[1-\left(\frac{P}{P_0}\right)\right]} \quad (2.1)$$

Donde V es el volumen de N₂ adsorbido a -196°C, V_m es el volumen de N₂ empleado para la formación de una monocapa, (P/P₀) es la presión relativa y C es la constante de B.E.T [8]. Por lo tanto, el cálculo de la superficie específica queda como S(m² g⁻¹)= 4.356V_m (cm³ g⁻¹), para lo cual es necesario aplicar linealización a la ecuación 2.1 y, con esto, poder calcular el valor de V_m a partir de la ecuación 2.2.

$$\frac{\left(\frac{P}{P_0}\right)}{\left[1-\left(\frac{P}{P_0}\right)\right]} = \frac{1}{CV_m} + \frac{(C-1)\left(\frac{P}{P_0}\right)}{CV_m} \quad (2.2)$$

Donde los gráficos obtenidos a partir de la forma $f(P/P_0) = (P/P_0) / [V(1 - (P/P_0))]$, generan líneas rectas a presiones bajas, generalmente en el rango de $0.05 < (P/P_0) < 0.25$. Con lo cual, la pendiente viene dada por $m = (C-1) / CV_m$ y la intersección con el eje y, por $y = 1/CV_m$, pudiéndose calcular, de esta manera, los valores de C y V_m [9].

2.2.3.- Modelo Dubinin-Radushkevich y Stoeckli

El modelo de Dubinin-Radushkevich (DR) se basa en el concepto de potencial de adsorción de Polanyi y la teoría de llenado de volumen de microporos [10]. La ecuación DR viene dada por [11]:

$$\frac{W}{W_0} = \exp \left[- \frac{BT^2}{\beta^2} \ln^2 \left(\frac{P_0}{P} \right) \right] \quad (2.3)$$

Donde:

W: Volumen de poros llenados en P/P_0 ($\text{cm}^3 \text{ g}^{-1}$)

W_0 : Volumen total de microporos ($\text{cm}^3 \text{ g}^{-1}$)

B: Constante estructural relacionada al ancho de la distribución de poros gaussianos (K^{-2})

T: Temperatura a la que se realiza la isoterma (K)

β : Constante de similitud, dependiendo del adsorbato (ejemplo: 1 para el caso del benceno) (-)

P_0/P : Inverso de la presión relativa del adsorbato

Linealizando la ecuación 2.3 se obtiene la formula aplicada para el cálculo del volumen total de microporos (ecuación 2.4), siendo $\log(W_0)$ la intersección de la recta [12].

$$\log(W) = \log(W_0) - D \log^2 \left(\frac{P_0}{P} \right) \quad (2.4)$$

Donde:

$$D: 0.434B(T/\beta)^2$$

La ecuación Stoeckli es usada para determinar la anchura media de los microporos en un rango de 0.4 a 2 nm [13,14].

$$L_0 = \frac{10.8}{E_0 - 11.4} \quad (2.5)$$

Una vez calculados los parámetros relacionados con los volúmenes de los poros, se pueden presentar tres escenarios.

- I. $W_0(N_2) < W_0(CO_2)$: Bajo grado de activación
- II. $W_0(N_2) = W_0(CO_2)$: Medio grado de activación
- III. $W_0(N_2) > W_0(CO_2)$: Alto grado de activación

2.2.4.- Modelo B.J.H

La distribución del tamaño de poro se puede determinar mediante la teoría de Barrett-Jyoner-Halenda (B.J.H) en poros con diámetro mayor a 5 nm, ya que en aquellos con valores inferiores es posible que se genere un error cercano al 20% [15]. El cálculo se realiza a partir de los datos obtenidos de la rama de adsorción o desorción de la isoterma, basándose en la ecuación de Kelvin (ecuación 2.6), la cual

se aplica específicamente a la condensación capilar y evaporación en poros con geometría cilíndrica a medida que la presión relativa tiende a 1 [16,17].

$$RT \ln \left(\frac{P_d}{P_0} \right) = - \frac{4\gamma V_m}{d} \quad (2.6)$$

Donde:

R: constante del gas ideal

T: temperatura de adsorción

P_d : presión de adsorción

P_0 : presión de vapor saturado

γ : tensión superficial

V_m : volumen molar líquido del adsorbato a T

d: diámetro de Kelvin del poro

2.2.5.- Teoría de la Densidad Funcional

Seaton et al [18], en 1989 propusieron el método de la teoría funcional de la densidad (DFT) para determinar la distribución del tamaño de poros mediante la aplicación a las isothermas de adsorción. Para el caso de carbones activados, se utiliza la teoría funcional de la densidad no local (NLDFE), la cual se basa en un potencial funcional dependiente de la densidad del fluido, que se desarrolla en las siguientes ecuaciones [19]:

$$\Omega_f[\rho_f(\mathbf{r})] = F_f[\rho_f(\mathbf{r})] - \int d\mathbf{r} \rho_f(\mathbf{r}) [\mu_f - U_{\text{ext}}(\mathbf{r})] \quad (2.7)$$

Donde:

r : vector de posición dentro del poro

$\rho_f(r)$: densidad del fluido

F_f : energía libre de Helmholtz del fluido

$U_{\text{ext}}(r)$: potencial externo efectivo solido-fluido

μ_f : potencial químico de adsorción

A partir del método DFT se han planteado otros métodos como la teoría funcional de la densidad de sólidos apagados (QSDFT), la cual es un método DFT multicomponente en el que el sólido es tratado como un componente del sistema adsorbato-adsorbente y es modelado usando la distribución de átomos sólidos [20].

2.2.6.- Microscopía Electrónica de Barrido (SEM)

La morfología superficial de los materiales fue visualizada por medio de Microscopía Electrónica de Barrido (SEM), la cual se fundamenta en el escaneo de la muestra mediante un haz de electrones enfocados que interactúan con los átomos de la muestra, proporcionando la topografía superficial de manera tridimensional [21]. Las micrografías fueron realizadas en el Centro de Instrumentación Científica de la Universidad de Granada, mediante el microscopio electrónico de alta resolución AURIGA (FIB-FESEM) Carl Zeiss SMT.

2.2.7.- Microscopía Electrónica de Transmisión (TEM)

Esta técnica se basa en la incisión sobre la muestra de un haz de electrones de alta energía. Se emplea la transmisión/dispersión de los electrones para formar imágenes, la difracción de los electrones para obtener información acerca de la

estructura cristalina y la emisión de rayos X característicos para conocer la composición elemental de la muestra [22]. Las imágenes de TEM se realizaron en el Centro de Instrumentación Científica de la Universidad de Granada, haciendo uso del microscopio electrónico de transmisión de referencia LIBRA I20 PLUS de Carls Zeiss SMT, permitiendo una resolución entre puntos y líneas de 0.34 y <0.20 nm respectivamente, además de una magnificación de 8-630.000X.

2.2.8.- Espectroscopía de fotoemisión de rayos X (XPS)

La técnica de XPS es usada para determinar la química superficial de las muestras en su parte más externa, se obtiene información semicuantitativa de los elementos que la forman hasta 5-10 nm de profundidad. Los experimentos fueron realizados en los Servicios Centrales de Apoyo a la Investigación de la Universidad de Málaga, donde se utilizó el espectrómetro de referencia ESCA 5701 de Physical Electronics (PHI), con una fuente de radiación $MgK\alpha$ ($h\nu = 1253.6$ eV) y un analizador de electrones semiesférico. La fuente de rayos X fue operada a 12 kV y 10 mA.

Las muestras se colocaron en un portamuestras que se introdujo en la cámara de análisis, donde se realizó una desgasificación al sistema hasta una presión inferior a los 10^{-8} Torr. Según la composición del material, las regiones estudiadas fueron las correspondientes a los elementos Carbono (C_{1s}), Oxígeno (O_{1s}), Boro (B_{1s}), Nitrógeno (N_{1s}), Fosforo (P_{2p}), Azufre (S_{2p}) y Manganeseo (Mn_{2p}), con el número de barridos adecuado para obtener la óptima relación señal/ruido. Los espectros resultantes fueron deconvolucionados mediante un método iterativo de ajuste, haciendo uso de funciones tipo Gaussianas-Lorentzianas para determinar el número de componentes, energía de ligadura de cada pico (B.E) y área de estos

(análisis cuantitativo). Se tomo como pico de referencia el enlace C=C (aromático) presente en la región C_{1s}, asignándole un valor de 248.6 eV.

2.2.9.- Espectroscopía RAMAN

La espectroscopia RAMAN es una técnica que brinda información acerca de la estructura y composición molecular [23], basándose en la dispersión de un haz de luz monocromático cuando incide sobre la muestra [24]. Dicho proceso da paso a dos tipos de dispersiones, la Rayleigh que no genera cambio de energía en los fotones, y la RAMAN en la cual algunos fotones sufren un cambio energético con la muestra.

Los espectros RAMAN fueron obtenidos en el Centro de Instrumentación Científica de la Universidad de Granada, haciendo uso de un espectrómetro Micro-Raman dispersivo JASCO NRS-5100, con un láser de diodo verde 532 nm.

2.2.10.- Difracción de rayos X (DRX)

La difracción de rayos X (DRX) se basa en la interferencia constructiva de las ondas electromagnéticas (rayos X) al impactar sobre los átomos de un elemento y dispersar los electrones que se encuentran alrededor del núcleo [25]. Con lo cual, se pueden obtener los difractogramas característicos de las fases de cada muestra.

Los DRX en polvo fueron registrados en un difractómetro BRUKER D8 DISCOVER usando radiación CuK α con $\lambda=0.1545$ nm., en un rango entre 5 a 100° (2 Θ).

2.2.11.- Espectroscopía infrarroja por transformada de Fourier (FTIR)

La espectroscopía FTIR se basa en las interacciones entre la muestra y la radiación electromagnética, las cuales generan una huella espectral característica de cada material [26].

Los espectros FTIR se realizaron en el Centro de Instrumentación Científica de la Universidad de Granada, con un espectrómetro NICOLET 20SXB con software OMNIC. Los espectros obtenidos fueron realizados mediante la medida de la transmitancia en la zona del infrarrojo medio (4000 a 400 cm^{-1}), con una resolución de 0.5 cm^{-1} . Los espectros se realizaron mediante la preparación de una pastilla de KBr con la correspondiente muestra, para mejorar la resolución del espectro.

Caracterización electroquímica

2.2.12.- Preparación electrodo RRDE

La caracterización electroquímica fue realizada usando un electrodo de disco anillo rotatorio (RRDE), acoplado a un potenciostato compacto (PGSTAT101). Las muestras fueron depositadas en el disco del RRDE mediante la deposición de una tinta previamente preparada. Las tintas se obtuvieron dispersando, mediante sonicación, 5 mg de mezcla en 1 mL de solución de Nafion (1:9; Nafion [5%]: Agua). Posteriormente, se depositaron 20 μL de la tinta preparada para finalmente ser secada con radiación infrarroja.

2.2.13.- Preparación electrodo para electro-Fenton

Los electrodos para electro-Fenton se prepararon mezclando la muestra respectiva, finamente molida, con el aglutinante politetrafluoroetileno (PTFE) en una proporción másica de 9:1. La mezcla resultante se secó durante toda la noche a

una temperatura de 80 °C. Finalmente, se depositaron 25 mg de la pasta final en cada cara de una lamina de grafito (3×1 cm), mediante acción mecánica, la cual se utilizó como soporte del catalizador.

2.2.14.- Voltametría Cíclica (CV)

La CV es una técnica ampliamente utilizada en electroquímica para investigar procesos de oxido-reducción en especies moleculares (figura 2.1) y reacciones químicas iniciadas por transferencia de electrones. La técnica se realiza aplicando un potencial al electrodo de trabajo, en un tiempo y velocidad de barrido determinada, en un rango de voltaje (ida y vuelta), de acuerdo con el cambio de potencial se puede medir la corriente de la reacción redox del material [27].

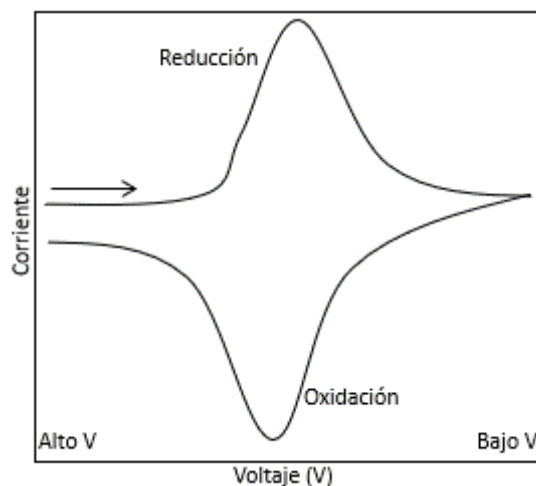


Figura 2.1. Voltamograma cíclico tradicional.

En este Trabajo se llevó a cabo haciendo uso del montaje potencióstato-RRDE, usando como electrolito hidróxido de potasio (KOH) a una concentración 0.1M.

Previo a las CV, se dejó saturando el sistema del gas a emplear (N_2 u O_2) durante un tiempo de 30 minutos. Las CV se realizaron en un rango de 0.4 a -0.8 V con velocidad de barrido de 50mV s^{-1} , a una velocidad de rotación del RRDE de 1000 rpm.

2.2.15.- Voltametría de Barrido Lineal (LSV)

La LSV es una técnica similar a la CV en la cual se aplica un rango de potencial, sin embargo, en este caso solo se mide una sección y no se realiza el ciclo completo (ida y vuelta). La LSV fue empleada haciendo uso del montaje potenciostato-RRDE con KOH [0.1M] como electrolito y burbujeo constante de O_2 en un rango de potencial de -0.8V a -0.4V , velocidad de escaneo de 5 mV s^{-1} y velocidades de rotación de 500 a 4000 rpm.

El número de electrones transferidos y la selectividad hacia H_2O_2 fueron calculados empleando las ecuaciones 2.8 y 2.9, las cuales se realizan utilizando los datos obtenidos mediante la técnica de disco anillo giratorio o RRDE por sus siglas en inglés.

$$n = \frac{4 \times I_D}{I_D + \frac{I_R}{N_C}} \quad (2.8)$$

$$\%H_2O_2 = \frac{200 \times \frac{I_R}{N_C}}{I_D + \frac{I_R}{N_C}} \quad (2.9)$$

Donde I_D e I_R son la corriente en medida en el disco y anillo respectivamente, y N_C es la eficiencia de colección del RRDE (0.249).

Se aplicó el modelo de Koutecky-Levich a los datos obtenidos de la técnica LSV, con la intención de calcular la cinética de densidad de corriente (J_K) conforme a la ecuación (2.10).

$$\frac{1}{J} = \frac{1}{J_K} + \frac{1}{0,2 nF(D_o^{2/3})\nu^{-1/6}C_o w^{1/2}} \quad (2.10)$$

Donde, J es la densidad de corriente, w velocidad de rotación, F constante de Faraday, n número de electrones transferidos por molécula de oxígeno, D_o coeficiente de difusión del oxígeno, ν viscosidad ($0.01 \text{ cm}^2 \text{ s}^{-1}$) y C_o concentración del oxígeno ($1.2 \times 10^{-6} \text{ mol cm}^{-3}$).

2.2.16.- Electro-Fenton

Electro-Fenton es uno de los procesos de oxidación avanzada electroquímica (EAOPs) más estudiados actualmente. Se fundamenta en la generación electroquímica de peróxido de hidrógeno (H_2O_2), por medio de la reacción de reducción de oxígeno (ORR), por la ruta de dos electrones. El H_2O_2 electrogenerado reacciona con el catalizador tipo Fenton para dar paso a la generación del radical hidroxilo ($\text{OH}\cdot$), el cual es un oxidante fuerte, capaz de degradar una amplia gama de contaminantes [28].

BIBLIOGRAPHY

- [1] Torres, C.E.I.; Quezada, T.E.S.; Kharissova, O. V; Kharisov, B.I.; G, M.I. Carbon-Based Aerogels and Xerogels : Synthesis , Properties , Oil Sorption Capacities , and DFT Simulations. *J. Environ. Chem. Eng.* 2021, 9, doi:10.1016/j.jece.2020.104886.
- [2] Smith, A.T.; Marie, A.; Zeng, S.; Liu, B.; Sun, L. Synthesis , Properties , and Applications of Graphene Oxide / Reduced Graphene Oxide and Their Nanocomposites. *Nano Mater. Sci.* 2019, 1, 31–47, doi:10.1016/j.nanoms.2019.02.004.
- [3] Marcano, D.C.; Kosynkin, D. V.; Berlin, J.M.; Sinitskii, A.; Sun, Z.; Slesarev, A.; Alemany, L.B.; Lu, W.; Tour, J.M. Improved Synthesis of Graphene Oxide. *ACS Nano* 2010, 4, 4806–4814, doi:10.1021/nn1006368.
- [4] Zaki, S.; Thian, C. A Review of the Synthesis of Activated Carbon for Biodiesel Production : Precursor , Preparation , and Modification. *Energy Convers. Manag. X* 2022, 13, 100152, doi:10.1016/j.ecmx.2021.100152.
- [5] Muttil, N.; Jagadeesan, S.; Chanda, A.; Duke, M. Production , Types , and Applications of Activated Carbon Derived from Waste Tyres : An Overview. *Appl. Sci.* 2023, doi:10.3390/app13010257.
- [6] Ahn, T.; Kim, J.H.; Yang, H.; Lee, J.W.; Kim, J. Formation Pathways of Magnetite Nanoparticles by Coprecipitation Method. *J. Supercrit. Fluids* 2012, 116, 6060–6076, doi:10.1021/jp211843g.
- [7] Shimizu, S.; Matubayasi, N. Surface Area Estimation: Replacing the Brunauer-Emmett-Teller Model with the Statistical Thermodynamic Fluctuation Theory. *Langmuir* 2022, 38, 7989–8002,

- doi:10.1021/acs.langmuir.2c00753.
- [8] Pomonis, P.J.; Petrakis, D.E.; Ladavos, A.K.; Kolonia, K.M.; Armatas, G.S.; Sklari, S.D.; Dragani, P.C.; Zarlaha, A.; Stathopoulos, V.N.; Sdoukos, A.T. A Novel Method for Estimating the C-Values of the BET Equation in the Whole Range $0 < P/P_0 < 1$ Using a Scatchard-Type Treatment of It. *Microporous Mesoporous Mater.* 2004, 69, 97–107, doi:10.1016/j.micromeso.2004.01.009.
- [9] Ladavos, A.K.; Katsoulidis, A.P.; Iosifidis, A.; Triantafyllidis, K.S.; Pinnavaia, T.J.; Pomonis, P.J. The BET Equation, the Inflection Points of N₂ Adsorption Isotherms and the Estimation of Specific Surface Area of Porous Solids. *Microporous Mesoporous Mater.* 2012, 151, 126–133, doi:10.1016/j.micromeso.2011.11.005.
- [10] Mastral, A.M.; García, T.; Murillo, R.; Callén, M.S.; López, J.M.; Navarro, M. V. Phenanthrene Adsorption on a Carbonaceous Material: Moisture and CO₂ Influence. *Stud. Surf. Sci. Catal.* 2002, 144, 283–290, doi:10.1016/s0167-2991(02)80146-x.
- [11] Lodewyckx, P.; Verhoeven, L. The Applicability of the Dubinin-Radushkevich Equation to the Very Low Pressure Region of Isotherms of Various Microporous Solids. *Stud. Surf. Sci. Catal.* 2002, 144, 731–735, doi:10.1016/s0167-2991(02)80203-8.
- [12] Turlapati, V.Y.; Prusty, B.K.; Yarlagadda, D.K.; Pal, S.K.; Raja, E. Analysis of Micropore Size Distribution Using Dubinin's Theory of Volume Filling - Effect of Particle Size on Pore Characterization of Organic-Rich Indian Shales. *J. Nat. Gas Sci. Eng.* 2022, 106, 104746, doi:10.1016/j.jngse.2022.104746.

- [13] Carrott, P.J.M.; Ribeiro Carrott, M.M.L. Evaluation of the Stoeckli Method for the Estimation of Micropore Size Distributions of Activated Charcoal Cloths. *Carbon* N. Y. 1999, 37, 647–656, doi:10.1016/S0008-6223(98)00240-1.
- [14] Fu, S.; Fang, Q.; Li, A.; Li, Z.; Han, J.; Dang, X.; Han, W. Accurate Characterization of Full Pore Size Distribution of Tight Sandstones by Low-Temperature Nitrogen Gas Adsorption and High-Pressure Mercury Intrusion Combination Method. *Energy Sci. Eng.* 2021, 9, 80–100, doi:10.1002/ese3.817.
- [15] Stine, K.J. *Application of Porous Materials to Carbohydrate Chemistry and Glycoscience*; 1st ed.; Elsevier Inc., 2017; Vol. 74;.
- [16] Yin, G.; Liu, Q.; Liu, Z.; Wu, W. Extension of Kelvin Equation to CO₂ Adsorption in Activated Carbon. *Fuel Process. Technol.* 2018, 174, 118–122, doi:10.1016/j.fuproc.2018.02.006.
- [17] Seaton, N.A.; Walton, J.P.R.B.; Quirk, N. A New Analysis Method for the Determination of the Pore Size Distribution of Porous Carbons from Nitrogen Adsorption Measurements. *Carbon* N. Y. 1989, 27, 853–861, doi:10.1016/0008-6223(89)90035-3.
- [18] Landers, J.; Gor, G.Y.; Neimark, A. V. Density Functional Theory Methods for Characterization of Porous Materials. *Colloids Surfaces A Physicochem. Eng. Asp.* 2013, 437, 3–32, doi:10.1016/j.colsurfa.2013.01.007.
- [19] Neimark, A. V.; Lin, Y.; Ravikovitch, P.I.; Thommes, M. Quenched Solid Density Functional Theory and Pore Size Analysis of Micro-Mesoporous Carbons. *Carbon* N. Y. 2009, 47, 1617–1628, doi:10.1016/j.carbon.2009.01.050.

- [20] Pallares-Rusiñol, A.; Bernuz, M.; Moura, S.L.; Fernández-Senac, C.; Rossi, R.; Martí, M.; Pividori, M.I. *Advances in Exosome Analysis*; 1st ed.; Elsevier Inc., 2023; Vol. 112; ISBN 9780443192845.
- [21] Surface, I. *Surface Micrography and Analysis*. *Exp. Methods Tribol.* 2004, 44, 165–220, doi:10.1016/s0167-8922(04)80024-5.
- [22] WOLTHUIS, R.; SCHUT, T.C.B.; CASPERS, P.J.; BUSCHMAN, H.P.J.; RÖMER, T.J.; BRUINING, H.A.; PUPPELS, G.J. *Raman Spectroscopic Methods for In Vitro and In Vivo Tissue Characterization*. *Fluoresc. Lumin. Probes Biol. Act.* 1999, 433–455, doi:10.1016/b978-012447836-7/50034-8.
- [23] Torrecilla, J.S.; Cancilla, J.C.; Perez-Calabuig, A.M.; Pradana-Lopez, S. *Spectroscopy to Evaluate the Quality Control of Extra-Virgin Olive Oils*. *Olives Olive Oil Heal. Dis. Prev.* 2020, 91–97, doi:10.1016/B978-0-12-819528-4.00042-0.
- [24] Ali, A.; Chiang, Y.W.; Santos, R.M. *X-Ray Diffraction Techniques for Mineral Characterization: A Review for Engineers of the Fundamentals, Applications, and Research Directions*. *Minerals* 2022, 12, doi:10.3390/min12020205.
- [25] Elgrishi, N.; Rountree, K.J.; McCarthy, B.D.; Rountree, E.S.; Eisenhart, T.T.; Dempsey, J.L. *A Practical Beginner’s Guide to Cyclic Voltammetry*. *J. Chem. Educ.* 2018, 95, 197–206, doi:10.1021/acs.jchemed.7b00361.
- [26] Fadlelmoula, A.; Pinho, D.; Carvalho, V.H.; Catarino, S.O.; Minas, G. *Fourier Transform Infrared (FTIR) Spectroscopy to Analyse Human Blood over the Last 20 Years: A Review towards Lab-on-a-Chip Devices*. *Micromachines* 2022, 13, doi:10.3390/mi13020187.
- [27] Shin, K.Y.; Oum, W.; Yu, D.J.; Kang, S.; Kim, E.B.; Kim, H.W.

Fundamentals of Cyclic Voltammetry. *J. Sens. Sci. Technol.* 2021, 30, 384–387, doi:10.46670/JSST.2021.30.6.384.

- [28] Oturan, N.; Oturan, M.A. *Electro-Fenton Process: Background, New Developments, and Applications*; Elsevier Inc., 2018; ISBN 9780128131602.

CHAPTER III: FACILE SYNTHESIS OF CARBON-BASED INKS TO DEVELOP METAL-FREE ORR ELECTROCATALYSTS FOR ELECTRO-FENTON REMOVAL OF AMOXICILLIN.



Article

Facile Synthesis of Carbon-Based Inks to Develop Metal-Free ORR Electrocatalysts for Electro-Fenton Removal of Amoxicillin

Laura Carolina Valencia-Valero [†], Edgar Fajardo-Puerto ^{*}, Abdelhakim Elmouwahidi , Esther Bailón-García, Francisco Carrasco-Marín and Agustín Francisco Pérez-Cadenas ^{*}

UGR-Carbon, Materiales Polifuncionales Basados en Carbono, Dpto. Química Inorgánica, Unidad de Excelencia de Química Aplicada a Biomedicina y Medioambiente, Universidad de Granada (UEQ-UGR), 18071 Granada, Spain; lauracarina.valencia@urv.cat (L.C.V.-V.); aelmouwahidi@ugr.es (A.E.); estherbg@ugr.es (E.B.-G.); fmarin@ugr.es (F.C.-M.)

^{*} Correspondence: edgarf1994@correo.ugr.es (E.F.-P.); afperez@ugr.es (A.F.P.-C.)

[†] Current address: Materials, Membrane and Encapsulation Technology, Chemical Engineering Department, Universitat Rovira i Virgili, 43001 Tarragona, Spain.

Abstract: The electro-Fenton process is based on the generation of hydroxyl radicals ($\text{OH}\cdot$) from hydroxide peroxide (H_2O_2) generated in situ by an oxygen reduction reaction (ORR). Catalysts based on carbon gels have aroused the interest of researchers as ORR catalysts due to their textural, chemical and even electrical properties. In this work, we synthesized metal-free electrocatalysts based on carbon gels doped with graphene oxide, which were conformed to a working electrode. The catalysts were prepared from organic-gel-based inks using painted (brush) and screen-printed methods free of binders. These new methods of electrode preparation were compared with the conventional pasted method on graphite supports using a binder. All these materials were tested for the electro-Fenton degradation of amoxicillin using a homemade magnetite coated with carbon ($\text{Fe}_3\text{O}_4/\text{C}$) as a Fenton catalyst. All catalysts showed very good behavior, but the one prepared by ink painting (brush) was the best one. The degradation of amoxicillin was close to 90% under optimal conditions ($[\text{Fe}_3\text{O}_4/\text{C}] = 100 \text{ mg L}^{-1}$, -0.55 V) with the catalyst prepared using the painted method with a brush, which had 14.59 mA cm^{-2} as J_k and a H_2O_2 electrogeneration close to 100% at the optimal voltage. These results show that carbon-gel-based electrocatalysts are not only very good at this type of application but can be adhered to graphite free of binders, thus enhancing all their catalytic properties.

Keywords: wastewater; ORR; electro-Fenton; carbon gels; xerogels



Citation: Valencia-Valero, L.C.; Fajardo-Puerto, E.; Elmouwahidi, A.; Bailón-García, E.; Carrasco-Marín, F.; Pérez-Cadenas, A.F. Facile Synthesis of Carbon-Based Inks to Develop Metal-Free ORR Electrocatalysts for Electro-Fenton Removal of Amoxicillin. *Gels* **2024**, *10*, 53. <https://doi.org/10.3390/gels10010053>

Academic Editors: Xiang Li and Yaofeng Zhu

Received: 18 December 2023

Revised: 4 January 2024

Accepted: 9 January 2024

Published: 11 January 2024



Copyright: © 2024 by the authors. Licensee MDPI, Basel, Switzerland. This article is an open access article distributed under the terms and conditions of the Creative Commons Attribution (CC BY) license (<https://creativecommons.org/licenses/by/4.0/>).

1. Introduction

Antibiotics are pharmaceutical compounds that are widely used for different infectious disease treatments in humans and animals, generating a possible effect on human and ecological health [1,2]. The principal problem associated with antibiotics is the generation of antibiotic resistance genes (ARGs), which reduces their efficacy against human and animal pathogens, posing a risk to public health [3–5].

Amoxicillin (AMX) is an antibiotic of class β -lactam, which is considered safe for use even in pregnant and lactating women; however, its metabolization in the human body is low, whereby between 70 and 90% of AMX is released to the environment unchanged [6–8]. Due to its solubility, biodegradability, stability and polarity, AMX is not degraded completely in wastewater treatment plants; for this reason, different methods (adsorption, advanced oxidation processes, etc.) [9–12] for the removal of this antibiotic from waters have been proposed [13].

Advanced oxidation processes (AOPs) are based on the generation of hydroxyl radicals ($\text{OH}\cdot$), which degrade organic components present in water solutions [14,15]. Some AOPs are as follows: photocatalysis, electrocatalysis, Fenton-like oxidation or persulfate

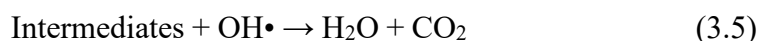
3.1.-INTRODUCTION

Antibiotics are pharmaceutical compounds that are widely used for different infectious diseases treatments in humans and animals, generating a possible effect on human and ecological health [1,2]. The principal problem associated with antibiotics is the generation of antibiotic resistance genes (ARGs), which reduces their efficacy against human and animal pathogens, posing a risk to public health [3-5].

Amoxicillin (AMX) is an antibiotic of class β -lactam, which is considered safe for use even in pregnant and lactating women; however, its metabolization in the human body is low, whereby between 70 to 90% of AMX is released to the environment unchanged [6-8]. Due to its solubility, biodegradability, stability and polarity, AMX is not degraded completely in wastewater treatment plants; for this reason, different methods (adsorption, advanced oxidation processes, etc.) [9-12] for the removal of this antibiotic from waters have been proposed [13].

Advanced oxidation processes (AOPs) are based on the generation of hydroxyl radicals ($\text{OH}\cdot$), which degrade organic components present in water solutions [14,15]. Some AOPs are as follows: photocatalysis, electrocatalysis, Fenton-like oxidation or persulfate oxidation [16]. Processes based on electrocatalysis take their name from electrochemical advanced oxidation processes (EAOPs), where generally no type of external chemical is required to treat contaminants in water solutions [17]. The electro-Fenton process (EF) is one of the most popular EAOPs, showing high mineralization levels due to the direct generation of hydrogen peroxide (H_2O_2) at the cathode by the reduction reaction of oxygen (ORR) through

a two-electron path ($2e^-$) (equation 3.1), and the formation of $\text{OH}\cdot$ radicals from the generated H_2O_2 by the Fenton catalyst (equation 3.2) [18-20].



The ORR catalyst has a key role in the EF process and, for this reason, it is crucial for the development of catalysts with high selectivity for H_2O_2 . Traditionally, ORR catalysts based on Pt and Pd are considered the best candidates; however, their high cost makes the use of these in the EF process difficult [21]. Carbon-based materials have been evaluated as ORR catalysts due to their low cost and high selectivity for H_2O_2 [22]. Qin et al. [23] synthesized hollow porous carbon spheres with high activity ORR $2e^-$ (higher than that reported in more advanced Fenton catalysts), which was attributed to the presence of sp^3 carbon and sp^2 defects. Garza-Campos et al. [24] developed a cathode with mesoporous carbon obtained using a soft template, with a current efficiency closer to 100%, attributed to ORR $2e^-$ predominance. Pishnamaz et al. [25] modified nickel foam with single-wall and multi-wall carbon nanotube (SWCNT and MWCNT, respectively) and found that SWCNTs produced more H_2O_2 than MWCNTs, due principally to their higher surface area. Graphene is another new carbon material studied as metal-free ORR catalyst. Wang et al. [26] fabricated an electrode of graphene aerogel and calculated the electron transfer number between 1 and 2 in the range of the selected

potential. Wang et al. [27] made a cathode of reduced graphene-oxide-grafted carbon fiber and determined that the modified electrode had a 45% higher H₂O₂ accumulation than the material without graphene. More specifically, carbon gels have recently and successfully been applied into an electro-Fenton process for antibiotic elimination from water [28], or simple ORR [29], and CO₂ electro-transformation [30] due to their unique textural and chemical characteristics.

The use of polytetrafluoroethylene (PTFE) emulsions as a binder in the preparation of electrodes based on carbon materials is very common [31,32]; however, it is possible that PTFE generates jams and blockages in pores, affecting the electrocatalytic yield. In this work, metal-free electrocatalysts based on carbon xerogel/graphene oxide (OG) were synthesized and used as ORR electrocatalysts in the degradation of amoxicillin (AMX) using an electro-Fenton process, which also involved the synthesis and use of a homemade carbon/magnetite catalyst as a heterogeneous Fenton catalyst. The ORR electrocatalysts were made from the development of a carbon/OG ink, which was deposited on the graphite cathode using two different painting methods, brush and screen printed, as well as the preparation of one ORR electrocatalyst using the same ink, PTFE, using a conventional method for comparison.

3.2.-EXPERIMENTAL

3.2.1.- Graphene Oxide (OG)

The OG was synthesized by a modified Hummers method [33], mixing graphite (4 g) with sulfuric acid (H₂SO₄) (100 mL), added drop by drop with agitation in an ice bath. Then, potassium permanganate (KMnO₄) (12 g) was added and the resulting mix was kept under constant agitation for 2 h at 35 °C. The obtained mix

was diluted with water (200 mL); subsequently, H₂O₂ [30% w v⁻¹] was added until a yellow solution formed. Then, the material was purified with hydrochloric acid and washed several times with water until neutral pH. Finally, the material was dried at 60 °C in 24 h.

The obtained solid was dispersed in distilled water (200 mL) and sonicated for 1 h; subsequently, the dispersion was centrifugated (20 min to 3000 rpm) to eliminate the oxide graphite particles. With the final solution, a suspension of OG [0.8 g L⁻¹] was prepared.

3.2.2.- Magnetite (Fe₃O₄)

The magnetite was synthesized by co-precipitation chemical method [34], mixing 50 mL of ferrous chloride with 100 mL of ferric chloride [0.5 M]. Then, 75 mL of ammonium hydroxide [25%] was added drop by drop, and the solution was maintained with constant agitation for 10 min. Finally, the obtained solid was separated and washed several times with water and ethanol. The final material, was dried for 8 h at 60 °C.

The coating with carbon was made following a typical sol-gel method [35], using resorcinol-formaldehyde as carbon precursors and 3% of magnetite. The procedure was carried out, with 11 mL of Span 80 (S) dissolved in 250 mL of n-heptane and heated at 70 °C with reflux and mechanical stirring (450 rpm) for 1 h. Then, the magnetite in solution (1.05 g in 25 mL of NH₄OH [30%]) was added and maintained for 2 h. Another solution was prepared with 22.5 g of resorcinol (R), 12.5 mL of formaldehyde (F) and 29 mL of water (W), which was added dropwise to the solution of n-heptane. The obtained gel was aged at 70 °C for 24 h under stirring. Then, the suspension was filtered and the solid was placed in acetone for 5

days (changing acetone twice daily). The obtained material was dried by infrared light and finally, carbonized at 900 °C by 2 h with N₂ flow at 300 mL min⁻¹ and a heating rate of 2 °C min⁻¹.

3.2.3.- Preparation of the Xerogel/OG ink

The xerogel was synthesized from resorcinol (R) (5 g) and formaldehyde (F) (7.35 g), and dissolved in water (OG suspension) (W). Then, 2-hydroxypidine (0.088 g) was added as catalyst (Z). The mixture was heated in a microwave at 400 W power, in an argon atmosphere, for two batches of 5 min, waiting between both batches for the ink to cool to room temperature. In all cases, the used molar relations were R/F 0.5, W/R 50, and R/Z 500.

Deposition methods

The xerogel/OG ink was deposited by different methods on graphite sheets (7cm × 1cm) used as support.

3.2.4.- Conventional catalyst (sample C)

For the conventional preparation of the electrode, the ink was previously dried in an oven at 100°C for 12 hours. Subsequently, it was carbonized in argon with a heating rate of 3 °C min⁻¹ up to 850 °C, maintaining this temperature for 1 h. The obtained carbon xerogel was grounded to a fine powder with which a paste of 150 mg of xerogel and polytetrafluoroethylene (PTFE) (60% suspension in water) was made, mixed homogeneously at a proportion of 90:10. This mixture was homogeneously pasted by mechanical method on both sides of the graphite sheet and dried at 80 °C.

3.2.5.- Painted catalyst (sample P)

The electrode was prepared using a brush to deposit the xerogel/OG ink in each support face until obtaining a constant mass of 0.5 g. After each deposition, the electrode was placed under infrared light by 1 minute. Finally, it was carbonized in argon with a heating rate of $3\text{ }^{\circ}\text{C min}^{-1}$ up to $850\text{ }^{\circ}\text{C}$, maintaining this temperature for 1 h.

3.2.6.- Screen printed catalyst (sample S)

This method was like the painted method, changing the brush to an airbrush for the ink deposition. The other conditions were equals.

Characterization

3.2.7.- Chemical and textural characterization

The Brunauer-Emmett-Teller (B.E.T), Dubinin-Radushkevich (DR) and Density Functional Theory (DFT) methods were applied to the data obtained from the N_2 adsorption isotherms at 77K to obtain the apparent surface area and micropore parameters. DR and DFT were used to calculate the total micropore volume (W_0/W_{DFT}) and the mean micropore width (L_0/L_{DFT}). The total pore volume was considered as the N_2 volume adsorbed at a relative pressure of 0.95 ($V_{0.95}$). Furthermore, the mesopore volume (V_{meso}) was obtained from the difference between $V_{0.95}$ and W_0 .

RAMAN spectroscopy was performed with a Micro-Raman spectrometer (JASCO NRS-5100, laser DXR 532 nm) in a range between 200 and 3000 cm^{-1} to 24 Mw.

The surface composition was obtained by X-ray photoelectron spectroscopy using an ESCA 5701 Physical Electronics (PHI) system (equipped with MgK α , anode, model PHI 04-548; X-ray source ($h\nu = 1253.6$ eV)) and hemispherical electron. For the analysis of the XPS peaks, the C_{1s} peak position was at 284.6 eV.

The samples morphology was observed by scanning electron microscope (SEM) and transmission electron microscopy (TEM) in the microscopies AURIGA (FIB-FESEM) and LIBRA 120 Plus, respectively, at the “Centro de Instrumentación Científica de la Universidad de Granada”.

3.2.8.- Electrochemical characterization

The electrochemical characterization was carried out in a cell of 3 electrodes controlled by a potentiostat multichannel Biologic VMP, using Ag/AgCl, Pt and a rotating ring–disk electrode (RRDE), as reference electrode, counter electrode and working electrode, respectively.

The RRDE was prepared with 10 μ L of a solution of 5 mg of material in 1 mL of a mix of Nafion [5%] and water (relation 1:9).

The cyclic voltametric (CV) experiments were carried out in N₂ or O₂ in a potential range of -0.75 V to -0.45 V, with a scan speed of 5 mVs⁻¹ and 50 mVs⁻¹. The linear sweep voltammetry (LSV) was carried out in O₂ at different rotation speeds (500, 1000, 1500, 2000, 2500, 3000 and 4000 rpm) with exploration speed of 5 mVs⁻¹ in the same potential range of CV. In the two cases, the support electrolyte used was KOH [0.1M]. For calculated the number of transfer electrons, the data obtained from LSV experiments were adjusted to the Koutecky-Levich model (equation 3.6) [36].

$$\frac{1}{J} = \frac{1}{J_K} + \frac{1}{0,2 nF(D_o^{2/3})v^{-1/6}C_o w^{1/2}} \quad (3.6)$$

Where, J is current density, J_K is current density kinetic, ω rotation speed, F is the Faraday constant, D_o ($1.9 \times 10^{-5} \text{ cm}^2 \text{ s}^{-1}$) is oxygen coefficient diffusion, ν ($0.01 \text{ cm}^2 \text{ s}^{-1}$) viscosity, C_o is the oxygen concentration ($1.2 \times 10^{-6} \text{ mol cm}^{-3}$).

3.2.9.- Electro-Fenton processes

The electro Fenton process was carried out using a standard three-electrode electrochemical cell with capacity for 0.125 L of solution at room temperature. The AMX solution was prepared with a dilution of Na_2SO_4 [0.5M] with continuous agitation. The potentiostat was maintained in potentiostatic mode at different evaluated values (-0.55 , -0.60 and -0.65 V). The reference electrode was Ag/AgCl, and the counter electrode used was platinum wire. The pH was of 6.0 (natural pH solution). As the Fenton catalyst, magnetite coated with carbon ($\text{Fe}_3\text{O}_4/\text{C}$) was used. AMX concentrations in solution were determined by a UV-vis spectrophotometer at 229 nm. As a general protocol, each type of electro-Fenton test was repeated three times with a new sample of each specific catalyst.

3.3.-RESULTS AND DISCUSSION

Catalysts ORR

3.3.1.- Porosity and surface area determination

The N_2 adsorption-desorption isotherms of the samples prepared by painting by brush (P), screen printing (S) and the conventional method (C) are shown in Figure 3.1. All samples show a mix of isotherms type I and IV with hysteresis loop type 4, which is typical of mesoporous materials [37]. The difference among the

samples could be attributed to the dispersion type effected in each method; due to the printed screen, the ink is subjected to a pressure difference, which can result in a better dispersion of the particles. The surface area values and the volume of micro (W) and mesopores are shown in Table 3.1, where it is evident that there are not significant differences among the samples, although sample S shows all the highest values and C the lowest mesopore volume.

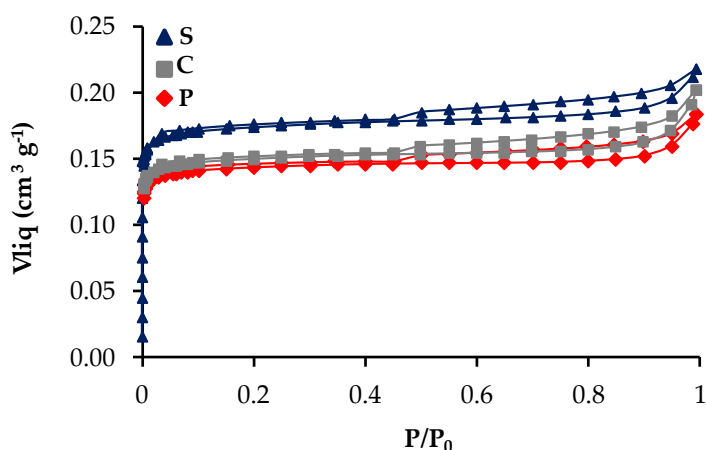


Figure 3.1. N₂ adsorption-desorption isotherms at 77K.

Table 3.1. Textural characteristics of all samples obtained by N₂ adsorption at 77K.

Sample	S _{B.E.T}	S _{DFT}	S _{DR}	W ₀	L ₀	W _{DFT}	L _{DFT}	V _{0.95}	V _{meso}
	m ² g ⁻¹	m ² g ⁻¹	m ² g ⁻¹	cm ³ g ⁻¹	nm	cm ³ g ⁻¹	nm	cm ³ g ⁻¹	cm ³ g ⁻¹
S	436	506	492.2	0.170	0.63	0.19	0.61	0.218	0.043
C	383	448	424.2	0.150	0.60	0.17	0.61	0.171	0.020
P	363	428	408.6	0.145	0.65	0.15	0.61	0.183	0.038

3.3.2.- Raman Characterization

The Raman spectra of the sample P, C and S are shown in figure 3.2 and were used to determine the degree of graphitization. All samples show the band associated to the vibrational modes of the graphite structure (G at 1590 cm^{-1}) and the graphite structure defects (D 1340 cm^{-1}) [38,39]. The intensity ratio I_D/I_G is used typically as an indicator of the defect density level [40]. The ratio I_D/I_G has values of 0.988, 0.976 and 0.982 for S, C and P, respectively, indicating that the samples have a good graphitization grade and that there is not significant difference among them.

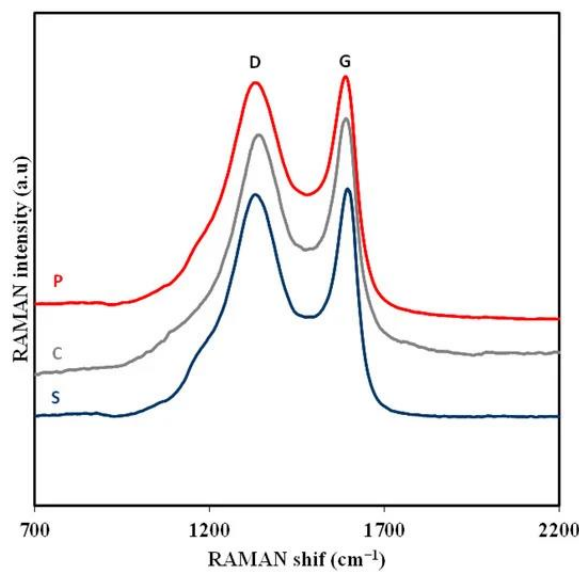


Figure 3.2. Raman spectra of all samples.

3.3.3.- XPS Characterization

The chemical composition of the surface was studied by XPS, and the C_{1s} and O_{1s} regions were analyzed in all the samples. All spectra are very similar among the samples. Figure 3.3 shows the three C_{1s} spectra as example. The deconvolution results and the binding energies peaks are collected in Table 3.2.

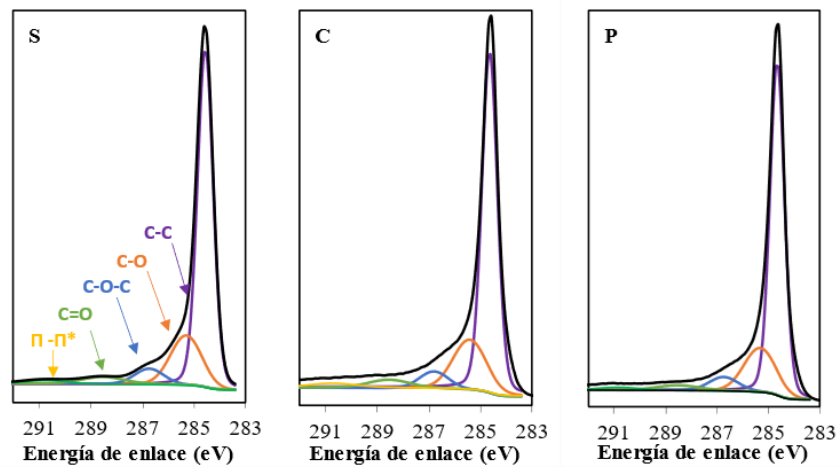


Figure 3.3. XPS spectra of C_{1s} regions.

We use as reference the 285.5 eV value to calibrate the C_{1s} spectra, and the peaks 284.6, 285.4, 286.8, 288.5 and 290.7 were attributed to C-C, C-O, C-O-C, C=O and CO₂ [41-45].

Table 3.2. Characterization data obtained from XPS in C_{1s} region.

Bond	Peak	S (%)	C (%)	P (%)
C-C	284.6	70.3	68.8	71.2
C-O	285.4	18.7	19.7	18.9
C-O-C	286.8	5.5	5.7	5.3
C=O	288.5	3.3	3.6	2.7
CO₂	290.7	2.1	2.2	1.9
Total C	---	93.8	93.0	94.1
Total O₂	---	6.2	7.0	5.9

The more significant difference among the samples is the content of oxygen, which is slightly higher in sample C. Therefore, the chemical composition of the samples can be considered practically equal.

3.3.4.- Morphology

The morphology of the samples was examined by SEM (see figure 3.4), and it was possible to observe significant differences among the samples, mainly in roughness. The sample with the greatest roughness was P, which shows several possible channels or slits that could facilitate access to more active sites.

The sample S is the smoothest and shows fewer microspheres exposed on the surface; meanwhile, in the C sample, it is possible to observe the binder that generates a thread that traps the carbon spheres, generating more agglomerations.

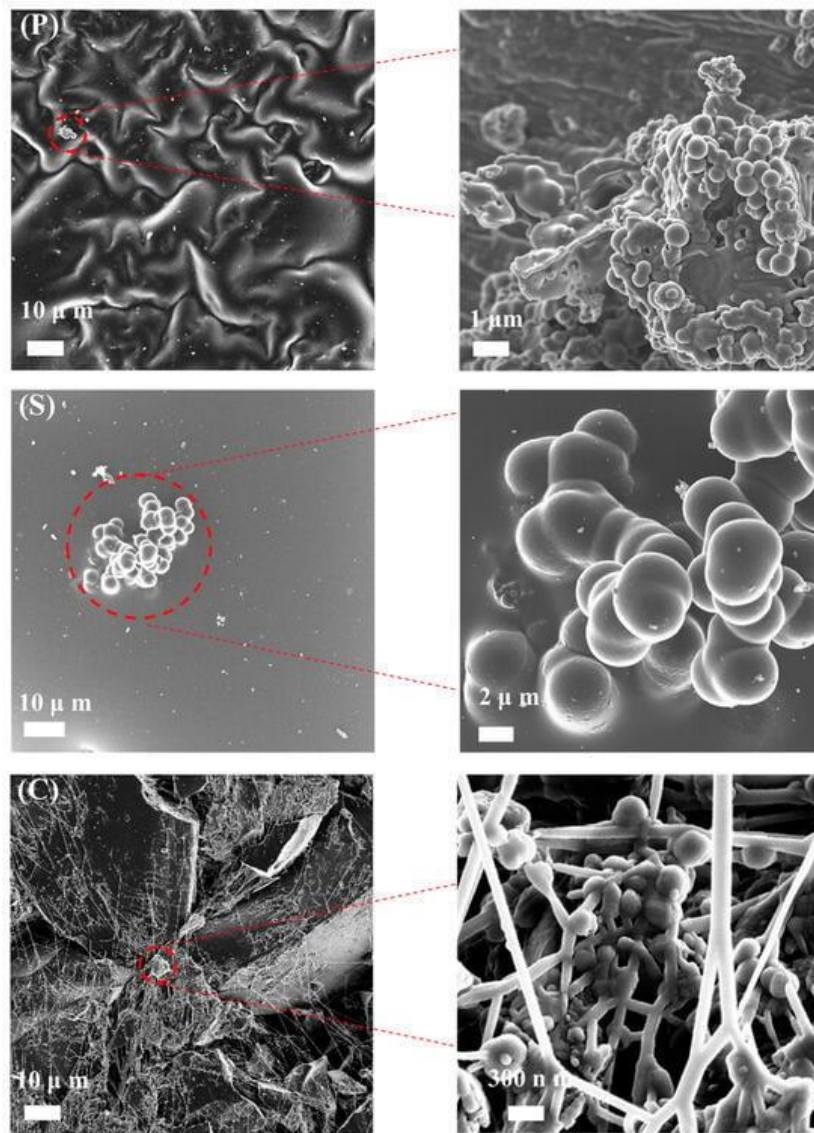


Figure 3.4. SEM images.

The morphology of the samples was examined by TEM (figure 3.5), where the OG structure can be observed with the typical texture (wrinkled sheets) and a good exfoliation of these [46,47]. At this level of magnification, all three samples look relatively similar.

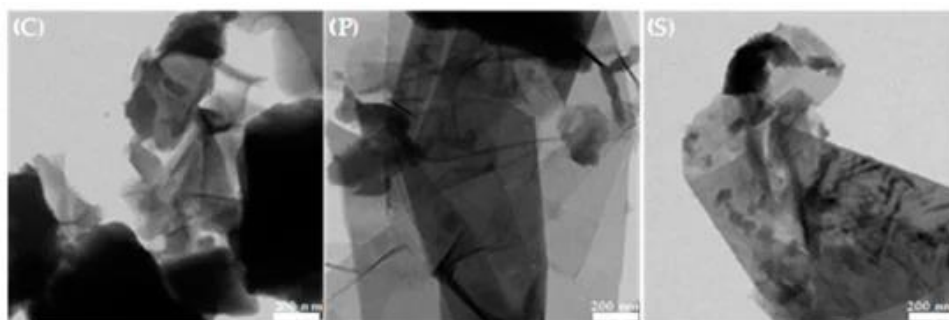


Figure 3.5. TEM images.

3.3.5.- Electrochemical Characterization

The Figure 3.6 shows the CV in presence and absence of O_2 , with the peaks characteristics of the oxygen reduction showing the activity as ORR catalyst.

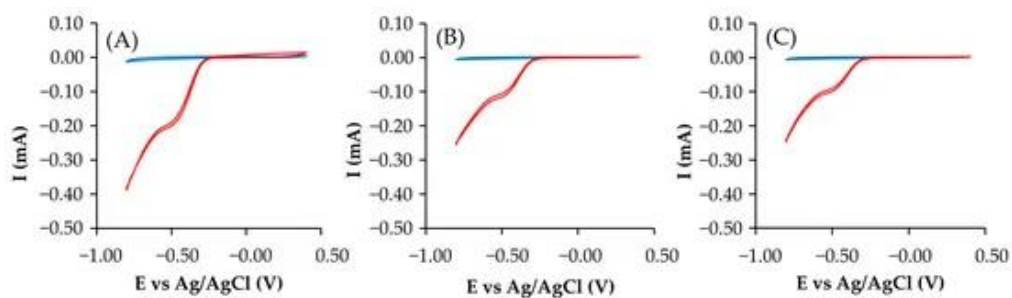


Figure 3.6. CV (A) sample C, (B) sample P, and (C) sample S; O_2 (red) and N_2 (blue).

The Figure 3.7 shows the number of electrons transferred in the reaction obtained with RRDE. All samples have a preferential selectivity to a two-electron path throughout the voltage range, especially sample P, and without apparent mechanic changes in the potential range studied. Some authors have attributed an improvement of conductivity to better electrochemical activities [48,49], however, the Raman spectra do not show significant differences among the samples.

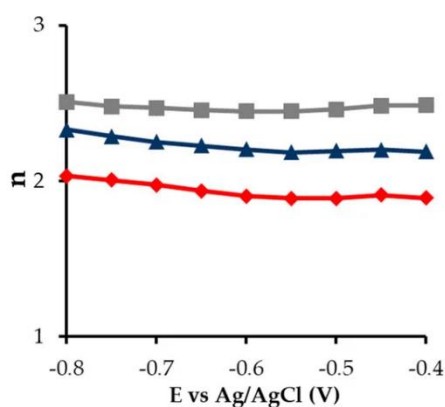


Figure 3.7. Number of transferred electrons ▲S, ■C and ◆P.

Table 3.3 shows the parameters of Koutecky-Levich equation, from which it is possible to obtain information about the reaction mechanism of these electrocatalysts [50,51]. In this context, all samples work close to a two-electron pathway mechanism.

Table 3.3. Parameters of Koutecky-Levich obtained at -0.8V , and initial potential.

Sample	J_K mA cm^{-2}	n	E° initial V
S	14.35	2.33	-0.25
C	9.00	2.50	-0.23
P	14.59	2.03	-0.25

On the other hand, the initial potential is more positive in the sample C, followed by P and S, which is related to better electron transfer ability [52]. The diffusion kinetic current density (J_K) shows much higher values for the samples S and P (14.35 and 14.59, respectively), which can be due to a combination of factors like lower oxygen content and a much higher mesoporosity, which could be a direct consequence of the new preparation method versus the conventional one. The direct positive relation between current density and ORR performance is very well known [53]. In terms of electrocatalytic results, sample P is slightly superior to sample S (higher J_K and n values and lower initial potential). Therefore, among these catalysts, sample P brings together the best combination of textural and electrochemical characteristics, such as higher J_K and mesopore volume, also showing a quite adequate electron transfer value. It is also important to highlight the type of morphology caused by the painting method in terms of microroughness that can improve the accessibility of the mesoporosity in particular, and of the active sites in general to the electrolyte.

Figure 3.8 shows the electrogeneration of H_2O_2 at each potential for the samples S, C and P. For all samples, the H_2O_2 production is constant in all potential

ranges, indicating that there are not changes of selectivity, maintaining a good stability at each potential. From these results, it is considered that the H_2O_2 production is heavily dependent on a good balance between the textural and electrochemical characteristic; the lowest J_K and mesopore volume of sample C could justify its penalty in the H_2O_2 generation sequence.

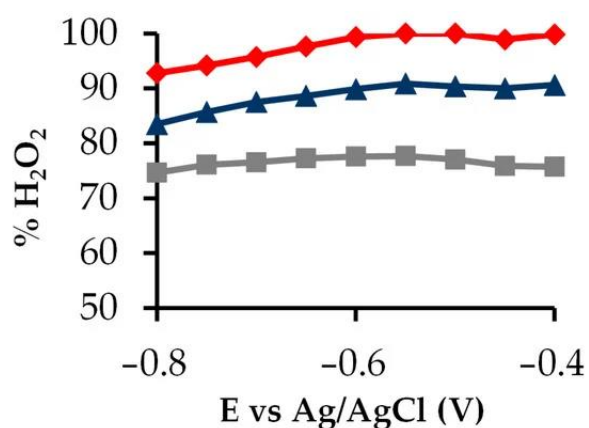


Figure 3.8. H_2O_2 electro generation at each potential with \blacktriangle S, \blacksquare C and \blacklozenge P.

Catalyst Fenton

3.3.6.- X-ray diffraction

The XRD of the Fenton catalyst can be observed in figure 3.9, where it is possible to observe a peak characteristic of the crystalline planes (220), (311), (400), (422), (511) and (440), typical of magnetite in the sample Fe_3O_4 [54,55], indicating that the synthesis was made successfully.

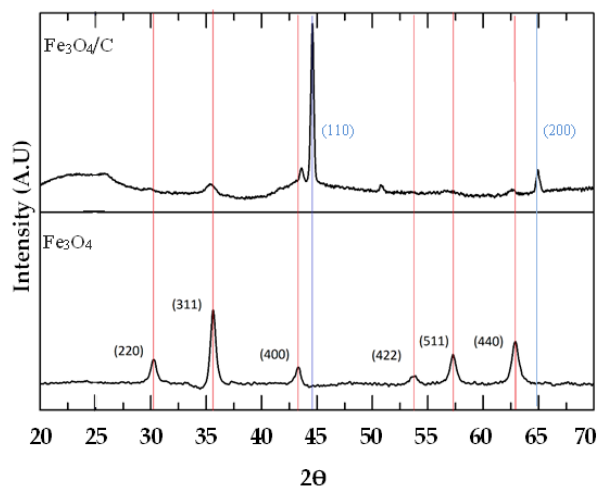


Figure 3.9. XRD patterns of Fe₃O₄/C and Fe₃O₄.

The peak (311) was used to determine the crystallite size by Scherrer's equation, giving a mean diameter of 12.9 nm as the result. The sample Fe₃O₄/C shows the peaks associated to the crystalline planes (110) and (200) of zero-valent iron (or pure Fe phase); the other peaks can easily be mistaken with magnetite peaks in small intensity [56,57]. These results indicate that the carbonization to 900 °C principally occasioned the magnetite passing to zero-valent iron.

3.3.7.- Morphology

Figure 3.10 shows SEM images of the homemade Fe₃O₄/C catalyst. It is formed by microspheres of different sizes, some of them partially fused.

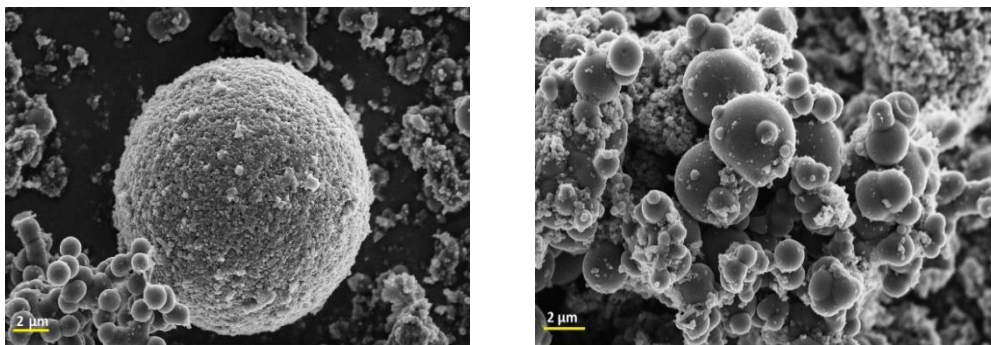


Figure 3.10. SEM Images of Fe₃O₄/C.

3.3.8.- Electro-Fenton experiments

The optimal conditions for the EF process were selected by a previous test of amoxicillin (AMX) degradation, which were evaluated: the Fenton catalyst concentration, the cathodic potential and obviously the effect of the deposition method on the electrocatalyst preparation.

Figure 3.11 shows the Fenton catalyst concentration effect, using sample P as the ORR catalyst. The degradation is better when the concentration increases from 50 to 100 mg L⁻¹, due principally to the fact that more Fe²⁺ in the solution can generate more •OH (eq 3.2). However, when the concentration is higher (150 mg L⁻¹), there are not significant improvements; this is due to some factors like the agglomeration between particles that can decrease the rate of OH desorption, which is one of the three key steps in the generation of hydroxyl radicals (adsorption, homolysis and desorption) and excessive accumulation of iron that finally eliminates the •OH [58-60]. Based on these results, the concentration of 100 mg L⁻¹ was selected as the most adequate for our experimental system.

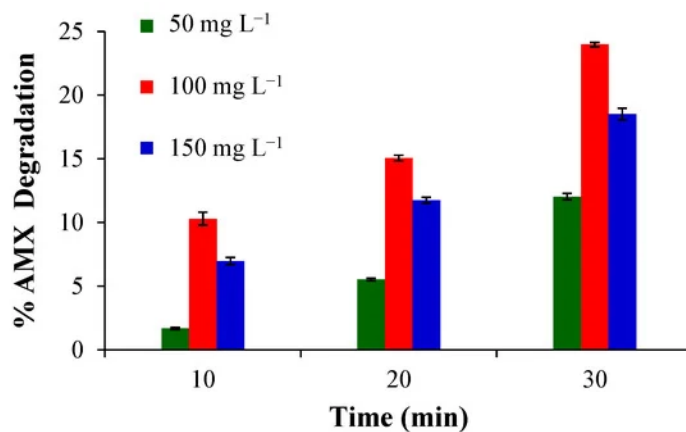


Figure 3.11. AMX degradation obtained using different concentrations of sample P.

On the other hand, three cathodic potential were tested in the range between -0.55 to -0.65 V (Figure 3.12), determining that the best potential was -0.55 V, as the highest percentage of degradation in our experimental conditions was obtained at this value.

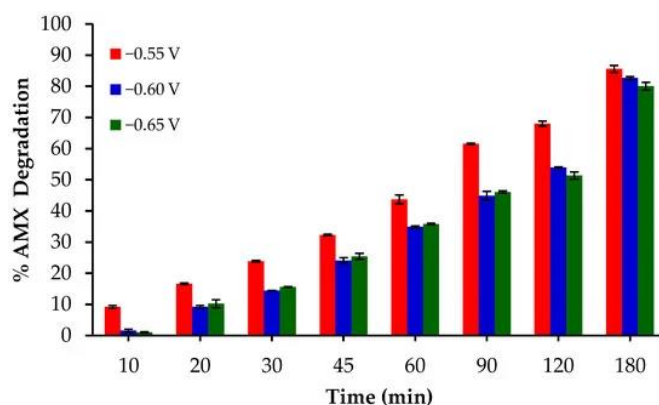


Figure 3.12. AMX degradation obtained at different potentials with the catalyst P.

The degradation of AMX between the voltage -0.60 and -0.65 , does not show significant differences, which could be due to a competence with the hydrogen evolution reaction (HER) or even an ORR $4e^-$ [61,62], decreasing the efficiency of the EF process. Besides, the use of lower potentials is always better from an economical point of view.

Finally figure 3.13 shows the deposition method effect in the degradation of AMX by EF. Over the entire reaction time range, sample P shows the highest percentage of AMX degradation, with samples P and S being better for this application than sample C, which shows the success of these new methods of preparation or deposition of electrocatalysts.

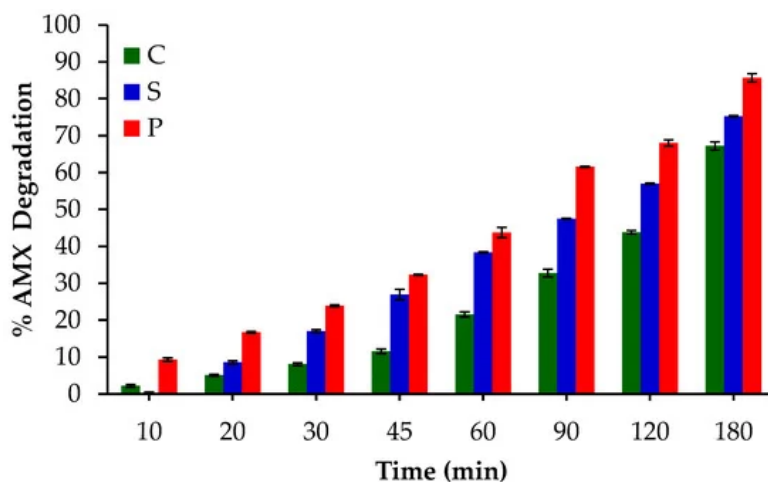


Figure 3.13. AMX degradation obtained with the catalysts prepared through the three different methods.

These results of AMX degradation are directly related to the ORR performance and H_2O_2 electrogeneration already discussed in Section 3.3.5. The painted method (sample P) produces a non-uniform micro-deposition generating micro-roughness, which leaves ORR active sites more exposed to the solution, improving the final AMX degradation. Additionally, the conventional method (sample C) is also limited by the use of a binder, which probably makes the electrocatalytic process less efficient. In a similar way, the screen-printed process (sample S), due to the excellent uniformity of the deposited layers, can limit the solution accessibility in comparative terms with sample P.

Finally, a minimum study of reusability was carried out with sample P, as this is a critical factor to determine a possible broader application. Therefore, the same prepared electrode was tested in the optimal EF conditions by five consecutive cycles. Figure 3.14 shows the AMX degradation kinetic after the first and fifth cycle of use, maintaining the EF system at the same degradation capacity after 60 minutes.

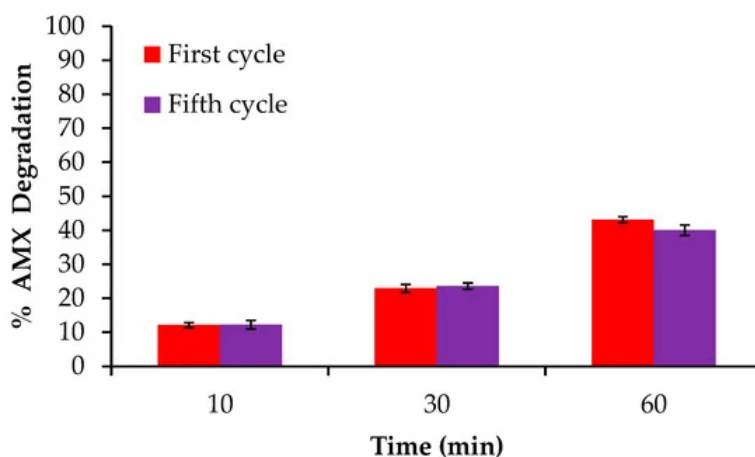


Figure 3.14. Reusability study carried out with the sample P.

3.4- CONCLUSIONS

The results obtained in this work show the successful synthesis of ORR catalysts based in carbon xerogels doped with graphene oxide, which could be conformed by different methods, with a very good performance to be coupled in electro-Fenton systems for amoxicillin degradation. In comparative terms, the conventional ORR electrocatalysts preparation method, consisting of a previous carbonization of the carbon precursor and its later deposition on the cathode using binders (sample C), can be broadly improved by the development of the carbon gel/OG-based ink discussed here. This ink can be deposited on the cathode using a brush (sample P) or an airbrush (sample S) and later carbonized.

In this way, sample P was the one that showed the best electrochemical behavior; consequently, the best result was obtained in the degradation of AMX (close to 90%) after its coupling to the EF system. The explanation of this result must be understood as a combination of different factors: the unique microroughness generated in the cathode together with the high volume of mesopores obtained provides a better set of ORR parameters (J_K 14.59 mA cm⁻², 2.03 transferred electrons and initial potential of -0.25 V), producing the greatest amount of H₂O₂ among the samples, which is essential for efficient electro-Fenton degradation of AMX.

BIBLIOGRAPHY

- [1] Qian, M.; Zhuo, F.; Li, Y.; Yi, P.; Gao, Y.; Zhou, W.; Sun, Y.; Chen, J.; Wu, X.L. Fe-N-C Catalyst Coated on Carbon Felt for Efficient Degradation of Antibiotics via Electro-Fenton Process. *Appl. Surf. Sci.* 2023, 609, doi:10.1016/j.apsusc.2022.155310.
- [2] Amarzadeh, M.; Salehizadeh, S.; Damavandi, S.; Mubarak, N.M.; Ghahrchi, M.; Ramavandi, B.; Shahamat, Y.D.; Nasseh, N. Statistical Modeling Optimization for Antibiotics Decomposition by Ultrasound/Electro-Fenton Integrated Process: Non-Carcinogenic Risk Assessment of Drinking Water. *J. Environ. Manage.* 2022, 324, 116333, doi:10.1016/j.jenvman.2022.116333.
- [3] Li, S.; Hua, T.; Yuan, C.S.; Li, B.; Zhu, X.; Li, F. Degradation Pathways, Microbial Community and Electricity Properties Analysis of Antibiotic Sulfamethoxazole by Bio-Electro-Fenton System. *Bioresour. Technol.* 2020, 298, 122501, doi:10.1016/j.biortech.2019.122501.
- [4] Jin, Y.; Huang, P.; Chen, X.; Li, L.-P.; Lin, C.-Y.; Chen, X.; Ding, R.; Liu, J.; Chen, R. Ciprofloxacin Degradation Performances and Mechanisms by the Heterogeneous Electro-Fenton with Flocculated Fermentation Biochar. *Environ. Pollut.* 2023, 324, 121425, doi:10.1016/j.envpol.2023.121425.
- [5] Li, S.; Wu, Y.; Zheng, H.; Li, H.; Zheng, Y.; Nan, J.; Ma, J.; Nagarajan, D.; Chang, J.S. Antibiotics Degradation by Advanced Oxidation Process (AOPs): Recent Advances in Ecotoxicity and Antibiotic-Resistance Genes Induction of Degradation Products. *Chemosphere* 2023, 311, 136977, doi:10.1016/j.chemosphere.2022.136977.

- [6] Cai, Y.; Yu, H.; Ren, L.; Ou, Y.; Jiang, S.; Chai, Y.; Chen, A.; Yan, B. Treatment of Amoxicillin-Containing Wastewater by *Trichoderma* Strains Selected from Activated Sludge. *Sci. Total Environ.* 2023, 867, 161565, doi:10.1016/j.scitotenv.2023.161565.
- [7] Armoudjian, Y.; Lin, Q.; Lammens, B.; Daele, J. Van; Annaert, P. Sensitive and Rapid Method for the Quantitation of Amoxicillin in Minipig Plasma and Milk by LC-MS/MS: A Contribution from the IMI ConcePTION Project. *J. Pharmacol. Toxicol. Methods* 2023, 107264, doi:10.1016/j.vascn.2023.107264.
- [8] Andrade, L.A.; Souza, G.B.M.; Dias, I.M.; Mour, L.C.; Viana, J.C. V; Oliveira, S.B.; Alonso, C.G. Degradation of Antibiotic Amoxicillin from Pharmaceutical Industry Wastewater into a Continuous Flow Reactor Using Supercritical Water Gasification. *Water Res.* 2023, 234, doi:10.1016/j.watres.2023.119826.
- [9] Laksaci, H.; Belhamdi, B.; Khelifi, O.; Khelifi, A. Elimination of Amoxicillin by Adsorption on Coffee Waste Based Activated Carbon. *J. Mol. Struct.* 2023, 1274, 134500, doi:10.1016/j.molstruc.2022.134500.
- [10] Ayanda, O.S.; Aremu, O.H.; Akintayo, C.O.; Sodeinde, K.O.; Igboama, W.N.; Oseghe, E.O.; Nelana, S.M. Sonocatalytic Degradation of Amoxicillin from Aquaculture Effluent by Zinc Oxide Nanoparticles. *Environ. Nanotechnology, Monit. Manag.* 2021, 16, 100513, doi:10.1016/j.enmm.2021.100513.
- [11] Li, W.; Zhou, R.; Zhou, R.; Weerasinghe, J.; Zhang, T.; Gissibl, A.; Cullen, P.J.; Speight, R.; Ken, K. Insights into Amoxicillin Degradation in Water by Non-Thermal Plasmas. *Chemosphere* 2022, 291, 132757,

- doi:10.1016/j.chemosphere.2021.132757.
- [12] Duong-nguyen, T.; Hoang, M.; Hue, N.; Quoc, C. Amoxicillin Degradation Ability of *Bacillus Cereus* C1 Isolated from Cat Fi Sh Pond Sludge in Vietnam. *Heliyon* 2022, 8, e11688, doi:10.1016/j.heliyon.2022.e11688.
- [13] Aryee, A.A.; Han, R.; Qu, L. Occurrence , Detection and Removal of Amoxicillin in Wastewater : A Review. *J. Clean. Prod.* 2022, 368, 133140, doi:10.1016/j.jclepro.2022.133140.
- [14] Alomar, T.S.; Hameed, B.H.; Usman, M.; Almomani, F.A.; Ba-abbad, M.M.; Khraisheh, M. Recent Advances on the Treatment of Oil Fields Produced Water by Adsorption and Advanced Oxidation Processes. *J. Water Process Eng.* 2022, 49, 103034, doi:10.1016/j.jwpe.2022.103034.
- [15] Hadi, M.; Rao, R.; Reddy, J. Recent Trends in the Applications of Sonochemical Reactors as an Advanced Oxidation Process for the Remediation of Microbial Hazards Associated with Water and Wastewater : A Critical Review. *Ultrason. Sonochem.* 2023, 94, 106302, doi:10.1016/j.ultsonch.2023.106302.
- [16] Zhai, C.; Chen, Y.; Huang, X.; Isaev, A.B.; Zhu, M. Recent Progress on Single-Atom Catalysts in Advanced Oxidation Processes for Water Treatment. *Environ. Funct. Mater.* 2022, 1, 219–229, doi:10.1016/j.efmat.2022.11.001.
- [17] Wei, J.; Shi, L.; Wu, X. Electrochemical Advanced Oxidation Process with Simultaneous Persulfate and Hydrogen Peroxide On-Site Generations for High Salinity Wastewater. 2023, 310, doi:10.1016/j.seppur.2023.123147.
- [18] Campos, S.; Lorca, J.; Vidal, J.; Calzadilla, W.; Toledo-neira, C.; Aranda, M.; Miralles-cuevas, S.; Cabrera-reina, A.; Salazar, R. Removal of

- Contaminants of Emerging Concern by Solar Photo Electro-Fenton Process in a Solar Electrochemical Raceway Pond Reactor. 2023, 169, 660–670, doi:10.1016/j.psep.2022.11.033.
- [19] Lai, S.; Zhao, H.; Qu, Z.; Tang, Z.; Yang, X.; Jiang, P. Promotion of Formaldehyde Degradation by Electro-Fenton : Controlling the Distribution of \cdot OH and Formaldehyde near Cathode to Increase the Reaction Probability. *Chemosphere* 2022, 307, 135776, doi:10.1016/j.chemosphere.2022.135776.
- [20] Wang, J.; Qin, J.; Liu, B.; Song, S. Reaction Mechanisms and Toxicity Evolution of Sulfamethoxazole Degradation by CoFe-N Doped C as Electro-Fenton Cathode. *Sep. Purif. Technol.* 2022, 298, 121655, doi:10.1016/j.seppur.2022.121655.
- [21] Tu, S.; Ning, Z.; Duan, X.; Zhao, X.; Chang, L. Efficient Electrochemical Hydrogen Peroxide Generation Using TiO_2/RGO Catalyst and Its Application in Electro-Fenton Degradation of Methyl Orange. *Colloids Surfaces A Physicochem. Eng. Asp.* 2022, 651, 129657, doi:10.1016/j.colsurfa.2022.129657.
- [22] Fajardo-Puerto, E.; Elmouwahidi, A.; Bailón-García, E.; Pérez-Cadenas, A.F.; Carrasco-Marín, F. From Fenton and ORR $2e^-$ -Type Catalysts to Bifunctional Electrodes for Environmental Remediation Using the Electro-Fenton Process. *Catalysts* 2023, 13, doi:10.3390/catal13040674.
- [23] Qin, X.; Wang, K.; Cao, P.; Su, Y.; Chen, S.; Yu, H.; Quan, X. Highly Efficient Electro-Fenton Process on Hollow Porous Carbon Spheres Enabled by Enhanced H_2O_2 Production and Fe^{2+} Regeneration. *J. Hazard. Mater.* 2023, 446, 130664, doi:10.1016/j.jhazmat.2022.130664.

- [24] Garza-Campos, B.; Morales-Acosta, D.; Hernández-Ramírez, A.; Guzmán-Mar, J.L.; Hinojosa-Reyes, L.; Manríquez, J.; Ruiz-Ruiz, E.J. Air Diffusion Electrodes Based on Synthetized Mesoporous Carbon for Application in Amoxicillin Degradation by Electro-Fenton and Solar Photo Electro-Fenton. *Electrochim. Acta* 2018, 269, 232–240, doi:10.1016/j.electacta.2018.02.139.
- [25] Molla, H.; Pishnamaz, N.; Farimaniraad, H.; Baghdadi, M.; Aminzadeh, B.; Mahpishanian, S. Application of Nickel Foam Cathode Modi Fi Ed by Single-Wall Carbon Nanotube in Electro-Fenton Process Coupled with Anodic Oxidation : Enhancing Organic Pollutants Removal. *J. Electroanal. Chem.* 2023, 929, 117130, doi:10.1016/j.jelechem.2022.117130.
- [26] Wang, Y.; Chen, J.; Gao, J.; Meng, H.; Chai, S.; Jian, Y.; Shi, L.; Wang, Y.; He, C. Selective Electrochemical H₂O₂ Generation on the Graphene Aerogel for Efficient Electro-Fenton Degradation of Ciprofloxacin. *Sep. Purif. Technol.* 2021, 272, 118884, doi:10.1016/j.seppur.2021.118884.
- [27] Wang, Z.; Olvera-vargas, H.; Vinicius, M.; Martins, S.; Garcia-rodriguez, O.; Garaj, S.; Lefebvre, O. High Performance and Durable Graphene-Grafted Cathode for Electro-Fenton Degradation of Tetramethyldecynediol. *Chem. Eng. J.* 2023, 455, 140643, doi:10.1016/j.cej.2022.140643.
- [28] Ramírez-Valencia, L.D.; Bailón-García, E.; Moral-Rodríguez, A.I.; Carrasco-Marín, F.; Pérez-Cadenas, A.F. Carbon Gels–Green Graphene Composites as Metal-Free Bifunctional Electro-Fenton Catalysts. *Gels* 2023, 9, doi:10.3390/gels9080665.
- [29] Briz-Amate, T.; Castelo-Quibén, J.; Bailón-García, E.; Abdelwahab, A.; Carrasco-Marín, F.; Pérez-Cadenas, A.F. Growing Tungsten Nanophases on Carbon Spheres Doped with Nitrogen. Behaviour as Electro-Catalysts for

- Oxygen Reduction Reaction. *Materials* (Basel). 2021, 14, doi:10.3390/ma14247716.
- [30] Pérez-Cadenas, A.F.; Ros, C.H.; Morales-Torres, S.; Pérez-Cadenas, M.; Kooyman, P.J.; Moreno-Castilla, C.; Kapteijn, F. Metal-Doped Carbon Xerogels for the Electro-Catalytic Conversion of CO₂ to Hydrocarbons. *Carbon* N. Y. 2013, 56, 324–331, doi:10.1016/j.carbon.2013.01.019.
- [31] Wang, S.; Ye, D.; Zhu, X.; Yang, Y.; Chen, J.; Liu, Z.; Chen, R.; Liao, Q. Beyond the Catalyst: A Robust and Omnidirectional Hydrophobic Triple-Phase Architecture for Ameliorating Air-Breathing H₂O₂ Electrosynthesis and Wastewater Remediation. *Sep. Purif. Technol.* 2023, 305, 122397, doi:10.1016/j.seppur.2022.122397.
- [32] Zhao, Z.; Hao, Y.; Wu, J.; Feng, Z.; Feng, F.; Li, Y.; Yang, Q. Development of a Three-Dimensional Electro-Fenton System Packed with C-PTFE / Fe–Co–C Hybrid Particle Electrodes for Simultaneous H₂O₂ Generation and Activation into •OH. *Sep. Purif. Technol.* 2023, 317, 123960, doi:10.1016/j.seppur.2023.123960.
- [33] Company, L.; William, B.; Offeman, R.E. Preparation of Graphitic Oxide. 1958, 89, 1958, doi:<https://doi.org/10.1021/ja01539a017>.
- [34] Shen, Y.F.; Tang, J.; Nie, Z.H.; Wang, Y.D.; Ren, Y.; Zuo, L. Preparation and Application of Magnetic Fe₃O₄ Nanoparticles for Wastewater Purification. 2009, 68, 312–319, doi:10.1016/j.seppur.2009.05.020.
- [35] Bailón-garcía, E.; Carrasco-marín, F.; Pérez-cadenas, A.F.; Maldonado-hódar, F.J. Chemoselective Pt-Catalysts Supported on Carbon-TiO₂ Composites for the Direct Hydrogenation of Citral to Unsaturated Alcohols. 2016, 344, 701–711, doi:10.1016/j.jcat.2016.09.026.

- [36] Fernández-sáez, N.; Villela-martinez, D.E.; Carrasco-marín, F.; Pérez-cadenas, A.F.; Pastrana-martínez, L.M. Heteroatom-Doped Graphene Aerogels and Carbon-Magnetite Catalysts for the Heterogeneous Electro-Fenton Degradation of Acetaminophen in Aqueous Solution. 2019, 378, 68–79, doi:10.1016/j.jcat.2019.08.020.
- [37] Elmouwahidi, A.; Bailón-García, E.; Pérez-Cadenas, A.F.; Maldonado-Hódar, F.J.; Carrasco-Marín, F. Activated Carbons from KOH and H₃PO₄-Activation of Olive Residues and Its Application as Supercapacitor Electrodes. *Electrochim. Acta* 2017, 229, 219–228, doi:10.1016/j.electacta.2017.01.152.
- [38] Aoki, A.; Ogasawara, T.; Aoki, T.; Ishida, Y.; Shimamura, Y. Raman Spectroscopy Used for Estimating the Effective Elastic Modulus of Carbon Nanotubes in Aligned Multi-Walled Carbon Nanotubes / Epoxy Composites under Tensile Loading. *Compos. Part A* 2023, 167, 107448, doi:10.1016/j.compositesa.2023.107448.
- [39] Bokobza, L.; Bruneel, J.; Couzi, M. Vibrational Spectroscopy Raman Spectroscopy as a Tool for the Analysis of Carbon-Based Materials (Highly Oriented Pyrolytic Graphite , Multilayer Graphene and Multiwall Carbon Nanotubes) and of Some of Their Elastomeric Composites. *Vib. Spectrosc.* 2014, 74, 57–63, doi:10.1016/j.vibspec.2014.07.009.
- [40] Li, Z.; Deng, L.; Kinloch, I.A.; Young, R.J. Raman Spectroscopy of Carbon Materials and Their Composites : Graphene , Nanotubes and Fibres. *Prog. Mater. Sci.* 2023, 135, 101089, doi:10.1016/j.pmatsci.2023.101089.
- [41] Jiang, M.; Xu, W.; Du, X.; Yang, X.; Wang, F.; Zhou, Y.; Pan, Y.; Lu, Y. Materials Today Sustainability An N , P , O-Doped Porous Carbon Electrode

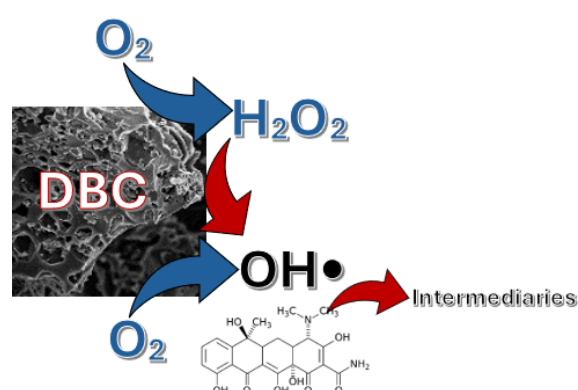
- Material Derived from a Lignin-Modified Chitosan Xerogel for a Supercapacitor. 2023, 22, doi:10.1016/j.mtsust.2023.100372.
- [42] Medina, O.E.; Galeano-caro, D.; Ocampo-p, R.; Carrasco-marín, F.; Franco, C.A.; Corte, F.B. Microporous and Mesoporous Materials Development of a Monolithic Carbon Xerogel-Metal Composite for Crude Oil Removal from Oil in-Saltwater Emulsions: Evaluation of Reuse Cycles. 2021, 327, doi:10.1016/j.micromeso.2021.111424.
- [43] Gaikwad, M.M.; Sarode, K.K.; Pathak, A.D.; Sharma, C.S. Ultrahigh Rate and High-Performance Lithium-Sulfur Batteries with Resorcinol-Formaldehyde Xerogel Derived Highly Porous Carbon Matrix as Sulfur Cathode Host. *Chem. Eng. J.* 2021, 425, 131521, doi:10.1016/j.cej.2021.131521.
- [44] Perciani, N.; Moraes, D.; Siervo, A. De; Moreira, T.; Campos, B.; Thim, P.; Alvares, L. Structure-Directing Ability of the Kraft-Lignin / Cellulose Carbon Xerogel for the Development of C-Nb₂O₅ Sunlight-Active Photocatalysts. *J. Photochem. Photobiol. A Chem.* 2023, 441, 114697, doi:10.1016/j.jphotochem.2023.114697.
- [45] Kim, C.; Lee, J.; Wang, W.; Fortner, J. Organic Functionalized Graphene Oxide Behavior in Water. *Nanomaterials* 2020, doi:10.3390/nano10061228.
- [46] Beeran, Y.; Bobnar, V.; Grohens, Y.; Thomas, S.; Kokol, V. Cellulose Nano Fiber-Reduced Graphene Oxide Xerogels and Cryogels for Dielectric and Electrochemical Storage Applications. *J. Polym. Sci. Part B: Polym. Phys.* 2018, 56, 260–270, doi:10.1016/j.polymer.2018.06.005.
- [47] Pham, H.D.; Pham, V.H.; Cuong, T.V. Synthesis of the Chemically Converted Graphene Xerogel with Superior Electrical Conductivity. *W.*

- ChemComm 2011, 9672–9674, doi:10.1039/c1cc13329b.
- [48] Gao, Y.; Zhu, W.; Li, Y.; Zhang, Q.; Chen, H.; Zhang, J.; Huang, T. Anthraquinone (AQS)/ Polyaniline (PANI) Modified Carbon Felt (CF) Cathode for Selective H₂O₂ Generation and Efficient Pollutant Removal In. *J. Environ. Manage.* 2022, 304, 114315, doi:10.1016/j.jenvman.2021.114315.
- [49] Wang, J.; Liu, B.; Liu, H.; Hu, X.; Zhou, S. Insight into the Mechanisms of BPS Degradation by Electro-Fenton Method Modified by Co-Based Nanoparticles on the Oxidized Carbon Cathode. *Chem. Eng. J.* 2022, 446, 137376, doi:10.1016/j.cej.2022.137376.
- [50] Chen, F.; Liu, H.; Yang, F.; Che, S.; Chen, N.; Xu, C.; Wu, N.; Sun, Y.; Yu, C.; Li, Y. Multifunctional Electrocatalyst Based on MoCoFe LDH Nanoarrays for the Coupling of High Efficiency Electro-Fenton and Water Splitting Process. 2023, 467, doi:10.1016/j.cej.2023.143274.
- [51] Wang, L.; Niu, J.; Gao, S.; Liu, Z.; Wu, S.; Huang, M.; Li, H.; Zhu, M.; Yuan, R. Breakthrough in Controlling Membrane Fouling and Complete Demulsification via Electro-Fenton Pathway : Principle and Mechanisms. *J. Memb. Sci.* 2023, 670, 121354, doi:10.1016/j.memsci.2023.121354.
- [52] Zhao, H.; Han, S.; Jia, J.; He, M.; An, K.; Tang, Z.; Lai, S.; Yang, X.; Wang, Z. The Effect of N-Doping on the Synergy between Adsorption and 2e⁻ ORR Performance of Activated Carbon Cathode in an Electro-Fenton System. *Chem. Eng. J.* 2023, 468, 143505, doi:10.1016/j.cej.2023.143505.
- [53] Sun, Y.; Deng, R.; Chi, C.; Chen, X.; Pan, Y.; Li, J.; Xia, X. One-Step Synthesis of S , N Dual-Element Doped RGO as an Efficient Electrocatalyst for ORR. *J. Electroanal. Chem.* 2023, 940, 117489,

- doi:10.1016/j.jelechem.2023.117489.
- [54] Alekseeva, O. V; Smirnova, D.N.; Noskov, A. V; Yu, O.; Kirilenko, M.A.; Agafonov, A. V Mesoporous Halloysite / Magnetite Composite : Synthesis , Characterization and in Vitro Evaluation of the Effect on the Bacteria Viability. *Mater. Today Commun.* 2022, 32, 103877, doi:10.1016/j.mtcomm.2022.103877.
- [55] Iglesias-rojas, D.; Bar, A.; Muro, I.G. De; Lezama, L.; Insausti, M. Getting Insight into How Iron (III) Oleate Precursors Affect the Features of Magnetite Nanoparticles. 2022, 316, 1–8, doi:10.1016/j.jssc.2022.123619.
- [56] Vinod, K.R.; Saravanan, P.; Sakar, M.; Balakumar, S. Insights into the Nitridation of Zero-Valent Iron Nanoparticles for the Facile Synthesis of Iron Nitride Nanoparticles. *RSC Adv.* 2016, 45850–45857, doi:10.1039/c6ra04935d.
- [57] Crane, R.A.; Scott, T.B. The Effect of Vacuum Annealing of Magnetite and Zero-Valent Iron Nanoparticles on the Removal of Aqueous Uranium. 2013, 2013, doi:10.1155/2013/173625.
- [58] Wang, C.; Jiang, R.; Yang, J.; Wang, P. Enhanced Heterogeneous Fenton Degradation of Organic Pollutants by CRC / Fe₃O₄ Catalyst at Neutral PH. 2022, 10, 1–8, doi:10.3389/fchem.2022.892424.
- [59] Hashemian, S.; Tabatabaee, M.; Gafari, M. Fenton Oxidation of Methyl Violet in Aqueous Solution. 2013, 2013, doi:10.1155/2013/509097.
- [60] Li, A.; Zhang, M.; Ma, W.; Li, D.; Xu, Y. Sugar-Disguised Bullets for Combating Multidrug-Resistant Bacteria Infections Based on an Oxygen Vacancy-Engineered Glucose-Functionalized MoO_{3-x} Photo-Coordinated Bienzyme. *Chem. Eng. J.* 2022, 431, 133943,

- doi:10.1016/j.cej.2021.133943.
- [61] Liang, J.; Zhang, Y.; Song, C.; Tang, D.; Sun, J. Double-Potential Electro-Fenton: A Novel Strategy Coupling Oxygen Reduction Reaction and $\text{Fe}^{2+}/\text{Fe}^{3+}$ Recycling. *Electrochem. commun.* 2018, 94, 55–58, doi:10.1016/j.elecom.2018.08.006.
- [62] Divyapriya, G.; Nambi, I.; Senthilnathan, J. Ferrocene Functionalized Graphene Based Electrode for the Electro-Fenton Oxidation of Ciprofloxacin. *Chemosphere* 2018, 209, 113–123, doi:10.1016/j.chemosphere.2018.05.148.

CHAPTER IV: DOPED BIO-CARBONS (S, N, P OR B) AS HIGHLY EFFICIENT DUAL CATALYSTS FOR THE DEGRADATION OF TETRACYCLINE THROUGH HETEROGENEOUS ELECTRO-FENTON PROCESS



Abstract

Bio-carbon (BC) obtained from agro-industrial waste was doped with different heteroatoms (S, N, B, P) to evaluate their potential as catalysts for the oxygen reduction reaction (ORR) and electro Fenton process. The samples underwent thorough characterization using techniques such as N₂ adsorption at 77K, CO₂ adsorption at -193K, X-ray photoelectron spectroscopy (XPS), and X-ray diffraction.

Electrochemical characterizations were conducted through cyclic voltammetry (CV) and linear sweep voltammetry (LSV). It was observed that all doped samples (S, N, B, P) exhibited enhanced ORR activity, with DBC-N demonstrating the highest performance, attributed to its superior J_k value (10.4 mA cm⁻²) and lowest E^o_{onset} (-0.14V). Furthermore, the circular economy aspect was considered in this study. The utilization of agro-industrial waste for bio-carbon production aligns with the principles of circular economy by repurposing waste materials and minimizing environmental impact. This approach not only offers a sustainable alternative to conventional catalyst synthesis methods but also contributes to reducing waste generation and promoting resource efficiency. In addition to ORR catalytic activity, all doped samples were evaluated as dual catalysts for the degradation of tetracycline through the heterogeneous electro Fenton process. Remarkably, all samples exhibited enhanced degradation levels (>40%), reaching a maximum of approximately 70% with the nitrogen-doped sample. This work highlights the potential of obtaining excellent metal-free ORR catalysts through a low-cost, circular economy-driven approach, with promising applications in environmental remediation processes such as the efficient decontamination of wastewater."

4.1.- INTRODUCTION

Recently, emerging pollutants (cleaning products, disinfectants, pharmaceuticals, etc.) have caused alarm in the scientific community, mainly because of their potential impact on public health [1]. Among these pollutants, pharmaceuticals, mainly antibiotics, have attracted attention because the presence of this type of substances in the environment generates problems such as the generation of resistance genes, which is a critical problem for human health, food security and water cleanliness [2-4]. In addition, most antibiotics are poorly metabolised (10-70%) in humans and animals, resulting in their return to the environment [5,6]. In addition, human consumption of antibiotics is projected to increase by nearly 15% to 200% by 2030 [7,8], exacerbating the problem of final disposal.

Tetracycline (TC) is a broad-spectrum antibiotic widely used in the treatment of human and animal diseases, but recently some researchers have focused on electrochemical advanced oxidation processes (EAOPs), which have been shown to have high mineralization rates for different types of pollutants [9]. Electro-Fenton (EF) has degraded a wide range of antibiotics (sulfadiazine, ciprofloxacin, cefalexin, oxcarbazepine, prednisolone, chloramphenicol and thiamphenicol), among which TC stands out [10-12]. EF is based on the generation of hydroxyl radicals ($\bullet\text{OH}$) resulting from the reaction of H_2O_2 (electrogenerated by the oxygen reduction pathway two electrons (ORR)) (equation. 4.1) and the Fenton catalyst (traditionally Fe^{2+}) (equation.4. 2) in an acidic medium [13-16].



It is possible to consider that the limiting step in the process is the electro generation of H_2O_2 [17], whereby currently has been searched new ORR catalysts with high selectivity towards the 2e^- . Traditionally, the platinum (Pt) is the ORR catalyst used for excellence, however, its high cost limits its use for industrial applications [18]. The carbon-based materials (example: graphene oxide, graphite felt, reduced graphene oxide, carbon felt, etc) have drawn attention due mainly to its low cost, durability, and good selectivity for ORR 2e^- [19-21]. However, the ORR activity of these materials is lower than Pt catalysts, whereby has been used the doped with heteroatoms for upgrade the catalytic activity. Atoms as oxygen (O), nitrogen (N), phosphorus (P), boron (B), and fluorine (F) had been showed capability for regulate the charge electric superficial of material, which is translate in a best donation of electrons, making that appear more active sites for ORR [22-24]. also, it has been founded that the mesoporosity is adequate for better transfer of oxygen in the catalysts enhancing the ORR activity, recently it has been founded that carbons materials obtained by alkali-activation induce to the obtaining of mesopores [25]. In summary, carbon materials with porous structure, good conductivity and with appropriate functional groups are promising for their use as electrocatalysts in ORR and electro Fenton process.

In this work, A bio-carbon has been produced from the waste of olive oil industry, specifically from the “alperujo”. The “alperujo” is the watery residue and plant fibre of the olive after oil extraction [26]. This “alperujo” contains the residues of the herbicides and phytosanitary products used, as well as a high concentration of polyphenols. All these products cause significant pollution at the production sites, both in the soil and in aquifers and rivers [27]. In large quantities, they can acidify the soil, making it saline and inhibiting plant growth. Alperujo also prevents

the oxygenation of water, causing anaerobic fermentation and the development of aquatic flora and fauna. Due to its phytotoxic and poorly biodegradable composition, it is one of the most polluting effluents in the agri-food production system that needs to be treated [28]. In this way, we promote the optimisation of resources and the use of waste, recycling it or giving it a new life to transform it into new products, in favour of the circular economy.

The carbon material obtained was hydrothermally doped with different heteroatoms (S, N, B and P) to be evaluated as ORR catalysts and in the EF reaction for the degradation of TC.

4.2.- EXPERIMENTAL

4.2.1.- Preparation of carbon materials

The bio-carbon was synthesized by a process carried out in a previous work [29]. In the first step, olive wastewater was carbonized at 300 °C for 2 h in a nitrogen flow at a rate of 60 cm³ min⁻¹, followed by chemical activation with solid KOH, physically mixing the carbonized material in a 1/1 mass ratio. The resulting mixture was treated at 840 °C for 2 h in a nitrogen flow of 60 cm³ min⁻¹. The final material was called BC.

The final BC sample was doped with nitrogen (N), Boron(B), Phosphorus(P) and sulfur (S) atoms using different precursors such as melamine (100 mg), phenylboronic acid (600 mg), triphenylphosphine (1 g) and 1-dodecanethiol (8 mL). The samples were prepared by mixing 1.5 g of BC and in 100 mL of deionized water in the case of N and B and 50 mL of ethanol and 50 mL of deionized water in the case of P and S. The mixture was then subjected to hydrothermal treatment

at 130 °C for 24 h. The final samples were called DBC- X(X is the heteroatom corresponding).

4.2.2.- Textural and Chemical characterization

The adsorption isotherm of N₂ (77 K) and CO₂ (273 K) were realized by using Quadrasorb equipment from Quantachrome Instruments, after degasification of the samples for 12 hours under vacuum of 10⁻⁶ mbar at 120 °C. The surface area of the samples was determined by applying the Brunauer-Emmett-Teller (B.E.T.) method, and the micropore volume of the samples was defined by applying the Dubinin-Radushkevich (DR) equation to the N₂ isotherms adsorption. The narrow micropores volume was determined by the application of the DR equation to the CO₂ isotherms.

The FTIR spectra were made using NICOLET IR200 equipment, in a range between 400 to 4000 cm⁻¹, obtaining the results in % Transmittance.

The composition and the chemical state of all samples material surface were obtained by X-ray Photoelectron Spectroscopy using ESCA 5701 equipment from Physical Electronics (PHI) System (equipped with MgK α anode, model PHI 04-548, X-ray source ($h\nu = 1253.6$ eV) and hemispherical electron detector). For the analysis of the XPS peaks, the C_{1s} peak position was used as reference to locate the other peaks and fixed at 284.6 eV. The fitting of the XPS peaks was done by least squares using Gaussian-Lorentzian peak sharps using XPSpeaks41 program.

4.2.3.- Electrochemical characterization: Oxygen electro reduction

For electrochemical measurements in ORR application, bio-carbon samples were mixed with 1 mL of nafion and 9 mL of deionized water, followed by sonication for 10 minutes. From the prepared solution, 1mL was taken and added

to 5 mg of samples, bio-carbon to then, the mixture was sonicated for 30 minutes. 20 μL of the final solution was taken to deposit on the disk of the rotating ring disc electrode (RRDE), with which the ORR activity was studied.

The activity for ORR was studied by the RRDE technique using an Autolab electrochemical system associated with a compact potentiostat/galvanostat (PGSTAT101). Electrochemical measurements were carried out in a standard three-electrode electrochemical cell at room temperature, using a Pt sheet as a counter electrode and an Ag/AgCl as reference electrode. The electrolyte was 100 ml of a solution of KOH 0.1M. Before each electrochemical measurement, the electrolyte was saturated with N_2 or O_2 by purging the necessary gas into the KOH 0.1M solution for 30 minutes. Cyclic voltammetry (CV) measurement was collected in a potential range of -0.80 to 0.40 V at 50 mV s^{-1} scan rate with the electrode at a rotational speed of 1000 rpm. Linear scanning voltammetry (LSV) for the ORR experiment was carried out with a potential range between -0.80 to 0.40 V at 50 mV s^{-1} with the electrode at rotational speeds varying from 500, 1000, 1500, 2000, 2500, 3000 to 3500 rpm.

The number of electrons transferred and the % of H_2O_2 selectivity were calculated using equations 5 and 6, [30,31].

$$n = \frac{4 \times I_D}{I_D + \frac{I_R}{N_C}} \quad (4.3)$$

$$\% \text{H}_2\text{O}_2 = \frac{200 \times \frac{I_R}{N_C}}{I_D + \frac{I_R}{N_C}} \quad (4.4)$$

Where I_D and I_R are the disk and ring current respectively, and N_C is the collection efficiency of the RRDE (0.249).

The current density (J_K) was obtained by Koutecky-Levich equation (equation 4.5).

$$\frac{1}{J} = \frac{1}{J_K} + \frac{1}{B \times \omega^{1/2}} \quad (4.5)$$

$$B = (0.62)n \times F \times A \times D^{2/3} \times \nu^{-1/6} \times C$$

Where F is Faraday's constant (96485 C mol^{-1}), n number of electrons transferred per oxygen molecule, A is the disc area of the RRDE (0.2475 cm^2), D diffusion coefficient of oxygen ($1.9 \cdot 10^{-5} \text{ cm}^2 \text{ s}^{-1}$), ν is kinematic viscosity ($0.01 \text{ cm}^2 \text{ s}^{-1}$) and finally C is the solubility of oxygen ($1.2 \cdot 10^{-6} \text{ mol cm}^{-3}$) [32,33].

4.2.4.- Electro Fenton process

The electro-Fenton process was carried out using a standard three-electrode electrochemical cell with capacity for 0.1 L of solution at room temperature. The TC concentration was approached 40 mg L^{-1} , using Na_2SO_4 [0.5M] as a supporting electrolyte with continuous agitation. Potentiostat was maintained in potentiostatic mode at -0.6V .

The working electrode was prepared by mixing DBC with polytetrafluoroethylene (PTFE) (60%) with mass ratio of (90:10) respectively, for subsequent drying at $100 \text{ }^\circ\text{C}$ for 12 h. Once dried, the obtained paste was deposited on a sheet of graphite ($3\text{cm} \times 1\text{cm}$) (25 mg on each face). The reference electrode was Ag/AgCl, and the counter electrode used was a platinum sheet in natural pH.

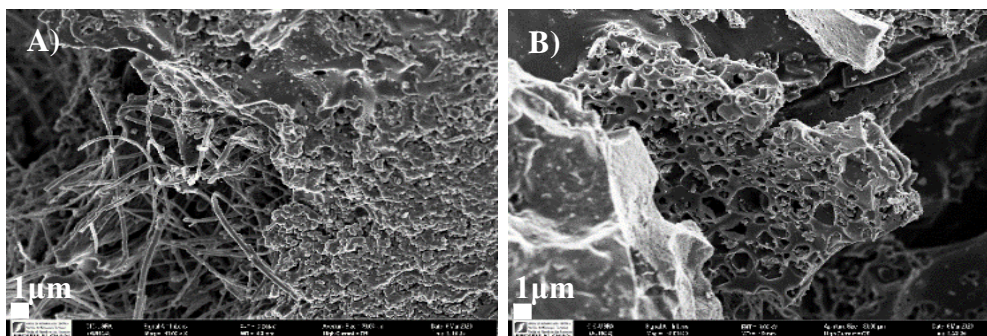
The TC concentration was measured by taking 2 mL samples each 5min. When the maximum absorption wavelength was 356.5 nm, the concentration of TC was determined by UV-vis spectrometry. Equation 4.6 was used to calculate the degradation percentage.

$$\%Degradation = \frac{C_0 - C_i}{C_0} \times 100 \quad (4.6)$$

4.3.- RESULTS AND DISCUSSIONS

4.3.1.- Morphological characterization

The figure 4.1 shows the scanning electron microscopy micrographs of the samples BC and DBC-N DBC-N was selected due to its electrochemical properties to evidence the possible differences between the original sample (BC) and the doped one (DBC-N). Typical SEM micrographs clearly reveal the differences in the morphology of the original and doped materials.



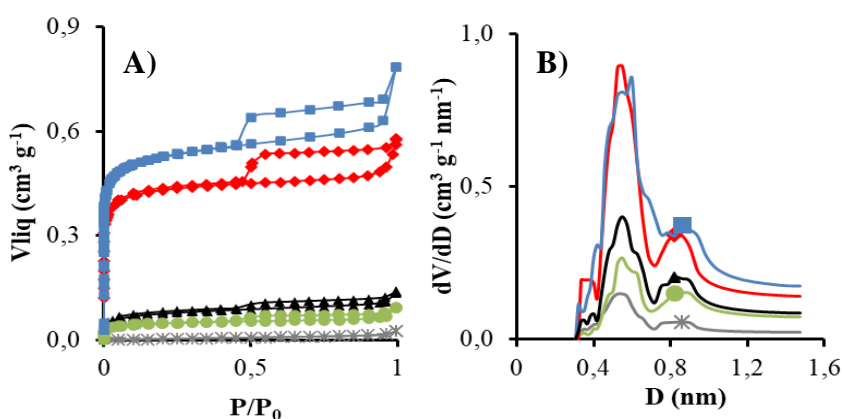
Figures 4.1. SEM microphotographs (10.00 KX) showing the morphology of samples A) BC and B) DBC-N.

Analysing the images, it is possible to observe that both samples have rough surfaces with cracks and holes of different sizes, which are related to the

degradation of the carbon framework. However, it is also possible to observe that the DBC-N surface was more damaged due to the presence of nitrogen-containing reactants which may aid to the development of bigger holes and interconnecting pores in a three-dimension network structure.

4.3.2.- Textural characterization

N₂ adsorption–desorption isotherms of all are depicted in figure 4.2A) and table 4.1. Based on the IUPAC classification, BC and DBC-N exhibit mixed type-I and type-IV isotherms, representative of micro and mesoporous materials, respectively [34].



Figures 4.2. Isotherms N₂ adsorption A) and Pore size distribution of all samples B) (■BC, ▲DBC-B, ◆DBC-N, *DBC-P and ●DBC-S).

DBC-B and DBC-S present an isotherm IV type characteristic of mesoporous solids, and the sample DBC-P show an isotherm type III typically associated with solids not porous. The volume of N₂ adsorbed at low relative pressures decreased with the doping process for all samples. Indicating that the doping reduced the surface area of the sample by blocking some porosity. Also, we can denote the

increase of the pore diameter calculated by N₂ adsorption indicating the development of mesoporous structure after doping of all samples. The adsorption of CO₂ gives information about the ultramicroporosity, i.e., micropores narrower than 0.7 nm, whereas the supermicroporosity is reached by the N₂ in absence of diffusion restrictions.

For all modified samples, $W_0(N_2) < W_0(CO_2)$, denoting the presence of narrow micropores or pores with constricted entrances, which prevent the access of N₂. Note that $L_0(N_2)$ also increased, corroborating this pore widening. Thus, the modifications of surface chemistry of the original sample decreased the surface area, the pore volume but increased the average pore diameter. The micropore size distribution of all samples is shown in Figure 4.2B). The micropore width of modified samples is very narrow, and a well-defined peak is obtained at about 0.6 nm. Thus, some porosity could be inaccessible to N₂ molecules during adsorption at -196 °C. The intensity of this peak is much higher for the original sample and the sample DBC-N but decreases for the other samples. This means that existing pores were destroyed or opened by surface modification processes due to the deterioration of the walls between adjacent micropores, which produced a reduction of surface area and micropore volume.

Table 4.1. Textural characteristics of all the samples obtained by N₂ adsorption isotherms at 77K and CO₂ at 0°C.

Sample	N ₂							CO ₂		
	S _{B.E.T}	S _{D.F.T}	W ₀	L ₀	V _{0.95}	V _{meso}	V _{D.F.T}	L ₀		
								(D.F.T)	W ₀	L ₀
BC	1297	1494	0.49	0.80	0.63	0.14	0.64	1.22	0.44	0.73
DBC-B	175	148	0.07	1.42	0.11	0.04	0.12	0.61	0.19	0.80
DBC-N	1061	1160	0.42	1.03	0.50	0.08	0.51	0.61	0.40	0.74
DBC-P	4	7	0.00	2.05	0.02	0.01	0.02	2.84	0.07	0.71
DBC-S	114	97	0.05	1.51	0.07	0.02	0.07	0.85	0.14	0.90

units: S (m² g⁻¹); W (cm³ g⁻¹); L (nm).

4.3.3.- Chemical characterization

The FTIR spectra figure 4.3 were obtained to have informations of diferents funtional groups in each sample. All samples showed vibrations bonds correspond to C-O, C=C and O-H (900-1300, 1500-1600 and 3500 cm⁻¹ bands, approximately) [35-38]. Also we can detect the presence of peaks associated with CO and CO₂ (2100 and 2400 cm⁻¹ bands, approximately) [39].

FTIR spectroscopy was additionally invoked to determine changes in the functional composition of doped samples, the sample DBC-N, The -O-H and -N-H stretching vibration modes were connected to the broad bands at about 3450 cm⁻¹. The C-H bond is represented by the weak band at roughly 2920 cm⁻¹, and the characteristic absorbance of C-H bonds is represented by the band at about 1600 cm⁻¹. The wide peak of 1100 cm⁻¹ is linked to the vibration of C-N stretching. The peak at 1630 cm⁻¹ is due to vibrations of aromatic C=C bonds and C=N bonds in the basal plane. N-H stretching vibrations at 3220 cm⁻¹ and N-H in-plane deformations at 1530

cm^{-1} may overlap with other bands. C–N stretching vibrations can be detected at 1455 cm^{-1} . A small peak at 880 cm^{-1} observed in the spectrum of N-C originates from C–O–C bonds. The broad and sharp peak at 1502 cm^{-1} is attributed to the presence of nitrogen as C–N and N–O groups

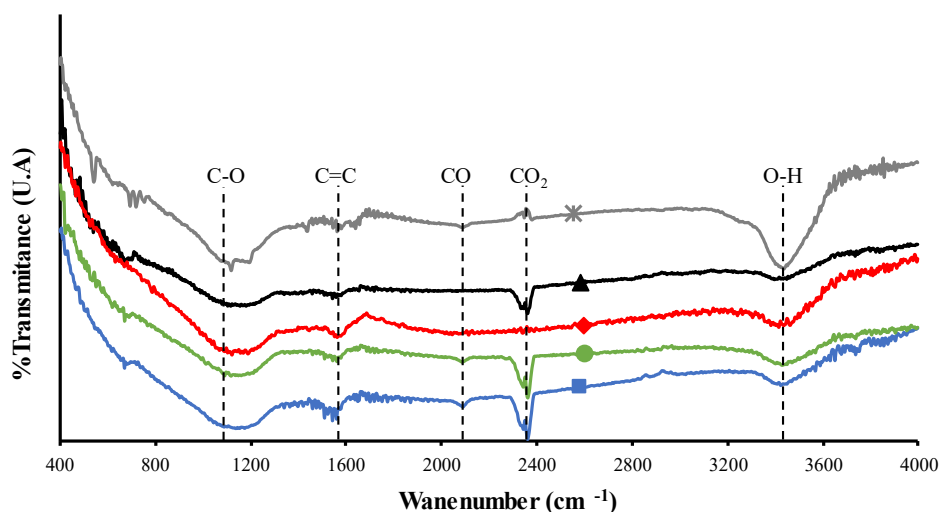


Figure 4.3. FTIR of ■ BC, ▲ DBC-B, ◆ DBC-N, * DBC-P and ● DBC-S.

For the sample DBC-S, with the increase in sulfur content, the water absorption band ($1650\text{-}1885 \text{ cm}^{-1}$) of carbons becomes stronger, possibly due to an increase in polarity in the carbon backbone. Therefore, the spectra shows several vibrations including SO_2 symmetric stretching ($1120\text{-}1190 \text{ cm}^{-1}$), S=O stretching ($1020\text{-}1060 \text{ cm}^{-1}$), C-S stretching ($600\text{-}700 \text{ cm}^{-1}$), and S-S stretching ($450\text{-}550 \text{ cm}^{-1}$).

The FTIR spectra of DBC-B, the presence of different peaks at 1120, 1168, and 1397 cm^{-1} and 696 cm^{-1} could be indexed to the vibrations of B-C stretching, B-O-H bending, B-O stretching and O-B-O bonds, respectively, confirming that a large quantity of B was doped into the carbon-based materials.

For the DBC-P, characteristic band associated with the C-C asymmetric stretching vibrations of phenyl-groups appeared at 1438 cm^{-1} . Although the band exhibited at 1438 cm^{-1} may arise from ring vibrations, it appears to be as well useful for the identification of the phenyl-phosphorus group. In addition, band corresponding to carbon-phosphorus bond (C-P) can be seen at 803 cm^{-1} . Also noticeable is the increase in the relative intensity of the bands at 3423 cm^{-1} in CK1P when compared to BC sample, thus suggesting that more -OH functional groups. FTIR spectra confirm the presence of doping atoms in all samples .

The XPS surface composition of all samples were obtained by the analysis of the electronic states of C, O, B, N, P and S atoms. The spectra of C_{1s} and O_{1s} are shown in figure 4.4. The binding energy (BE) scale was referenced to the C_{1s} of graphitic carbon, set at 284.6 eV. The peaks in the carbon region was attributed to the bonds C=C (284.6 eV), C-C (285.6 eV), C-O (286.9 eV), C=O (287.7 eV), O=C-C (289.4 eV) and π - π^* (290.9 eV) [40]. The peaks in the oxygen region were attributed to the bonds C=O (531.0 eV), C-OH (532.3 eV) and O-C-O (533.3 eV) [41].

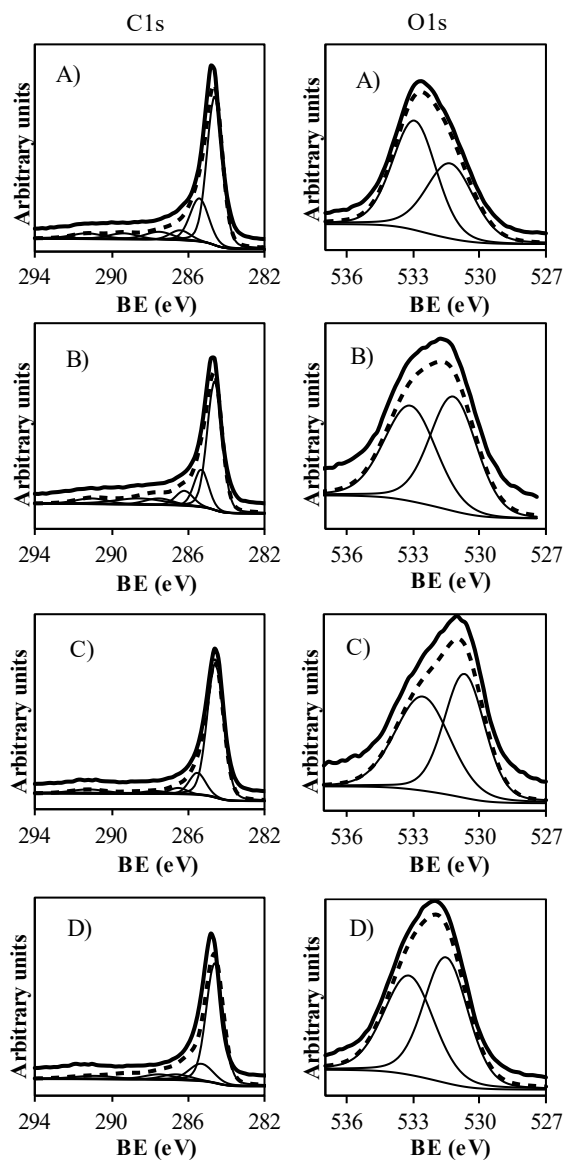


Figure 4.4. C_{1s} and O_{1s} XPS spectra of A) DBC-B, B) DBC-N, C) DBC-P and D) DBC-S.

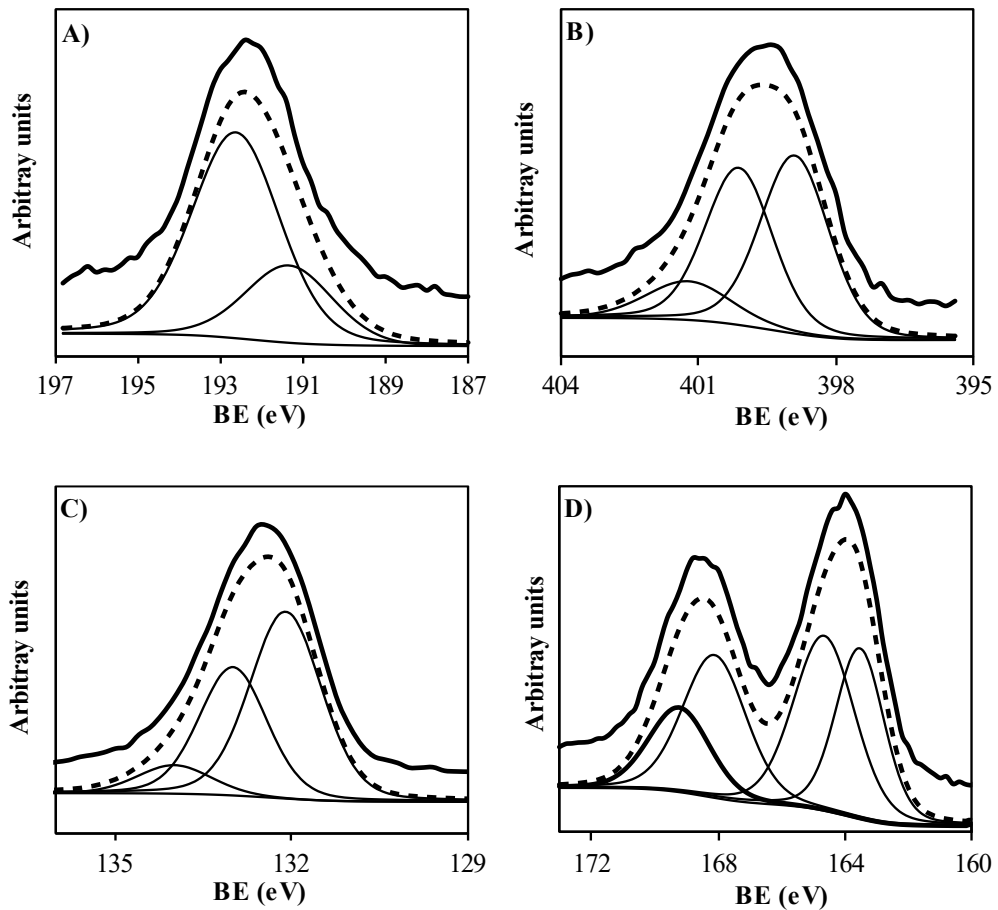


Figure 4.5. XPS spectrum of each respective heteroatom in the samples A) DBC-B, B) DBC-N, C) DBC-P and D) DBC-S.

The analysis of the spectrums was summarized in the table 4.2, where are show the different percentages of each element analysed by XPS.

Table 4.2. XPS summary of all samples.

Sample	C _{1s}	% peak	O _{1s}	% peak	B, N, P, or S	% peak	% wt
BC	284.6	66	531.4	39			
	285.8	17	533	61			
	287.5	7					
	289	5					
	290	4					
	291	1					
DBC-B	284.6	59.65	532.95	57.24	192.62	72.44	5.60
	285.4	20.88	531.34	42.76	191.33	27.56	
	286.4	5.83					
	287.5	5.33					
	289.4	4.36					
	291.3	3.94					
DBC-N	284.6	56.50	531.17	52.23	398.90	47.13	4.09
	285.3	15.94	533.12	47.77	400.12	40.40	
	286.2	8.01			401.22	12.48	
	287.5	6.03					
	288.5	8.42					
	291.0	5.10					
DBC-P	284.6	75.62	530.67	49.22	132.10	55.26	4.28
	285.5	12.66	532.55	50.78	133.00	35.74	
	286.5	3.95			134.00	9.00	
	287.7	1.72					
	288.9	1.11					
	291.2	4.94					
DBC-S	284.6	63.88	531.53	53.04	163.52	24.97	2.16
	285.3	13.67	533.21	46.96	164.68	32.11	
	286.6	5.83			168.11	27.38	
	287.5	4.59			169.23	15.54	
	289.2	4.41					
	291.1	3.60					

The results show that the samples DBC-N and DBC-B have more carbonyl group (C=O) (287.4 eV in C_{1s} and 531.1 eV in O_{1s}) [42], which are candidates for enhanced the ORR activity [43]. Analyzing the other compounds, we found the presence of the bonds B-CO₂ (192.6 eV) and B-N (191.3 eV) [44,45] in the sample DBC-B, which it is possible attributable to N atoms presents in the matrix carbon. The sample DBC-P shows the presence of the bonds C-P (132.1 eV), C-PO₂ (133 eV), C-O-PO₃ (134 eV) [46,38]. On the other hand, the bonds C-SH (163.5 eV), R₂-SO (164.7 eV), C-OSO₃H (168.11 eV) and C-O-SO₂-O-C (169.23 eV) were found in the sample DBC-S [47,48]. In DBC-N the N_{1s} spectra, show the peaks corresponding to N-pyridine (398.9 eV), N-pyrrole (399.6 eV) and N-graphitic (400.9 eV) [49,50]. It Has been found that the N-pyridine has couple of performance the selectivity towards H₂O₂, while that N-pyrrole is more active for H₂O [51].

4.3.4.- Electrochemical characterization

Figure 4.6 shows the CV of all samples in nitrogen and oxygen saturated medium, it. In absence of O₂, the electrochemical behavior of all samples could be related to the porous texture and, in this way, it's possible to observe significative differences in the negative potential region in absence of O₂, which is mainly remarkable in the samples DBC-P and DBC-S with respect to the other samples, which is possibly attributed to the lowest surface area, which is theoretically proportional to the capacitance [52]. Furthermore, this better behavior could be related to the improved hydrophilicity of the surface due to the presence of heteroatoms which improves the electrolyte-surface contact favoring the diffusion of the ions, this leads to a decrease in the resistance of the electrodes, enhancing their performance for energy storage. In the presence of O₂, all samples display oxygen reduction peaks from -0,1V, which show electrocatalytic activity for

oxygen electro reduction. indicating that all samples are electro-active to the O₂ electro reduction. Moreover, an increase in the double layer capacitance is found in oxygen saturated KOH regarding. N₂-saturated solutions which could be ascribed to the pseudo capacitance contributions due to faradic process involving heteroatoms.

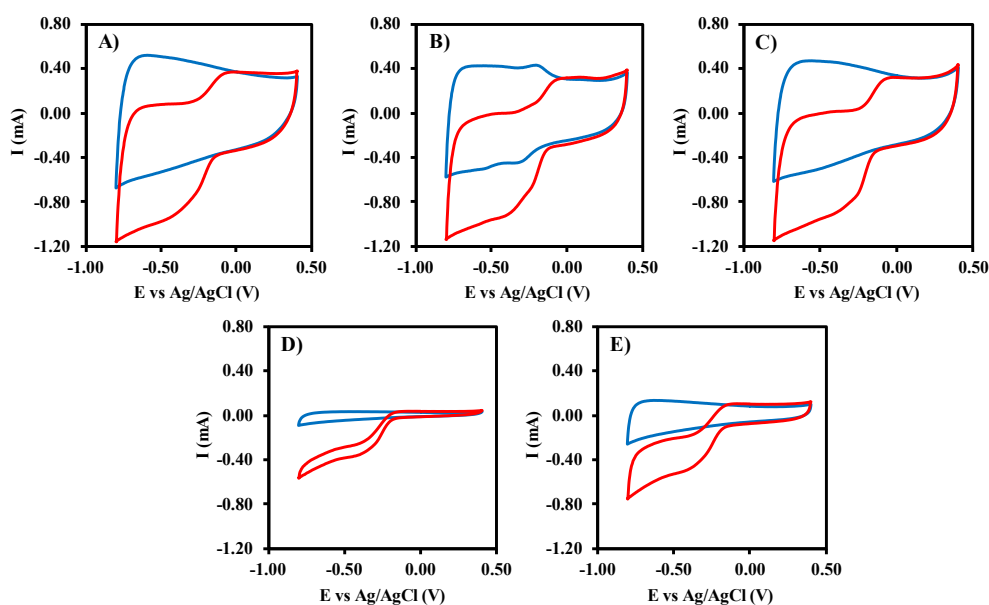


Figure 4.6. CV of A) BC, B) DBC-B, C) DBC-N, D) DBC-P and E) DBC-S; O₂ (red) and N₂ (blue).

The catalytic mechanism is very important for determining the application of the samples, due to that the ORR can develop in two ways (equations 4.4 and 4.5) [53,54], where the way for 2 electrons is the one necessary for electro-Fenton. To determine the catalytic mechanism of the samples, it was needed to make the LSV experiments with different rotation speeds (figure 4.7). The Koutecky-Levich

equation was used for adjusting the curves obtained and calculating the number of electrons transferred of all samples in different potentials was calculated (figure 4.8).

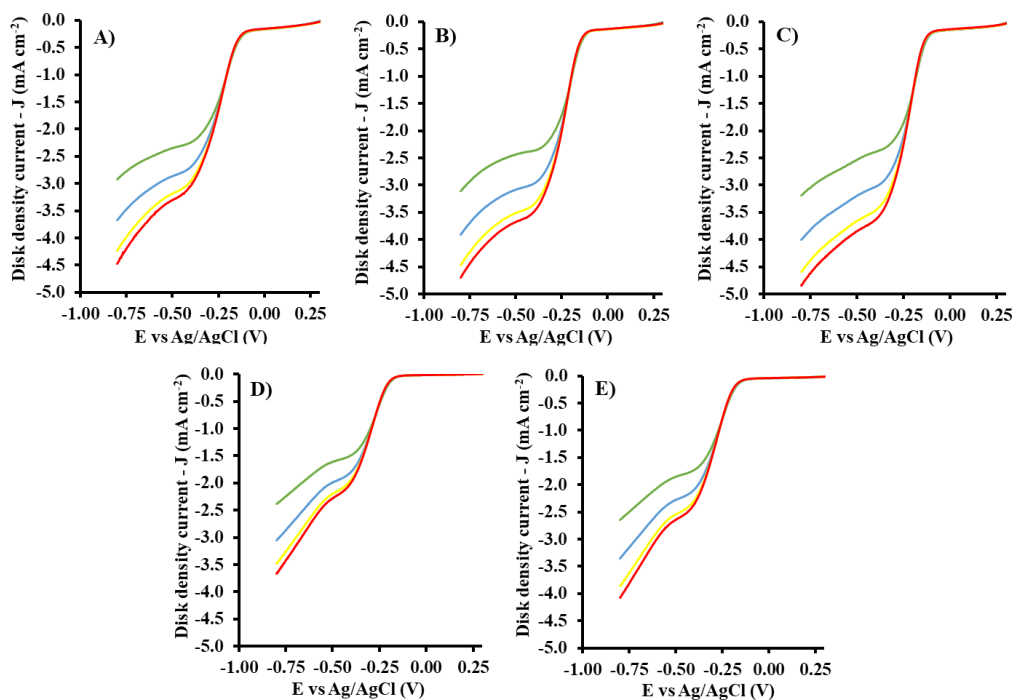


Figure 4.7. LSV of A) BC, B) DBC-B, C) DBC-N, D) DBC-P, E) DBC-S; at different RPM 1000, 2000, 3000 and 3500.

Table 4.3. XPS summary of all samples.

Sample	J_K (mA cm ⁻²)	n	E°onset (V)
BC	5.57	2.65	-0.15
DBC-B	9.56	2.76	-0.15
DBC-N	10.38	2.79	-0.14
DBC-P	8.61	2.69	-0.20
DBC-S	9.38	2.80	-0.19

Figure 4.8 illustrates the LSV curves to 3500 rpm, number of transferred electrons and selectivity to H₂O₂. These results show that the DBC-N sample had the higher current density, which is need from the point of view economic and possible industrial applications [55]. The sample BC has the higher number of transferred electrons and hence the lower selectivity toward H₂O₂ which indicates that the doped with different heteroatoms improve the ORR 2e⁻. In the literature, it was showed that the energy for 2e⁻ was lower than for 4e⁻, meanwhile that the N doping is ideal due to the oxygen energy absorption principally for the pyrrolic N which is similar to S; and the P who can act as an electron-donor resulting in a change of sp² to sp³ C bond which is considered as an active site for ORR [56-58].

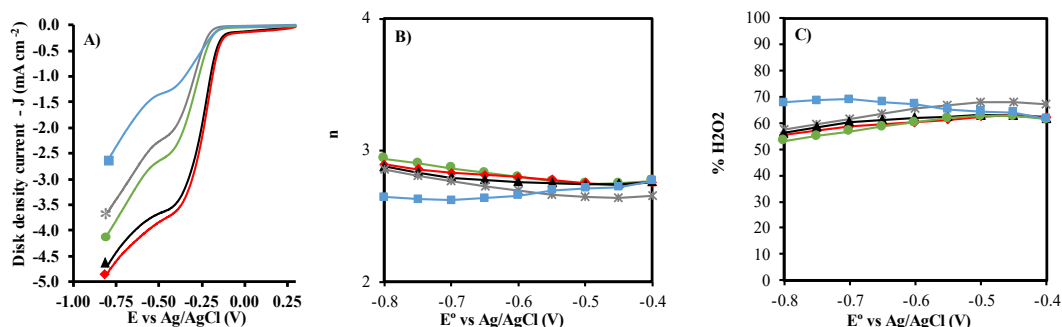


Figure 4.8. A) LSV curves to 3500 rpm, B) number of electrons transferred and C) selectivity to H₂O₂ of ■ BC, ▲ DBC-B, ◆ DBC-N, * DBC-P and ● DBC-S.

Figure 4.9 shows the Tafel plot of specific kinetic current density, which is needed to calculate the Tafel slope. That is a method to compare between samples that have faster oxygen kinetic in the electrochemical reactions and thus to choose a better ORR electrocatalyst [59,60]. In the literature it is reported that the Tafel slope values give indication regarding the rate of increase in current density with increase in overpotential. The lower the Tafel slope value, the greater the rate of increase in current density and subsequently higher is the activity, a value of 120 mV dec⁻¹ indicates that the determining step is the first electron transfer. When the value is 60 mV dec⁻¹ the first electron transfer is given by a chemical step, and with 40 mV dec⁻¹ the determining step is the second electron transfer. The values for Tafel diagram of each sample were 45.21 mV dec⁻¹, 44.33 mV dec⁻¹, 30,35 mV dec⁻¹, 23,5 mV dec⁻¹ and 26,34 mV dec⁻¹ for BC, DBC-B, DBC-N, DBC-P and DBC-S respectively. Furthermore, it is known that with lower values, the catalyst is better electrocatalytically [61]. Moreover, Tafel slope is also an indicator of the effectiveness of electrocatalytic performance.

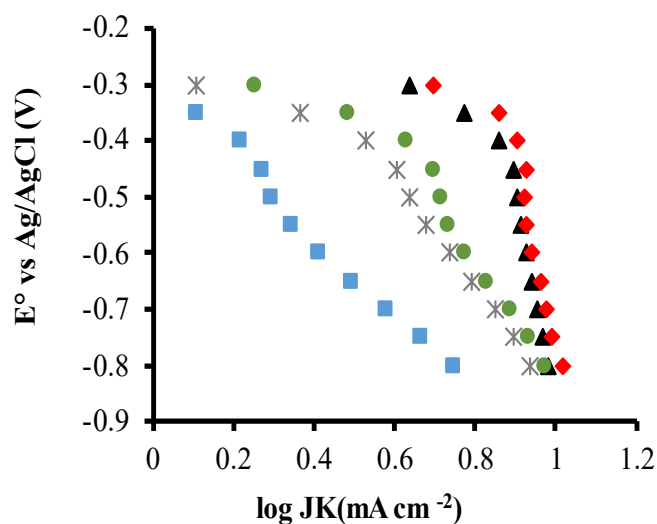


Figure 4.9. Tafel plot of specific kinetic current density for ■ BC, ▲ DBC-B, ◆ DBC-N, * DBC-P and ● DBC-S.

4.3.5.- Electro-Fenton process

All samples were selected to be evaluated for TC degradation by EF process. The bio-carbons were evaluated without a Fenton catalyst to determinate a possible degradation in one pot with a unique catalyst capable of generating H₂O₂ and activating it to •OH (figure 4.10).

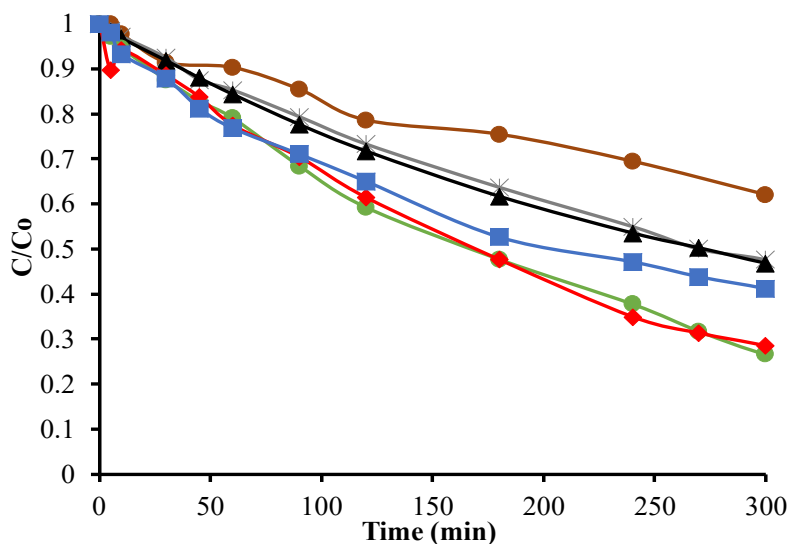


Figure 4.10. Degradation of Tetracycline by Electro-Fenton with ● Graphite (support), ■ BC, ▲ DBC-B, ◆ DBC-N, * DBC-P and ● DBC-S.

Figure 4.10 shows that the maximum TC degradation was obtained with the DBC-S and DBC-N catalyst. From the ORR and electro Fenton degradation results, it is possible to say that the best sample was DBC-N, due to the highest J_K value (Table 4.3) and the high TC degradation value, which is possibly due to the fact that N graphitic and N pyridinic are couple able to generate H_2O_2 and degrade to $\cdot OH$ [62]. Graphitic-N was suggested to be the two-electron ORR site, both graphitic-N and pyridinic-N were regarded as sites for H_2O_2 activation to $\cdot OH$. In addition, graphitic-N and N vacancies were proposed as the electroactive sites for O_2 and $\cdot O_2$ formation. On the other hand, in the literature, it has been reported through density functional theory (DFT) calculations that sulfur doping has the ability to enhance the O_2 adsorption energy, which is favorable for the oxygen reduction reaction (ORR) [63]. However, it does not significantly alter the

desorption of the OOH intermediate (crucial for the $2e^-$ ORR), indicating that it may be very effective in improving ORR activity through a two-electron pathway, similar to nitrogen doping. This is supported by the results obtained in this study, where the electrochemical properties (selectivity, J_k) and tetracycline degradation are very similar in both DBC-N and DBC-S samples.

4.4.- CONCLUSIONS

The results obtained in this report show that The XPS results confirm a correct doped of even atoms, all samples close to 5% except DBC-S which had a 2% of S approximately and consequently the effectiveness of the method used for doping process. The heteroatoms doping (B, N, P and S) gives as result an improvement in the electrochemical properties (current density J_k) and an increase of the H_2O_2 selectivity (more than 50%) for all modified samples. On the other hand, all samples showed a higher degradation activity of TC by EF, degrading close of 70% of contaminant in 300 minutes, which is possibly attributed to the generation of $\bullet OH$ way 3 electrons.

BIBLIOGRAPHY

- [1] Munoz, M.; Garcia-Muñoz, P.; Pliego, G.; De Pedro, Z.M.; Zazo, J.A.; Casas, J.A.; Rodriguez, J.J. Application of Intensified Fenton Oxidation to the Treatment of Hospital Wastewater: Kinetics, Ecotoxicity and Disinfection. *J. Environ. Chem. Eng.* 2016, 4, 4107–4112, doi:10.1016/j.jece.2016.09.019.
- [2] Zhang, Y.; Zhao, Y.G.; Maqbool, F.; Hu, Y. Removal of Antibiotics Pollutants in Wastewater by UV-Based Advanced Oxidation Processes: Influence of Water Matrix Components, Processes Optimization and Application: A Review. *J. Water Process Eng.* 2022, 45, 102496, doi:10.1016/j.jwpe.2021.102496.
- [3] Geng, J.; Zhang, H.; Zhang, Z.; Gao, J.; Wang, S.; Hu, X.; Li, J. Enhanced Electro-Fenton Oxidation by Introducing Three-Phase Interface with Simultaneous Optimization of O₂ and Pollutant Transfer for Effective Tetracycline Hydrochloride Removal. *Chem. Eng. J.* 2022, 450, doi:10.1016/j.cej.2022.137891.
- [4] Qian, M.; Zhuo, F.; Li, Y.; Yi, P.; Gao, Y.; Zhou, W.; Sun, Y.; Chen, J.; Wu, X.L. Fe-N-C Catalyst Coated on Carbon Felt for Efficient Degradation of Antibiotics via Electro-Fenton Process. *Appl. Surf. Sci.* 2023, 609, doi:10.1016/j.apsusc.2022.155310.
- [5] Gao, Y.; Wang, Q.; Ji, G.; Li, A. Degradation of Antibiotic Pollutants by Persulfate Activated with Various Carbon Materials. *Chem. Eng. J.* 2022, 429, 132387, doi:10.1016/j.cej.2021.132387.
- [6] Xie, Y.; Kong, F.; Mi, Z.; Huang, H.; Xia, C.; Ma, Z.; Li, S.; Zhang, Q.;

- Meng, Z. High-Efficiency Removal of Antibiotics by Self-Assembly Formation of Layered Double Hydroxides in Wastewater. *SSRN Electron. J.* 2022, 52, 103502, doi:10.2139/ssrn.4184120.
- [7] Liu, D.; Xu, Y.Y.; Junaid, M.; Zhu, Y.G.; Wang, J. Distribution, Transfer, Ecological and Human Health Risks of Antibiotics in Bay Ecosystems. *Environ. Int.* 2022, 158, 106949, doi:10.1016/j.envint.2021.106949.
- [8] Song, X.; Jo, C.H.; Han, L.; Zhou, M. Recent Advance in Microbial Fuel Cell Reactor Configuration and Coupling Technologies for Removal of Antibiotic Pollutants. *Curr. Opin. Electrochem.* 2022, 31, 100833, doi:10.1016/j.coelec.2021.100833.
- [9] Chi, C.; Huo, B.; Liang, Z.; Hu, C.; Sun, Q.; Zhou, S. Study on Tetracycline Degradation in Wastewater Based on Zero-Valent Nano Iron Assisted Micro-Nano Bubbles. *Alexandria Eng. J.* 2024, 86, 577–583, doi:10.1016/j.aej.2023.12.004.
- [10] Moratalla, Á.; Araújo, D.M.; Moura, G.O.M.A.; Lacasa, E.; Cañizares, P.; Rodrigo, M.A.; Sáez, C. Pressurized Electro-Fenton for the Reduction of the Environmental Impact of Antibiotics. *Sep. Purif. Technol.* 2021, 276, doi:10.1016/j.seppur.2021.119398.
- [11] Zhang, X.; Zhang, Y.; Yu, Z.; Wei, X.; Wu, W.D.; Wang, X.; Wu, Z. Facile Synthesis of Mesoporous Anatase/Rutile/Hematite Triple Heterojunctions for Superior Heterogeneous Photo-Fenton Catalysis. *Appl. Catal. B Environ.* 2020, 263, 118335, doi:10.1016/j.apcatb.2019.118335.
- [12] Li, S.; Liu, Y.; Ge, R.; Yang, S.; Zhai, Y.; Hua, T.; Ondon, B.S.; Zhou, Q.; Li, F. Microbial Electro-Fenton: A Promising System for Antibiotics Resistance Genes Degradation and Energy Generation. *Sci. Total Environ.*

- 2020, 699, 134160, doi:10.1016/j.scitotenv.2019.134160.
- [13] Liu, Z.; Wan, J.; Ma, Y.; Wang, Y. In Situ Synthesis of FeOCl @ MoS₂ on Graphite Felt as Novel Electro-Fenton Cathode for Efficient Degradation of Antibiotic Ciprofloxacin at Mild pH. *Chemosphere* 2021, 273, 129747, doi:10.1016/j.chemosphere.2021.129747.
- [14] Puga, A.; Rosales, E.; Pazos, M.; Sanromán, M.A. Prompt Removal of Antibiotic by Adsorption/Electro-Fenton Degradation Using an Iron-Doped Perlite as Heterogeneous Catalyst. *Process Saf. Environ. Prot.* 2020, 144, 100–110, doi:10.1016/j.psep.2020.07.021.
- [15] Xing, L.; Wei, J.; Liu, X.; Zhang, Y.; Xu, M.; Li, J.; Pan, G.; Li, J. Application of Energy Sustainable Utilization Strategy for Highly Efficient Electro-Fenton Treatment of Antibiotics. *J. Environ. Chem. Eng.* 2022, 10, 107059, doi:10.1016/j.jece.2021.107059.
- [16] Xin, S.; Huo, S.; Xin, Y.; Gao, M.; Wang, Y.; Liu, W.; Zhang, C.; Ma, X. Heterogeneous Photo-Electro-Fenton Degradation of Tetracycline through Nitrogen/Oxygen Self-Doped Porous Biochar Supported CuFeO₂ Multifunctional Cathode Catalyst under Visible Light. *Appl. Catal. B Environ.* 2022, 312, 121442, doi:10.1016/j.apcatb.2022.121442.
- [17] Yu, F.; Wang, Y.; Ma, H. Enhancing the Yield of H₂O₂ from Oxygen Reduction Reaction Performance by Hierarchically Porous Carbon Modified Active Carbon Fiber as an Effective Cathode Used in Electro-Fenton. *J. Electroanal. Chem.* 2019, 838, 57–65, doi:10.1016/j.jelechem.2019.02.036.
- [18] Thor, S.H.; Ho, L.N.; Ong, S.A.; Abidin, C.Z.A.; Heah, C.Y.; Ong, Y.P.; Yap, K.L. A Sustainable Photocatalytic Fuel Cell Integrated Photo-Electro-Fenton Hybrid System Using KOH Activated Carbon Felt Cathodes for

- Enhanced Amaranth Degradation and Electricity Generation. *Sep. Purif. Technol.* 2022, 292, 121041, doi:10.1016/j.seppur.2022.121041.
- [19] Cheng, S.; Liu, Y.; Shen, C.; Jiang, B.; Liu, F.; Li, A. Enhanced Flow-through Electro-Fenton Process Based on RGO Aerogel Cathode: Essential Role of Sodium Tetrapolyphosphate. *J. Environ. Chem. Eng.* 2022, 10, 108842, doi:10.1016/j.jece.2022.108842.
- [20] Liu, Z. jun; Wan, J. quan; Yan, Z. cheng; Wang, Y.; Ma, Y. wen Efficient Removal of Ciprofloxacin by Heterogeneous Electro-Fenton Using Natural Air-Cathode. *Chem. Eng. J.* 2022, 433, 133767, doi:10.1016/j.cej.2021.133767.
- [21] Zhang, J.; Wang, D.; Zhao, F.; Feng, J.; Feng, H.; Luo, J.; Tang, W. Ferrate Modified Carbon Felt as Excellent Heterogeneous Electro-Fenton Cathode for Chloramphenicol Degradation. *Water Res.* 2022, 227, 119324, doi:10.1016/j.watres.2022.119324.
- [22] Li, X.; Yang, H.; Ma, H.; Zhi, H.G.; Li, D.; Zheng, X. Carbonaceous Materials Applied for Cathode Electro-Fenton Technology on the Emerging Contaminants Degradation. *Process Saf. Environ. Prot.* 2023, 169, 186–198, doi:10.1016/j.psep.2022.11.037.
- [23] Chen, C.; Tian, M.; Han, H.; Wu, D.; Chen, Y.; Gao, Z.; Gao, S.; Jiang, K. N, P-Dual Doped Carbonaceous Catalysts Derived from Bifunctional-Salt Activation for Effective Electro-Fenton Degradation on Waterborne Organic Pollutions. *Electrochim. Acta* 2021, 389, 138732, doi:10.1016/j.electacta.2021.138732.
- [24] Han, S.; Wang, Z.; Pi, X.; Wu, C.; Wang, X.; Wang, Y.; Liu, X.; Zhao, H. Promotion of Tetracycline Degradation by Electro-Fenton: Controlling the

- Reaction Zone by N-Doped Modified Activated Carbon Cathode. *J. Clean. Prod.* 2022, 370, 133524, doi:10.1016/j.jclepro.2022.133524.
- [25] Shen, J.; Wu, Y.; Yang, Y.; Zhou, Q.; Liu, X.; Wei, T.; Yu, X.; Yu, Y.; Li, H.; Fang, T. Dyeing Sludge Carbons Activated by Alkali-Etching for Outperformed 4-Chlorophenol Degradation in Electro-Fenton Process. *J. Water Process Eng.* 2022, 49, 103103, doi:10.1016/j.jwpe.2022.103103.
- [26] Irigaray, B.; Dauber, C.; Carreras, T.; Fern, A.; Ib, E.; Vieitez, I.; Albores, S.; Adriana, G. Response Surface Methodology for the Optimization of Biophenols Recovery from “ Alperujo ” Using Supercritical Fluid Extraction . Comparison between Arbequina and Coratina Cultivars. 2022, 180, doi:10.1016/j.supflu.2021.105460.
- [27] Moreno-Maroto, J.M.; Uceda-Rodríguez, M.; Cobo-Ceacero, C.J.; de Hoces, M.C.; MartínLara, M.Á.; Cotes-Palomino, T.; López García, A.B.; Martínez-García, C. Recycling of ‘Alperujo’ (Olive Pomace) as a Key Component in the Sintering of Lightweight Aggregates. *J. Clean. Prod.* 2019, 239, doi:10.1016/j.jclepro.2019.118041.
- [28] Ladero, M.; Calvo, L. Enzymatic Production of Biodiesel from Alperujo Oil in Supercritical CO₂. *J. Supercrit. Fluids* 2021, 171, 105184, doi:10.1016/j.supflu.2021.105184.
- [29] Elmouwahidi, A.; Bailón-García, E.; Pérez-Cadenas, A.F.; Maldonado-Hódar, F.J.; Carrasco-Marín, F. Activated Carbons from KOH and H₃PO₄-Activation of Olive Residues and Its Application as Supercapacitor Electrodes. *Electrochim. Acta* 2017, 229, 219–228, doi:10.1016/j.electacta.2017.01.152.
- [30] Zhou, R.; Zheng, Y.; Jaroniec, M.; Qiao, S.Z. Determination of the Electron

- Transfer Number for the Oxygen Reduction Reaction: From Theory to Experiment. *ACS Catal.* 2016, 6, 4720–4728, doi:10.1021/acscatal.6b01581.
- [31] Jiang, K.; Back, S.; Akey, A.J.; Xia, C.; Hu, Y.; Liang, W.; Schaak, D.; Stavitski, E.; Nørskov, J.K.; Siahrostami, S.; et al. Highly Selective Oxygen Reduction to Hydrogen Peroxide on Transition Metal Single Atom Coordination. *Nat. Commun.* 2019, 10, doi:10.1038/s41467-019-11992-2.
- [32] Xu, S.; Kim, Y.; Higgins, D.; Yusuf, M.; Jaramillo, T.F.; Prinz, F.B. Building upon the Koutecky-Levich Equation for Evaluation of Next-Generation Oxygen Reduction Reaction Catalysts. *Electrochim. Acta* 2017, 255, 99–108, doi:10.1016/j.electacta.2017.09.145.
- [33] Brocato, S.; Lau, C.; Atanassov, P. Mechanistic Study of Direct Electron Transfer in Bilirubin Oxidase. *Electrochim. Acta* 2012, 61, 44–49, doi:10.1016/j.electacta.2011.11.074.
- [34] Alcañiz-Monge, J.; Pérez-Cadenas, M.; Lozano-Castelló, D. Influence of Pore Size Distribution on Water Adsorption on Silica Gels. *J. Porous Mater.* 2010, 17, 409–416, doi:10.1007/s10934-009-9317-0.
- [35] Mojoudi, N.; Mirghaffari, N.; Soleimani, M.; Shariatmadari, H.; Belver, C.; Bedia, J. Phenol Adsorption on High Microporous Activated Carbons Prepared from Oily Sludge: Equilibrium, Kinetic and Thermodynamic Studies. *Sci. Rep.* 2019, 9, 1–12, doi:10.1038/s41598-019-55794-4.
- [36] Saka, C. BET, TG-DTG, FT-IR, SEM, Iodine Number Analysis and Preparation of Activated Carbon from Acorn Shell by Chemical Activation with ZnCl₂. *J. Anal. Appl. Pyrolysis* 2012, 95, 21–24, doi:10.1016/j.jaap.2011.12.020.
- [37] Li, X.; Jiang, D.; Zhang, J.; Lin, Q.; Chen, Z.; Huang, Z. The Dispersion of

- Boron Carbide Powder in Aqueous Media. *J. Eur. Ceram. Soc.* 2013, 33, 1655–1663, doi:10.1016/j.jeurceramsoc.2013.02.001.
- [38] Kalaiyarasan, G.; Joseph, J.; Kumar, P. Phosphorus-Doped Carbon Quantum Dots as Fluorometric Probes for Iron Detection. *ACS Omega* 2020, 5, 22278–22288, doi:10.1021/acsomega.0c02627.
- [39] Wang, Z.; Wu, M.; Chen, G.; Zhang, M.; Sun, T.; Burra, K.G.; Guo, S.; Chen, Y.; Yang, S.; Li, Z.; et al. Co-Pyrolysis Characteristics of Waste Tire and Maize Stalk Using TGA, FTIR and Py-GC/MS Analysis. *Fuel* 2023, 337, 127206, doi:10.1016/j.fuel.2022.127206.
- [40] Elmouwahidi, A.; Castelo-Quibén, J.; Vivo-Vilches, J.F.; Pérez-Cadenas, A.F.; Maldonado-Hódar, F.J.; Carrasco-Marín, F. Activated Carbons from Agricultural Waste Solvothermally Doped with Sulphur as Electrodes for Supercapacitors. *Chem. Eng. J.* 2018, 334, 1835–1841, doi:10.1016/j.cej.2017.11.141.
- [41] Das, S.K.; Dickinson, C.; Brougham, F.; Marsili, E. Synthesis, Characterization and Catalytic Activity of Gold Nanoparticles Biosynthesized with *Rhizopus Oryzae* Protein Extract. *Green Chem.* 2012, doi:10.1039/c2gc16676c.
- [42] Velo-Gala, I.; López-Peñalver, J.J.; Sánchez-Polo, M.; Rivera-Utrilla, J. Surface Modifications of Activated Carbon by Gamma Irradiation. *Carbon* N. Y. 2014, 67, 236–249, doi:10.1016/j.carbon.2013.09.087.
- [43] Zhou, W.; Xie, L.; Gao, J.; Nazari, R.; Zhao, H.; Meng, X.; Sun, F.; Zhao, G.; Ma, J. Selective H₂O₂ Electrosynthesis by O-Doped and Transition-Metal-O-Doped Carbon Cathodes via O₂ Electroreduction: A Critical Review. *Chem. Eng. J.* 2021, 410, 128368, doi:10.1016/j.cej.2020.128368.

- [44] Zare, M.; Moradi, L. Preparation of Hollow Mesoporous Boron Nitride Spheres with Surface Decorated by CuO : A Bifunctional Acid-Base Catalyst for the Green Synthesis of Some Heterocyclic [3 , 3 , 3] Propellane Derivatives in Water Media. *Appl. Surf. Sci.* 2022, 582, 152454, doi:10.1016/j.apsusc.2022.152454.
- [45] Matsoso, J.B.; Sofer, Z.; Matsoso, J.B.; Jellett, C. Simultaneous Microwave-Assisted Reduction and B/N Co-Doping of Graphene Oxide for Selective Recognition of VOCs. *J. Mater. Chem. C* 2022, 10, doi:10.1039/d1tc05453h.
- [46] Elmouwahidi, A.; Bailón-garcía, E.; Pérez-cadenas, A.F.; Maldonado-hódar, F.J.; Carrasco-marín, F. Activated Carbons from KOH and H3PO4 Activation of Olive Residues and Its Application as Supercapacitor Electrodes. *Electrochim. Acta* 2017, 229, 219–228, doi:10.1016/j.electacta.2017.01.152.
- [47] Elmouwahidi, A.; Vivo-Vilches, J.F.; Pérez-Cadenas, A.F.; Maldonado-Hódar, F.J.; Carrasco-Marín, F. Free Metal Oxygen-Reduction Electro-Catalysts Obtained from Biomass Residue of the Olive Oil Industry. *Chem. Eng. J.* 2016, 306, 1109–1115, doi:10.1016/j.cej.2016.08.042.
- [48] Gooch, N.W.; Hlady, V. Two Surface Gradients of Polyethylene Glycol for a Reduction in Protein Adsorption. *Surf. Innov.* 2015, 3, 172–180, doi:10.1680/jsuin.15.00005.Two.
- [49] Cao, Y.; Si, W.; Hao, Q.; Li, Z.; Lei, W.; Xia, X.; Li, J.; Wang, F.; Liu, Y. One-Pot Fabrication of Hemin-N-C Composite with Enhanced Electrocatalysis and Application to H2O2 Sensing. *Electrochim. Acta* 2018, 261, 206–213, doi:10.1016/j.electacta.2017.12.111.
- [50] Li, Y.; Yang, J.; Huang, J.; Zhou, Y.; Xu, K.; Zhao, N.; Cheng, X. Soft

- Template-Assisted Method for Synthesis of Nitrogen and Sulfur Co-Doped Three-Dimensional Reduced Graphene Oxide as an Efficient Metal Free Catalyst for Oxygen Reduction Reaction. *Carbon* N. Y. 2017, 122, 237–246, doi:10.1016/j.carbon.2017.06.046.
- [51] Xing, Z.; Jin, R.; Chen, X.; Chen, B.; Zhou, J.; Tian, B.; Li, Y.; Fan, D. Self-Templating Construction of N, P-Co-Doped Carbon Nanosheets for Efficient Electrocatalytic Oxygen Reduction Reaction. *Chem. Eng. J.* 2021, 410, 128015, doi:10.1016/j.cej.2020.128015.
- [52] Xu, B.; Wu, F.; Chen, R.; Cao, G.; Chen, S.; Zhou, Z.; Yang, Y. Highly Mesoporous and High Surface Area Carbon: A High Capacitance Electrode Material for EDLCs with Various Electrolytes. *Electrochem. commun.* 2008, 10, 795–797, doi:10.1016/j.elecom.2008.02.033.
- [53] Bajracharya, S.; ElMekawy, A.; Srikanth, S.; Pant, D. Cathodes for Microbial Fuel Cells. *Microb. Electrochem. Fuel Cells Fundam. Appl.* 2016, 179–213, doi:10.1016/B978-1-78242-375-1.00006-X.
- [54] Qin, Z.; Zhao, J. 1 T-MoSe₂ Monolayer Supported Single Pd Atom as a Highly-Efficient Bifunctional Catalyst for ORR/OER. *J. Colloid Interface Sci.* 2022, 605, 155–162, doi:10.1016/j.jcis.2021.07.087.
- [55] Zhang, L.; Shi, Z.; Lin, Y.; Chong, F.; Qi, Y. Design Strategies for Large Current Density Hydrogen Evolution Reaction. *Front. Chem.* 2022, 10, 1–7, doi:10.3389/fchem.2022.866415.
- [56] Xia, Y.; Zhao, X.; Xia, C.; Wu, Z.; Zhu, P.; Yoon, J.; Kim, T.; Bai, X.; Gao, G.; Hu, Y.; et al. Highly Active and Selective Oxygen Reduction to H₂O₂ on Boron-Doped Carbon for High Production Rates. *Nat. Commun.* 2021, doi:10.1038/s41467-021-24329-9.

- [57] Lu, J.; Liu, X.; Chen, Q.; Zhou, J. Coupling Effect of Nitrogen-Doped Carbon Black and Carbon Nanotube in Assembly Gas Diffusion Electrode for H₂O₂ Electro-Generation and Recalcitrant Pollutant Degradation. *Sep. Purif. Technol.* 2021, 265, 118493, doi:10.1016/j.seppur.2021.118493.
- [58] Huang, J.; Wang, M.; Luo, S.; Li, Z.; Ge, Y. In Situ Preparation of Highly Graphitized N-Doped Biochar Geopolymer Composites for Efficient Catalytic Degradation of Tetracycline in Water by H₂O₂. *Environ. Res.* 2023, 219, 115166, doi:10.1016/j.envres.2022.115166.
- [59] Das, A.; Roy, D.; Kumar Das, B.; Ansari, M.I.; Chattopadhyay, K.K.; Sarkar, S. Zinc Doping Induced WS₂ Accelerating the HER and ORR Kinetics: A Theoretical and Experimental Validation. *Catal. Today* 2022, 1–11, doi:10.1016/j.cattod.2022.10.003.
- [60] Kiran, G.K.; Sreekanth, T.V.M.; Yoo, K.; Kim, J. Bifunctional Electrocatalytic Activity of Two-Dimensional Multilayered Vanadium Carbide (MXene) for ORR and OER. *Mater. Chem. Phys.* 2023, 296, 127272, doi:10.1016/j.matchemphys.2022.127272.
- [61] Elmouwahidi, A.; Bailón-García, E.; Pérez-Cadenas, A.F.; Castelo-Quibén, J.; Carrasco-Marín, F. Carbon-Vanadium Composites as Non-Precious Catalysts for Electro-Reduction of Oxygen. *Carbon N. Y.* 2019, 144, 289–300, doi:10.1016/j.carbon.2018.12.038.
- [62] Su, P.; Zhou, M.; Lu, X.; Yang, W.; Ren, G.; Cai, J. Electrochemical Catalytic Mechanism of N-Doped Graphene for Enhanced H₂O₂ Yield and in-Situ Degradation of Organic Pollutant. *Appl. Catal. B Environ.* 2019, 245, 583–595, doi:10.1016/j.apcatb.2018.12.075.
- [63] Zhu, Y.; Deng, F.; Qiu, S.; Ma, F.; Zheng, Y.; Lian, R. Enhanced Electro-

Fenton Degradation of Sulfonamides Using the N, S Co-Doped Cathode: Mechanism for H₂O₂ Formation and Pollutants Decay. *J. Hazard. Mater.* 2021, 403, 123950, doi:10.1016/j.jhazmat.2020.123950.

CHAPTER V: SIZE CONTROL OF CARBON XEROGEL SPHERES AS KEY FACTOR GOVERNING THE H₂O₂ SELECTIVITY IN METAL-FREE BIFUNCTIONAL ELECTRO-FENTON CATALYSTS FOR TETRACYCLINE DEGRADATION

Abstract

Carbon xerogel spheres co-doped with nitrogen and eco-graphene were synthesized using a typical solvothermal method. The results indicate that the incorporation of eco-graphene enhances the electrochemical properties, such as current density (J_K) and the selectivity for the four transferred electrons (n). Additionally, nitrogen doping has a significant effect on the degradation efficiency, varying with the size of the carbon xerogel spheres, which could be attributed to the type of nitrogenous group doped in the carbon material. The degradation efficiency improved in the nanometric spheres (48.3% to 61.6%) but decreased in the micrometric-scale spheres (58.6% to 53.4%). This effect was attributed to the N-functional groups present in each sample, with N-CNS-5 exhibiting a higher percentage of graphitic nitrogen (35.7%) compared to N-CMS-5 (15.3%). These findings highlight the critical role of sphere size in determining the type of N-functional groups present in the sample. Leading to enhanced degradation of pollutants as a result of the electro-Fenton process.

5.1.- INTRODUCTION

Low rainfall and high temperatures are leading to increasingly extreme drought conditions. In this context of water scarcity, wastewater reuse is essential. However, the presence of emerging pollutants in water makes its reuse difficult, as such pollutants represent an environmental and human health risk [1]. Antibiotics are being detected in the wastewater in increasing amounts due to the rapid development of urbanization, which generates a more serious problem in the form of antibiotic resistance genes [2,3]. Conventional treatment plants cannot effectively remove these pollutants, so there is an urgent need to develop effective technologies to address this problem [4,5]. The advanced oxidation processes (AOPs) have shown excellent results in the degradation of antibiotics, thanks to the generation of hydroxyl radicals (OH•). Specifically, the electro-Fenton (EF) process has been studied due to its advantages associated principally with the risks, transport and storage of peroxide hydrogen (H₂O₂), since the H₂O₂ is produced directly in the cathode of EF [6] in mild conditions and does not involve other hazardous materials [7]. The electro-generation of H₂O₂ in EF is based on the oxygen reaction reduction (ORR) via two electrons (2e⁻) pathway (equation 5.1).



However, the main problems associated with the EF are the slow regeneration of Fe(II) (equation 5.2), which is responsible of the H₂O₂ transformation into OH• (equation 5.3), and the competitive route of ORR four electrons (4e⁻) (equation 5.4) which decrease the H₂O₂ production, and therefore the overall efficiency of the process [8–10].



Carbon materials are promising candidates as electrodes for $2e^-$ ORR due to carbon's good properties such as high electrical conductivity, electrochemical stability, low cost, non-toxicity, high overpotential for H_2 evolution, and low decomposition of H_2O_2 [11,12]. Some carbon materials used in the H_2O_2 electro-generation with promising results included graphite modified with polypyrrole/multiwalled carbon nanotube (MWCNT) [13], inks based on different carbon materials (activated carbon, carbon graphite and carbon black) [14], vulcan XC-72 carbon with niobium oxide (Nb_2O_5) [15] and biochar's [16,17], among others. An alternative that is usually used to improve the H_2O_2 production is nitrogen (N) doping/functionalization. Y. Zhang et al. [18] synthesized hierarchical porous O, N co-doped porous carbon nanosheet (ONPC) for the selective reduction of O_2 to H_2O_2 , demonstrating that the pyrrolic-N and C=O motifs enhance the H_2O_2 generation. F. Wu et al. [19] also synthesized N, O co-doped graphite nanosheet corroborating that the different oxygen-containing functional groups and N species affects the H_2O_2 generation. In this case, the combination of epoxy and graphitic N was identified as the most favorable configuration with the lowest theoretical overpotential for H_2O_2 generation. In turn, X. Wang et al. [20] used density functional theory (DFT) calculations to analyze the effect of O, N co-doping of carbon nanosheets on the H_2O_2 selectivity. They demonstrated that the binding strength of $^*\text{OOH}$ was optimized by the co-doping of oxygen and nitrogen at certain content, and that the O/N-C_COOH site exhibits a lower theoretical overpotential

for H₂O₂ formation than O-C-COOH site. Thus, besides the nitrogen doping level, the nitrogen speciation is also crucial for the selective reduction of oxygen to hydrogen peroxide (ORR to H₂O₂). Various nitrogen configurations can exist in nitrogen-doped carbon materials, such as N-pyridinic, N-pyrrolic, N-graphitic, N-quaternary, and N-oxide [21]. Y. Yang et al. [22] investigated the efficiency of a nitrogen-doped carbon electrocatalyst in selectively producing H₂O₂ from O₂, suggesting that disordered carbon defects and pyrrolic-N structures are pivotal in enhancing H₂O₂ generation. S. Han et al. [23] also evidenced that the nature of the nitrogen groups is key to controlling the H₂O₂ selectivity. They showed that Pyridinic-N and graphitic-N enhanced the 2e⁻ ORR selectivity of the cathode and promoted ·OH generation at acidic pH. Y. Zhu et al. [24] synthesized N-doped carbons by pyrolysis of three N-precursors (2,6-diaminopurine, 2,4,6-tripyridin-2-yl-1,3,5-triazine and 1h-1,2,4-triazole-3,5-diamine). All N-doped carbons presented an enhanced H₂O₂ production in relation to graphite, since N doping provides active sites for oxygen reduction, improving ORR activity. However, the types and proportions of N-functional groups are different in the three materials. All samples contained a high amount of high proportion of pyrrolic N content, which favors the H₂O₂ accumulation. However, the sample prepared from 1h-1,2,4-triazole-3,5-diamine showed the highest H₂O₂ accumulation among the three nitrogen doped cathodes, which was attributed to the high electroactive surface area and pyrrolic N (60.45%) incorporation. Y. Sun et al. [25] studied a series of nitrogen-doped porous carbon materials for ORR to H₂O₂, indicating that pyridinic-N plays a crucial mechanistic role in acidic conditions, whereas graphitic-N acts as the active site in neutral and alkaline environments. J. Zhang et al. [26] identified graphitic-N as the active site for the 2e⁻ ORR to H₂O₂ on nitrogen-doped carbons.

Interestingly, these same nitrogen species have been proposed as active sites for the $4e^-$ ORR to H_2O . Consequently, the significance of nitrogen speciation in promoting ORR remains contentious and subject to debate. It is probable that a combination of carbon defects and specific nitrogen sites facilitates the $2e^-$ pathway for ORR to H_2O_2 . However, more extended observation in literature have indicated that N-pyridinic tends to enhance the four-electron oxygen reduction reaction (ORR) by facilitating electron donation, whereas N-pyrrolic aids in accelerating the two-electron ORR [27,28]. Additionally, graphitic-N has also been identified as the superior active site for the $2e^-$ ORR to H_2O_2 . Regarding oxidized N, simulated calculations from other research suggest that the free energy of oxygen adsorption in the ORR process on oxidized nitrogen is notably higher compared to that of other nitrogen species, indicating its unfavorable contribution to H_2O_2 generation [29].

Although H_2O_2 generation is improving, the EF process still necessitates the utilization of two catalysts: one tailored for oxygen reduction to H_2O_2 and another Fenton-type catalyst for converting H_2O_2 to hydroxyl radicals. In recent years, there have been numerous endeavors to create materials that possess dual functionality for electroreduction of oxygen to H_2O_2 and Fenton reactions. However, crafting heterogeneous EF catalysts with high selectivity and activity towards ORR through the two-electron pathway remains challenging. This is because transition metals, which are primarily responsible for Fenton reactions, typically catalyze oxygen reduction via the $4e^-$ pathway, which does not yield H_2O_2 . To overcome these limitations, researcher worldwide have recently started to study the use of carbonaceous materials as possible bifunctional catalysts, which are capable of directly generating OH^\bullet without the need for transition metal or Fenton-type catalysts.

As shown above, carbonaceous materials are optimal catalysts for ORR $2 e^-$. However, it has recently been shown that well-developed mesoporosity can be more beneficial for ORR, as unlike nano- or micropores, which can easily be blocked, mesopores can allow adequate transfer of reactants, products and/or electrons, which can lead to the reduction of H_2O_2 with an additional electron (equation 5.5)[30].



Tan et al. [31] demonstrated that nitrogen-doped porous carbon (NPC) can activate H_2O_2 to $OH\bullet$, which was attributed to the enhanced hydrogen peroxide adsorption on the N-graphitic sites. They [32] also showed the bifunctionality of ordered mesoporous carbon, which proved to be active for $OH\bullet$ generation from ORR; the catalytic activity was associated with the nano-confinement in the mesoporous structure and C-O-C groups. Carbonaceous materials doped with transition metals (Fe or Mn) have also been proposed as catalysts for the in situ generation of $OH\bullet$ via a three-electron ORR reaction (equation 5.6) [33,34].



In this work, free-metals bifunctional electrocatalysts based on carbon spheres doped with N functional groups were synthesized and their behavior as electrodes in the ORR $3e^-$ was analyzed with regard to the degradation of tetracycline, which was used as antibiotic reference. The effect of the carbon microsphere size on the stabilization of different N functional groups, and consequently, the electro-Fenton activity, as well as the improvement of conductivity of samples by adding ecographene, were deeply analyzed. The control of the selectivity to three- or two-

electrons pathways, which was achieved by changing the operational voltage was also evaluated.

5.2.- EXPERIMENTAL

5.2.1.- Eco-graphene (EG)

To achieve a more environmentally friendly process, the synthesis of Eco-graphene (EG) was conducted according to procedures reported in the literature [35]. The process involved hydrolyzing glucose in ammonia/CTAB solution followed by a hydrothermal process. CTAB was dissolved in a 0.5 M glucose solution with a CTAB/glucose molar ratio of 1.5/8. Ammonium hydroxide was then added to adjust pH to 11. The solution was treated in an autoclave at 270 °C for 4 h, cooled slowly, and the product was collected by filtration. After being washed with distilled water, it was dried at 70 °C under vacuum for two days.

5.2.2.- Carbon xerogel spheres (CS)

We synthesized CS using two different methods, aiming to employ an operationally simpler process (solvothermal) compared to one that offers more favorable conditions for synthesis (65 °C in atmospheric pressure).

The carbon xerogel nanospheres (CNS) were synthesized with different percentages of EG (0, 1, 3 and 5 wt.%). The synthesis was carried out following a typical solvothermal process [36]. Briefly, a solution composed of 67.2 mL of ethanol (98%), 168 mL of deionized water, and 1.5 mL of NH₄OH (28%) was prepared. Then, 1.68 g of resorcinol was dissolved and the appropriate quantity of eco-graphene for each doping percentage was dispersed. Finally, 2.35 mL of formaldehyde was added, and the mixture was sonicated for 10 min. The

homogeneous solution was transferred to a Teflon reactor in a stainless-steel autoclave and treated at 100°C for 24 hours. The obtained solid was recovered by centrifugation and immersed in acetone. The acetone was changed twice daily for three days to exchange the water within the pores, with the aim of reducing the porosity shrinkage during the subsequent drying process. Finally, the organic gel was dried using a microwave oven (800 W) under argon flow at 300 W during a 1 min cycle until it reached a constant weight and then carbonized at 850°C for 2 h with a heating rate of 1.5 °C min⁻¹ under a continuous flow of nitrogen gas (150 mL min⁻¹).

The carbon xerogels spheres with micrometric size (CMS) were obtained by an inverse microemulsion polymerization of resorcinol (R) and formaldehyde (F) within an organic medium [37]. To achieve this, a mixture composed of R, F and water (W) in the molar ratios of R/F = 0.5 and R/W = 0.067 was prepared. Then, the corresponding amount of EG required to obtain the desired wt % in the final carbon material was added and the mixture was sonicated for 10 min. The mixture was pre-gelled for 1 h at 65°C in a sealed vessel and then added dropwise to a solution of 22 mL of Span 80 (S) and 900 mL of n-heptane under stirring (650 rpm) and reflux at 65°C. The molar ratio of R/S was 4.42. This solution was maintained at 65 °C under reflux and stirring for 24 h. Subsequently, the gel was filtered and immersed in acetone. The acetone was replaced twice daily for five days to aid in the exchange of water within the pores and removal of the surfactant Span 80. Finally, the organic gels were dried and carbonized in the same conditions described above.

The samples were labeled as carbon xerogels micro or nanospheres (CMS of CNS, respectively) followed by the wt % of EG in the final carbon xerogel, e.g.,

CMS-3 means that carbon xerogel microspheres were doped with 3 wt. % of eco-graphene.

5.2.3.- N-doped Carbon xerogel spheres (N-CS)

The N doping of carbon spheres was carried out using melamine as nitrogen source. The melamine in a mass melamine/carbon of 1:1 was dissolved in ethanol (98%) and mixed with the carbon xerogel. The mixture was stirred for 2 h and then dried in infrared light. Finally, the solid was thermally treated at 650 °C for 1 h under a N₂ flow (150 mL min⁻¹) with a heating rate of 10 °C min⁻¹. The samples were labeled as N-CYS-Z, where Y is the sphere size (M: Micro or N: nano), Z is the EG wt % and N indicates the nitrogen doping (if there is no “Y”, it means that N-doping was not performed).

5.2.4.- Chemical and textural characterization

The textural properties of samples were studied by N₂ adsorption isotherms at 77K. the Brunauer-Emmelt-Teller (B.E.T) method, Dubinin-Radushkevich (DR) equation, and density functional theory (DFT) were applied to obtain the specific surface area (S_{BET}), micropore volume (W₀) and width (L₀), and the pore size distribution, respectively. The N₂ volume adsorbed at the relative pressure of 0.95 was used as the total pore volume (V_{0.95}). The mesopore volume (V_{meso}) was calculated as the difference between V_{0.95} and W₀.

Raman spectroscopy was used to analyze the graphitization degree of samples. The spectra were recorded at 24 Mw in a range from 200 to 3000 cm⁻¹ using a Micro-Raman JASCO NRS-5100 dispersive spectrophotometer equipped with a 532 nm laser.

The surface composition was determined by X-ray photoelectron spectroscopy (XPS) using a Kratos Axis Ultra-DLD spectrometer equipped with a hemispherical electron analyzer connected to a detector DLD (delay-line detector) and an Al-K α monochromator of a power of 600 W. The C_{1s} peak position at 284.6 eV was used as internal reference for binding energy correction.

The morphology of the samples was studied by scanning electron microscopy (SEM) in an AURIGA FIB-FESEM microscope and by transmission electron microscopy (TEM) in a LIBRA 120 Plus microscope. Microphotographs were analyzed by the appropriate software (ImageJ 1.54f) to obtain the spheres size distributions.

5.2.5.- Electrochemical characterization

The electrochemical characterization was performed in a Biological VMP Multichannel potentiostat using a rotating ring-disk electrode (RRDE) as working electrode, a Ag/AgCl as a reference electrode, and a Pt wire as counter electrode. The carbon spheres-based samples were deposited onto the Glassy Carbon tip of the RRDE. To achieve this, an ink composed of 5 mg of sample and 1 mL of Nafion water solution in a volumetric ratio of 1:9 (Nafion 5% solution water) was prepared, and 20 μ L of this ink was deposited on the tip and was dried by infrared radiation.

Cyclic voltammetries (CV) were conducted in N₂- or O₂-saturated 0.1 M KOH solutions in a range from 0.4 V to -0.8 V (vs. Ag/AgCl) at two scan rate (5 mVs⁻¹ and 50 mVs⁻¹) while the RRDE rotated at 1000 rpm. The linear sweep voltammetry (LSV) was carried out in O₂-saturated 0.1 M KOH solutions at different rotation rates (500, 1000, 1500, 2000, 2500, 3000, 3500, 4000 rpm) in a working window from 0.4 to -0.8 V (vs. Ag/AgCl) at a sweep rate of 5 mVs⁻¹. The LSV were fitted

to the Koutecky-Levich model to calculate the number of electrons transferred (n) and the kinetic density current (J_K). Based on the disk and platinum ring current measurements, the overall electron transfer number (n) and the $H_2O_2\%$ were calculated by means of the equations 5.7 and 5.8, respectively.

$$n = \frac{4 \cdot I_D}{I_D - \frac{I_R}{N}} \quad (5.7)$$

$$H_2O_2(\%) = 100 \cdot \frac{2 \cdot \frac{I_R}{N}}{I_D - \frac{I_R}{N}} \quad (5.8)$$

where I_R and I_D are the ring and disk currents, respectively and N is the collection efficiency of RRDE (0.245).

5.2.6.- Electro-Fenton Processes

The electro-Fenton process was carried out in a three-electrodes glass cell controlled by a Biological VMP multichannel potentiostat (BioLogic Science Instruments VMP3 0216) using Ag/AgCl as reference electrode, a Pt-wire as the counter electrode and a graphite paper on which the sample was pasted as the EF working electrode. For the preparation of the EF electrodes, a homogeneous paste was prepared by mixing finely milled carbon xerogel spheres and polytetrafluoroethylene (PTFE) binder in a mass ratio of 9:1. The paste was dried at 80 °C overnight and, finally, 50 mg of this paste was coated on graphite paper with an area of 3 cm × 1 cm.

To study the dual-functional electrocatalysts in Electro-Fenton (EF) tests, tetracycline (TTC) was chosen as the emerging pollutant. Tetracycline adsorption kinetics and isotherms were performed on the working electrode prior to the EF tests to determine the amount of time required to achieve the adsorption equilibrium

and the adsorption capacity, respectively. Once the adsorption capacity had been determined, the working electrode was put in contact with a tetracycline solution of the appropriate TTC concentration in 0.5 M Na₂SO₄ to obtain a final concentration of 3.4×10^{-5} M after reaching the adsorption equilibrium. Once the adsorption equilibrium was achieved, the TTC solution was saturated with bubbling O₂ for 30 min before the EF experiment started and continuously bubbled through the experiment. During the EF experiment, 1 mL aliquots were periodically taken from the glass cell at specified time intervals. The concentration of TTC in each aliquot was immediately analyzed at 358 nm using a UV-spectrophotometer model UV-2600i Shimadzu.

5.3.- RESULTS AND DISCUSSION

5.3.1.- Morphological characterization

SEM images of bare carbon nano and microspheres (CNS and CMS, respectively) and ecographene (EG) doped carbon spheres (CNS-3, CNS-5 and CMS-5) are collected in figure 5.1. Isolated spheres smaller than 1.6 μm were obtained via the hydrothermal method (CNS), whereas spheres of up to 24 μm were obtained via the inverse emulsion method [37] (CMS). Notably, a cleaner and more perfect surface was observed in CNS in comparison to CMS, with which a more rugous and imperfect surface was obtained. This result could be associated with the oxygen concentration in each sample. It has been reported that hydrophilicity and roughness are inversely proportional to the oxygen amount [38], which can be derived from the synthesis method, where according to the literature, the solvothermal method, due to high temperature and pressure, can incorporate oxygen

into the final material [39]. In both series, CNS and CMS, doping with EG affected the sphere size distribution, causing the size to decrease with a concurrent increase in the EG doping. The size of CNS decreased from a mean size of 1.21 μm to 510 and 440 nm with the addition of 3 and 5 wt. % of EG, respectively; the size of CMS also decreased from a mean size of 17.42 μm to 4.13 μm when 5 wt.% of EG was added. The EG could interfere in the sol-gel polymerization, creating nucleation centers which favors the creation of more spheres of smaller size instead of a sphere's growth. In any case, EG seems not to affect the shape or rugosity of the spheres.

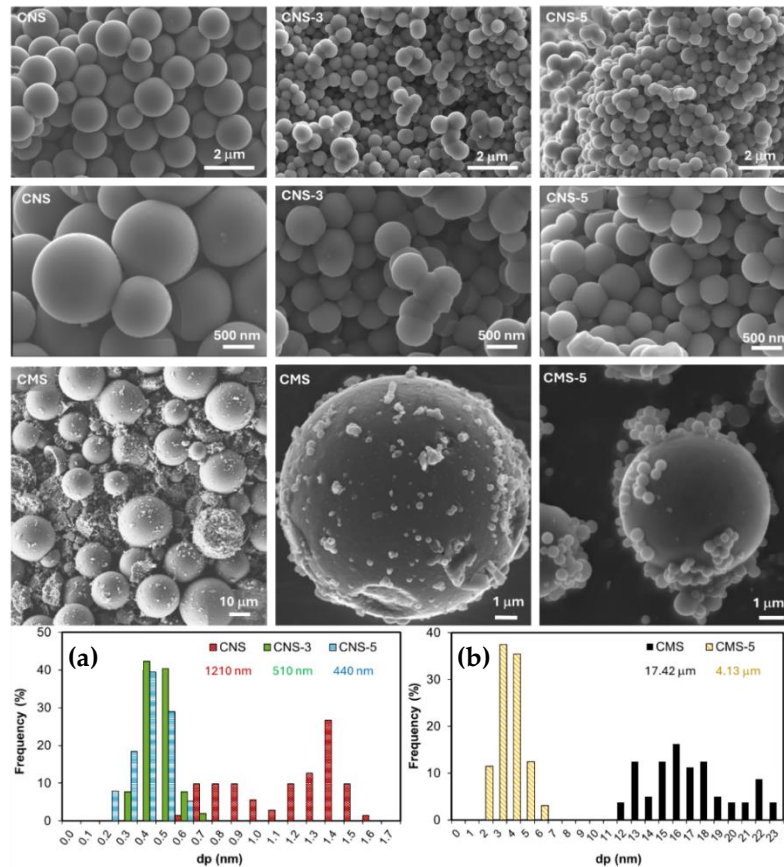


Figure 5.1. SEM images of carbon nano (CNS) and macrospheres (CMS) without ecographene and with 3 % (CNS-3) and 5 % (CNS-5 and CMS-5) of ecographene and particles size distribution of nano (a) and micro-sized spheres (b) obtained from analysis of SEM images.

TEM was used to try to observe the EG distribution in the samples. TEM images are collected in figure 5.2. The same findings can be derived from the analysis of TEM images. Once again, larger particles are evident in the non-EG

doped samples (CNS and CMS), whereas spheres that are smaller in size are observed in samples doped with eco-graphene. However, significant differences could be observed between micro and nanospheres. Nanospheres seems to be more dense and less porous, with more uniform surfaces than microspheres, on which surface rugosity and internal voids can be clearly identified. In turn, the synthesized eco-graphene (EG) comprises smooth and seemingly defect-free nanosheets. It is noteworthy that some eco-graphene sheets are uniformly distributed in close proximity around the spheres in all eco-graphene-doped samples, which could allow a better distribution of loads or electronic transfer, which would be beneficial for the ORR.

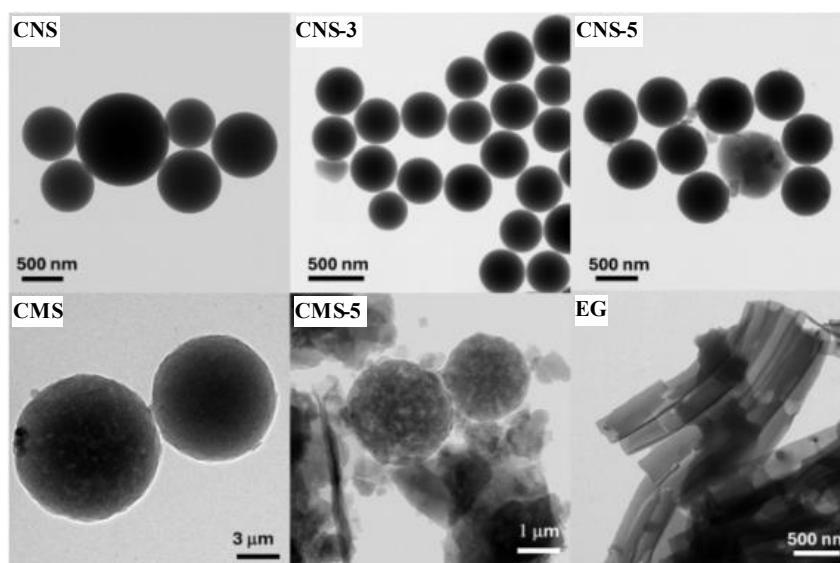


Figure 5.2. TEM images of ecographene (EG) and carbon nano (CNS) and macrospheres (CMS) without ecographene and with 3 % (CNS-3) and 5 % (CNS-5 and CMS-5) of ecographene.

5.3.2.- Textural characterization

The porous texture of samples was analyzed by N_2 and CO_2 adsorption at -196 and 0 °C, respectively. N_2 isotherms are depicted in figure 5.3 and results from the data analysis are included in table 5.1. A type I isotherms is obtained, denoting the presence of micropores in all samples. In samples doped with EG (both micro and nanospheres), there is an increase in N_2 adsorption at intermediate relative pressures, which indicates the creation of some mesoporosity in the samples by the addition of EG (V_{meso} , table 5.1). Moreover, the N-doping results in a reduction in microporosity due to the blockage of wider micropores by the fixed N-functional groups. It is important to highlight that despite both CMS and CNS presenting a similar surface area and pore volume, carbon nanospheres are mainly ultramicroporous with micropores of around 0.51 nm, whereas carbon microspheres present wider micropores of a mean size of 1.19 nm.

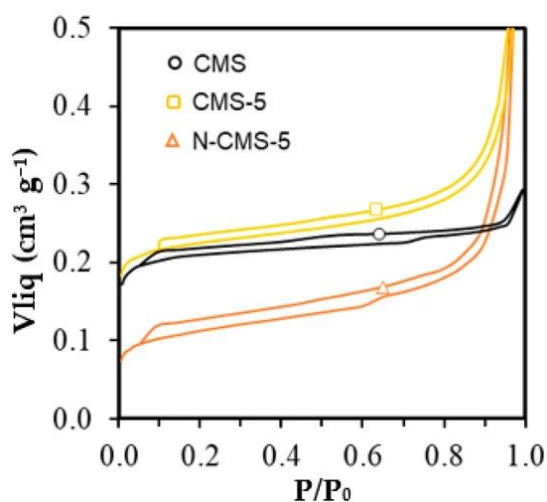


Figure 5.3. N_2 -adsorption/desorption isotherms of CMS series.

Table 5.1. textural characteristics of all samples obtained by N₂ and CO₂ adsorption and Raman intensity ratio (I_D/I_G) and D and G positions.

Sample	N ₂ -isotherm					CO ₂ -isotherm		Raman		
	S _{BET}	W ₀	L ₀	V _{0.95}	V _{meso}	W ₀	L ₀	I _D /I _G	D position	G position
	m ² g ⁻¹	cm ³ g ⁻¹	nm	cm ³ g ⁻¹	cm ³ g ⁻¹	cm ³ g ⁻¹	nm	n.a.	cm ⁻¹	cm ⁻¹
EG	1	0.00	-	0.00	0.00	-	-	0.78	1363	1563
CNS	560	0.23	0.51	0.27	0.00	-	-	1.00	1344	1588
CNS-1	-	-	-	-	-	-	-	0.98	1340	1587
CNS-3	-	-	-	-	-	-	-	0.98	1341	1587
CNS-5								0.97	1341	1585
N-CNS-5								0.98	1338	1583
CMS	501	0.20	1.19	0.23	0.03	0.26	0.56	1.05	1343	1590
CMS-5	555	0.23	0.86	0.41	0.18	0.24	0.56	1.00	1340	1587
N-CMS-5	260	0.11	1.60	0.32	0.21	0.24	0.56	1.01	1343	1590

5.3.3.- Raman characterization

The degree of graphitization of all samples was analyzed by Raman spectroscopy and the results are collected in table 5.1 and figure 5.4. Two bands at around 1345 and 1587 cm⁻¹ were identified: these are referred to as defect (D) and graphitization (G) bands, respectively. The G peak arises from the in-plane stretching motion among sp² carbon atoms, whereas the D band is attributed to structural defects, edge effects, and unpaired sp² carbon bonds, disrupting the symmetry [40]. The variation in the position, width, and intensity of the Raman bands is used to determine the structural order of the material. The intensity ratio I_D/I_G is indicative of carbon structural ordering, with a significantly lower ratio

correlating to a higher degree of graphitization. According to the Raman spectra (figure 5.4), the change in the band position of D and G peaks and the intensity ratio (I_D/I_G) in the pure eco-graphene and EG-doped carbon spheres clearly confirm the different degrees of graphitization. Note that the G peak is much intense than the D peak for EG, showing a low I_D/I_G ratio (0.78), which denotes the high graphitization degree of eco-graphene. The I_G is also significantly higher than I_D for carbon nanospheres (CNS) in contrast to CMS samples where I_D is higher than I_G , denoting a higher defects concentration in carbon microspheres regarding carbon nanospheres. The addition of EG to both carbon spheres (nano and micro) decreases the I_D/I_G ratio, thus increasing the degree of graphitization of carbon spheres to a greater extent at a higher EG concentration. The G band position also shifts to a higher wavenumber with the amorphization degree of samples [40]; thus, G band shifts from 1563 cm^{-1} in EG to 1588 and 1590 cm^{-1} in CNS and CMS, respectively. This shift is lower at higher EG contents corroborating the improvement of graphitization of samples with the EG content. It is also important to highlight that the N-doping does not highly affect the graphitization degree of samples, as has been mentioned in the literature [41,42].

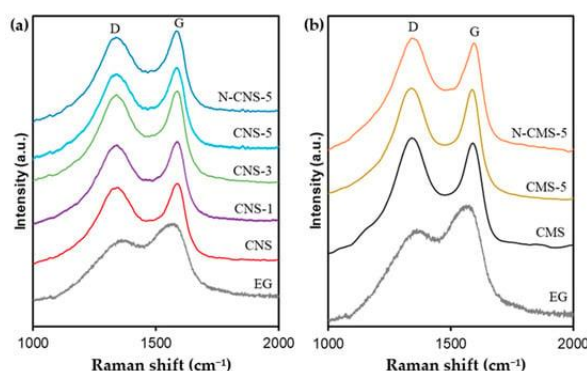


Figure 5.4. Raman spectra of a) CNS and b) CMS series.

5.3.4.- Elemental analysis and XPS

The Elemental composition of samples was analyzed by elemental analysis to identify the amount of nitrogen within the samples after the N-doping with melamine, and the results are shown in table 5.2. It is observed that the increase in eco-graphene in both nano and microspheres series increases the nitrogen content. The presence of nitrogen can be attributed to the process of synthesizing eco-graphene. During the hydrothermal process at 270 °C, CTAB molecules decompose, releasing nitrogen and hydrogen gases. These gases interact with the graphitic structure, resulting in nitrogen doping and a reduction in the oxidized structure, respectively. After treatment with melamine, an increase in the N content is observed in all samples. However, the nitrogen content depends on the size of the carbon spheres. The N content of CNS is around 3%, whereas the N fixed in CMS is almost twice that amount. Gong et al. [43] illustrated that imperfections in carbon structures, such as defects, edges, and functionalized carbon atoms, are energetically favorable for the incorporation of nitrogen atoms compared to the basal plane on the surface of carbon materials. Thus, the higher functionalization degree in carbon microspheres could be related to the greater amount of defective and porous surface accessible to the N precursor salt of carbon microspheres, which favors the melamine-surface interaction and consequently, N doping.

Table 5.2. Analysis of the elemental composition.

Sample	Elemental composition (%)			
	C	H	O	N
CNS	95.46	0.34	4.15	0.05
N-CNS	87.15	0.95	8.67	3.23
CNS-1	95.38	0.33	4.20	0.09
CNS-3	95.00	0.33	4.53	0.14
CNS-5	95.93	0.35	3.51	0.21
N-CNS-5	89.18	0.67	7.74	2.41
CMS	95.96	0.33	3.71	0.00
CMS-5	96.00	0.35	3.42	0.23
N-CMS-5	90.10	0.25	3.57	6.08

The surface chemistry of more representative samples was analyzed by XPS. Six peaks are required to fit the C_{1s} region at 284.6 eV, 285.3 eV, 286.6 eV, 288.0 eV, 289.9 eV and 291.7 eV ($\pi-\pi^*$) attributed to C=C, C-C, C-O, C=O, COO- and $\pi-\pi^*$ transition in the aromatic systems, respectively (figure 5.5). Note that the peak's positions and peak's contributions are quite similar in all samples, indicating that the carbon surface chemistry of samples was not modified after the eco-graphene and N doping. In turn, the O_{1s} region (figure 5.5) is deconvolved in three peaks assigned to quinone functional groups at 530.8 eV, C=O at 532.3 eV and C-O at 533.5 eV [40]. The presence of quinone functional groups in N- and EG-doped samples is justified by the fixation of these groups after the thermal treatment or by the presence of these functional groups in the added EG. Note that in pure EG (table 5.3), quinone functional groups represent 30.8 % of O_{1s} spectra. However, it is important to highlight that the quinone contribution is not detected in CMS samples

in which nitrogen is not detected by elemental analysis, whereas CNS presents an 8.1 % contribution and nitrogen is detected by elemental analysis and XPS, although nitrogen or eco-graphene doping is not performed. This behavior can be explained based on the different synthesis methods used in CMS and CNS samples. In CMS sample, any nitrogen containing reactant is used, whereas urea is used in the hydrothermal synthesis of carbon nanospheres (CNS) which could be decomposed and fixed in the carbon matrix under the pressurized hydrothermal method. The quinone contribution and N content increases, as expected after the nitrogen doping. Note that although the total N content analyzed by elemental analysis in N-doped CMS (6.08 wt.%) is twice that observed for N-doped CNS (2.41 wt. %), the nitrogen content in N-CMS-5 (5.1 wt. %) is lower than in N-CNS-5 (9.1 wt. %). This difference of both technics is explained based on the N-functional groups distribution and carbon spheres porosity. Both carbon micro and nanospheres are microporous materials with similar surface area. However, wide micropores with a size of 1.19 nm with the presence of some mesoporosity is observed in microspheres whereas mesoporosity is not detected in nanospheres in which ultramicropores (0.51 nm) are present. The wide micropores allow the melamine solution to be accessed at all levels of porosity and thus, N-functional groups are distributed throughout the microspheres with varying porosity, whereas this melamine aqueous solution cannot enter ultramicroporous surfaces, and thus avoids the functionalization of the internal nanospheres surface. Since the XPS is a surface technique, only a few nm of the surface is analyzed. The N_{XPS} content (5.1 wt.%) of CNS is much higher than the total N detected by EA (2.41 wt. %) because N-groups are mainly localized on the external surface. In the case of CMS, N_{XPS}

(5.1 wt. %) is similar to N_{EA} (6.1 wt.%), since the N-functional groups are distributed homogeneously.

The N-containing functional groups of samples are analyzed by deconvolution of the N_{1s} region (figure 5.5). Three peaks are detected at 398.4 eV (Pyridinic-N), 399.9 eV (Pyrrolic/Pyridonic-N) and 401.0 eV (graphitic-N). Note that the distribution of N-containing functional groups is very different depending on the carbon size (Figure 5.5 and table 5.3). In N-doped carbon microspheres (N-CMS-5), Pyridinic-N and Pyrrolic/Pyridonic-N are predominant, whereas quaternary-N only represents a 15.3 %. However, quaternary-N increases significantly in N-doped carbon nanospheres (30.6 %) at expense of a decrease in pyridinic N. Since the nitrogen doping method is the same in both carbon nano and microspheres, the size of the carbon spheres and consequently, the surface texture and defects seem to be crucial for the selective introduction of graphitic-N. The nature of the N-functional groups determines the ORR selectivity, so the different groups distribution in CMS and CNS samples determine their Electro-Fenton behavior.

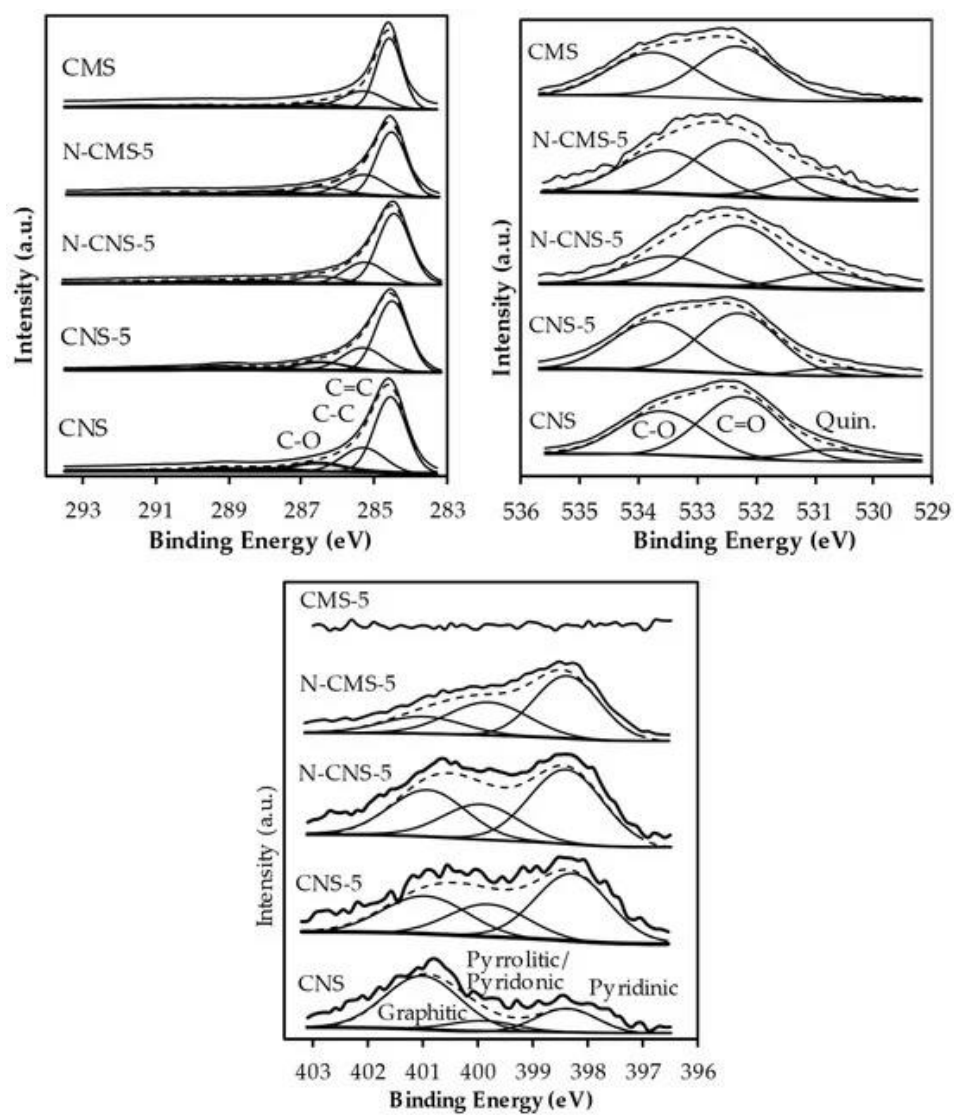


Figure 5.5. XPS patterns.

Table 5.3. Surface chemical composition determined by XPS.

Sample	C _{1s}			O _{1s}			N _{1s}			C _{XPS} (%)	O _{XPS} (%)	N _{XPS} (%)
	BE (eV)	%peak	Assign	BE (eV)	% peak	Assign.	BE (eV)	% peak	Assign.			
CMS	284.6	59.3	C=C	532.4	54.1	C=O				96.1	3.9	-
	285.3	23.1	C-C	533.8	45.9	C-O						
	286.6	8.0	C-O									
	288.1	3.3	C=O									
	289.8	4.1	COO-									
	291.4	2.2	$\pi-\pi^*$									
N-CMS-5	284.6	55.2	C=C	530.8	12.2	Quin.	398.4	56.6	Pyridinic	92.4	2.5	5.1
	285.3	23.4	C-C	532.3	50.3	C=O	399.8	28.1	Pyrrolic/Pyridonic			
	286.6	9.7	C-O	533.5	37.5	C-O	401.0	15.3	Graphitic			
	288.0	4.9	C=O									
	289.9	4.2	COO-									
	291.5	2.6	$\pi-\pi^*$									
CNS	284.6	56.6	C=C	530.7	8.1	Quin.	398.4	23.7	Pyridinic	92.3	7.1	0.6
	285.3	23.7	C-C	532.3	53.2	C=O	399.9	11.1	Pyrrolic/Pyridonic			
	286.6	9.4	C-O	533.6	38.7	C-O	401.0	65.2	Graphitic			
	288.0	4.2	C=O									
	289.3	3.9	COO-									
	290.9	2.2	$\pi-\pi^*$									
CNS-5	284.6	55.8	C=C	530.7	6.2	Quin.	398.4	47.4	Pyridinic	90.9	8.7	0.4
	285.4	23.1	C-C	532.3	50.1	C=O	399.9	22.7	Pyrrolic/Pyridonic			
	286.6	10.9	C-O	533.7	43.7	C-O	400.9	29.9	Graphitic			
	288.0	4.4	C=O									
	289.3	3.9	COO-									
	290.9	1.9	$\pi-\pi^*$									
N-CNS-5	284.6	57.8	C=C	530.8	13.8	Quin.	398.3	39.5	Pyridinic	85.6	5.2	9.1
	285.4	22.2	C-C	532.3	59.3	C=O	399.8	24.8	Pyrrolic/Pyridonic			
	286.6	8.9	C-O	533.5	26.8	C-O	401.0	35.7	Graphitic			
	288.2	5.2	C=O									
	289.8	3.4	COO-									
	291.5	2.5	$\pi-\pi^*$									
Eco-G	284.5	72.8	C=C	530.6	30.9	Quinone	398.4	47.4	Pyridinic	75.7	11.3	13.1
	285.7	20.9	C-C	532.0	69.1	C=O	399.6	47.2	Pyrrolic/Pyridonic			
	286.9	6.3	C-O				401.8	5.4	Graphitic			

5.3.5.- Electrochemical characterization

Prior to analyze the behavior of samples as electrodes for the electro-Fenton degradation of drugs in wastewater, their catalytic performance in the generation of H_2O_2 and/or $\cdot\text{OH}$ radicals need to be evaluated. To this end, the oxygen reduction reaction was analyzed using a rotating ring-disk electrode (RRDE). First, cyclic voltammograms were performed under a constant flow of nitrogen and oxygen and the results are shown in the figure 5.6. At first glance, an increase in the current intensity near -0.2 V vs Ag/AgCl is observed when the electrolyte is saturated with O_2 in comparison with N_2 , suggesting that all samples are active in the oxygen reduction reaction (ORR). The varying electrochemical responses of samples under N_2 bubbling conditions (figure 5.6, blue line) may be attributed to differences in conductivity, graphitization degree, textural properties and surface chemistry [44]. The area enclosed in the cyclic voltammograms (CVs), representing the capacitance, clearly is affected by the EG doping and the size of the spheres. EG presents a very low capacitance due to the reduced surface area on which the electrical double layer could form. Although CMS and CNS present similar textural properties (S_{BET} and $W_0(\text{N}_2)$, table 5.1) and surface chemistry (elemental composition, table 5.2), the capacitance of CMS is much higher than that of CNS. It is well-established that the optimal specific capacitance is achieved when pores fall within the range of 0.7-1 nm. Pores smaller than 0.5 nm are too narrow for effective electrolyte diffusion and the formation of double layers [45,46]. Conversely, while mesopores (2-50 nm) may not contribute as significantly as micropores to the formation of double layers, they can enhance the formation of electric double-layer capacitors (EDLC) at high charge rates by facilitating electrolyte diffusion through the carbon network to the active sites within

micropores. The pores size in CMS is around 1 nm with the presence of some mesoporosity, whereas ultramicropores of around 0.5 nm without mesoporosity are observed in CNS; This explanation elucidates the distinct capacitance behavior observed in CMS and CNS samples. According to previous studies, it is understood that microporosity can enhance the current diffusion into the pores, thereby increasing capacitance (as evidenced by a higher area of cyclic voltammetry under an oxygen atmosphere) [47]. Regardless of the size of the carbon spheres (CNS or CMS), the enclosed area increases with the increase of EG doping. The enhancement in capacitance resulting from an increase in EG content can be attributed to the enhancement of conductivity and graphitization degree in the samples. It is widely recognized that improved electrical conductivity leads to significant enhancements in energy and power densities, as well as specific capacitance [48]. However, it is important to highlight that N-doping has a different effect on nanospheres (CNS) compared to macrospheres (CMS). In both cases, the surface area decreases upon N-doping, but whereas in CMS-5 the capacitance increases with N-doping in CNS-5, the capacitance decreases. Notably, pseudofaradaic peaks are observed in N-CMS-5 but are not clearly identified in N-CNS-5. This can be ascribed to the porosity blockage and different nitrogen distribution of the functional groups. Peng Zhao et al. [49] observed that the capacitance of N-doped NCTs is improved when abundant pyrrolic-N are presented on the surface of the material. K. Tian et al. [50] also identified pyrrolic nitrogen species as highly active pseudocapacitive sites in nitrogen-doped carbon materials employed as supercapacitors. The pseudocapacitance of these carbon materials exhibits a positive correlation with the pyrrolic nitrogen content. In CMS-5, the S_{BET} decreases from 555 to 260 $\text{m}^2 \text{g}^{-1}$ upon N-doping, but a high amount of

pyrrolic/pyridonic-N is fixed (around 28 %) which compensates for the decrease in porosity and increases the capacitance. In CNS-5, the porosity is highly blocked and fewer highly active pyrrolic/pyridonic-N (24 %) active sites are obtained, which enhances the decrease in pseudocapacity as a result of the porosity blockage.

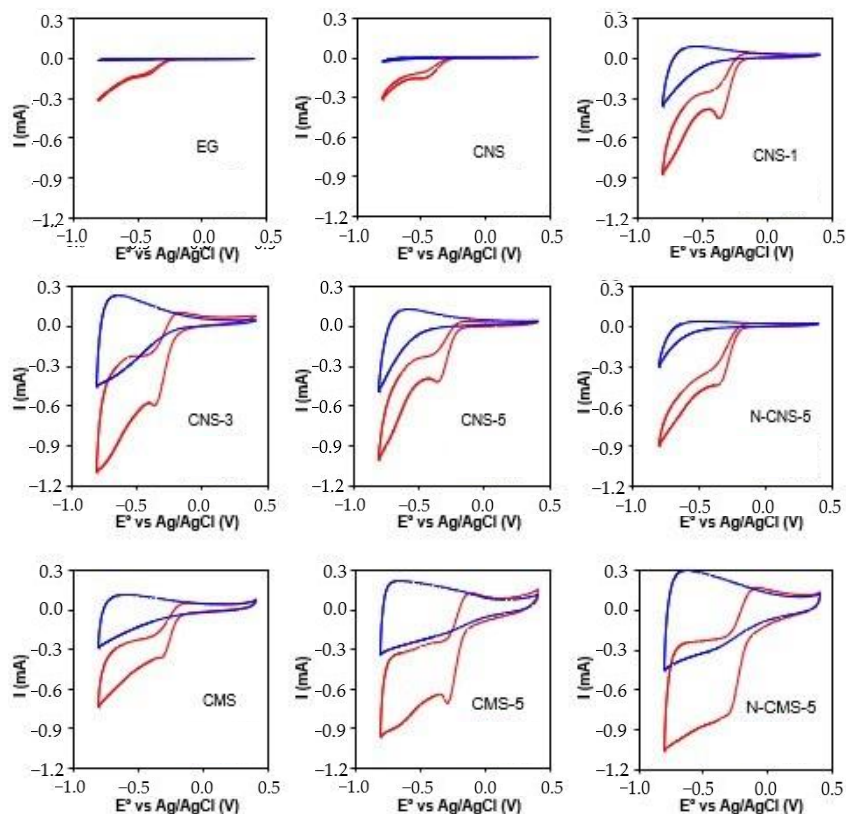


Figure 5.6. Cyclic voltammograms at 50 mV s^{-1} and 1000 rpm under N_2 flow (blue line) and O_2 flow (red line).

Linear Sweep Voltammetries (LSV) were performed at different rotation speeds to obtain information about the kinetic current density (J_K) in the ORR as

well as the reaction mechanism by determining the number of electrons transferred (n). Figure 5.7 a, b show LSV at 3500 rpm for all the tested materials. The introduction of eco-graphene, both in micro and nanospheres, enhances catalytic activity. As the percentage of eco-graphene increases, greater activity is observed (see J_K values in table 5.4). This can be attributed to the improved electron transfer to carbon microspheres that is facilitated by eco-graphene, leading to enhanced efficiency in the ORR process. However, note that the activity of carbon microspheres (CMS) is greater than that of the carbon nanospheres (CNS) which can be explained based on the intrinsic carbon xerogels defects and the exposed surface area. The intrinsic defects serve as active sites to rapidly adsorb O_2 and accelerate its transformation [51]. As was confirmed by N_2 -isotherms, the CNS porosity is composed mainly of narrower ultramicropores that are less accessible to the electrolyte and reactants than CMS porosity; thus, CNS has less active site surface for ORR than CMS. Moreover, Raman spectroscopy shows that the CNS surface presents fewer defects than the CMS surface, providing a smaller number of active sites for ORR conversion. Figure 5.7 c and d show the number of electron transfers versus the potential for all samples. An almost-pure two-electron pathway was obtained with EG of H_2O_2 being the main product ($> 90\%$). The two- e^- pathway is also the main route also for pure microspheres and nanospheres (CMS and CNS) in all potential range. However, the addition of EG does not have a significant effect on the electrons transferred at a potential lower than -0.5 , which is (n) in all cases near to 2.5-2.6 (table 5.4), similar to the findings for pure carbon spheres. Nonetheless, at a potential higher than -0.5 , the addition of EG increases the number of electrons transferred (n) mainly obtaining a $3e^-$ pathway.

In the electro-Fenton context, the conventional understanding suggests that a two-electron transfer is the typical route for generating hydrogen peroxide in-situ (equation 5.1), followed by its conversion into hydroxyl radicals by a Fenton catalyst (equation 5.3). However, previous studies have shown the viability of a three-electron pathway [52] which directly generates $\cdot\text{OH}$ radicals. Recently, Miao et al. [53] proposed a mechanism to elucidate this alternate pathway. According to their proposal, oxygen undergoes reduction to form adsorbed H_2O_2 , which then directly generates hydroxyl radicals without necessitating desorption (equation 5.6) via one-electron ORR. Thus, the three-electron pathway observed in our samples could be explained based on (i) the materials under consideration potentially possessing active sites capable of facilitating both the reaction outlined in equation 5.1 generating H_2O_2 via $2e^-$ ORR and that described in equation 5.6 at potential higher than -0.5 V obtaining $\cdot\text{OH}$ radicals via $1e^-$ ORR and/or (ii) at this potential, the ORR via 4 electron pathway becoming important and obtaining a competitive production of H_2O_2 and H_2O . L. Xie et al. [54] identified the $3e^-$ pathway in Cu/CoSe₂/C catalyst, which exhibits remarkable activity for $\cdot\text{OH}$ generation. Using DFT, they performed calculations which demonstrated that Co sites exhibit an easy H_2O_2 formation process, but a considerable energy barrier of 0.26 eV is required to form $\cdot\text{OH}$, meaning that it is favorable for H_2O_2 desorption. The transfer of n is almost constant with the voltage for all two-electron samples (EG, CMS, CNS) whereas a mechanism change is observed at -0.5 V for EG-doped samples. This could manifest that the introduction of new sites for H_2O_2 conversion to $\cdot\text{OH}$ radical is the most plausible route in EG-doped samples, rather than the competitive production of water but, potential higher than -0.5 V is required to activate this transformation.

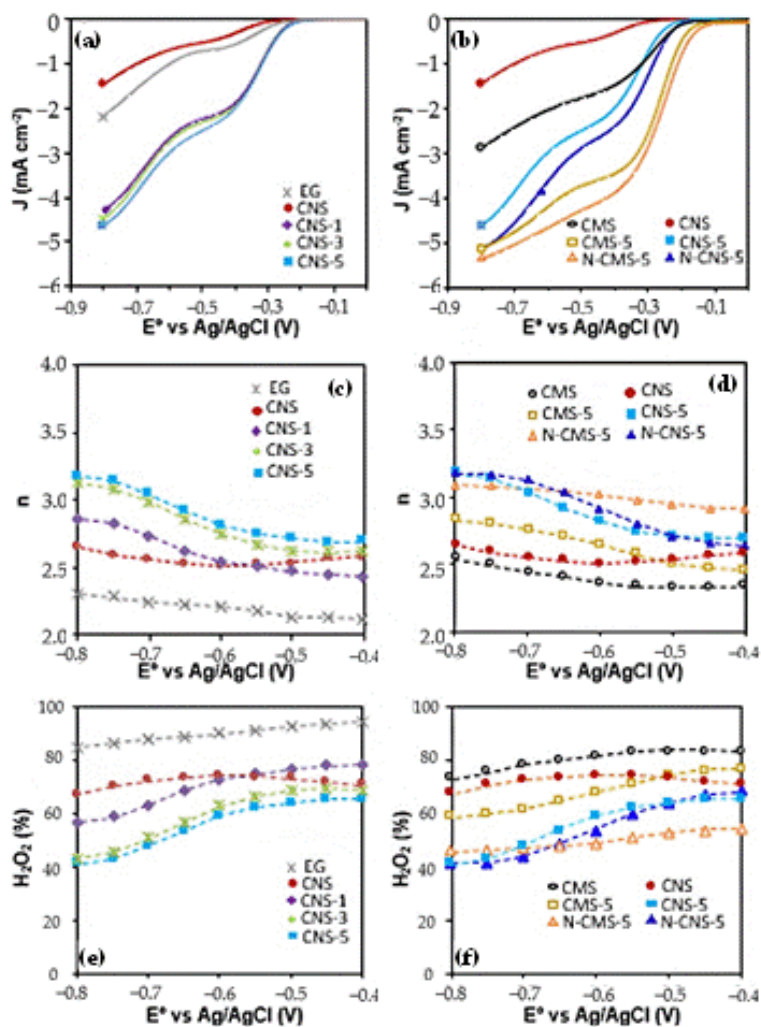


Figure 5.7. a,b) LSV at 3500 rpm, c,d) number of electrons transferred and e,f) % H_2O_2 produced; a, c and e reflects the effect of EG doping and b, d and f the effect of sphere size and N-doping.

Table 5.4. Electrochemical parameters obtained from the analysis of LSV curves.

Sample	E_{onset} (V)	$J_k \text{ mAcm}^{-2}$		n		H_2O_2 (%)	
		-0.8 V	-0.4 V	-0.8 V	-0.4 V	-0.8 V	-0.4 V
EG	-0.26	5.27	0.67	2.31	2.12	84.72	94.10
CNS	-0.28	1.90	0.28	2.65	2.58	67.36	70.76
CNS-1	-0.23	9.62	2.89	2.87	2.54	56.63	78.24
CNS-3	-0.23	10.05	2.95	3.13	2.63	43.28	68.60
CNS-5	-0.23	10.81	3.07	3.18	2.69	40.99	65.27
N-CNS-5	-0.22	14.13	3.96	3.18	2.64	41.10	68.05
CMS	-0.19	4.60	1.99	2.54	2.34	73.04	83.18
CMS-5	-0.18	14.16	8.66	2.83	2.47	58.47	76.72
N-CMS-5	-0.15	16.10	9.45	3.10	2.91	45.62	54.43

On the other hand, N-doping increases the ORR activity in both CMS and CNS series (figure 5.7b and table 5.4). It is well known that nitrogen functional groups have been proposed as active sites for the ORR, improving its catalytic performance [29,55]. It is important to highlight that although the N-content fixed on carbon microspheres is double that on carbon nanospheres, the catalytic improvement achieved in nanospheres by N-doping, N-CNS-5, is much high than in carbon microspheres, N-CMS-5, in relation to their non-N-doped counterpart (see table 5.4, J_k values). Moreover, the effect of N-doping on the ORR selectivity is very different depending on the size of the carbon sphere (figure 5.7d and table 5.4). The N doping has a different effect on the selectivity depending on the size of the carbon

spheres. The n transferred and its profile vs E° do not change after N-doping of carbon nanospheres (CNS-5 vs N-CNS-5), whereas the number of electrons increases to a value higher than three and it is univariable with the potential for N-CMS-5 sample regarding CMS-5. This different behavior is attributed to the different N functional groups distribution obtained on the carbon surface depending on the size of the sphere. XPS results revealed that pyridinic and pyrrolic/pyridonic are the main N-functional groups on carbon microspheres surface, whereas Graphitic-N are predominant in carbon nanospheres. The literature indicated that N-pyridinic tends to enhance the four-electron oxygen reduction reaction (ORR) by facilitating electron donation, whereas N-pyrrolic and graphitic-N, mainly the latter, aid in accelerating the two-electron ORR [24,27,28]. Note that the amount of $2e^-$ ORR actives sites account for 60.5 % in N-CNS-5, with 35.7 % being graphitic-N groups in comparison with the 43.4 % of $2e^-$ ORR actives sites and 15.3 % of graphitic-N of N-CMS-5. Since mainly N-pyridinic groups are introduced in carbon microspheres, the selectivity to the H_2O production is enhanced, increasing the n transferred. However, N graphitic dominates in carbon nanospheres and thus, the activity of N-doped CNS increases (see J_K) but the selectivity to the production of H_2O_2 and $\cdot OH$ radicals remains high. It is important to highlight that N-doping in CMS enhanced the four-electron pathway in all potential range, which corroborates the notion that the three-electron pathway observed in EG-doped carbon spheres seems to be ascribed to the production of H_2O_2 and its conversion to OH radicals rather than the enhancement of the four-electron pathway only occurs in a defined range of potentials.

To corroborate the above finding, the H_2O_2 generation was determined using a rotating disk electrode (figure 5.7e, f). EG, CMS and CNS, which are

predominantly $2e^-$ catalyst, produce $> 75\%$ of H_2O_2 in all potential ranges. Doping with EG favors the introduction of new sites for the direct conversion of H_2O_2 to $\cdot OH$ radicals active at potential higher than -0.5 V, and thus, the amount of H_2O_2 detected is around 70 % for a potential lower than -0.5 V and then decreases to 40 % at higher potential, although the n transferred only increases from 2.7 to 3.1 eV, corroborating the H_2O_2 transformation to $\cdot OH$ radicals.

5.3.6.- Electro-Fenton experiments

Since $\cdot OH$ radicals seem to be produced in EG-CNS and mainly N-CNS samples, the N-CNS-5 sample is presented as an excellent EF catalyst. Thus, samples doped with nitrogen and 5 % of eco-graphene with both carbon spheres sizes (CMS-5, CNS-5, N-CMS-5 and N-CMS-5) were selected to evaluate the catalytic performance in the EF degradation of tetracycline (TTC) at a potential of -0.8 V to ensure high activity and selectivity to OH radicals. To clearly identify the degree of degradation attributed to the electro-Fenton process, the adsorption process was first eliminated by saturating the working electrode with TTC at room temperature, in the dark, and setting the initial concentration at 3.4×10^{-5} M. The reaction was then initiated by applying the selected potential with constant O_2 bubbling, and TTC degradation was monitored over time. The results are shown in figure 5.8. As expected, all samples are active in the EF process, which is attributed to the capability of samples to produce $\cdot OH$ radicals through the electro-reduction of O_2 via three-electrons. It is crucial to emphasize that in a previous study, the possibility of TTC degradation solely through oxidation with H_2O_2 or via a simple oxidation-reduction process induced by the applied current was ruled out [34]. However, the EF activity of samples depends on the N-doping and the size of the carbon sphere. A degradation of 48.3 % is obtained after 240 min using CNS-5 as

an electrode. The activity of their micro-sized counterpart, CMS-5, is 58.6 % at 240 min. This higher activity is explained based on the higher ORR activity and thus, OH radicals generation. CMS sample present a more accessible porosity and more defective surface, providing a greater number of actives sites for ORR. When analyzing the effect of the N-doping, it is important to highlight that the introduction of N has a positive or negative effect depending on the size of the carbon spheres, since as it was previously pointed out, the carbon size affects the nature of functional groups anchored on the carbon spheres and, consequently, the ORR selectivity and $\cdot\text{OH}$ radicals production. In this way, while doping with N increases degradation from 48.3 % to 61.6 % in sample CNS-5, it decreases from 58.6 % to 53.4 % in sample CMS-5. As was pointed out in ORR, the number of electrons remains invariable after N-doping in CNS-5 sample, showing a high selectivity to the $3e^-$ pathway, but the activity (see J_K values) highly increases due to the selective anchoring of graphitic-N, which are active sites for H_2O_2 generation. However, for the CMS-5 sample, the activity increases due to the introduction of active sites for ORR (N-functional groups) but selectivity to $\cdot\text{OH}$ radicals generation decreases due to the enhanced anchoring of pyridinic-N, which are highly selective to H_2O production.

Considering the obtained results, the miniaturization of the carbon-spheres from micro to nanospheres via more ecofriendly synthesis routes (hydrothermal methods) is an excellent strategy to control the nature of nitrogen functional groups and, thus, enhance the $\cdot\text{OH}$ radicals generation for drug degradation. However, this synthesis method provides carbon nanospheres with a less defective surface and less accessible porosity that do not favor the ORR activity. Thus, in future works, the use of polymerization catalysts could be used to control the carbon sphere size

and the pore size distribution, as well as activation protocols to make the designed porosity more accessible and create surface defects to enhance the ORR activity and, thus, the TTC degradation.

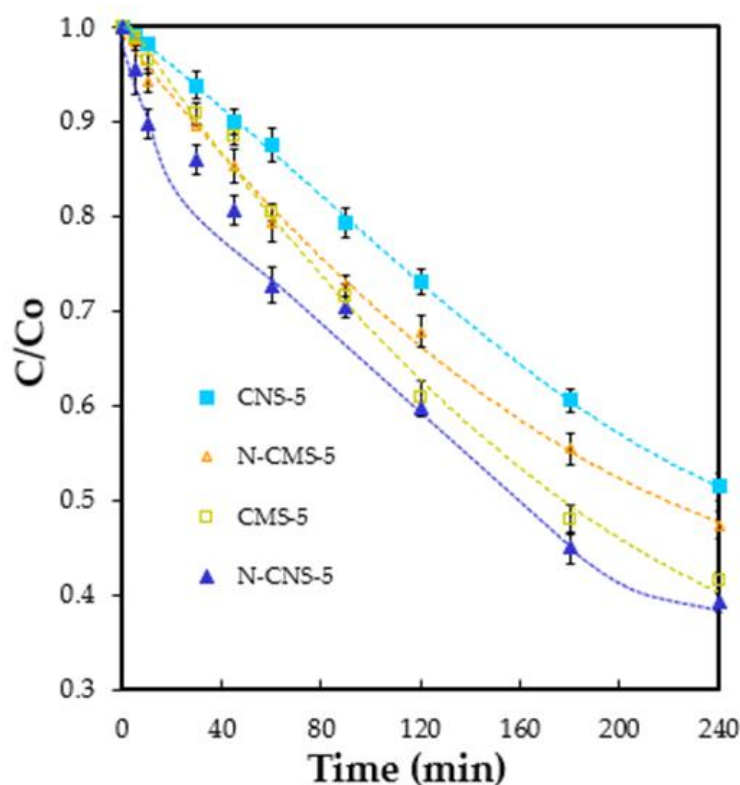


Figure 5.8. Normalized TTC concentration vs time at potential of -0.8 V for eco-graphene doped and N-eco-graphene doped microspheres and nanospheres.

In general, our results demonstrate that it is possible to obtain metal-free catalysts capable of directly generating $\cdot\text{OH}$ radicals, making them excellent candidates for new bifunctional electro-Fenton catalysts. Table 5.5 provides a summary of other bifunctional metal-free catalysts based on carbon materials.

Table 5.5. Bifunctional catalysts employed in electro Fenton degradation process, reported in literature.

Catalyst	n	Pollutant	Experiment conditions	Time (min)	%Degradation	Ref
OCNT-80 (O-doped carbon nanotubes)	2.5 to 2.6 (-0.3 to -1.0V vs SCE)	Phenol	-0.4V vs SCE, pH = 6.5	60	99.2	[51]
NGE (Nitrogen-doped Graphene)	2.1 to 2.5 (-0.6 to -1.2V vs Ag/AgCl)	Phenol	pH neutral	180	93.6	[56]
PPC (O and F doped porous carbon)	2.1 to 2.2 (-0.4 to -1.6V vs Ag/AgCl)	Sulfame-razine	-1.5V vs Ag/AgCl, pH = 3	180	90.1	[57]
ACSS (Activated carbon wrapped with stainless steel)	-----	RB19	100 mA, pH = 7	720	61.5	[12]
N,S-EEGr (Nitrogen and sulfur co-doped graphene)	2.22 to 2.27 (-1.0 to 0.0V vs SCE)	Phenol	6.25 mA cm ⁻² , pH = 7	15	100	[58]

Based on the findings presented in the literature, it is evident that the samples synthesized in this study show promise. Unlike other approaches, our synthesis methods are more environmentally friendly, as they do not involve the use of sulfuric acid. Additionally, operationally, our methods are simpler in some cases. Furthermore, our carbon xerogels exhibit a selectivity closer to three electrons in the ORR compared to those reported in other studies. While the ORR $3e^-$ route is proposed as the principal pathway for the degradation of pollutants by electro-Fenton in these studies, the selectivity values are below 2.6.

5.4.- CONCLUSIONS

Based on the findings of this study, it can be concluded that the hydrothermal method not only offers operational simplicity but also enables the synthesis of metal-free carbonaceous catalysts with bifunctional activity in electro-Fenton processes for tetracycline degradation. Furthermore, doping with EG significantly boosts the current density of the electrocatalytic reaction, while parameter n tends to increase.

The size of the carbon spheres was identified as a critical factor in the impact of nitrogen doping. For instance, in CNS-5, the degradation of TTC increased from 48.3% to 61.6%, whereas in CMS-5 it decreased from 58.6% to 53.4%. This disparity can be primarily attributed to the nitrogenous groups present in each sample, as revealed by XPS analysis. Specifically, the N-CMS-5 sample exhibited a higher concentration of pyridinic nitrogen, which favors water production, whereas the N-CNS-5 sample had a higher concentration of graphitic nitrogen, which promotes H_2O_2 generation.

BIBLIOGRAPHY

- [1] Song, Y.; Meng, C.; Lyu, Y.; Liu, Y.; Li, Y.; Jiang, Z.; Jiang, K.; Hu, C. Self-Cleaning Fouling Attachment on near-Infrared Responsive Photocatalytic Membrane for Continuous Dynamic Removing Antibiotics in Sewage Effluent Environment. *Water Res.* 2024, 248, 120867, doi:10.1016/j.watres.2023.120867.
- [2] Fang, Y.; Lin, G.; Liu, Y.; Zhang, J. Advanced Treatment of Antibiotic-Polluted Wastewater by a Consortium Composed of Bacteria and Mixed Cyanobacteria ☆. *Environ. Pollut.* 2024, 344, 123293, doi:10.1016/j.envpol.2024.123293.
- [3] Chen, A.; Wang, H.; Zhan, X.; Gong, K.; Xie, W.; Liang, W. Applications and Synergistic Degradation Mechanisms of NZVI-Modified Biochar for the Remediation of Organic Polluted Soil and Water: A Review. *Sci. Total Environ.* 2024, 911, 168548, doi:10.1016/j.scitotenv.2023.168548.
- [4] Li, S.; Gao, M.; Dong, H.; Jiang, Y.; Liang, W.; Jiang, J.; Ho, S.H.; Li, F. Deciphering the Fate of Antibiotic Resistance Genes in Norfloxacin Wastewater Treated by a Bio-Electro-Fenton System. *Bioresour. Technol.* 2022, 364, 128110, doi:10.1016/j.biortech.2022.128110.
- [5] Zhong, D.; Zhang, J.; Huang, J.; Ma, W.; Li, K.; Li, J.; Zhang, S.; Li, Z. Accelerated Electron Transfer Process via MOF-Derived FeCo/C for Enhanced Degradation of Antibiotic Contaminants towards Heterogeneous Electro-Fenton System. *Chemosphere* 2023, 335, 138994, doi:10.1016/j.chemosphere.2023.138994.
- [6] Hu, J.; Cheng, W.; Zhao, Y.; Song, Y.; Xu, H.; Zhou, H.; Yang, H.; Sun, J.;

- Chi, R. The Synergistic Effect of Oxygen Vacancies and Acidic Properties of $\text{SO}_4^{2-}/\text{Ce}_x\text{Zr}_{1-x}\text{O}_2$ on Enhancing the Electro-Fenton Performance in Antibiotics Wastewater Treatment. *Sep. Purif. Technol.* 2024, 330, 125233, doi:10.1016/j.seppur.2023.125233.
- [7] Xu, A.; Liu, W.; Yang, Z.; Cao, L.; Sirés, I.; Zhang, Q.; Zhang, Y. Waste Tire Upcycling for the Efficient Electrogeneration of H_2O_2 in Advanced Degradation of the Antibiotic Tinidazole by Electro-Fenton Process. *J. Clean. Prod.* 2023, 430, doi:10.1016/j.jclepro.2023.139661.
- [8] Lu, W.; Chen, N.; Feng, C.; Deng, Y.; Feng, Z.; Hu, Y.; Liu, T.; Hu, W. A Bifunctional Graphene-Based Cathode for Wastewater Treatment in Heterogeneous Electro-Fenton: Taking Textile, Old Landfill Leachate and Simulated Antibiotic Wastewater as Examples. *Chem. Eng. J.* 2023, 468, 143780, doi:10.1016/j.cej.2023.143780.
- [9] Lai, S.; Zhao, H.; Qu, Z.; Tang, Z.; Yang, X.; Jiang, P. Promotion of Formaldehyde Degradation by Electro-Fenton : Controlling the Distribution of $\cdot\text{OH}$ and Formaldehyde near Cathode to Increase the Reaction Probability. *Chemosphere* 2022, 307, 135776, doi:10.1016/j.chemosphere.2022.135776.
- [10] Li, Y.; Yao, B.; Chen, Y.; Zhou, Y.; Duan, X. Metal-Organic Frameworks (MOFs) as Efficient Catalysts for Electro-Fenton (EF) Reactions: Current Progress and Prospects. *Chem. Eng. J.* 2023, 463, 142287, doi:10.1016/j.cej.2023.142287.
- [11] Robles, I.; Martínez, R.J.; Banda-alem, J.A.; Salazar-l, M.L.; Manríquez, J.; García-espinoza, D.; Godínez, L.A. Surface Oxidation Pre-Treatment on Activated Carbon : Effect on Its Cathode Performance in Electro-Fenton

- Processes. 2023, 34, doi:10.1016/j.mtcomm.2022.105290.
- [12] Zhou, W.; Rajic, L.; Chen, L.; Kou, K.; Ding, Y.; Meng, X.; Wang, Y.; Mulaw, B.; Gao, J.; Qin, Y.; et al. Activated Carbon as Effective Cathode Material in Iron-Free Electro-Fenton Process: Integrated H₂O₂ Electrogeneration, Activation, and Pollutants Adsorption. *Electrochim. Acta* 2019, 296, 317–326, doi:10.1016/j.electacta.2018.11.052.
- [13] Babaei-sati, R.; Parsa, J.B. Electrogeneration of H₂O₂ Using Graphite Cathode Modified with Electrochemically Synthesized Polypyrrole / MWCNT Nanocomposite for Electro-Fenton Process. *J. Ind. Eng. Chem.* 2017, 52, 270–276, doi:10.1016/j.jiec.2017.03.056.
- [14] Rivera-vera, C.; Rodrigo-rodrigo, M.A.; Saez, C.; Thiam, A.; Salazar-gonz, R. Electrogeneration of H₂O₂ through Carbon-Based Ink on Al Foam for Electro-Fenton Treatment of Micropollutants in Water. 2024, 348, doi:10.1016/j.chemosphere.2023.140764.
- [15] Trench, A.B.; Moura, J.P.C.; Antonin, V.S.; Gentil, T.C.; Lanza, M.R.V.; Santos, M.C. Using a Novel Gas Diffusion Electrode Based on Vulcan XC-72 Carbon Modified with Nb₂O₅ Nanorods for Enhancing H₂O₂ Electrogeneration. *J. Electroanal. Chem.* 2023, 946, doi:10.1016/j.jelechem.2023.117732.
- [16] Hu, X.; Wang, J.; Jin, T.; Li, Z.; Tsang, Y.F.; Liu, B. Efficient H₂O₂ Generation and Bisphenol A Degradation in Electro-Fenton of O-Doped Porous Biochar Cathode Derived from Spirit-Based Distiller's Grains. *Process Saf. Environ. Prot.* 2022, 166, 99–107, doi:10.1016/j.psep.2022.08.017.
- [17] Wang, W.; Li, W.; Li, H.; Xu, C.; Zhao, G.; Ren, Y. Kapok Fiber Derived

- Biochar as an Efficient Electro-Catalyst for H₂O₂ in-Situ Generation in an Electro-Fenton System for Sulfamethoxazole Degradation. *J. Water Process Eng.* 2022, 50, 103311, doi:10.1016/j.jwpe.2022.103311.
- [18] Zhang, Y.; Zhan, L.; Hu, L.; Fan, G. Oxygen-Assisted One-Step Fabrication and Concomitant Regulation of Hierarchical Carbon Nanosheet Assemblies with Conjugated Binding Configurations for Promoted H₂O₂ Electrosynthesis. *Fuel* 2023, 354, doi:10.1016/j.fuel.2023.129300.
- [19] Wu, F.; Nan, J.; Wang, T.; Ge, Z.; Liu, B.; Chen, M.; Ye, X. Highly Selective Electrosynthesis of H₂O₂ by N, O Co-Doped Graphite Nanosheets for Efficient Electro-Fenton Degradation of p-Nitrophenol. *J. Hazard. Mater.* 2023, 446, 130733, doi:10.1016/j.jhazmat.2023.130733.
- [20] Wang, X.; Liu, Y.; Liu, Z.; Li, Z.; Zhang, T.; Cheng, Y.; Lei, L.; Yang, B.; Hou, Y. Highly Efficient Electrosynthesis of H₂O₂ in Acidic Electrolyte on Metal-Free Heteroatoms Co-Doped Carbon Nanosheets and Simultaneously Promoting Fenton Process. *Chinese Chem. Lett.* 2023, 108926, doi:10.1016/j.ccllet.2023.108926.
- [21] Wang, Y.; Waterhouse, G.I.N.; Shang, L.; Zhang, T. Electrocatalytic Oxygen Reduction to Hydrogen Peroxide: From Homogeneous to Heterogeneous Electrocatalysis. *Adv. Energy Mater.* 2021, 11, 1–27, doi:10.1002/aenm.202003323.
- [22] Yang, Y.; He, F.; Shen, Y.; Chen, X.; Mei, H.; Liu, S.; Zhang, Y. A Biomass Derived N/C-Catalyst for the Electrochemical Production of Hydrogen Peroxide. *Chem. Commun.* 2017, doi:10.1039/C7CC04819J.
- [23] Han, S.; Wang, Z.; Pi, X.; Wu, C.; Wang, X.; Wang, Y.; Liu, X.; Zhao, H. Promotion of Tetracycline Degradation by Electro-Fenton: Controlling the

- Reaction Zone by N-Doped Modified Activated Carbon Cathode. *J. Clean. Prod.* 2022, 370, 133524, doi:10.1016/j.jclepro.2022.133524.
- [24] Zhu, Y.; Qiu, S.; Deng, F.; Ma, F.; Zheng, Y. Degradation of Sulfathiazole by Electro-Fenton Using a Nitrogen-Doped Cathode and a BDD Anode: Insight into the H₂O₂ Generation and Radical Oxidation. *Sci. Total Environ.* 2020, 722, 137853, doi:10.1016/j.scitotenv.2020.137853.
- [25] Sun, Y.; Li, S.; Jovanov, Z.P.; Bernsmeier, D.; Wang, H.; Paul, B.; Wang, X.; Kühn, S.; Strasser, P. Structure, Activity, and Faradaic Efficiency of Nitrogen-Doped Porous Carbon Catalysts for Direct Electrochemical Hydrogen Peroxide Production. *ChemSusChem* 2018, 11, 3388–3395, doi:10.1002/cssc.201801583.
- [26] Zhang, J.; Zhang, G.; Jin, S.; Zhou, Y.; Ji, Q.; Lan, H. Graphitic N in Nitrogen-Doped Carbon Promotes Hydrogen Peroxide Synthesis from Electrocatalytic Oxygen Reduction. *Carbon N. Y.* 2020, 163, 154–161, doi:10.1016/j.carbon.2020.02.084.
- [27] Tian, M.; Zhu, Y.; Zhang, D.; Wang, M.; Chen, Y.; Yang, Y.; Gao, S. Pyrrolic-Nitrogen-Rich Biomass-Derived Catalyst for Sustainable Degradation of Organic Pollutant via a Self-Powered Electro-Fenton Process. *Nano Energy* 2019, 64, 103940, doi:10.1016/j.nanoen.2019.103940.
- [28] Chen, J.; Wang, X.; Cui, X.; Yang, G.; Zheng, W. Amorphous Carbon Enriched with Pyridinic Nitrogen as an Efficient Metal-Free Electrocatalyst for Oxygen Reduction Reaction. 2014, 557–559, doi:10.1039/c3cc47519k.
- [29] Quílez-Bermejo, J.; Melle-Franco, M.; San-Fabián, E.; Morallón, E.; Cazorla-Amorós, D. Towards Understanding the Active Sites for the ORR

- in N-Doped Carbon Materials through Fine-Tuning of Nitrogen Functionalities: An Experimental and Computational Approach. *J. Mater. Chem. A* 2019, 7, 24239–24250, doi:10.1039/c9ta07932g.
- [30] Zhe-lun, P.; Xu-fang, Q. Porous Carbons for Use in Electro-Fenton and Fenton-like Reactions. *NEW CARBON Mater.* 2022, 37, 180–195, doi:10.1016/S1872-5805(22)60578-X.
- [31] Tan, Z.; Qin, X.; Cao, P.; Chen, S.; Yu, H.; Su, Y.; Quan, X. Enhanced Electrochemical-Activation of H₂O₂ to Produce •OH by Regulating the Adsorption of H₂O₂ on Nitrogen-Doped Porous Carbon for Organic Pollutants Removal. *J. Hazard. Mater.* 2023, 458, 131925, doi:10.1016/j.jhazmat.2023.131925.
- [32] Tan, L.; Liu, Y.; Zhu, G.; Fan, X.; Quan, X. Metal-Free Electro-Fenton Degradation of Perfluorooctanoic Acid with Efficient Ordered Mesoporous Carbon Catalyst. *Sci. Total Environ.* 2023, 875, 162725, doi:10.1016/j.scitotenv.2023.162725.
- [33] Yang, Q.; Chu, L.; Wu, T.; Zhou, Y.; Liu, C.; Cang, L. Investigation of Dual-Functional Carbon Cathode Catalysts from Agricultural Wastes in the Heterogeneous Electro-Fenton Process. *Appl. Catal. B Environ.* 2023, 337, 123018, doi:10.1016/j.apcatb.2023.123018.
- [34] Barranco Lopez, A.; Morales-Rodríguez, A.I.; Fajardo-Puerto, E.; Elmouwahidi, A.; Bailón-García, E. Highly Graphitic Fe-Doped Carbon Xerogels as Dual-Functional Electro-Fenton Catalysts for the Degradation of Tetracycline in Wastewater. *Environ. Res.* 2023, 228, doi:10.1016/j.envres.2023.115757.
- [35] Mohamed, M.A.A.; Elessawy, N.A.; Carrasco-Marín, F.; Hamad, H.A.F. A

- Novel One-Pot Facile Economic Approach for the Mass Synthesis of Exfoliated Multilayered Nitrogen-Doped Graphene-like Nanosheets: New Insights into the Mechanistic Study. *Phys. Chem. Chem. Phys.* 2019, 21, 13611–13622, doi:10.1039/c9cp01418g.
- [36] Moreno-castilla, C.; García-rosero, H.; Carrasco-marín, F. Synthesis and Characterization of Solid Polymer and Carbon Spheres Derived from an Emulsion Polymerization Reaction of Different Phenolic Compounds with Formaldehyde. *Colloids Surfaces A Physicochem. Eng. Asp.* 2017, 520, 488–496, doi:10.1016/j.colsurfa.2017.02.021.
- [37] Ramírez-Valencia, L.D.; Bailón-García, E.; Moral-Rodríguez, A.I.; Carrasco-Marín, F.; Pérez-Cadenas, A.F. Carbon Gels–Green Graphene Composites as Metal-Free Bifunctional Electro-Fenton Catalysts. *Gels* 2023, 9, doi:10.3390/gels9080665.
- [38] Alegre, C.; Sebastián, D.; Lázaro, M.J. Carbon Xerogels Electrochemical Oxidation and Correlation with Their Physico-Chemical Properties. *Carbon N. Y.* 2019, 144, 382–394, doi:10.1016/j.carbon.2018.12.065.
- [39] Zhao, M.; Ma, X.; Yan, S.; Xiao, H.; Li, Y.; Hu, T.; Zheng, Z.; Jia, J.; Wu, H. Solvothermal Synthesis of Oxygen-Incorporated MoS_{2-x} Nanosheets with Abundant Undercoordinated Mo for Efficient Hydrogen Evolution. *Int. J. Hydrogen Energy* 2020, 45, 19133–19143, doi:10.1016/j.ijhydene.2020.05.003.
- [40] Dibale, A.A.; Su, W.-N.; Tamirat, A.G.; Pan, C.-J.; Aragaw, B.A.; Chen, H.-M.; Chen, C.H.; Hwang, B.-J. The Synergetic Effect of Graphene on Cu₂O Nanowire Arrays as a Highly Efficient Hydrogen Evolution Photocathode in Water Splitting. *Mater. Chem. A* 2014, 18383–18397,

- doi:10.1039/C4TA03464C.
- [41] Wassner, M.; Eckardt, M.; Reyer, A.; Diemant, T.; Elsaesser, M.S.; Behm, R.J.; Hüsing, N. Synthesis of Amorphous and Graphitized Porous Nitrogen-Doped Carbon Spheres as Oxygen Reduction Reaction Catalysts. 2020, 1–15, doi:10.3762/bjnano.11.1.
- [42] Hunter, R.D.; Hayward, E.C.; Smales, G.J.; Kulak, A.; De, S.G.; Schnepf, Z. The Effect of Nitrogen on the Synthesis of Porous Carbons by Iron-Catalyzed Graphitization. *Mater. Adv.* 2023, 2070–2077, doi:10.1039/d3ma00039g.
- [43] Gong, Y.; Shi, G.; Zhang, Z.; Zhou, W.; Jung, J.; Gao, W.; Ma, L.; Yang, Y.; Yang, S.; You, G.; et al. Direct Chemical Conversion of Graphene to Boron- and Nitrogen- and Carbon-Containing Atomic Layers. *Nat. Commun.* 2014, doi:10.1038/ncomms4193.
- [44] Elmouwahidi, A.; Bailón-García, E.; Pérez-Cadenas, A.F.; Castelo-Quibén, J.; Carrasco-Marín, F. Carbon-Vanadium Composites as Non-Precious Catalysts for Electro-Reduction of Oxygen. *Carbon N. Y.* 2019, 144, 289–300, doi:10.1016/j.carbon.2018.12.038.
- [45] Rufford, T.E.; Hulicova-jurcakova, D.; Zhu, Z.; Lu, G.Q. Empirical Analysis of the Contributions of Mesopores and Micropores to the Double-Layer Capacitance of Carbons. *J. Phys. Chem.* 2009, 19335–19343.
- [46] Vallerot, J.; Bourrat, X.; Mouchon, A.; Chollon, G. Quantitative Structural and Textural Assessment of Laminar Pyrocarbons through Raman Spectroscopy, Electron Diffraction and Few Other Techniques. *Carbon N. Y.* 2006, 44, 1833–1844, doi:10.1016/j.carbon.2005.12.029.
- [47] Elmouwahidi, A.; Bailón-garcía, E.; Pérez-cadenas, A.F.; Maldonado-hódar,

- F.J.; Carrasco-marín, F. Activated Carbons from KOH and H₃PO₄ Activation of Olive Residues and Its Application as Supercapacitor Electrodes. *Electrochim. Acta* 2017, 229, 219–228, doi:10.1016/j.electacta.2017.01.152.
- [48] Canal-rodríguez, M.; Arenillas, A.; Men, J.A.; Ramos-fern, G.; Rodríguez-pastor, I.; Martín-gullon, I. Determinant in Fluence of the Electrical Conductivity versus Surface Area on the Performance of Graphene Oxide-Doped Carbon Xerogel Supercapacitors. *Carbon N. Y.* 2018, 126, 456–463, doi:10.1016/j.carbon.2017.10.025.
- [49] Zhao, P.; Shen, B.; Yang, M.; Chen, L.; Shi, G.; Lu, F. Effect of Nitrogen Species on Electrochemical Properties of N-Doped Carbon Nanotubes Derived from Co-Pyrolysis of Low-Density Polyethylene and Melamine. *J. Energy Storage* 2023, 67, 107569, doi:10.1016/j.est.2023.107569.
- [50] Tian, K.; Wang, J.; Cao, L.; Yang, W.; Guo, W.; Liu, S.; Li, W.; Wang, F.; Li, X.; Xu, Z.; et al. Single-Site Pyrrolic-Nitrogen-Doped Sp²-Hybridized Carbon Materials and Their Pseudocapacitance. *Nat. Commun.* 2–11, doi:10.1038/s41467-020-17727-y.
- [51] Qin, X.; Zhao, K.; Quan, X.; Cao, P.; Chen, S.; Yu, H. Highly Efficient Metal-Free Electro-Fenton Degradation of Organic Contaminants on a Bifunctional Catalyst. *J. Hazard. Mater.* 2021, 416, 125859, doi:10.1016/j.jhazmat.2021.125859.
- [52] Noël, J.; Latus, A.; Lagrost, C.; Volanschi, E.; Hapiot, P. Evidence for OH Radical Production during Electrocatalysis of Oxygen Reduction on Pt Surfaces: Consequences and Application. *Am. Chem. Soc.* 2012, 2835–2841, doi:doi.org/10.1021/ja211663t.

- [53] Miao, F.; Gao, M.; Yu, X.; Xiao, P.; Wang, M.; Wang, Y.; Wang, S.; Wang, X. TiO₂ Electrocatalysis via Three-Electron Oxygen Reduction for Highly Efficient Generation of Hydroxyl Radicals. *Electrochem. commun.* 2020, 113, 106687, doi:10.1016/j.elecom.2020.106687.
- [54] Xie, L.; Wang, P.; Zheng, W.; Zhan, S.; Xia, Y.; Liu, Y.; Yang, W.; Li, Y. The Strong Metal–Support Interactions Induced Electrocatalytic Three-Electron Oxygen Reduction to Hydroxyl Radicals for Water Treatment. *Environ. Sci.* 2023, 120, 1–8, doi:doi.org/10.1073/pnas.230798912.
- [55] Skorupska, M.; Ilnicka, A.; Lukaszewicz, J.P. The Effect of Nitrogen Species on the Catalytic Properties of N-Doped Graphene. *Sci. Rep.* 2021, 11, 1–11, doi:10.1038/s41598-021-03403-8.
- [56] Su, P.; Zhou, M.; Song, G.; Du, X.; Lu, X. Efficient H₂O₂ Generation and Spontaneous OH Conversion for In-Situ Phenol Degradation on Nitrogen-Doped Graphene: Pyrolysis Temperature Regulation and Catalyst Regeneration Mechanism. *J. Hazard. Mater.* 2020, 397, 122681, doi:10.1016/j.jhazmat.2020.122681.
- [57] Li, Y.; Cao, W.X.; Zuo, X.J. O- and F-Doped Porous Carbon Bifunctional Catalyst Derived from Polyvinylidene Fluoride for Sulfamerazine Removal in the Metal-Free Electro-Fenton Process. *Environ. Res.* 2022, 212, 113508, doi:10.1016/j.envres.2022.113508.
- [58] Yang, W.; Zhou, M.; Mai, L.; Ou, H.; Oturan, N.; Oturan, M.A.; Zeng, E.Y. Generation of Hydroxyl Radicals by Metal-Free Bifunctional Electrocatalysts for Enhanced Organics Removal. *Sci. Total Environ.* 2021, 791, 148107, doi:10.1016/j.scitotenv.2021.148107.

CHAPTER VI: MANGANESE DOPED CARBON SPHERES AS AN EFFICIENT CATALYST FOR OXYGEN REDUCTION REACTION



Abstract

Carbon spheres were synthesized using the inverse emulsion sol-gel method and impregnated with varying proportions of manganese oxide, utilizing $KMnO_4$ as a precursor. Three different manganese loadings were incorporated, approximately 10%, 20%, and 30%. The resulting materials underwent comprehensive characterization using various techniques, including N_2 and CO_2 adsorption/desorption isotherms, X-ray photoelectron spectroscopy (XPS), and scanning electron microscopy (SEM). The catalytic activity of the materials was assessed through electrochemical analyses, specifically Cyclic Voltammetry (CV) and Linear Sweep Voltammetry (LSV). The results showed that an optimal manganese percentage provided superior performance in the Oxygen Electroreduction Reaction. A lower manganese content demonstrated increased selectivity towards H_2O_2 production. In contrast, the material with 30% manganese loading showed improved performance in the ORR pathway, transferring four electrons with low selectivity towards H_2O_2 .

6.1.- INTRODUCTION

The development of industries and population growth has increased the demand for energy, creating a global problem that requires new renewable and environmentally friendly energy sources [1]. As a result, fuel cells have gained attention [2,3], due to their ability to convert chemical energy into electrical energy through fuel oxidation [4] in the anode. Several fuels have been proposed for use in fuel cells, including methanol (CH₃OH), dimethyl ether (CH₃OCH₃), sodium borohydride (NaBH₄), hydrazine (N₂H₄), formic acid (HCOOH), and ammonia borane (NH₃BH₃). During the process, the C-H, B-H, N-H or N-N bonds of these fuels are transformed into C=O, H=O, B=O, N≡N, generating electric energy [5]. However, when hydrogen (H₂) is used as the fuel, only water is produced as a by-product [6].

The cathodic oxygen reduction reaction (ORR) is considered to be the key step in fuel cells due to its slow reaction rate [7-9]. The ORR in an aqueous medium generally takes place via two pathways: two electrons (2e⁻) (equation 6.1) and four electrons (4e⁻) (equation 6.2) [10-12]. In fuel cells, the most desirable pathway for the oxygen reduction reaction (ORR) is the 4-electron pathway. This is because the 2-electron pathway can cause catalyst degradation due to the production of hydrogen peroxide (H₂O₂) [13].



Traditionally, Pt/C has been used as the cathode catalyst for ORR in fuel cells. However, due to its high cost and scarcity, it is difficult to use at an industrial level [14-16]. To overcome these problems, carbon materials have been studied due to

their high specific surface area, good electronic conductivity, and high pore volume [17,18]. Carbon xerogel is a highly used carbon material in fuel cells due to its controllable textural structure and pore size [19-21]. However, it is necessary to increase its ORR activity to make it competitive with the traditional Pt/C catalyst.

Doping carbon materials with heteroatoms or transition metals is an alternative strategy to increase ORR activity and selectivity towards the $4 e^-$ [22-24]. The materials doped specifically with different compound of non-noble metals, had been showed an ORR activity similar or even superior to Pt/C [25]. Among non-precious metals, cobalt (Co) and manganese (Mn) have exhibited excellent catalytic activity for ORR [26-28]. However, recently, carbon materials doped with Mn have shown better results as they have higher selectivity towards 4 electrons (better than Co) and lower carbon monoxide (CO) poisoning compared to vanadium [29,30]. Li et al. [31] synthesized hollow carbon cavities decorated with manganese-nitrogen. This resulted in a selectivity of 20% for H_2O_2 and approximately 3.5 electrons transferred (n). Jiang et al. [32] prepared and characterized a promising catalyst for ORR in fuel cell applications by doping a biochar with iron and manganese, resulting in a n value of 3.96. Lu et al. [33] synthesized a composite of manganese-polypyrrole-carbon nanotube (Mn-PPY-CNT) with $n=2.87$ and an yield in air-cathode microbial fuel cells, similar to the Pt/C. Villanueva-Martínez et al. [34] determined a synergistic effect of carbon nanofibers(CNF) with manganese oxide in the form of nanowires(MONW), increasing the number of electrons from 2.7 and 2.9 respectively to 3.5 in the composite MONW/CNF. With the reported in the literature, the Mn can be considered as a metal ideal for doped the carbon materials and increase the selectivity to ORR $4e^-$ for its use as catalyst ORR in fuel cells.

Manganese-doped carbon spheres are a promising alternative to precious metal catalysts, like platinum, for oxygen electroreduction reactions in fuel cells and other electrochemical devices. They are prepared through a combination of carbonization and doping processes. Carbon spheres are used as the carbon support, providing a high surface area and structural stability. Manganese is incorporated into the carbon matrix to enhance the electrocatalytic properties. Manganese-doped carbon spheres are advantageous catalysts for oxygen electroreduction due to their abundance and low cost as a transition metal. This makes them a more economical alternative to precious metals like platinum. Additionally, they exhibit excellent electrocatalytic activity towards the oxygen reduction reaction, enabling efficient conversion of oxygen with high efficiency and lower overpotential. The carbon support provides structural stability to the catalyst, preventing degradation and improving its long-term stability under the harsh operating conditions of fuel cells. The electrocatalytic properties of carbon spheres doped with manganese can be adjusted by varying the doping level, morphology, and surface properties. This enables optimization based on specific application requirements.

In summary, carbon spheres doped with manganese are a viable alternative to precious metal catalysts for oxygen electroreduction. They are cost-effective, highly active, stable, and tunable, making them attractive candidates for various electrochemical applications, particularly in fuel cells. Further research and development in this field will likely lead to more improvements and the realization of more efficient and affordable energy conversion devices.

In this work carbon spheres were synthesized by the inverse emulsion sol-gel method from resorcinol and formaldehyde as carbon precursors. The spheres were then impregnated with different percentages of manganese. The catalyst

performances of different manganese-doped carbon materials for the oxygen electro-reduction reaction were examined and analysed in terms of pore structure and metal content.

6.2.- EXPERIMENTAL

6.2.1.- Synthesis of carbon spheres doped with manganese

The manganese doped carbon, was prepared in two steps. First, polymer xerogel spheres were created through inverse-emulsion sol-gel polymerization of resorcinol and formaldehyde in an organic medium, as described in previous work [35]. Synthesis was performed by dissolving span 80 (S) in 900 mL of n-heptane and heating at 70 °C under reflux and stirring (450 rpm). The pre-gelled mixture of resorcinol (R), formaldehyde (F), and water (W), 65 °C for 1 h, was added dropwise to the above solution. The molar ratios of the mixture were R/F=1/2, R/W=1/14, and R/S=4.5.

The gel was aged at 70 °C for 24 hours with stirring. Afterward, the suspension was filtered, and the solid obtained was soaked in acetone for 5 days, changing the acetone twice daily. This process removed the Span and replaced the water within the pores with acetone. The gel was dried using microwave heating under an argon atmosphere in 1-minute intervals at 300 W until a constant weight was achieved. A Saivod MS-287W microwave oven was used for this purpose. The gel was then carbonized at 900 °C for 2 hours in a tubular furnace under a 300 cm³ min⁻¹ N₂ flow at a heating rate of 1 °C min⁻¹ to allow for the gentle removal of pyrolysis gases.

In the second step, 100mg of carbon spheres were dispersed in 20 ml of 5.10⁻³ M sulphuric acid and subjected to ultrasonic treatment for 15 minutes. Subsequently, varying amounts of manganese precursor (KMnO₄, Sigma Aldrich)

were dissolved in 5 ml of $5 \cdot 10^{-3}$ M sulphuric acid and added dropwise to the carbon sphere dispersion. After impregnation, the mixture was agitated for six hours, washed with distilled water, and dried at 80 °C for 12 hours. The resulting samples were labeled as SC-MnX (X: 10, 20, and 30).

6.2.2.- Textural and chemical characterization of carbon spheres

The surface area and pore texture were characterized by adsorption of N₂ at -196 °C and CO₂ at 0 °C using an Autosorb-1 system and an ASAP 2020 equipment from Quatachrome and Micromeritics, respectively. Prior to this, the carbon samples were degassed at 120 °C for 12 hours under vacuum. The Dubinin-Radushkevich (DR) equation was used to determine the total micropore volume, while the BET method was used to determine the BET surface area from the N₂ adsorption isotherms. Additionally, the DR equation was used to determine the narrow micropores volume from the CO₂ isotherms. The pore size distribution was determined by applying quenched solid density functional theory (QSDFT) to the N₂ isotherms.

The total Mn content of the composites was determined by combustion of the carbon by thermogravimetric analysis using a Thermogravimetric Analyser (TGA) SHIMADZU mod. TGA-50H with a vertical furnace design and a maximum accuracy of 0.001 mg. The surface chemistry of the carbon samples was characterised by X-ray photoelectron spectroscopy using an Escalab 200R system (VG Scientific Co.) equipped with a MgK α X-ray source ($h\nu = 1253.6$ eV) and a hemispherical electron. For the analysis of the XPS peaks, the position of the C1s peak at 284.6 eV was used as a reference to locate the other peaks. The XPS peaks

were fitted by least squares minimization using Gaussian-Lorentzian peak sharps and a Shirley's type background.

The morphology of the carbon spheres was studied by scanning electron microscopy (SEM) and optical microscopy using a LEO (Carl Zeiss) GEMINI-1530 microscope and an OLYMPUS BX51 microscope, respectively. The images were analysed using the appropriate software (IJ.JAR, from Java) to determine the mean particle size of the carbon spheres and the corresponding histograms. For this purpose, a minimum of 1000 particles from different microphotographs were analysed and their diameter was calculated by the program, assuming a spherical shape.

6.2.3.- Electrochemical measurements

The prepared carbon manganese doped materials were used as electrode. For electrochemical analysis, a mixture of 1 mL of Nafion and 9 mL of deionized water was prepared, followed by 10 minutes of sonication. From this mixture, 1 mL was extracted and combined with 5 mg of SC-MnX (where X represents the percentage of manganese), and further sonicated for 30 minutes. Subsequently, 20 μ L of the resulting solution was applied, depositing 10 μ L onto the rotating ring disc electrode (RRDE) for the investigation of ORR activity.

The activity for ORR was investigated by the RRDE technique using a Metrohm Autolab PGSTAT101 electrochemical system. Electrochemical measurements were performed in a standard three-electrode electrochemical cell at room temperature. A Pt plate was used as the counter electrode and an Ag/AgCl reference electrode. The electrolyte was a solution of KOH 0.1M prepared with deionised water. Before each electrochemical measurement, the electrolyte was

saturated with N₂ or O₂ by bubbling the required gas into the KOH 0.1 M solution for 30 minutes at room temperature. Cyclic voltammetry (CV) was performed in the KOH 0.1M solution saturated with N₂ or O₂ in the range -0.80 to 0.40 V at 50 mV s⁻¹ with the electrode rotating at 1000 rpm. Linear scanning voltammetry (LSV) for ORR was performed in the potential range -0.80 to 0.40 V at 50 mV s⁻¹ with the electrode at speeds of 500, 1000, 1500, 2000, 2500, 3000 and 3500 rpm.

The equation 6.4 and 6.5 were used to calculate the number of electrons transferred and H₂O₂ selectivity from the data obtained in the RRDE experiment [36,37].

$$n = \frac{4 \times I_D}{I_D + \frac{I_R}{N_C}} \quad (6.3)$$

$$\%H_2O_2 = \frac{200 \times \frac{I_R}{N_C}}{I_D + \frac{I_R}{N_C}} \quad (6.4)$$

Where, I_D and I_R are the disk current and ring current respectively, and N_C is the collection efficiency of the RRDE (0,249).

The current density (J_K) was obtained by Koutecky-Levich equation (equation 6.6).

$$\frac{1}{J} = \frac{1}{J_K} + \frac{1}{B \times \omega^{1/2}} \quad (6.6)$$

$$B = (0.62)n \times F \times A \times D^{2/3} \times \nu^{-1/6} \times C$$

Where F is Faraday's constant ($96485000 \text{ mC mol}^{-1}$), n number of electrons transferred per oxygen molecule, A is area of disc of RRDE (0.2475 cm^2), D diffusion coefficient of oxygen ($1.9 \times 10^{-5} \text{ cm}^2 \text{ s}^{-1}$), ν is kinematic viscosity ($0,01 \text{ cm}^2 \text{ s}^{-1}$) and finally C the solubility of oxygen ($1.2 \times 10^{-6} \text{ mol cm}^{-3}$) [38,39].

6.3.- RESULTS AND DISCUSSION

6.3.1.- Textural and chemical characterizations

The figure 6.1 shows the TGA analysis of manganese doped samples, where the exact amount of manganese oxide was determined. The final residual mass after the TGA experiments was considered as the amount of inorganic phase. In this way, the actual percentage of manganese oxide on the doped sample was 9.22, 21.96 and 31.86 wt% for SC-Mn10, SC-Mn20 and SC-Mn30 respectively (see Table 6.1). Comparing the TGA results with the theoretical ones, it can be seen that the real percentages are very close to the theoretical ones, in accordance with the good doping method used.

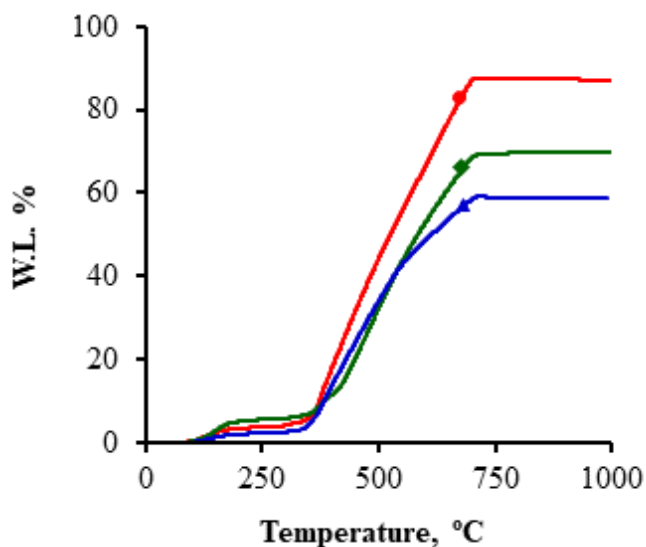


Figure 6.1. ATG of ●SC-Mn10, ◆SC-Mn20 and ▲SC-Mn30.

Figure 6.2 shows the XRD of manganese doped carbon spheres, the XRD pattern would typically consist of several characteristic peaks corresponding to the crystal lattice planes of the carbon material and the presence of manganese. The carbon material itself, being amorphous or nanocrystalline in nature, would show broad diffraction peaks rather than sharp ones at low angles (2θ), indicative of either an amorphous carbon structure or small crystalline domains of carbon. These peaks typically appear centered around 20-30 degrees. Additionally, there are discernible peaks attributed to the presence of manganese within the doped carbon spheres. The positions and intensities of these peaks vary depending on the crystallographic structure of the manganese phase present, such as MnOx (e.g., MnO₂, Mn₂O₃, Mn₃O₄, etc.), in each sample.

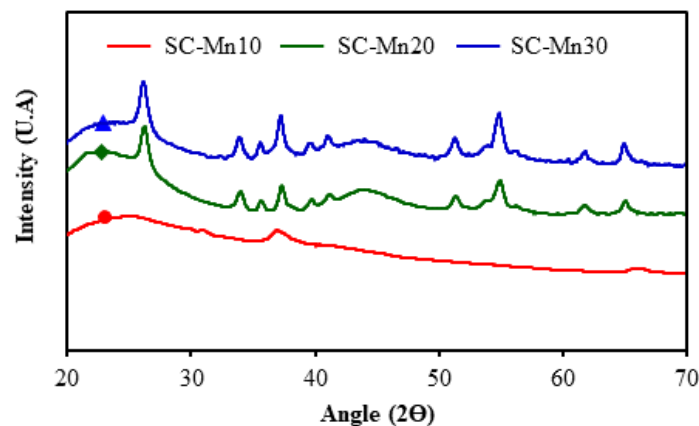


Figure 6.2. XRD of doped carbon manganese samples: ● SC-Mn10, ◆ SC-Mn20 and ▲ SC-Mn30.

The manganese doped carbon shows intense diffraction peaks indicating a high crystallinity. However, the diffraction peaks become more intense depending on the manganese oxide content. We can observe different peaks associated to some species of Mn, indicating the presence of manganese in different oxidation states. For sample SC-Mn10, the interlayer reflection typical of γ -MnO₂ was observed with two peaks starting from the XRD spectra (peaks $2\theta = 36.8$ and 66.2). For the other samples, increasing the manganese content, a new crystalline phase emerges, finding well-defined peaks centered on approximately, $26.2^\circ(112)$, $33.7^\circ(103)$, $35.4^\circ(211)$, $37.2^\circ(220)^\circ$, $51.4^\circ(105)$, $54.8^\circ(303)$, $61.8^\circ(224)$ and $64.9^\circ(400)$ [40,41] characteristics of the spinel structure Mn₃O₄ according to the ICDD PDF card no. 04-004-8640, which theoretically contains high spin Mn²⁺ (d⁵) and Mn³⁺ (d⁴) ions in a 1:2 ratio: occupying the tetrahedral and octahedral sites, respectively, of a normal spinel [42-44]. From these results, it would be expected that the better catalytic results

will be obtained with these samples due to the presence of Mn_3O_4 , which is a species considered highly active for promoting OH generation by ORR [45]. Higher Mn^{3+} content in Mn_3O_4 is believed to improve electro-catalytic performance due to the single electron occupation in the s^* -orbital (eg) of Mn^{3+} .

Figure 6.3a shows the N_2 adsorption-desorption isotherms of SC- MnO_x samples. The SC- MnO_x samples were showed isotherm type IV characteristic for mesoporous materials. From figure 6.3a, is important to mention that the sample with the lowest amount of Mn showed the highest adsorbed volume.

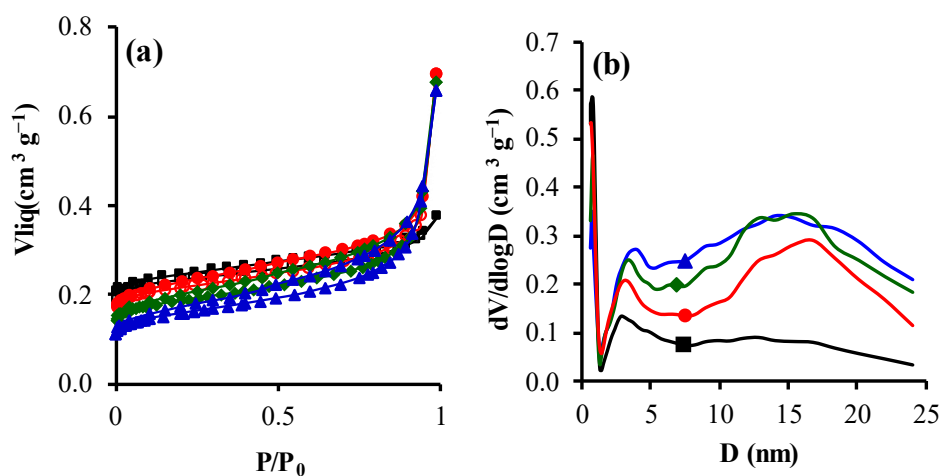


Figure 6.3. (a) N_2 adsorption-desorption isotherms at $-196\text{ }^\circ\text{C}$. (b) Pore size distribution obtained applying QSDFT method to the N_2 adsorption-desorption isotherms. Samples ■SC, ●SC-Mn10, ◆SC-Mn20 and ▲SC-Mn30.

The Brunauer, Emmett and Teller method was applied to the N_2 adsorption isotherms data to obtain the BET surface area (S_{BET}) (Table 6.1).

Table 6.1. Textural characteristics of all samples.

Sample	S_{BET}	$W_0(\text{N}_2)$	$L_0(\text{N}_2)$	$V_{0.95}$	V_{meso}	W_0	L_0	% Mn
	$\text{m}^2 \text{g}^{-1}$	$\text{cm}^3 \text{g}^{-1}$	nm	$\text{cm}^3 \text{g}^{-1}$	$\text{cm}^3 \text{g}^{-1}$	$\text{cm}^3 \text{g}^{-1}$	nm	TGA
SC	571	0.23	0.76	0.330	0.10	0.275	0.56	0
SC-Mn10	530	0.21	0.78	0.380	0.17	0.239	0.55	9.22
SC-Mn20	447	0.18	0.86	0.395	0.22	0.194	0.50	21.96
SC-Mn30	362	0.14	0.87	0.411	0.27	0.164	0.46	31.86

The results indicate that Mn may cause pore blockage and for this reason the BET surface area and pore volume decrease as the amount of Mn increases. This agrees with what is shown in the isotherms of N_2 (figure. 6.3a), due to a blockage in the pores there is a limitation of the access of the gas to the total pore volume of the material. It is an important problem because a reduction in the surface area can reduce the electrochemical activity due to a lack of accessibility of the electrolyte to the total pore volume. It can also be observed that as the percentage of MnO_x increases, the total porosity ($V_{0.95}$) increases, favored by a development of the mesopore volume (V_{mes}), figure. 6.3b.

The results of CO_2 and N_2 adsorption experiments are compared to analyze the micropore size distribution. CO_2 adsorption provides information about narrow microporosity, or ultra-micropores, which are micropores with a diameter less than 0.7 nm. Total microporosity can be obtained from the N_2 isotherm only in the absence of diffusion restrictions, or supermicropores. Figures 6.4a and 6.4b show how the ultra and supermicropore volume vary with changes in manganese content. The micropore volume, $W_0(\text{N}_2)$ decreases, and the pores become wider ($L_0(\text{N}_2)$)

increases) as the manganese oxide content increases, as shown in table 6.1. Additionally, the ultra-microporosity ($W_0(\text{CO}_2)$) progressively decreases and the mean pore size also decreases (figure. 6.4a). It is worth noting that for all samples, $W_0(\text{N}_2) < W_0(\text{CO}_2)$, which denotes diffusion restrictions of N_2 into the microporosity induced by the narrow microporosity of the carbon phase. By increasing the percentage of manganese oxide, the difference between $W_0(\text{N}_2)$ and $W_0(\text{CO}_2)$ decreases. Additionally, the micropore size (L_0) decreases progressively. These results can be explained by the gasification of the carbon structure by the reduction of MnO_4^- to MnO_2 , Mn_2O_3 or MnO . This gasification can destroy the pore walls, causing a widening and an increase in the mesopore volume (figure 6.3 and table 6.1), and at the same time a transformation of the micropore in the mesopores, leading to a decrease in the total micropore volume and the S_{BET} , table 6.1 [46].

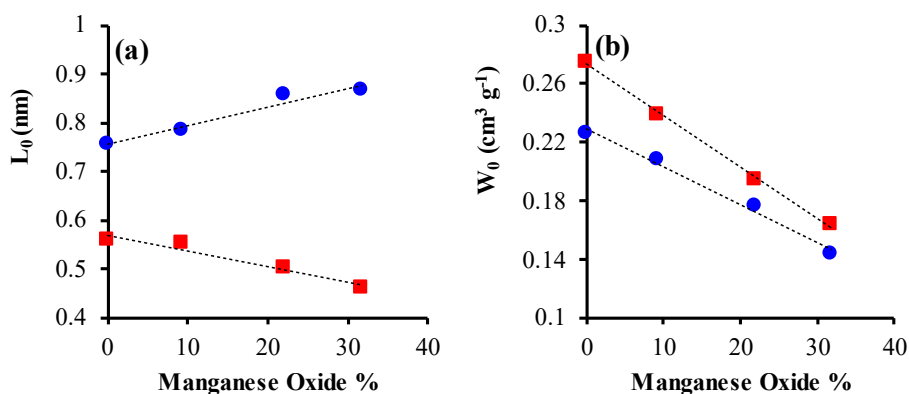


Figure 6.4. Variation of L_0 and W_0 with manganese oxide content. ■ data form CO_2 adsorption at 0°C ; ● data form N_2 adsorption at -196°C .

Figure 6.5 shows the scanning electron microscopy (SEM) of the samples, there are no significant differences between the samples. The main difference is the particles of Mn agglomerates on the surface of the carbon xerogel spheres, corresponding to the amount of Mn added. Furthermore, the images clearly show the presence of Mn_3O_4 particles homogeneously distributed on the clean and smooth surface of the carbon spheres.

As expected, the density of Mn_3O_4 particles on the surface increases with the theoretical manganese content.

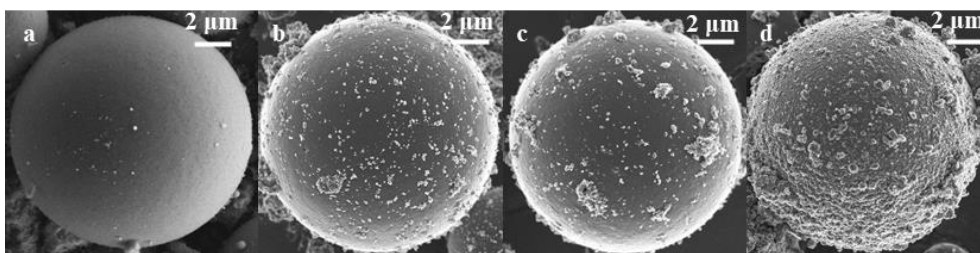


Figure 6.5. Scanning electron microscopy images of SC (a), SC-Mn10 (b), SC-Mn20 (c) and SC-Mn30 (d).

The scanning electron microscope (SEM) images confirm that the manganese oxide particles agglomerate on the external surface of the carbon xerogel spheres, blocking the pores of the samples. This is consistent with the BET surface area and pore size distribution.

The XPS technique allows us to identify the surface chemical composition of solids and the electronic state of each analysed element. We used XPS characterization to investigate the surface elemental compositions and valence states of manganese-doped carbon spheres. The high-resolution XPS spectra allowed us to determine the surface composition of SC, as shown in table 6.2. The

high resolution C1s core level spectrum presented in figure. 6.6a can be deconvoluted into six components, which are C=C (284.6 eV), C-C (285.2±0.2 eV) [47], C-O (286.6 eV), RO-C=O (287.6 eV) and O=C=O and π - π^* (>290 eV). Importantly, the decrease in FWHM for the C=C peak indicates an increase in the crystallinity of the graphitic structure due to the gasification of the more reactive sites formed mainly by the C-C bond. This increase in the graphitic structure of our samples improves their electrical conductivity, which is a critical factor in the performance of the electrodes.

Figure 6.6c shows the high resolution Mn_{2p} XPS spectra, in which two peaks can be fitted into four peaks at 642.2 eV, 644.1 eV assigned to Mn²⁺ (2p_{3/2}), Mn³⁺ (2p_{3/2}), species, respectively. However, the last peak has not been analysed because it is the result of spin-orbit splitting [48]. The amount percentual of valence states of Mn (table 6.2). These results show that SC-Mn30 have highest Mn (II) concentration and the lowest Mn (III) concentration, The higher Mn³⁺ content in manganese carbon doped sample should be ascribed to the more disorders and surface defects produced by raising of thermal treatment temperature. It is believed that higher Mn³⁺ content can lead to better electro-catalytic performance, due to the single electron occupation in σ^* -orbital (eg) of Mn³⁺ [49]. The peak separation between Mn 2p_{3/2} and the lowest component of O_{1s} (figure 6.6a) is 11.9 eV is also consistent with the reported value of Mn-O for the Mn₃O₄ [50] which confirms the result obtained by XRD analysis.

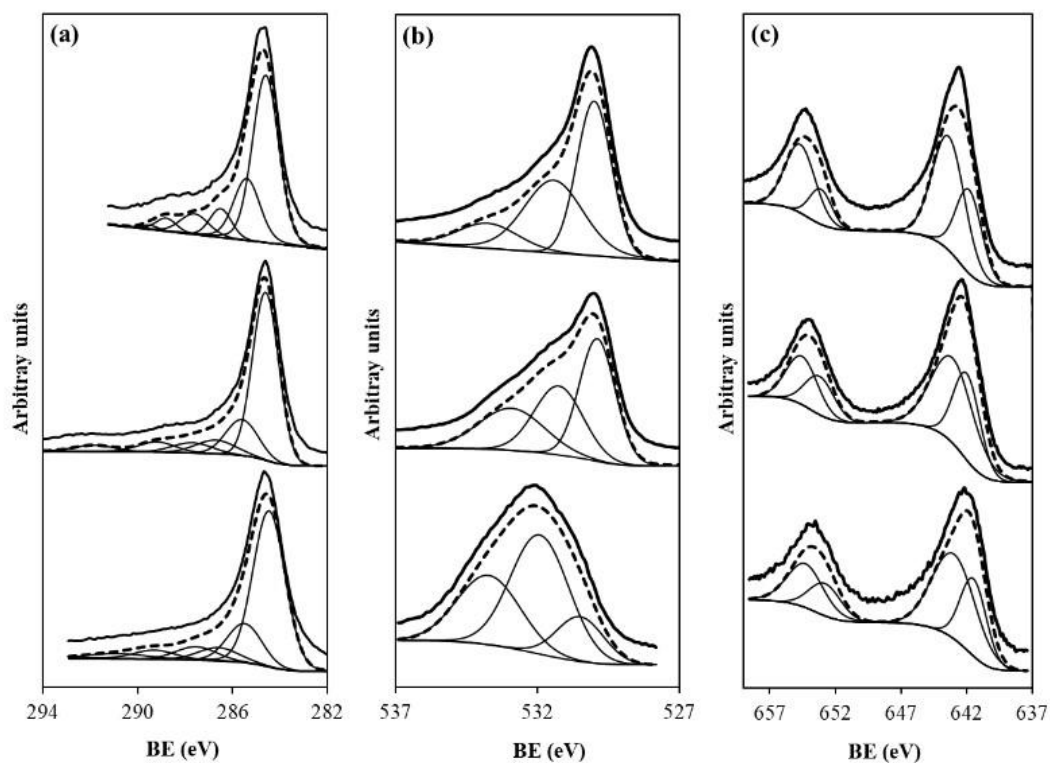


Figure 6.6. Spectral regions of SC-Mn10, SC-Mn20 and SC-Mn30, a) O_{1s}, b) C_{1s} and c) Mn_{2p}.

6.3.2.- Electrochemical characterization

Figure 6.7 show the results for SC, SC-Mn10, SC-Mn20 and SC-Mn30 (A, B, C and D, respectively), all CV curves (Both N₂ and O₂ saturated) appear strong redox peaks, the peak at ca. 0 V vs. Ag/AgCl was attributed to Mn³⁺/Mn²⁺ redox because the area of the peak at ca. 0 V vs. Ag/AgCl increases with greater Mn concentration (Mn content changes from 8.0 to 24.8%).

On the other hand, in the absence of oxygen O_2 , the area of the CV depends on the porous texture as well as the surface chemistry, in this way, SC-Mn20 presents the highest electrochemical capacitance. while SC-Mn10 presents the lowest one. Furthermore, the development of a quasi-rectangular shape is indicative of the co-existence of a high surface area and relatively high conductance.

In the presence of O_2 , all samples show a peak associated with the oxidoreduction of oxygen, being actives for the ORR. Moreover, an increase in the double layer capacitance is found in oxygen saturated KOH regarding N_2 -saturated solutions which could be ascribed to the pseudo capacitance contributions. due to the faradic process involving magnesium species.

The sample SC-Mn10 have the lowest electrochemical capacitance while SC-Mn20 presents the highest. Typically, the capacitance depends on porous texture and surface chemistry. It is possible that the amount of Mn has an optimal value for obtaining the better capacitance, due to the fact that the highest was obtained with the middle value (20.5%). Note also that this sample is more active for ORR than other ones which will be better observed after analyzing LSV experiments.

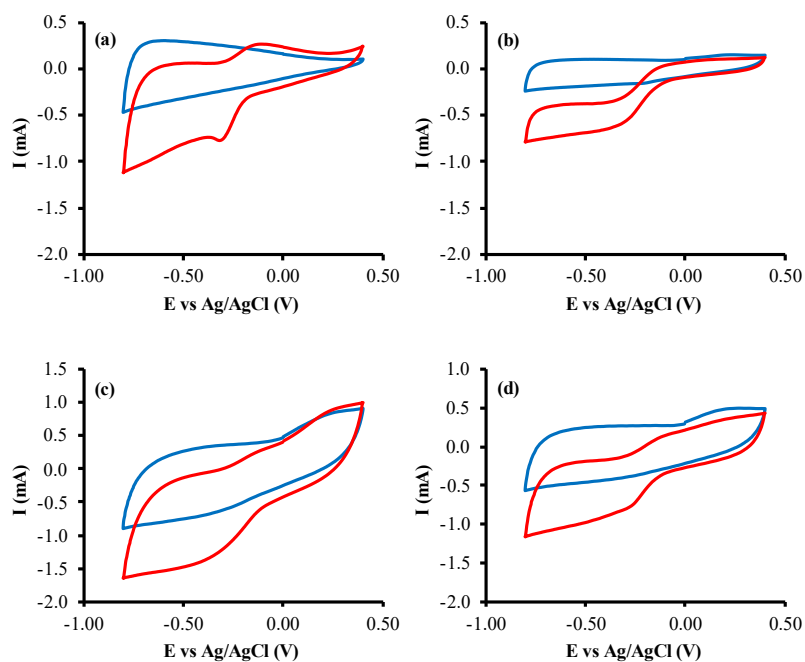


Figure 6.7. CV of (a) SC, (b) SC-Mn10, (c) SC-Mn20, (d) SC-Mn30 in N_2 (blue) and O_2 (red).

It is important to know by which mechanism determines the catalytic behavior of the tested sample and try to improve the catalyst in order to enhance the second one. To study that, LSV experiments were performed at different RRDE rotation speeds (data shown in figure 6.8). The obtained curves were adjusted to Koutecky-Levich equation to obtain the number of electrons transferred at each potential for the different samples and results were plotted in figure 6.9. To explain the above mechanism, we correlate the generation of new oxidation states due to lowering of dimension. Mn_3O_4 possesses Mn (II) at tetrahedral site and Mn (III) at octahedral site being a spinel structure. The

presence of two redox oxidation states (Mn^{2+} and Mn^{3+}), results in proper charge-distribution and favorable charge-transfer to adsorbed oxygen, leading to catalytic activity of the catalyst. We observe from XPS results that formation of Mn (III) was higher. This Mn (III) oxidation states have been reported to show higher ORR activity due to a single electron in e_g orbital. The e_g antibonding orbitals of Mn (III) overlap with adsorbed oxygen, affecting the Mn-O bond strength and improves the catalytic activity.

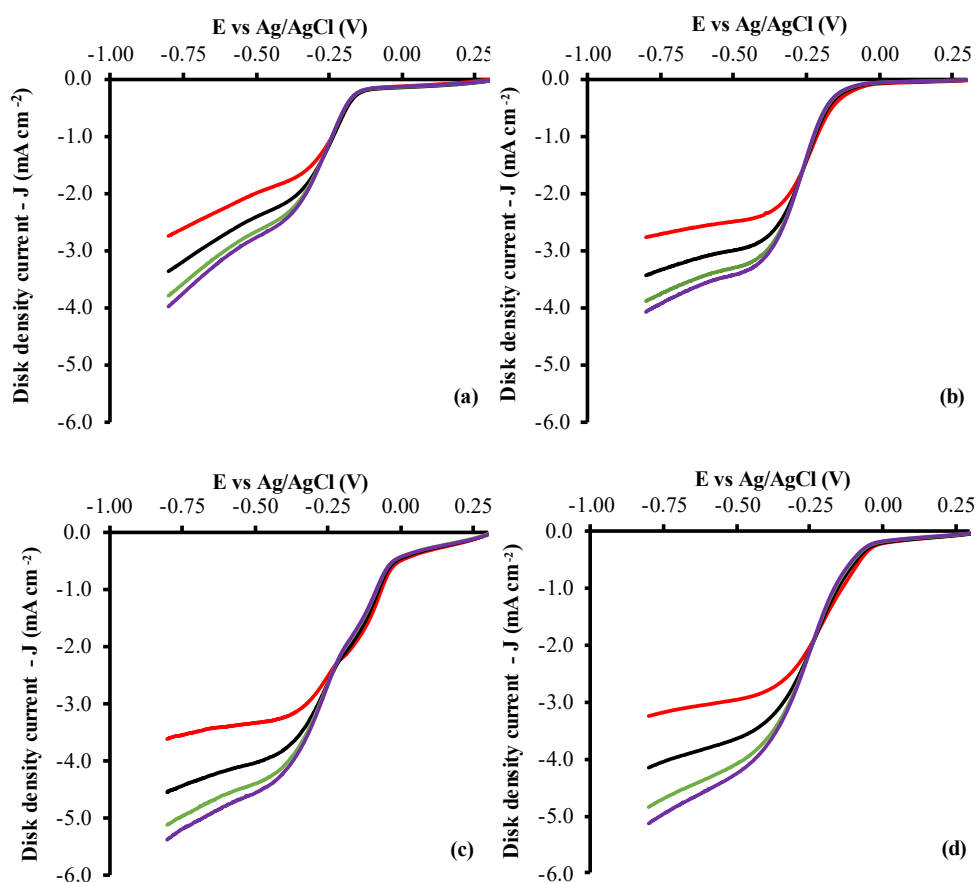


Figure 6.8. LSV at different rotation speed for (a) SC, (b) SC-Mn10, (c) SC-Mn20 and (d) SC-Mn30, at **1000**, **2000**, **3000** and **3500** rpm.

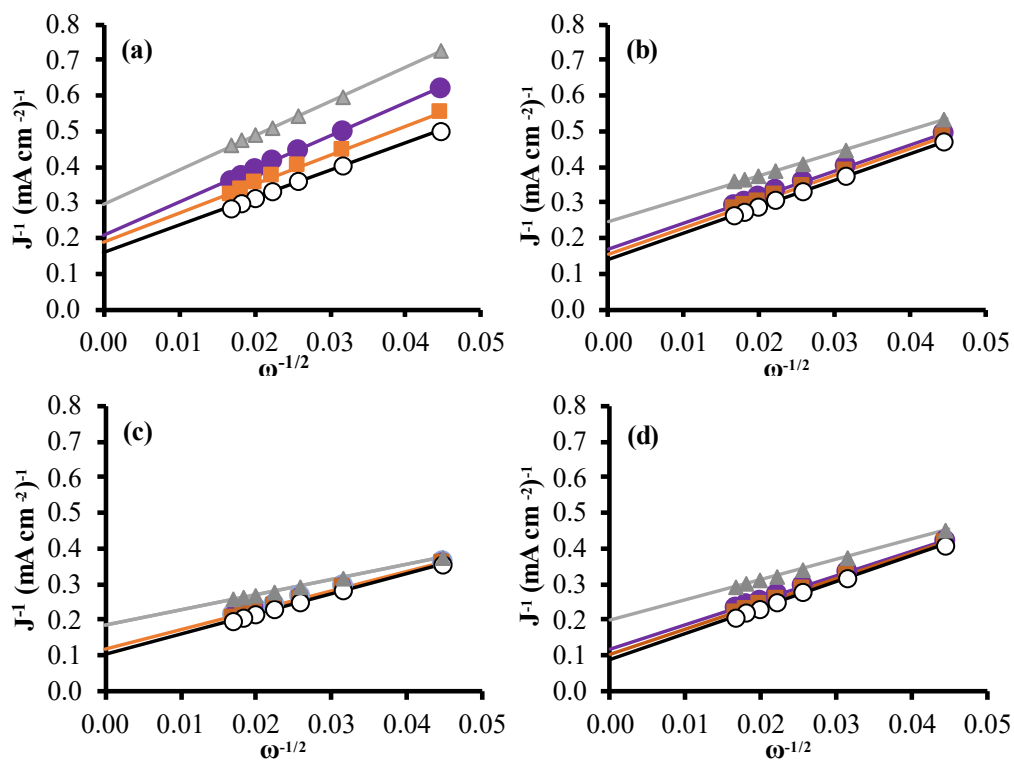


Figure 6.9. K-L plots, for (a) SC, (b) SC-Mn10, (c) SC-Mn20 and (d) SC-Mn30, at different electrochemical potentials ● (-0.5V), ■ (-0.6V), ○ (-0.7V), ▲ (-0.8V).

The table 6.3, show the electrochemical parameter obtained from the LSV curves (E_{onset} , number of electrons transferred and J_K), from these results, is possible determinate that the optimal amount of manganese is closer to the 20%.

Table 6.3. Electrochemical parameters.

Sample	E_{onset} (V)	J_k (mA cm ⁻²)	-0.6V	
			n	%H ₂ O ₂
SC	-0.17	7.55	2.99	54.67
SC-Mn10	-0.17	8.36	3.05	43.62
SC-Mn20	-0.09	10.90	3.58	20.94
SC-Mn30	-0.12	5.97	3.48	25.90

The figure 6.10 shows the number of electrons transferred and selectivity for H₂O₂ of all the samples. The SC-Mn20 show to be the sample more active for ORR pathway 4 electrons, with lowest selectivity to H₂O₂. Which is attributable to all properties show previously, more specifically the amount of Mn (III) due to that has been founded that this state of valence is the key for the ORR [51], From this result, it is shown that the Mn improves the electrochemical properties, however, a Mn excess result unfavorable due to that decreases J_K value. Which is possibly attributable to the reduction of surface area or blocked porosity of material. Based on the disk and ring currents, we calculated the peroxide yield and electron transfer number (figure 6.10). For the SC-Mn20, the yield of peroxide was less than 20% over the potential range from -0.60 to -0.4 V vs. Ag/AgCl and increased to ~20% at higher overpotential (-0.8 V vs. Ag/AgCl). Correspondingly, the average electron transfer number of the samples doped with more of 10% of Mn was ~3.6 from -0.60 to -0.4 V and decreased to ~3.4 at -0.8 V. Furthermore, figure 6.11b show the dependence of the electron number transferred with the manganese oxide percentage, the result shows a good correlation indicating that manganese

percentage is a crucial parameter in the reaction of electroreduction of oxygens. These results suggest that the ORR pathway catalyzed by the SC-Mn_x is mainly through a four-electron process, but the proportion of two-electron reduction increased at high overpotentials and with a lower percentage of manganese oxide.

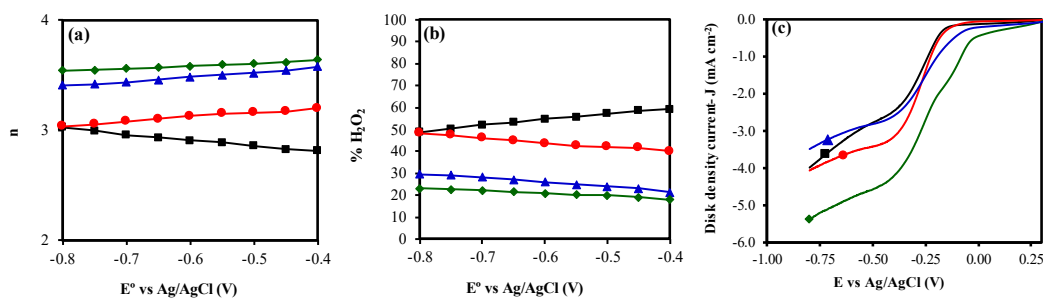


Figure 6.10. Number of (a) electrons transferred, (b) selectivity for H_2O_2 and (c) LSV curves at 3500 rpm of ■SC, ●SC-Mn10, ◆SC-Mn20 and ▲SC-Mn30.

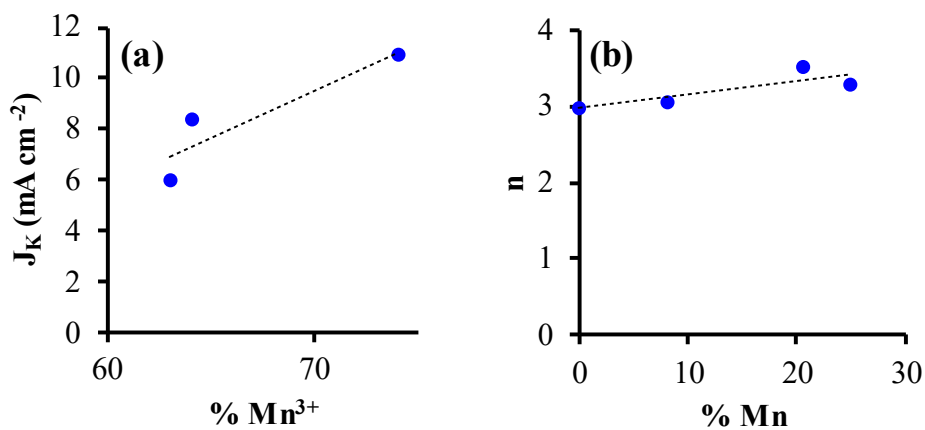


Figure 6.11. Correlation of (a) J_K with $\% Mn^{3+}$ and (b) n with $\% Mn$.

6.4.- CONCLUSIONS

In conclusion, a novel Mn doped carbon sphere by a simple one-pot hydrothermal method for high performance ORR catalysis has been developed. The introduction of Mn_3O_4 to carbon sphere is novel and led to improved activity of the catalyst. The Mn decreases the surface area B.E.T but increases the number of electrons transferred near to 4 electrons and reduces the H_2O_2 generation. However, a higher Mn oxide amount can result in a lower current density that can affect the electroactivity catalytic. XRD indicates the stabilization of Mn_3O_4 with Mn^{2+} and Mn^{3+} state in these composites; therefore, XPS reveals the presence of Mn^{+3} and Mn^{2+} in which Mn^{+3} was higher. Moreover, the presence of Manganese oxide greatly affects the textural characteristics of carbon spheres. New porosity is created, and the existing porosity opened increasing the Mn_3O_4 contents which is denoted by the increase of the meso and micropores volumes and the micropores. For improve the ORR is necessary that the catalyst doped with Mn have a good relation Mn(II)/Mn(III) due to that the transfer between the ions can result in a better transfer electronic. The transferred electron number in the ORR catalyzed by the SC-Mn composite is close to 4, which suggests that the composite catalyzed ORR proceeds along a highly efficient path.

Thus, the carbon sphere doped Mn_3O_4 represents a new type of low cost, environmentally benign and highly active ORR catalyst which should be useful for metal–air batteries or fuel cells in alkaline conditions.

BIBLIOGRAPHY

- [1] Ghorbanzade Zaferani, S.P.; Amiri, M.K.; Sarmasti Emami, M.R.; Zahmatkesh, S.; Hajiaghaei-Keshteli, M.; Panchal, H. Prediction and Optimization of Sustainable Fuel Cells Behavior Using Artificial Intelligence Algorithms. *Int. J. Hydrogen Energy* 2023, doi:10.1016/j.ijhydene.2023.03.335.
- [2] Jafari, M.; Gharibi, H.; Kazemi, M.; Heydari, A.; Zhiani, M.; Parnian, M.J. Metal-Nitrogen Co-Doped Hierarchical Porous Carbon Derived from the Bimetallic Metal-Organic Framework as ORR Electrocatalyst for Passive Alkaline Direct Ethanol Fuel Cell. *J. Electroanal. Chem.* 2022, 920, 116620, doi:10.1016/j.jelechem.2022.116620.
- [3] Sikeyi, L.L.; Ntuli, T.D.; Mongwe, T.H.; Maxakato, N.W.; Coville, N.J.; Maubane-Nkadimeng, M.S. Platinum Nanoparticles Loaded on Pristine and Boron Oxide Modified Carbon Nano-Onions for Enhanced Ammonia Electrooxidation in Alkaline Direct Ammonia Fuel Cells. *J. Electroanal. Chem.* 2022, 917, 116411, doi:10.1016/j.jelechem.2022.116411.
- [4] Jaleh, B.; Nasrollahzadeh, M.; Eslamipanah, M.; Nasri, A.; Shabanlou, E.; Manwar, N.R.; Zboril, R.; Fornasiero, P.; Gawande, M.B. The Role of Carbon-Based Materials for Fuel Cells Performance. *Carbon N. Y.* 2022, 198, 301–352, doi:10.1016/j.carbon.2022.07.023.
- [5] Zhang, Y.; Peng, Y.; Wan, Q.; Ye, D.; Wang, A.; Zhang, L.; Jiang, W.; Liu, Y.; Li, J.; Zhuang, X.; et al. Fuel Cell Power Source Based on Decaborane with High Energy Density and Low Crossover. *Mater. Today Energy* 2023, 32, 101244, doi:10.1016/j.mtener.2022.101244.

- [6] Fu, Z.; Lu, L.; Zhang, C.; Xu, Q.; Zhang, X.; Gao, Z.; Li, J. Fuel Cell and Hydrogen in Maritime Application: A Review on Aspects of Technology, Cost and Regulations. *Sustain. Energy Technol. Assessments* 2023, 57, 103181, doi:10.1016/j.seta.2023.103181.
- [7] Subran, N.; Ajit, K.; Krishnan, H. Biochar Electrode from Banana Peduncle as Heteroatom Doped ORR Catalyst. *Mater. Today Proc.* 2023, doi:10.1016/j.matpr.2023.03.407.
- [8] Zhang, T.; Wang, H.; Zhang, J.; Ma, J.; Wang, Z.; Liu, J.; Gong, X. Carbon Charge Population and Oxygen Molecular Transport Regulated by Program-Doping for Highly Efficient 4e-ORR. *Chem. Eng. J.* 2022, 444, 136560, doi:10.1016/j.cej.2022.136560.
- [9] Seyed Bagheri, S.M.; Gharibi, H.; Zhiani, M. Introduction of a New Active and Stable Cathode Catalyst Based on Bimetal-Organic Frameworks/PPy-Sheet for Alkaline Direct Ethanol Fuel Cell. *Int. J. Hydrogen Energy* 2022, 47, 23552–23569, doi:10.1016/j.ijhydene.2022.05.142.
- [10] Yamamoto, N.; Matsumura, D.; Hagihara, Y.; Tanaka, K.; Hasegawa, Y.; Ishii, K.; Tanaka, H. Investigation of Hydrogen Superoxide Adsorption during ORR on Pt/C Catalyst in Acidic Solution for PEFC by in-Situ High Energy Resolution XAFS. *J. Power Sources* 2023, 557, 232508, doi:10.1016/j.jpowsour.2022.232508.
- [11] Gridin, V.; Du, J.; Haller, S.; Theis, P.; Hofmann, K.; Wiberg, G.K.H.; Kramm, U.I.; Arenz, M. GDE vs RDE: Impact of Operation Conditions on Intrinsic Catalytic Parameters of FeNC Catalyst for the Oxygen Reduction Reaction. *Electrochim. Acta* 2023, 444, 142012, doi:10.1016/j.electacta.2023.142012.

- [12] Aysla Costa De Oliveira, M.; D'Epifanio, A.; Ohnuki, H.; Mecheri, B. Platinum Group Metal-Free Catalysts for Oxygen Reduction Reaction: Applications in Microbial Fuel Cells. *Catalysts* 2020, 10, 1–22, doi:10.3390/catal10050475.
- [13] Das, S.; Ghosh, S.; Kuila, T.; Murmu, N.C.; Kundu, A. Biomass-Derived Advanced Carbon-Based Electrocatalysts for Oxygen Reduction Reaction. *Biomass* 2022, 2, 155–177, doi:10.3390/biomass2030010.
- [14] Sivaraman, R.; Oplencia, M.J.C.; Majdi, A.; Patra, I.; Kadhem Abid, M.; Hammid, A.T.; Derakhshandeh, M. Design a Promising Non-Precious Electro-Catalyst for Oxygen Reduction Reaction in Fuel Cells. *Int. J. Hydrogen Energy* 2022, doi:10.1016/j.ijhydene.2022.04.241.
- [15] Mishra, K.; Kumar Thakur, V.; Singh Siwal, S. Graphitic Carbon Nitride Based Palladium Nanoparticles: A Homemade Anode Electrode Catalyst for Efficient Direct Methanol Fuel Cells Application. *Mater. Today Proc.* 2022, 56, 107–111, doi:10.1016/j.matpr.2021.12.342.
- [16] Rao, C.; Zhao, Z.; Wen, Z.; Xu, Q.; Chen, K.; Zhang, T.; Ci, S. N-Doped Macroporous Carbon Loading Mo₂C as Cathode Electrocatalyst of Hybrid Neutral-Alkaline Microbial Electrolysis Cells for H₂ Generation. *Electrochim. Acta* 2022, 431, 141142, doi:10.1016/j.electacta.2022.141142.
- [17] Wang, X.; Yuan, T.; Liang, J.; Yang, J.; Xie, Y.; Li, L.; Zhang, W. FeN_x Nanoparticles Embedded in Three-Dimensional N-Doped Carbon Nanofibers as Efficient Oxygen Reduction Reaction Electrocatalyst for Microbial Fuel Cells in Alkaline and Neutral Media. *Int. J. Hydrogen Energy* 2022, 47, 23608–23617, doi:10.1016/j.ijhydene.2022.05.176.
- [18] Xiang, X.; Zhang, X.; Yan, B.; Wang, K.; Wang, Y.; Lyu, D.; Xi, S.; Qun

- Tian, Z.; Kang Shen, P. Atomic Iron Coordinated by Nitrogen Doped Carbon Nanoparticles Synthesized via a Synchronous Complexation-Polymerization Strategy as Efficient Oxygen Reduction Reaction Electrocatalysts for Zinc-Air Battery and Fuel Cell Application. *Chem. Eng. J.* 2022, 440, 135721, doi:10.1016/j.cej.2022.135721.
- [19] Thapa, B. Sen; Seetharaman, S.; Chetty, R.; Chandra, T.S. Xerogel Based Catalyst for Improved Cathode Performance in Microbial Fuel Cells. *Enzyme Microb. Technol.* 2019, 124, 1–8, doi:10.1016/j.enzmictec.2019.01.007.
- [20] Canal-Rodríguez, M.; Rey-Raap, N.; Menéndez, J.Á.; Montes-Morán, M.A.; Figueiredo, J.L.; Pereira, M.F.R.; Arenillas, A. Effect of Porous Structure on Doping and the Catalytic Performance of Carbon Xerogels towards the Oxygen Reduction Reaction. *Microporous Mesoporous Mater.* 2020, 293, doi:10.1016/j.micromeso.2019.109811.
- [21] Figueiredo, J.L.; Pereira, M.F.R. Synthesis and Functionalization of Carbon Xerogels to Be Used as Supports for Fuel Cell Catalysts. *J. Energy Chem.* 2013, 22, 195–201, doi:10.1016/S2095-4956(13)60025-X.
- [22] Wang, H.; Wei, L.; Shen, J. Iron-Gelatin Aerogel Derivative as High-Performance Oxygen Reduction Reaction Electrocatalysts in Microbial Fuel Cells. *Int. J. Hydrogen Energy* 2022, 47, 17982–17991, doi:10.1016/j.ijhydene.2022.03.276.
- [23] Akula, S.; Mooste, M.; Kozlova, J.; Käärik, M.; Treshchalov, A.; Kikas, A.; Kisand, V.; Aruväli, J.; Paiste, P.; Tamm, A.; et al. Transition Metal (Fe, Co, Mn, Cu) Containing Nitrogen-Doped Porous Carbon as Efficient Oxygen Reduction Electrocatalysts for Anion Exchange Membrane Fuel Cells.

- Chem. Eng. J. 2023, 458, doi:10.1016/j.cej.2023.141468.
- [24] Ge, C.; Li, Q.; Hu, M.; Wang, G.; Xiao, L.; Lu, J.; Zhuang, L. Application of Rock-Salt-Type Co–Mn Oxides for Alkaline Polymer Electrolyte Fuel Cells. *J. Power Sources* 2022, 520, 1–6, doi:10.1016/j.jpowsour.2021.230868.
- [25] Sang, Y.; Fu, A.; Li, H.; Zhang, J.; Li, Z.; Li, H.; Zhao, X.S.; Guo, P. Experimental and Theoretical Studies on the Effect of Functional Groups on Carbon Nanotubes to Its Oxygen Reduction Reaction Activity. *Colloids Surfaces A Physicochem. Eng. Asp.* 2016, 506, 476–484, doi:10.1016/j.colsurfa.2016.07.008.
- [26] Zhao, T.; Niu, S.; Wu, X.; Wu, Q.; Ma, Z.; Jiang, J.; Huang, Y.; Wang, H.; Li, Q.; Cai, Y. Manganese Decoration Tailored Nitrogen Doping for Boosted Oxygen Reduction Electrocatalysis of Co-NC. *J. Alloys Compd.* 2022, 924, 166532, doi:10.1016/j.jallcom.2022.166532.
- [27] Flores-Lasluisa, J.X.; Huerta, F.; Cazorla-Amorós, D.; Morallón, E. Manganese Oxides/LaMnO₃ Perovskite Materials and Their Application in the Oxygen Reduction Reaction. *Energy* 2022, 247, doi:10.1016/j.energy.2022.123456.
- [28] Zhang, M.; Gao, J.; Hong, W.; Wang, X.; Tian, Q.; An, Z.; Wang, L.; Yao, H.; Liu, Y.; Zhao, X.; et al. Bimetallic Mn and Co Encased within Bamboo-like N-Doped Carbon Nanotubes as Efficient Oxygen Reduction Reaction Electrocatalysts. *J. Colloid Interface Sci.* 2019, 537, 238–246, doi:10.1016/j.jcis.2018.11.022.
- [29] Lilloja, J.; Kibena-Pöldsepp, E.; Sarapuu, A.; Käärik, M.; Kozlova, J.; Paiste, P.; Kikas, A.; Treshchalov, A.; Leis, J.; Tamm, A.; et al. Transition Metal

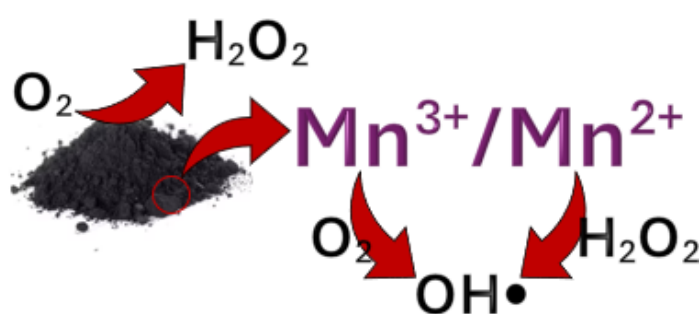
- and Nitrogen-Doped Mesoporous Carbons as Cathode Catalysts for Anion-Exchange Membrane Fuel Cells. *Appl. Catal. B Environ.* 2022, 306, doi:10.1016/j.apcatb.2022.121113.
- [30] Ding, Z.; Cai, M.; Hui, X. Potential of Vanadium (V) Doped CNT(10, 0) and Manganese (Mn) Doped Carbon Nanocage (C60) as Catalysts for Oxygen Reduction Reaction in Fuel Cells. *Inorg. Chem. Commun.* 2022, 135, 109095, doi:10.1016/j.inoche.2021.109095.
- [31] Li, Q.; Zhao, T.; He, C.; Cai, Y.; Wu, Q.; Huang, Y. Hollow Carbon Cavities Decorated with Highly Dispersed Manganese-Nitrogen Moieties for Efficient Metal-Air Batteries. *Electrochim. Acta* 2022, 410, 139975, doi:10.1016/j.electacta.2022.139975.
- [32] Jiang, J.; Zhang, S.; Li, S.; Zeng, W.; Li, F.; Wang, W. Magnetized Manganese-Doped Watermelon Rind Biochar as a Novel Low-Cost Catalyst for Improving Oxygen Reduction Reaction in Microbial Fuel Cells. *Sci. Total Environ.* 2022, 802, 149989, doi:10.1016/j.scitotenv.2021.149989.
- [33] Lu, M.; Guo, L.; Kharkwal, S.; Yong, H.; Fong, S.; Li, Y. Manganese e Polypyrrole e Carbon Nanotube , a New Oxygen Reduction Catalyst for Air-Cathode Microbial Fuel Cells. *J. Power Sources* 2013, 221, 381–386, doi:10.1016/j.jpowsour.2012.08.034.
- [34] Villanueva-Martínez, N.I.; Alegre, C.; Martínez-Visús, I.; Lázaro, M.J. Bifunctional Oxygen Electrocatalysts Based on Non-Critical Raw Materials: Carbon Nanostructures and Iron-Doped Manganese Oxide Nanowires. *Catal. Today* 2023, 114083, doi:10.1016/j.cattod.2023.114083.
- [35] Elmouwahidi, A.; Bailón-García, E.; Pérez-Cadenas, A.F.; Castelo-Quibén, J.; Carrasco-Marín, F. Carbon-Vanadium Composites as Non-Precious

- Catalysts for Electro-Reduction of Oxygen. *Carbon* N. Y. 2019, 144, 289–300, doi:10.1016/j.carbon.2018.12.038.
- [36] Zhou, R.; Zheng, Y.; Jaroniec, M.; Qiao, S.Z. Determination of the Electron Transfer Number for the Oxygen Reduction Reaction: From Theory to Experiment. *ACS Catal.* 2016, 6, 4720–4728, doi:10.1021/acscatal.6b01581.
- [37] Jiang, K.; Back, S.; Akey, A.J.; Xia, C.; Hu, Y.; Liang, W.; Schaak, D.; Stavitski, E.; Nørskov, J.K.; Siahrostami, S.; et al. Highly Selective Oxygen Reduction to Hydrogen Peroxide on Transition Metal Single Atom Coordination. *Nat. Commun.* 2019, 10, doi:10.1038/s41467-019-11992-2.
- [38] Xu, S.; Kim, Y.; Higgins, D.; Yusuf, M.; Jaramillo, T.F.; Prinz, F.B. Building upon the Koutecky-Levich Equation for Evaluation of Next-Generation Oxygen Reduction Reaction Catalysts. *Electrochim. Acta* 2017, 255, 99–108, doi:10.1016/j.electacta.2017.09.145.
- [39] Brocato, S.; Lau, C.; Atanassov, P. Mechanistic Study of Direct Electron Transfer in Bilirubin Oxidase. *Electrochim. Acta* 2012, 61, 44–49, doi:10.1016/j.electacta.2011.11.074.
- [40] Chowde Gowda, C.; Mathur, A.; Parui, A.; Kumbhakar, P.; Pandey, P.; Sharma, S.; Chandra, A.; Singh, A.K.; Halder, A.; Tiwary, C.S. Understanding the Electrocatalysis OER and ORR Activity of Ultrathin Spinel Mn_3O_4 . *J. Ind. Eng. Chem.* 2022, 113, 153–160, doi:10.1016/j.jiec.2022.05.024.
- [41] He, Y.; Aasen, D.; Yu, H.; Labbe, M.; Ivey, D.G.; Veinot, J.G.C. Mn_3O_4 nanoparticle-Decorated Hollow Mesoporous Carbon Spheres as an Efficient Catalyst for Oxygen Reduction Reaction in Zn-Air Batteries. *Nanoscale Adv.* 2020, 2, 3367–3374, doi:10.1039/d0na00428f.

- [42] Madhuri, S.; Shilpa Chakra, C.; Sadhana, K.; Divya, V. Sketchy Synthesis of Mn₃O₄, Mn₃O₄/AC and Mn₃O₄/CNT Composites for Application of/in Energy Cache. *Mater. Today Proc.* 2022, 65, 2812–2818, doi:10.1016/j.matpr.2022.06.247.
- [43] Wang, B.; Yu, J.; Lu, Q.; Xiao, Z.; Ma, X.; Feng, Y. Preparation of Mn₃O₄ Microspheres via Glow Discharge Electrolysis Plasma as a High-Capacitance Supercapacitor Electrode Material. *J. Alloys Compd.* 2022, 926, 166775, doi:10.1016/j.jallcom.2022.166775.
- [44] Moses Ezhil Raj, A.; Victoria, S.G.; Jothy, V.B.; Ravidhas, C.; Wollschläger, J.; Suendorf, M.; Neumann, M.; Jayachandran, M.; Sanjeeviraja, C. XRD and XPS Characterization of Mixed Valence Mn₃O₄ Hausmannite Thin Films Prepared by Chemical Spray Pyrolysis Technique. *Appl. Surf. Sci.* 2010, 256, 2920–2926, doi:10.1016/j.apsusc.2009.11.051.
- [45] Weng, Z.; Li, J.; Weng, Y.; Feng, M.; Zhuang, Z.; Yu, Y. Surfactant-Free Porous Nano-Mn₃O₄ as a Recyclable Fenton-like Reagent That Can Rapidly Scavenge Phenolics without H₂O₂. *J. Mater. Chem. A* 2017, 5, 15650–15660, doi:10.1039/c7ta04042c.
- [46] Moreno-Castilla, C.; Ferro-García, M.A.; Joly, J.P.; Bautista-Toledo, I.; Carrasco-Marín, F.; Rivera-Utrilla, J. Activated Carbon Surface Modifications by Nitric Acid, Hydrogen Peroxide, and Ammonium Peroxydisulfate Treatments. *Langmuir* 1995, 11, 4386–4392, doi:10.1021/la00011a035.
- [47] Nansé, G.; Papirer, E.; Fioux, P.; Moguet, F.; Tressaud, A. Fluorination of Carbon Blacks. An X-Ray Photoelectron Spectroscopy Study. Part II. XPS Study of a Furnace Carbon Black Treated with Gaseous Fluorine at

- Temperatures below 100°C. Influence of the Reaction Parameters and of the Activation of the Carbon Blac. *Carbon N. Y.* 1997, 35, 371–388, doi:10.1016/S0008-6223(97)89609-1.
- [48] Stebounova, L. V.; Gonzalez-Pech, N.I.; Peters, T.M.; Grassian, V.H. Physicochemical Properties of Air Discharge-Generated Manganese Oxide Nanoparticles: Comparison to Welding Fumes. *Environ. Sci. Nano* 2018, 5, 696–707, doi:10.1039/c7en01046j.
- [49] Suntivich, J.; May, K.J.; Gasteiger, H.A.; Goodenough, J.B.; Shao-horn, Y.; Calle-vallejo, F.; Oscar, A.D.; Kolb, M.J.; Koper, M.T.M.; Suntivich, J.; et al. A Perovskite Oxide Optimized for Molecular Orbital Principles. *Science* (80-.). 2011, 334, 2010–2012, doi:10.1126/science.1212858.
- [50] Toupin, M.; Brousse, T.; Bélanger, D. Influence of Microstructure on the Charge Storage Properties of Chemically Synthesized Manganese Dioxide. *Chem. Mater.* 2002, 14, 3946–3952, doi:10.1021/cm020408q.
- [51] Bai, F.; He, Y.; Xu, L.; Wang, Y.; Wang, Y.; Hao, Z.; Li, F. Improved ORR/OER Bifunctional Catalytic Performance of Amorphous Manganese Oxides Prepared by Photochemical Metal-Organic Deposition. *RSC Adv.* 2022, 12, 2408–2415, doi:10.1039/d1ra08618a.

CHAPTER VII: ANTIBIOTIC DEGRADATION VIA FENTON PROCESS ASSISTED BY A 3-ELECTRON OXYGEN REDUCTION REACTION PATHWAY CATALYZED BY BIO-CARBON-MANGANESE COMPOSITES



Abstract

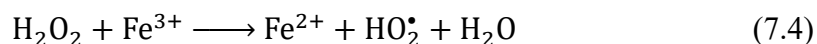
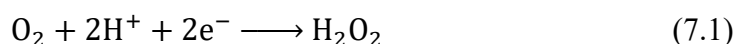
Bio-carbon-manganese composites obtained from olive mill wastewater were successfully prepared using manganese acetate as manganese source and olive wastewater as carbon precursor. The samples were chemically and texturally characterized by N₂ and CO₂ adsorption at 77 K and 273 K respectively, X-ray photoelectron spectroscopy (XPS) and X-ray diffraction. Electrochemical characterizations were studied by cyclic voltammetry (CV) and linear sweep voltammetry (LSV). Samples were evaluated in the electro-Fenton degradation of tetracycline in a typical system of three electrodes under natural conditions of pH and temperature (6.5 and 25 °C). The results show that the catalysts have a high catalytic power capable of degrading tetracycline (approx. 70 %) by a 3-electron oxygen reduction reaction pathway in which hydroxyl radicals are generated in situ and thus obviating the need for two catalysts (ORR and Fenton).

7.1.- INTRODUCTION

The contamination of water with antibiotics has become a global concern due to the associated risks to both the environment and public health. This includes the emergence of super-resistant bacteria that can cause new diseases and are able to tolerate treatments that were previously effective [1,2]. In general, the most widely used antibiotics worldwide are tetracycline (TTC), quinolone, aminoglycoside, macrolide and sulfonamide [3]. TTC due to its low cost and broad antimicrobial spectrum is used in both humans and animals, however, due to its low metabolism it has been found even in drinking water [4]. Conventional methods for degrading this type of contaminant, such as biological processes, filtration, coagulation, flocculation, sedimentation, adsorption, and membrane processes, have proven to be inadequate or inefficient. Therefore, it is necessary to explore new processes capable of partially or completely mineralizing these molecules [5-9].

Advanced oxidation processes (AOPs) are a highly regarded option for reducing various persistent pollutants in water due to the generation of hydroxyl radicals (OH^\bullet) that have a high oxidative capacity (2.8 V vs RH) capable of partially or completely mineralizing a broad range of pollutants. These radicals are produced on-site when using AOPs, which provides a powerful, alternative method for eliminating persistent pollutants in water [10-12]. The electro Fenton (EF) process is a notable AOP due to its high rate of electro-generated H_2O_2 , low production of iron sludge, and environmentally friendly nature [13]. In general, the EF process is based in the *in situ* production of H_2O_2 from the oxygen reduction reaction via 2 electrons (ORR 2e^-) (equation 7.1) at the cathode, generation of OH^\bullet by reacting

the Fenton-like catalyst (usually Fe^{+2}) with H_2O_2 (equation 7.2) and finally, regeneration of Fe^{+2} in the cathode (equation 7.3) and by interaction with H_2O_2 (equation 5.4) [14-17].



As can be seen, the cathode material is a determining factor in the efficiency of the EF process [18]. So recently different types of materials have been used among which noble metals [19,20], metal oxides [21,22] carbonaceous materials stand out [23-25]. However, carbonaceous materials stand out mainly for their low cost, good stability and abundance [26,27]. Various carbonaceous materials, in order to reduce costs, have been made from different biomasses such as bamboo [28], black soybean [29], inner layer of *torreya grandis* [30], waste wood (balsa wood) [31], water hyacinth [32], cellulose [33], and recently thinking about the circular economy, sewage sludge has been used as sources of biocarbon [34]. However, the main drawback with this type of carbon materials is the low activity and slow kinetics [35-37], so it is necessary to find a strategy to overcome this limitation and ameliorate the catalytic performances of carbon materials.

In general, doping with transition metals has resulted in a strategy to improve the ORR activity of carbonaceous materials, since in addition to this, transition metal ions can serve as electron donors to generate OH^\bullet from H_2O_2 [38]. Among the transition metals, MnOx oxides stand out, due to their different applications such

as catalysis, energy storage, and specifically in the electrochemical advanced oxidation processes (EAOP) [39]. MnO_2 has been shown to have the ability to dissociate H_2O_2 to OH^\bullet at a faster reaction rate [40]. However, the application of carbonaceous materials doped with Mn as possible bifunctional catalysts for the generation direct of OH^\bullet by a 3-electron pathway has not yet been studied.

In the present work, a biocarbon obtained from "*alpechín*" olive mill wastewater generated from the production of olive oil [41] was synthesized through chemical activation process and doped with manganese with three different methods and loadings. The synthesized composite materials were evaluated in an environmental remediation process as tetracycline degradation by the electro-Fenton process.

7.2.- EXPERIMENTAL

7.2.1.- Synthesis of bio-carbon-manganese composites

A bio-carbon denominated CK2 was the base for the development of the composite series. The CK2 was prepared from olive mill wastewater by chemical activation with potassium hydroxide (KOH), the preparation details and textural characterization are reported in previous works [42]. Manganese acetate ($(\text{CH}_3\text{COO})_2\text{Mn}\cdot 4\text{H}_2\text{O}$, Sigma Aldrich) was used as manganese precursor. Different amounts of the manganese acetate were dissolved in water and were added drop wise onto the corresponding amount of bio-carbon.

After impregnation, the prepared mixture was treated by three different methods. The composites were noted CK2-Mn-X-Y; X corresponds to the method used for the preparation and Y traduces the theoretical manganese percentage.

The first sample was calcined (after impregnation with 10 % of manganese) at 330 °C for 1 h under nitrogen gas (300 mL min⁻¹) and 1 h under CO₂ flow. The corresponding sample was noted CK2-Mn-1-10. The second sample was prepared by adding H₂O₂ (25 mL g⁻¹ carbon) to the impregnated samples and, after that, the samples were calcined at 330 °C for 2 h under 300 mL min⁻¹ of nitrogen. The corresponding composites were noted CK2-Mn-2-10, CK2-Mn-2-25, and CK2-Mn-2-60. The last sample was prepared by a few modifications of the second method, the impregnated sample was calcined at 330 °C for 2 h under 300 mL min⁻¹ of nitrogen before to be treated with H₂O₂ (25 mL g⁻¹ carbon), CK2-Mn-3-10.

7.2.2.- Textural and chemical characterization

The textural characterization was obtained by using a Autosorb equipment from Quantachrome system. N₂ adsorption isotherm at -196 °C and CO₂ at 0 °C were obtained. The B.E.T. and Dubinin-Radushkevich (DR) methods, were applied to the nitrogen and carbon dioxide isotherms, respectively, to obtain the apparent surface area, total micropore volume (W₀ with N₂), narrow micropore volume (W₀ with CO₂) and mean micropore width (L₀) [43-45]. The pore size distribution (PSD) was determined by applying Quenched Solid Density Functional Theory (QSDFT) to the N₂ adsorption isotherms, assuming slit-shaped pores.

The crystallinity of manganese oxide particles of all CK2-Mn-X-Y composites were investigated by X-ray diffraction Bruker D8 advance with Cu K α radiation.

The surface chemistry of the samples was obtained by X-ray photoelectron spectroscopy using ESCA 5701 from Physical Electronics (PHI) system (equipped with MgK α anode, model PHI 04-548. X-ray source (h ν = 1253.6 eV) and hemispherical electron energy analyzer). For the analysis of the XPS peaks, the C_{1s}

peak position was set at 284.6 eV and used as reference to locate the other peaks. The XPS peaks were fitted using Gaussian-Lorentzian peak shapes and a Shirley background through the least squares method, utilizing XPS peaks 4.1.

7.2.3.- Electrochemical characterization

The activity for ORR was studied with the RRDE technique by using an Autolab electrochemical system, Metrohm, associated with a compact potentiostat/galvanostat (PGSTAT101). The working electrode was prepared by depositing on the RRDE tip 20 μL of a ink, consisting of 5 mg of sample dispersed in 1 mL of a Nafion solution (1/9 v:v Nafion 5 %/water), and dried under infrared radiation. Electrochemical measurements were carried out in a standard three-electrode electrochemical cell at room temperature. Using a Pt sheet as a counter electrode and an Ag/AgCl reference electrode. The electrolyte was a solution of KOH 0.1M prepared in deionized water. Before each electrochemical measurement, the electrolyte was saturated with N_2 or O_2 by purging the necessary gas into the KOH 0.1M solution at room temperature for 30 minutes. Cyclic voltammetry (CV) was collected in the KOH 0.1M solution saturated with N_2 or O_2 in a range of 0.40 to -0.80 V at 50mV s^{-1} with the electrode at a rotational speed of 1000 rpm. Linear scanning voltammetry (LSV) for the ORR was carried out with a potential range between 0.40 V to -0.80 at 50mV s^{-1} with the electrode at rotational speeds of 500, 1000, 1500, 2000, 2500, 3000 and 3500 rpm.

The number of electrons transferred and H_2O_2 selectivity were calculated using the equations (7.5) and (7.6), that is calculated from the data obtained in the RRDE during the experiment [46,47].

$$n = \frac{4 \times I_D}{I_D + \frac{I_R}{N_C}} \quad (7.5)$$

$$\%H_2O_2 = \frac{200 \times \frac{I_R}{N_C}}{I_D + \frac{I_R}{N_C}} \quad (7.6)$$

where, I_D and I_R are the disk and ring current respectively, and N_C is the collection efficiency of the RRDE (0.249).

The current density (J_K) was obtained by Koutecky-Levich equation (7.7).

$$\frac{1}{J} = \frac{1}{J_K} + \frac{1}{B \times \omega^{1/2}} \quad (7.7)$$

with $B = (0.62)n \times F \times A \times D^{2/3} \times \nu^{-1/6} \times C$

where F is Faraday's constant ($96485332 \text{ mC mol}^{-1}$), n number of electrons transferred per oxygen molecule, A is the disc area of the RRDE (0.2475 cm^2), D diffusion coefficient of oxygen ($1.9 \times 10^{-5} \text{ cm}^2 \text{ s}^{-1}$), ν is kinematic viscosity ($0.01 \text{ cm}^2 \text{ s}^{-1}$) and finally C is the solubility of oxygen ($1.2 \times 10^{-6} \text{ mol cm}^{-3}$) [48,49].

7.2.4.- Electro Fenton processes

The electro Fenton process was carried out using a standard three-electrode electrochemical cell with capacity for 150 mL of solution at room temperature. The TTC concentration approached 40 mg L^{-1} , using Na_2SO_4 [0.5M] as a supporting electrolyte with continuous agitation. Potentiostat was maintained in potentiostatic mode at -0.6 V .

The working electrode was prepared by mixing 45 mg of CK2-Mn-X-Y with 8.5 mg of 60% PTFE, for subsequent drying at $100 \text{ }^\circ\text{C}$ for 12 h. Once dried, a paste

was obtained that was deposited on a sheet of graphite (50 mg on each face). While the reference electrode was Ag/AgCl, and the counter electrode used was a platinum sheet. The working pH was 6.5, as is natural of the TTC solution. TTC concentrations in solution were determined by a UV-vis spectrophotometer at a wavelength of 356.5 nm.

7.3.- RESULTS AND DISCUSSIONS

7.3.1.- Porosity and surface area of bio-carbon-manganese composites

Figure 7.1 shows the N₂ adsorption-desorption isotherms of CK2-Mn-X-Y samples. Textural properties of the composites were examined by N₂ adsorption-desorption isotherm measurements. All samples show an hybrid type I-IV isotherm, with a high N₂ adsorption at low relative pressures and an hysteresis loop at intermediates ones, indicating the presence of micropores and mesopores [50]. Also, the samples CK2-Mn-3-10, CK2-Mn-1-10 and CK2-Mn-2-60, present a peak associated to capillary condensation. Note that the addition of Mn to the samples produce a blockage of the porosity in all cases, however this porosity depletion depends on the final precursor decomposition treatment. From figure 7.1, it is possible to observe that the H₂O₂ activation before to carbonization (CK2-Mn-2-10) results in the better preservation of the porosity, due possibly to the chemical attack in the porous texture of the sample (CK2) which leads to the generation of new porosity. Finally, it is highlighted that the Mn amount directly affect the porosity, the higher the Mn content, the higher the porosity decrease, associated to the blockage of the pores of the carbon matrix by the manganese particles, this is possible observe in the samples CK2-Mn-2 with different Mn charge (10, 25 and 60).

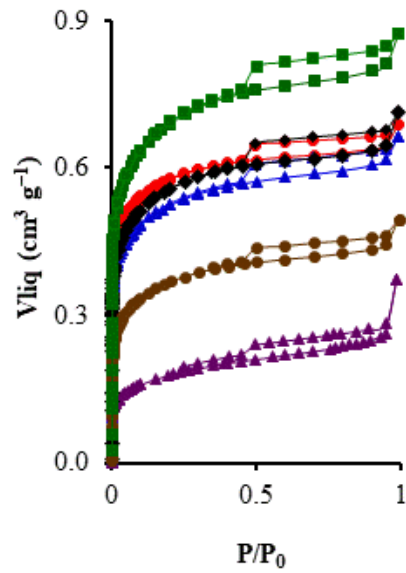


Figure 7.1. Isotherms N₂ adsorption of all the sample CK2, ■; CK2-Mn-1-10, ●; CK2-Mn-2-10, ◆; CK2-Mn-3-10, ▲; CK2-Mn-2-25, ●; CK2-Mn-2-60, ▲.

The B.E.T surface area (S_{BET}), micropore surface area (S_{micro}), mesopore surface area (S_{DFT}), and pore volume (V_{DFT}) of CK2-Mn-X-Y samples are listed in Table 7.1.

Table 7.1. Textural characteristics of all the samples obtained by N₂ adsorption isotherms at -196 °C and CO₂ at 0 °C.

Sample	N ₂			CO ₂	
	S _{BET}	W ₀	L ₀	W ₀	L ₀
	m ² g ⁻¹	cm ³ g ⁻¹	nm	cm ³ g ⁻¹	nm
CK2	1672	0.66	1.33	0.38	0.68
CK2-Mn-1-10	1232	0.50	1.32	0.29	0.67
CK2-Mn-2-10	1380	0.56	1.33	0.31	0.67
CK2-Mn-3-10	1257	0.50	1.31	0.87	1.28
CK2-Mn-2-25	945	0.37	1.33	0.22	0.82
CK2-Mn-2-60	412	0.16	1.40	0.10	0.73

The same results can be observed analyzing table 7.1. The original bio-carbon presents a surface area as high as 1672 m² g⁻¹. This porosity decreases after the incorporation of Mn; however, this porosity decrease is less pronounced when the pristine carbon is treated with H₂O₂ before the manganese decomposition at 330 °C. The physical activation with CO₂ result in a micropore volume lower than with the other methods (chemical activation) decreasing from 0.38 (CK2) to 0.29 cm³ g⁻¹, indicating the blockage of the ultramicroporosity by the Mn nanoparticles or an opening of such porosity by the CO₂ treatment which is agrees whit the reported in the literature [51]. By the other hand, the decrease in narrow micropore volume and

total micropore volume, of the samples CK2-Mn-2-25 and Ck-2-Mn-60, can be attributed to pore enlargement and blockage of these pores with Mn particles, which result in a decrease of B.E.T surface area, indicating a lower developing of microporosity [52]. The sample CK2-Mn-3-10 have a $L_0(\text{CO}_2)$ greater than 0.7 nm and a $W_0(\text{N}_2) < W_0(\text{CO}_2)$ indicating a diffusional problem of N_2 which is translate in a bad activation degree, due to restrictions in the microporosity, while the other samples have $W_0(\text{N}_2) > W_0(\text{CO}_2)$ that is typic of an adequate activation degree.

7.3.2.- X-ray diffraction of the composites

Figure 7.2 shows the XRD diffractograms of the CK2-Mn-X-Y samples, we can observe different peaks associated to some species of Mn, indicating the presence of manganese in different oxidation states. Is possible to determine the peaks to approximately 18° , 29° , 32° , 36° , 38° , 44° , 58° , 60° and 65° , associated to the planes (101), (112), (103), (211), (004), (220), (321), (224) and (400) characteristics of spinel structure Mn_3O_4 (CK2-Mn-3-10) [53-55]. While the peaks closer to 35° , 40° and 59° correspond to the crystalline planes (111), (100) and (220) of MnO (CK2-Mn-3-60) [56-58]. The samples CK2-Mn-1-10 and CK2-Mn-2-10 present spectra corresponding to a practically amorphous specimens, so it is raising that dispersion of manganese particles was better in these two materials. Increasing the manganese content, a new crystalline phase emerges finding well defined peaks of MnO crystalline phase form for CK2-Mn-2-25 and CK2-Mn-2-60 samples.

From this results, would be expected that the better catalytic results will be obtained with the samples with 10% of Mn, due to the presence of Mn_3O_4 , which is a specie considered active for promote the OH^* generation by ORR [59].

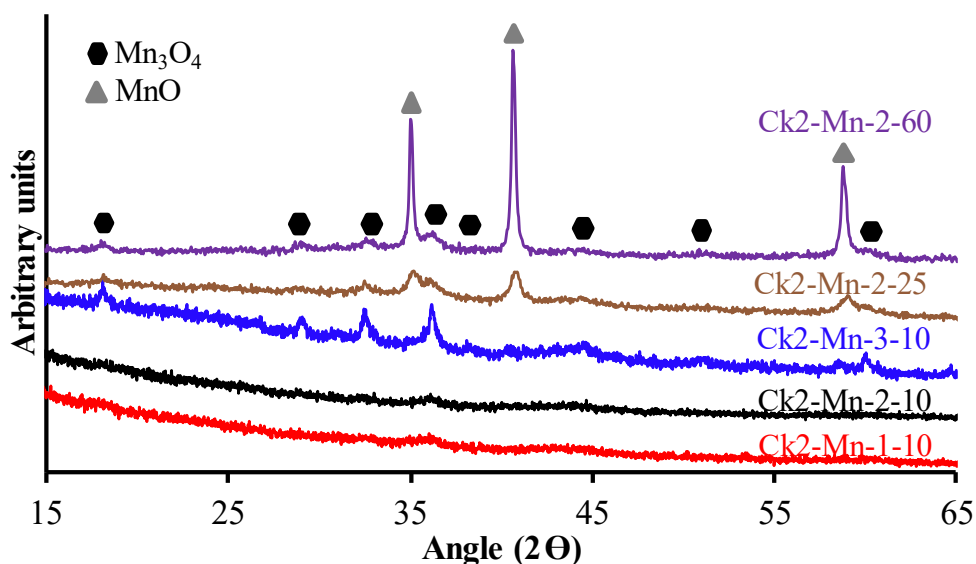


Figure 7.2. X-ray diffraction of the composites.

7.3.3.- XPS spectra

Figure 7.3 and 7.4 shows the XP spectra for the signals C_{1s} , O_{1s} and Mn_{2p} . From the deconvolution of XP spectra the surface composition of samples were determined and the results were compiled in tables 7.2. The peaks obtained from the deconvolution of C_{1s} spectrum, were related to C=C (284.6 eV), C-O (285.7 eV), C=O (287 eV), O-C=O (288.4 eV) CO_2 or $\pi-\pi^*$ bonds and plasmon (290 and 291.6 eV) [60-64]. The peaks from O_{1s} , were deconvoluted in O-Mn (530.0 eV), O=C (531.4 eV), and O-C (533.4 eV) [65,66]. From Mn_{2p} the peaks detected were Mn^{2+} (641.6 eV) and Mn^{3+} (643.4 eV) [67-71].

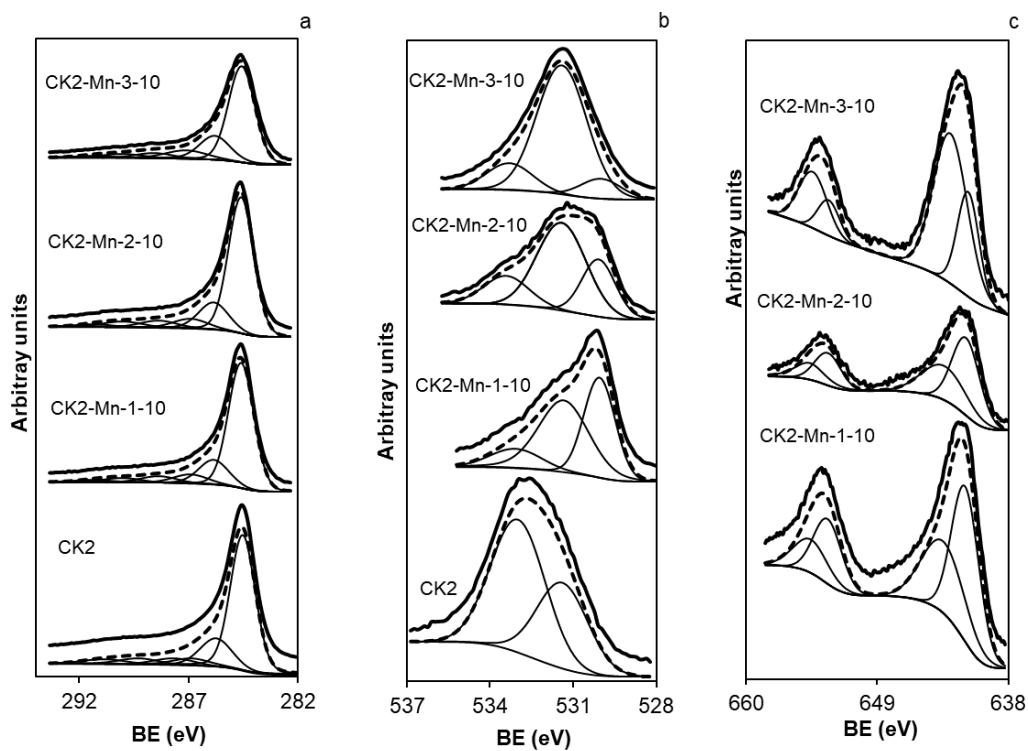


Figure. 7.3. XPS spectra of a) C_{1s}, b) O_{1s} and c) Mn_{2p} for original activated carbon CK2 and samples prepared with different impregnation methods and 10 % of manganese loading.

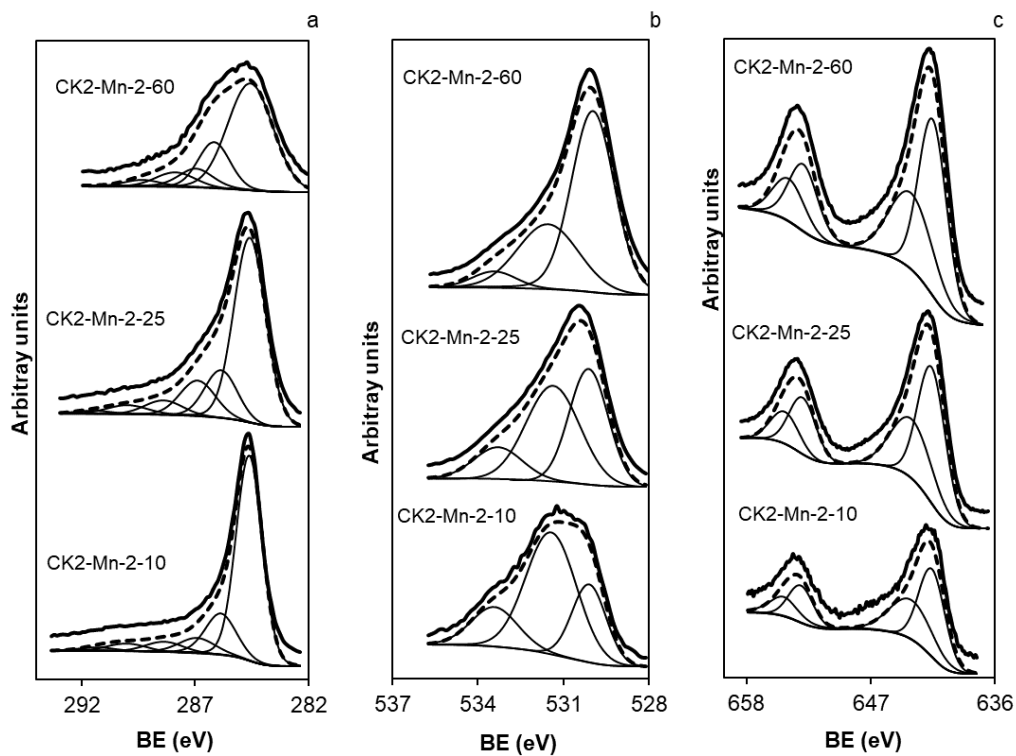


Figure. 7.4.-XPS spectra of a) C_{1s}, b) O_{1s} and c) Mn_{2p} for samples prepared with different amount of manganese.

Table 7.2a. Compositional characterization by XPS analysis of CK2-MN-X-10.

Sample	C _{1s}	FWHM	peak	O _{1s}	peak	O	Mn _{2p3/2}	peak	Mn	Mn ³⁺ /Mn ²⁺
CK2	284.5	1.34	64	531.4	38	6.0				
	285.8		18	533.0	62					
	286.9		5							
	287.7		5							
	289.3		4							
	290.9		3							
CK2-Mn-1-10	284.6	1.37	67	530.0	39	11.9	641.6	58	14.6	0.70
	285.9		16	531.3	49		643.5	42		
	286.9		7	533.1	12					
	288.4		5							
	290.0		4							
	291.3		1							
CK2-Mn-2-10	284.6	1.37	66	530.1	25	8.8	641.6	58	7.6	0.72
	285.9		17	531.4	57		643.4	42		
	286.9		7	533.4	18					
	288.4		5							
	290.0		4							
	291.3		2							
CK2-Mn-3-10	284.6	1.41	63	530.0	9	18.3	641.7	31	17.7	2.25
	285.8		18	531.4	76		643.2	69		
	287.1		9	533.3	15					
	288.6		5							
	290.0		4							
	291.4		2							

Table 7.2b. Compositional characterization by XPS analysis of CK2-Mn-2-Y.

Sample	C _{1s}	FWHM	peak	O _{1s}	peak	O	Mn _{2p3/2}	peak	Mn	Mn ³⁺ /Mn ²⁺
CK2-Mn-2-10	284.6	1.37	66	530.1	25	8.8	641.6	58	7.6	0.72
	285.9		17	531.4	57		643.4	42		
	286.9		7	533.4	18					
	288.4		5							
	290.0		4							
	291.3		2							
CK2-Mn-2-25	284.6	1.66	61	530.1	40	25.6	641.6	61	32.9	0.66
	285.9		16	531.4	46		643.4	39		
	286.9		13	533.3	14					
	288.4		5							
	290.0		4							
	291.5		1							
CK2-Mn-2-60	284.6	2.45	64	530.0	63	35.5	641.5	60	52.8	0.64
	286.0		13	531.5	32		643.4	40		
	287.0		13	533.4	5					
	288.4		6							
	289.9		3							
	291.6		1							

From the results obtained it can be concluded that all samples present similar composition profiles with the same chemical species being found in all cases. However, several significant facts are worth noting. The first one is the increase in the C peak width at 284.6 eV which is indicative of an increase in the defects present in the graphitic crystals or a decrease in the size of the microcrystals, both facts will influence the electrical conductivity of the catalysts. Secondly, there is a noticeable increase in the O content when Mn is introduced into the catalysts, this is due to the oxidation produced by the reduction of KMnO₄ during the heat treatment. With respect to the Mn spectrum, two clearly differentiated species Mn²⁺ and Mn³⁺ are

detected in all samples. However, a clear difference appears for sample CK2-Mn-3-10 for which the $\text{Mn}^{3+}/\text{Mn}^{2+}$ ratio is higher than for the rest of the samples, which is indicative of the formation of Mn_3O_4 due to the oxidation treatment carried out with H_2O_2 , which agrees with the data obtained by XRD. For the rest of the samples this ratio varies very little, between 0.64 and 0.71 indicating that part of the Mn^{2+} formed by the reduction treatment can be oxidised superficially to Mn^{3+} by exposure to air.

7.3.4.- Electrochemical characterization

The CV results are shown in Figure 7.5, where is possible to observe that all samples have ORR activity. The sample CK2-Mn-2-10, showed the higher capacitance attributed principally to the type of porosity and large specific surface [72]. These better behaviors could be related to the improved hydrophilicity of the surface due to the increase in the oxygen surface groups and the presence of MnO_x which improves the electrolyte-surface contact favoring the diffusion of the ions; and the optimization of the pore structure by the presence of MnO_x . This leads to a decrease in the resistance of the electrodes, enhancing their performance for energy storage.

Based on its chemical composition and textural characteristics, sample CK2-Mn-2-10 is expected to have better ORR activity and higher capacitance compared to the other samples. There is no visible OPR peak when the electrolyte is saturated with N_2 . In contrast, a well-defined ORR peak is observed in the O_2 -saturated 0.1 M KOH solution, demonstrating the excellent electrocatalytic activity for ORR. More interestingly, all CV curves (Both N_2 and O_2 saturated) appear strong redox peaks, the peak at ca. 0 V vs. Ag/AgCl was attributed to $\text{Mn}^{2+}/\text{Mn}^{3+}$ redox because

the area of the peak at ca. 0 V vs. Ag/AgCl increases with greater Mn concentration (Mn content changes from 10 to 60) [73] and especially with the amount of Mn^{2+} and Mn^{3+} present in the sample.

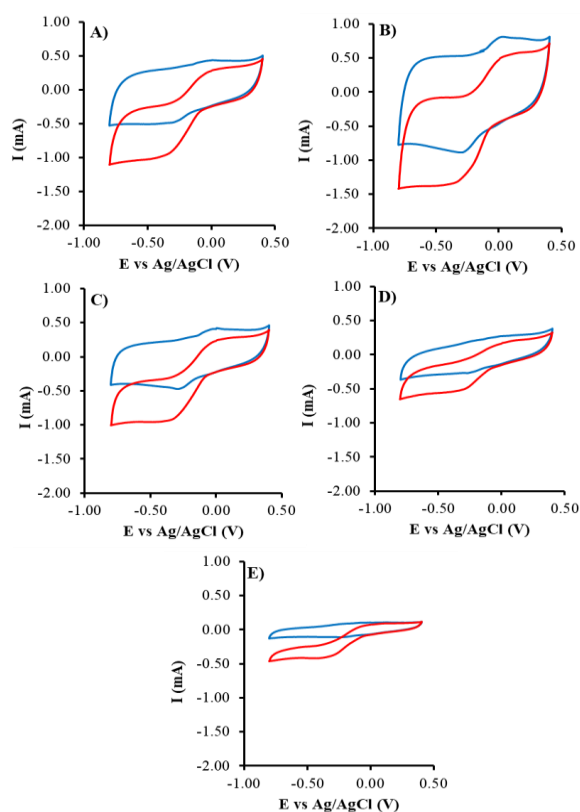


Figure. 7.5.- CV of A) CK2-Mn-1-10, B) CK2-Mn-2-10, C) CK2-Mn-3-10, D) CK2-Mn-2-25, E) CK2-Mn-2-60 in N_2 (blue) and O_2 (red).

In this line, table 7.3 shows that the highest J_K value was obtained with the pre-activated sample with H_2O_2 (CK2-Mn-2-10) which possibly is due in one part to the well dispersed manganese phase and also to the highest surface area, that allows

more current to pass into matrix, for the same could explain the J_K value lower of CK2-Mn-2-25 and CK2-Mn-2-60.

Table 7.3. Current density J_K .

Sample	J_K (mA cm⁻²)
CK2	7.39
CK2-Mn-1-10	8.99
CK2-Mn-2-10	11.37
CK2-Mn-3-10	10.68
CK2-Mn-2-25	7.44
CK2-Mn-2-60	2.68

Figure. 7.6 and 7.7 show the correlation between J_K and the Mn^{3+}/Mn^{2+} amount and $S_{B.E.T}$ respectively. The correlation coefficient of R^2 was closer to 1 in $S_{B.E.T}$ (0.98) than with Mn^{3+}/Mn^{2+} amount (0.94), indicating that although the manganese can to be an active site for the ORR, the current density is affected principally for the $S_{B.E.T}$. [74]. In this case, we can say that physical activation gives as result a higher surface area that is traduced in a better J_K , which is an important parameter for the different electrochemical applications.

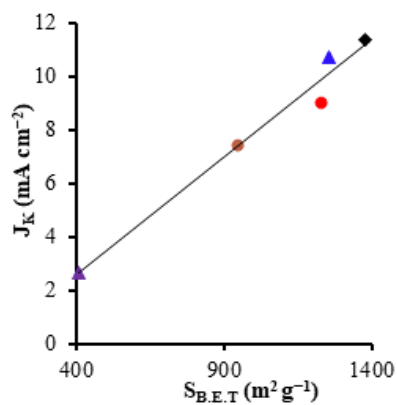


Figure. 7.6.- Correlation between the current density and the surface area B.E.T. of CK2-Mn-1-10, ●; CK2-Mn-2-10, ◆; CK2-Mn-3-10, ▲; CK2-Mn-2-25, ●; CK2-Mn-2-60, ▲.

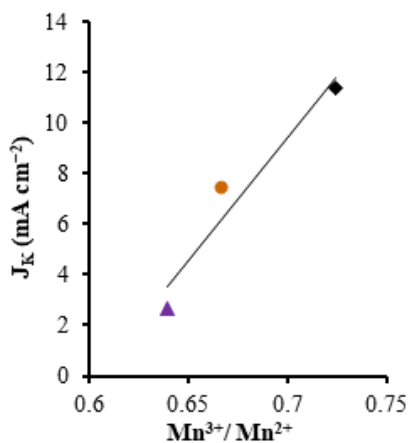


Figure. 7.7.- Correlation between the current density and the Mn³⁺/Mn²⁺ ratio of CK2-Mn-2-10, ◆; CK2-Mn-2-25, ●; CK2-Mn-2-60, ▲.

Figure 7.8 shows the number of electrons transferred and selectivity to H_2O_2 . Where is possible to observe that the presence of Mn increase the number of electrons transferred, this is favorable for the ORR $4e^-$, however for the case of H_2O_2 generation is necessary values closer to 2 electrons, with a high selectivity to H_2O_2 , for this is possible to suppose that the best catalyst for electro-Fenton was obtained by using the samples CK2-Mn-1-10 and CK2-Mn-3-10 (14.9 and 16.6 respectively) which have higher amounts of manganese on the external surface area compared to the sample CK2-Mn-2-10, and also, a higher surfaces areas compared to other samples with higher amounts of manganese CK2-Mn-2-25 and CK2-Mn-2-60. In this case we can observe that both the amount of Mn and the surface porosity could be important parameters for the number of electrons transferred. Nevertheless, according to XRD results, the increasing from 10 to 60 wt.% Mn on the same series significant chemical changes occurred: sample CK2-Mn-2-10 only could show some Mn_3O_4 phase while the presence of MnO appear in sample CK2-Mn-2-25, and in sample CK2-Mn-2-60 as the main one phase. On the other hand, sample CK2-Mn-3-10 which show higher and better-defined peaks of Mn_3O_4 is the one which produces larger amount of H_2O_2 and show n-value closer to 3.

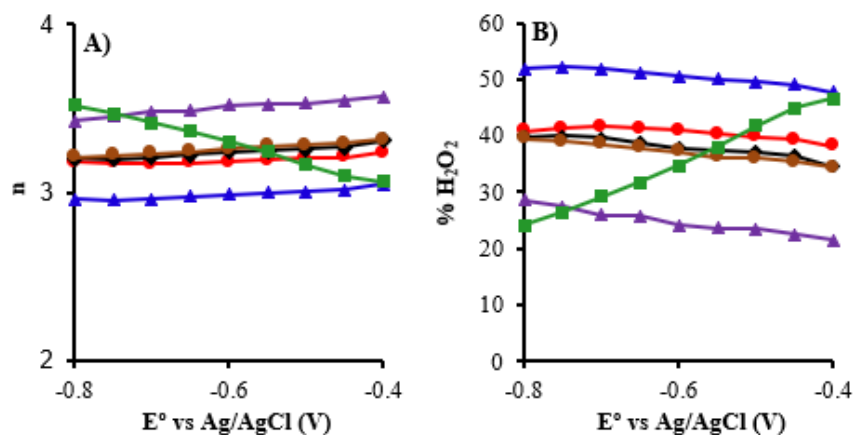


Figure. 7.8.- A) Number of electrons transferred and B) Selectivity to H_2O_2 of CK2, ■; CK2-Mn-1-10, ●; CK2-Mn-2-10, ◆; CK2-Mn-3-10, ▲; CK2-Mn-2-25, ●; CK2-Mn-2-60, ▲.

7.3.5.- Electro-Fenton

Since the presence of MnO phase doesn't favor the desired ORR performance, only samples with a 10 wt.% of Mn were checked in the electro-Fenton tests. In this way, figure 7.9 shows the tetracycline degradation with the above-mentioned samples as well as only graphite (electrode-support material on which the prepared samples are pasted for the electro-Fenton tests).

Additionally, were made electro-Fenton test in N_2 with H_2O_2 and N_2 without H_2O_2 (figure 7.10), it is with the objective to evaluate the effect of hydrogen peroxide and of the support.

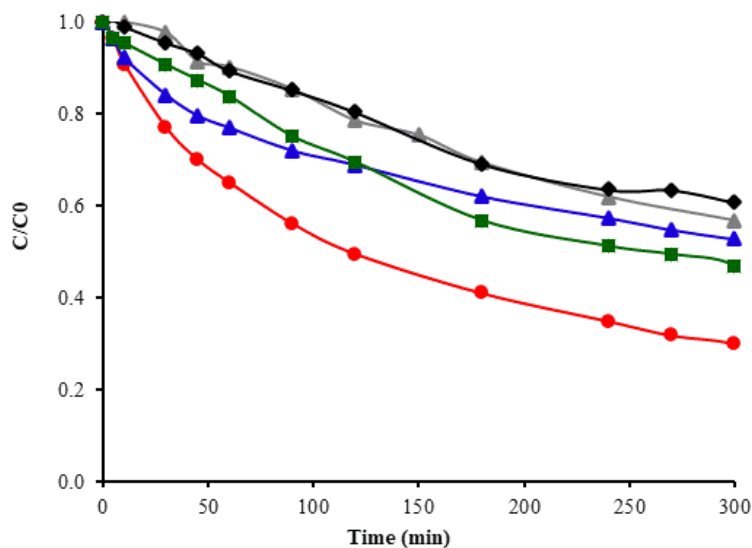


Figure. 7.9.- TTC degradation by electro Fenton with: Graphite, ▲; CK2, ■; CK2-Mn-1-10, ●; CK2-Mn-2-10, ◆; CK2-Mn-3-10, ▲.

The TTC degradation in presence only of O_2 followed an order of CK2-Mn-1-10 > CK2 > CK2-Mn-3-10 > Graphite > CK2-Mn-2-10, whereby the sample CK2-Mn-1-10 was used for evaluated its activity in presence of N_2 with H_2O_2 . The TTC degradation in presence of N_2 showed a lower value compared with the O_2 (figure 7.10), with this experiment have established that the O_2 presence have an important effect on the system, much more than the direct addition of H_2O_2 and obviously than only the presence of N_2 with total absence of O_2 and H_2O_2 .

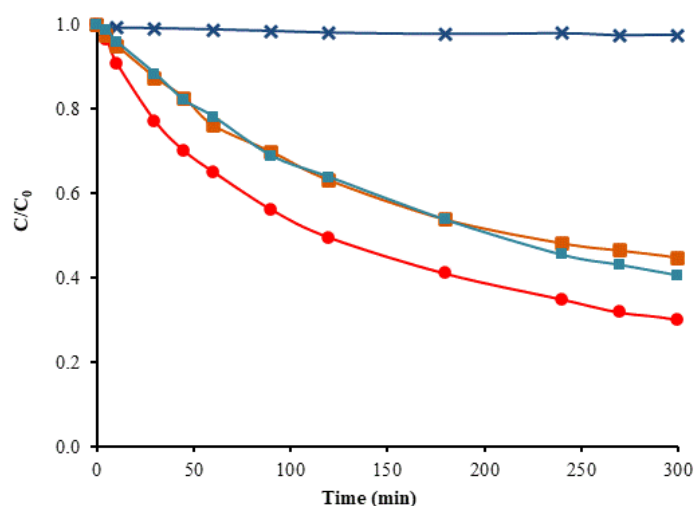
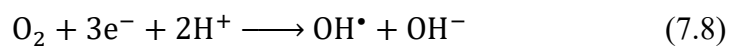
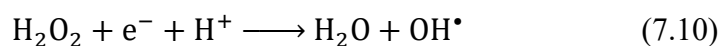
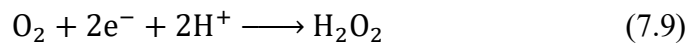


Figure. 7.10.- TTC degradation by electro Fenton with: CK2-Mn-1-10 in O₂, ●; CK2-Mn-1-10 in Fenton traditional, ■; CK2-Mn-1-10 in N₂ and H₂O₂, ■; H₂O₂ without catalyst, ✕.

These results could hide a probable 3 electrons ORR (equation 7.8) pathway with direct formation of hydroxyl radicals (OH[•]) which would enhance the tetracycline degradation, as it has been observed in figure 7.10 by comparing the effect of H₂O₂ addition versus the O₂ bubbling [75].



However, not it's possible dismiss the route by a electro Fenton traditional with the ORR pathway 2 electrons with an initial reduction of O₂ to H₂O₂ (equation 7.9) [76].



In this process the $\text{Mn}^{3+}/\text{Mn}^{2+}$ redox cycle in the spinel structure is crucial since electrons could be provided. Besides, the following way would be working on parallel:



However, with our results it could be proposed that the surface area B.E.T have an effect more significant in the TTC degradation ($R^2 > 0.6$) by affecting the value of J_K , which could be attributed to greater degree of access to the active sites.

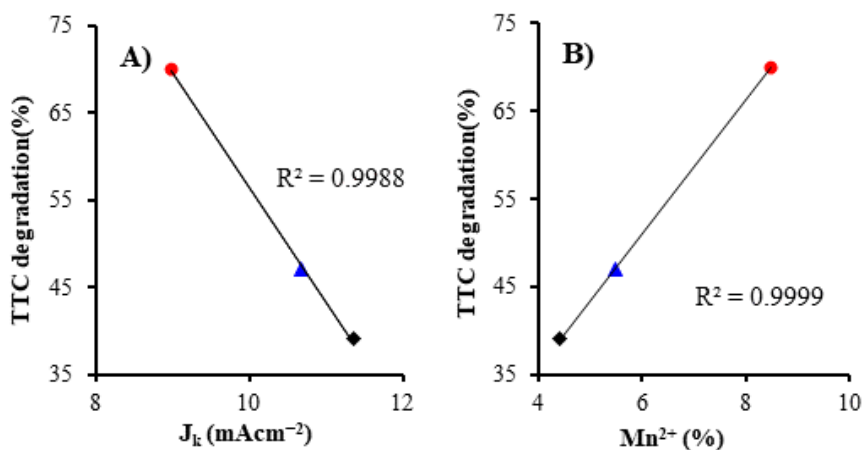


Figure. 7.11.- Correlation between the TC degradation and the J_K value (A) and % of Mn^{2+} (B), of CK2-Mn-1-10, ●; CK2-Mn-2-10, ◆; CK2-Mn-3-10, ▲.

In fact, it seems that a relationship between the Mn^{2+} values and tetracycline degradation occur: CK2-Mn-1-10 (8.42 Mn^{2+} ; 70% TTC removal), CK2-Mn-3-10 (5.48 Mn^{2+} ; 47% TTC removal), and CK2-Mn-2-10 (4.40 Mn^{2+} ; 39% TTC removal). The relevance Mn^{2+} , could be explained by the interaction between the Mn^{2+} and H_2O_2 that can generate OH^{\bullet} radicals (Fenton traditional) and of the possible generation direct of OH^{\bullet} radicals (ORR $3e^-$ proposed) with the Mn^{3+} could propose as active site for this route. We propose that a good relation between Mn^{2+} percentage and the surface area can be key in the catalytic activity for degrading the tetracycline. So, we can conclude that the tetracycline degradation depends on the J_K which depends on the surface area and the percentage of manganese $2+$ which interacts with H_2O_2 generating OH^{\bullet} radicals.

7.4.- CONCLUSIONS

Two series of bio-carbon-manganese composites have been prepared with bifunctional behavior in the electro-Fenton process: H_2O_2 generation from ORR, and hydroxyl radical formation. Moreover, the hydroxyl radicals can be formed by two different ways, i) H_2O_2 decomposition on Mn phases as heterogeneous Fenton, or ii) by H_2O_2 reduction in one pot way directly from the ORR following a pathway or 3 electrons. Besides, the current density during the ORR is directly proportional to the surface area of these materials. The development of Mn_3O_4 phase by a right preparation method into these composites seem to be the clue to both mentioned processes can take place, as consequence of the Mn^{+3}/Mn^{+2} redox cycles that can occur in the spinel structure. This bifunctional behavior makes possible the antibiotic degradation in water solutions by a process in which H_2O_2 don't have to be added because it is in situ produced in such any way.

BIBLIOGRAPHY

- [1] Garza-Campos, B.; Morales-Acosta, D.; Hernández-Ramírez, A.; Guzmán-Mar, J.L.; Hinojosa-Reyes, L.; Manríquez, J.; Ruiz-Ruiz, E.J. Air Diffusion Electrodes Based on Synthesized Mesoporous Carbon for Application in Amoxicillin Degradation by Electro-Fenton and Solar Photo Electro-Fenton. *Electrochim. Acta* 2018, 269, 232–240, doi:10.1016/j.electacta.2018.02.139.
- [2] Ahmadi, A.; Zarei, M.; Hassani, A.; Ebratkhahan, M.; Olad, A. Facile Synthesis of Iron(II) Doped Carbonaceous Aerogel as a Three-Dimensional Cathode and Its Excellent Performance in Electro-Fenton Degradation of Ceftazidime from Water Solution. *Sep. Purif. Technol.* 2021, 278, 119559, doi:10.1016/j.seppur.2021.119559.
- [3] Pan, Y.; Zhang, Y.; Zhou, M.; Cai, J.; Tian, Y. Enhanced Removal of Antibiotics from Secondary Wastewater Effluents by Novel UV/Pre-Magnetized Fe⁰/H₂O₂ Process. *Water Res.* 2019, 153, 144–159, doi:10.1016/j.watres.2018.12.063.
- [4] Qin, J.; Ruan, Y.; Yi, L.; Sun, H.; Qi, Q.; Zhao, L.; Xiong, Y.; Wang, J.; Fang, D. Tetracycline (TC) Degradation via Hydrodynamic Cavitation (HC) Combined Fenton's Reagent: Optimizing Geometric and Operation Parameters. *Chem. Eng. Process. - Process Intensif.* 2022, 172, 108801, doi:10.1016/j.cep.2022.108801.
- [5] Du, X.; Fu, W.; Su, P.; Zhang, Q.; Zhou, M. FeMo@porous Carbon Derived from MIL-53(Fe)@MoO₃ as Excellent Heterogeneous Electro-Fenton Catalyst: Co-Catalysis of Mo. *J. Environ. Sci. (China)* 2023, 127, 652–666, doi:10.1016/j.jes.2022.06.031.

- [6] Yang, C.; Fan, Y.; Shang, S.; Li, P.; Li, X. yan Fabrication of a Permeable SnO₂-Sb Reactive Anodic Filter for High-Efficiency Electrochemical Oxidation of Antibiotics in Wastewater. *Environ. Int.* 2021, 157, doi:10.1016/j.envint.2021.106827.
- [7] Akbari, M.Z.; Xu, Y.; Lu, Z.; Peng, L. Review of Antibiotics Treatment by Advance Oxidation Processes. *Environ. Adv.* 2021, 5, 100111, doi:10.1016/j.envadv.2021.100111.
- [8] Yuan, Q.; Qu, S.; Li, R.; Huo, Z.Y.; Gao, Y.; Luo, Y. Degradation of Antibiotics by Electrochemical Advanced Oxidation Processes (EAOPs): Performance, Mechanisms, and Perspectives. *Sci. Total Environ.* 2023, 856, 159092, doi:10.1016/j.scitotenv.2022.159092.
- [9] Wang, J.; Zhuan, R. Degradation of Antibiotics by Advanced Oxidation Processes: An Overview. *Sci. Total Environ.* 2020, 701, 135023, doi:10.1016/j.scitotenv.2019.135023.
- [10] Midassi, S.; Bedoui, A.; Bensalah, N. Efficient Degradation of Chloroquine Drug by Electro-Fenton Oxidation: Effects of Operating Conditions and Degradation Mechanism. *Chemosphere* 2020, 260, 127558, doi:10.1016/j.chemosphere.2020.127558.
- [11] Cao, P.; Zhao, K.; Quan, X.; Chen, S.; Yu, H. Efficient and Stable Heterogeneous Electro-Fenton System Using Iron Oxides Embedded in Cu, N Co-Doped Hollow Porous Carbon as Functional Electrocatalyst. *Sep. Purif. Technol.* 2020, 238, 116424, doi:10.1016/j.seppur.2019.116424.
- [12] Le, T.T.; Hoang, V.C.; Zhang, W.; Kim, J.M.; Kim, J.; Moon, G. hee; Kim, S.H. Mesoporous Sulfur-Modified Metal Oxide Cathodes for Efficient Electro-Fenton Systems. *Chem. Eng. J. Adv.* 2022, 12, 100371,

- doi:10.1016/j.ceja.2022.100371.
- [13] Puga, A.; Rosales, E.; Pazos, M.; Sanromán, M.A. Prompt Removal of Antibiotic by Adsorption / Electro-Fenton Degradation Using an Iron-Doped Perlite as Heterogeneous Catalyst. 2020, 144, 100–110, doi:10.1016/j.psep.2020.07.021.
- [14] Arellano, M.; Oturan, N.; Oturan, M.A.; Pazos, M.; Sanromán, M.Á.; González-Romero, E. Differential Pulse Voltammetry as a Powerful Tool to Monitor the Electro-Fenton Process. *Electrochim. Acta* 2020, 354, doi:10.1016/j.electacta.2020.136740.
- [15] Ganzenko, O.; Trelu, C.; Oturan, N.; Huguenot, D.; Péchaud, Y.; van Hullebusch, E.D.; Oturan, M.A. Electro-Fenton Treatment of a Complex Pharmaceutical Mixture: Mineralization Efficiency and Biodegradability Enhancement. *Chemosphere* 2020, 253, doi:10.1016/j.chemosphere.2020.126659.
- [16] Chai, Y.; Qin, P.; Zhang, J.; Li, T.; Dai, Z.; Wu, Z. Simultaneous Removal of Fe(II) and Mn(II) from Acid Mine Wastewater by Electro-Fenton Process. *Process Saf. Environ. Prot.* 2020, 143, 76–90, doi:10.1016/j.psep.2020.06.026.
- [17] Deng, F.; Olvera-Vargas, H.; Zhou, M.; Qiu, S.; Sirés, I.; Brillas, E. Critical Review on the Mechanisms of Fe²⁺ Regeneration in the Electro-Fenton Process: Fundamentals and Boosting Strategies. *Chem. Rev.* 2023, 123, 4635–4662, doi:10.1021/acs.chemrev.2c00684.
- [18] Wang, J.; Qin, J.; Liu, B.; Song, S. Reaction Mechanisms and Toxicity Evolution of Sulfamethoxazole Degradation by CoFe-N Doped C as Electro-Fenton Cathode. *Sep. Purif. Technol.* 2022, 298, 121655,

- doi:10.1016/j.seppur.2022.121655.
- [19] Verdaguer-Casadevall, A.; Deiana, D.; Karamad, M.; Siahrostami, S.; Malacrida, P.; Hansen, T.W.; Rossmeisl, J.; Chorkendorff, I.; Stephens, I.E.L. Trends in the Electrochemical Synthesis of H₂O₂: Enhancing Activity and Selectivity by Electrocatalytic Site Engineering. *Nano Lett.* 2014, 14, 1603–1608, doi:10.1021/nl500037x.
- [20] He, D.; Zhong, L.; Gan, S.; Xie, J.; Wang, W.; Liu, Z.; Guo, W.; Yang, X.; Niu, L. Hydrogen Peroxide Electrosynthesis via Regulating the Oxygen Reduction Reaction Pathway on Pt Noble Metal with Ion Poisoning. *Electrochim. Acta* 2021, 371, 137721, doi:10.1016/j.electacta.2021.137721.
- [21] Choe, Y.J.; Kim, J.; Byun, J.Y.; Kim, S.H. An Electro-Fenton System with Magnetite Coated Stainless Steel Mesh as Cathode. *Catal. Today* 2021, 359, 16–22, doi:10.1016/j.cattod.2019.06.062.
- [22] Gholizadeh, A.M.; Zarei, M.; Ebratkhahan, M.; Hasanzadeh, A. Phenazopyridine Degradation by Electro-Fenton Process with Magnetite Nanoparticles-Activated Carbon Cathode, Artificial Neural Networks Modeling. *J. Environ. Chem. Eng.* 2021, 9, 104999, doi:10.1016/j.jece.2020.104999.
- [23] Zarei, M.; Beheshti Nahand, F.; Khataee, A.; Hasanzadeh, A. Removal of Nalidixic Acid from Aqueous Solutions Using a Cathode Containing Three-Dimensional Graphene. *J. Water Process Eng.* 2019, 32, 100978, doi:10.1016/j.jwpe.2019.100978.
- [24] Scialdone, O.; Galia, A.; Sabatino, S. Electro-Generation of H₂O₂ and Abatement of Organic Pollutant in Water by an Electro-Fenton Process in a Microfluidic Reactor. *Electrochem. commun.* 2013, 26, 45–47,

- doi:10.1016/j.elecom.2012.10.006.
- [25] Nair, K.M.; Kumaravel, V.; Pillai, S.C. Carbonaceous Cathode Materials for Electro-Fenton Technology: Mechanism, Kinetics, Recent Advances, Opportunities and Challenges. *Chemosphere* 2021, 269, 129325, doi:10.1016/j.chemosphere.2020.129325.
- [26] Ahmad, A.; Priyadarshini, M.; Yadav, S. The Potential of Biochar-Based Catalysts in Removal of Persistent Organic Pollutants from Wastewater : A Review. *Chem. Eng. Res. Des.* 2022, 187, 470–496, doi:10.1016/j.cherd.2022.09.024.
- [27] Xin, S.; Huo, S.; Zhang, C.; Ma, X.; Liu, W.; Xin, Y.; Gao, M. Coupling Nitrogen/Oxygen Self-Doped Biomass Porous Carbon Cathode Catalyst with CuFeO₂/Biochar Particle Catalyst for the Heterogeneous Visible-Light Driven Photo-Electro-Fenton Degradation of Tetracycline. *Appl. Catal. B Environ.* 2022, 305, 121024, doi:10.1016/j.apcatb.2021.121024.
- [28] Zhou, W.; Li, F.; Su, Y.; Li, J.; Chen, S.; Xie, L.; Wei, S.; Meng, X.; Rajic, L.; Gao, J.; et al. O-Doped Graphitic Granular Biochar Enables Pollutants Removal via Simultaneous H₂O₂ Generation and Activation in Neutral Fe-Free Electro-Fenton Process. *Sep. Purif. Technol.* 2021, 262, 118327, doi:10.1016/j.seppur.2021.118327.
- [29] Hu, X.; Deng, Y.; Zhou, J.; Liu, B.; Yang, A.; Jin, T.; Fai Tsang, Y. N- and O Self-Doped Biomass Porous Carbon Cathode in an Electro-Fenton System for Chloramphenicol Degradation. *Sep. Purif. Technol.* 2020, 251, 117376, doi:10.1016/j.seppur.2020.117376.
- [30] Gao, M.; Wang, W.K.; Zheng, Y.M.; Zhao, Q.B.; Yu, H.Q. Hierarchically Porous Biochar for Supercapacitor and Electrochemical H₂O₂ Production.

- Chem. Eng. J. 2020, 402, 126171, doi:10.1016/j.cej.2020.126171.
- [31] Deng, F.; Olvera-Vargas, H.; Garcia-Rodriguez, O.; Zhu, Y.; Jiang, J.; Qiu, S.; Yang, J. Waste-Wood-Derived Biochar Cathode and Its Application in Electro-Fenton for Sulfathiazole Treatment at Alkaline PH with Pyrophosphate Electrolyte. *J. Hazard. Mater.* 2019, 377, 249–258, doi:10.1016/j.jhazmat.2019.05.077.
- [32] Liang, J.; Tang, D.; Huang, L.; Chen, Y.; Ren, W.; Sun, J. High Oxygen Reduction Reaction Performance Nitrogen-Doped Biochar Cathode: A Strategy for Comprehensive Utilizing Nitrogen and Carbon in Water Hyacinth. *Bioresour. Technol.* 2018, 267, 524–531, doi:10.1016/j.biortech.2018.07.085.
- [33] Sun, C.; Chen, T.; Huang, Q.; Duan, X.; Zhan, M.; Ji, L.; Li, X.; Wang, S.; Yan, J. Biochar Cathode: Reinforcing Electro-Fenton Pathway against Four-Electron Reduction by Controlled Carbonization and Surface Chemistry. *Sci. Total Environ.* 2021, 754, 142136, doi:10.1016/j.scitotenv.2020.142136.
- [34] Gopinath, A.; Divyapriya, G.; Srivastava, V.; Laiju, A.R.; Nidheesh, P. V.; Kumar, M.S. Conversion of Sewage Sludge into Biochar: A Potential Resource in Water and Wastewater Treatment. *Environ. Res.* 2021, 194, 110656, doi:10.1016/j.envres.2020.110656.
- [35] Dessalle, A.; Quílez-Bermejo, J.; Fierro, V.; Xu, F.; Celzard, A. Recent Progress in the Development of Efficient Biomass-Based ORR Electrocatalysts. *Carbon N. Y.* 2023, 203, 237–260, doi:10.1016/j.carbon.2022.11.073.
- [36] Quílez-Bermejo, J.; Morallón, E.; Cazorla-Amorós, D. On the Deactivation of N-Doped Carbon Materials Active Sites during Oxygen Reduction

- Reaction. *Carbon* N. Y. 2022, 189, 548–560, doi:10.1016/j.carbon.2021.12.086.
- [37] Zhang, T.; Wang, H.; Zhang, J.; Ma, J.; Wang, Z.; Liu, J.; Gong, X. Carbon Charge Population and Oxygen Molecular Transport Regulated by Program-Doping for Highly Efficient 4e-ORR. *Chem. Eng. J.* 2022, 444, 136560, doi:10.1016/j.cej.2022.136560.
- [38] Li, Y.; Wang, C.; Pan, S.; Zhao, X.; Liu, N. Mn Doping Improves In-Situ H₂O₂ Generation and Activation in Electro-Fenton Process by Fe/Mn@CC Cathode Using High-Temperature Shock Technique. *Chemosphere* 2022, 307, 136074, doi:10.1016/j.chemosphere.2022.136074.
- [39] Abbas, Z.I.; Abbas, A.S. Oxidative Degradation of Phenolic Wastewater by Electro-Fenton Process Using MnO₂-Graphite Electrode. *J. Environ. Chem. Eng.* 2019, 7, 103108, doi:10.1016/j.jece.2019.103108.
- [40] Li, D.; Sun, T.; Wang, L.; Wang, N. Enhanced Electro-Catalytic Generation of Hydrogen Peroxide and Hydroxyl Radical for Degradation of Phenol Wastewater Using MnO₂/Nano-G|Foam-Ni/Pd Composite Cathode. *Electrochim. Acta* 2018, 282, 416–426, doi:10.1016/j.electacta.2018.06.075.
- [41] Rubio, J.A.; Fdez-Güelfo, L.A.; Romero-García, L.I.; Wilkie, A.C.; García-Morales, J.L. Co-Digestion of Two-Phase Olive-Mill Waste and Cattle Manure: Influence of Solids Content on Process Performance. *Fuel* 2022, 322, 124187, doi:10.1016/j.fuel.2022.124187.
- [42] Elmouwahidi, A.; Bailón-garcía, E.; Pérez-cadenas, A.F.; Maldonado-hódar, F.J.; Carrasco-marín, F. Activated Carbons from KOH and H₃PO₄ Activation of Olive Residues and Its Application as Supercapacitor Electrodes. *Electrochim. Acta* 2017, 229, 219–228,

- doi:10.1016/j.electacta.2017.01.152.
- [43] Walton, K.S.; Snurr, R.Q. Applicability of the BET Method for Determining Surface Areas of Microporous Metal-Organic Frameworks. *J. Am. Chem. Soc.* 2007, 129, 8552–8556, doi:10.1021/ja071174k.
- [44] Raja, P.M. V.; Barron, A.R. 2 .3: BET Surface Area Analysis of Nanoparticles; 2019; Vol. i;
- [45] Nguyen, C.; Do, D.D. The Dubinin-Radushkevich Equation and the Underlying Microscopic Adsorption Description. *Carbon N. Y.* 2001, 39, 1327–1336, doi:10.1016/S0008-6223(00)00265-7.
- [46] Zhou, R.; Zheng, Y.; Jaroniec, M.; Qiao, S.Z. Determination of the Electron Transfer Number for the Oxygen Reduction Reaction: From Theory to Experiment. *ACS Catal.* 2016, 6, 4720–4728, doi:10.1021/acscatal.6b01581.
- [47] Jiang, K.; Back, S.; Akey, A.J.; Xia, C.; Hu, Y.; Liang, W.; Schaak, D.; Stavitski, E.; Nørskov, J.K.; Siahrostami, S.; et al. Highly Selective Oxygen Reduction to Hydrogen Peroxide on Transition Metal Single Atom Coordination. *Nat. Commun.* 2019, 10, doi:10.1038/s41467-019-11992-2.
- [48] Xu, S.; Kim, Y.; Higgins, D.; Yusuf, M.; Jaramillo, T.F.; Prinz, F.B. Building upon the Koutecky-Levich Equation for Evaluation of Next-Generation Oxygen Reduction Reaction Catalysts. *Electrochim. Acta* 2017, 255, 99–108, doi:10.1016/j.electacta.2017.09.145.
- [49] Brocato, S.; Lau, C.; Atanassov, P. Mechanistic Study of Direct Electron Transfer in Bilirubin Oxidase. *Electrochim. Acta* 2012, 61, 44–49, doi:10.1016/j.electacta.2011.11.074.
- [50] Alcañiz-Monge, J.; Pérez-Cadenas, M.; Lozano-Castelló, D. Influence of Pore Size Distribution on Water Adsorption on Silica Gels. *J. Porous Mater.*

- 2010, 17, 409–416, doi:10.1007/s10934-009-9317-0.
- [51] Hong, S.M.; Jang, E.; Dysart, A.D.; Pol, V.G.; Lee, K.B. CO₂ Capture in the Sustainable Wheat-Derived Activated Microporous Carbon Compartments. *Sci. Rep.* 2016, 6, 1–10, doi:10.1038/srep34590.
- [52] Alcañiz-Monge, J.; Linares-Solano, A.; Rand, B. Mechanism of Adsorption of Water in Carbon Micropores as Revealed by a Study of Activated Carbon Fibers. *J. Phys. Chem. B* 2002, 106, 3209–3216, doi:10.1021/jp014388b.
- [53] Madhuri, S.; Shilpa Chakra, C.; Sadhana, K.; Divya, V. Sketchy Synthesis of Mn₃O₄, Mn₃O₄/AC and Mn₃O₄/CNT Composites for Application of/in Energy Cache. *Mater. Today Proc.* 2022, 65, 2812–2818, doi:10.1016/j.matpr.2022.06.247.
- [54] Wang, B.; Yu, J.; Lu, Q.; Xiao, Z.; Ma, X.; Feng, Y. Preparation of Mn₃O₄ Microspheres via Glow Discharge Electrolysis Plasma as a High-Capacitance Supercapacitor Electrode Material. *J. Alloys Compd.* 2022, 926, 166775, doi:10.1016/j.jallcom.2022.166775.
- [55] Moses Ezhil Raj, A.; Victoria, S.G.; Jothy, V.B.; Ravidhas, C.; Wollschläger, J.; Suendorf, M.; Neumann, M.; Jayachandran, M.; Sanjeeviraja, C. XRD and XPS Characterization of Mixed Valence Mn₃O₄ Hausmannite Thin Films Prepared by Chemical Spray Pyrolysis Technique. *Appl. Surf. Sci.* 2010, 256, 2920–2926, doi:10.1016/j.apsusc.2009.11.051.
- [56] Feng, T.; Li, H.; Tan, J.; Liang, Y.; Zhu, W.; Zhang, S.; Wu, M. Synthesis, Characterization and Electrochemical Behavior of Zn-Doped MnO/C Submicrospheres for Lithium Ion Batteries. *J. Alloys Compd.* 2022, 897, 163153, doi:10.1016/j.jallcom.2021.163153.
- [57] Li, Z.; Xiao, S.; Wang, Y.; Zhu, Z.; Li, X.; Niu, X.; Kong, Q.; Jiang, J.; Chen,

- J.S. Fast and Stable Na Insertion/Deinsertion in Double-Shell Hollow MnO Nanospheres. *J. Alloys Compd.* 2022, 920, 165449, doi:10.1016/j.jallcom.2022.165449.
- [58] Ruan, Y.; Lei, H.; Xue, W.; Wang, T.; Song, S.; Xu, H.; Yu, Y.; Zhang, G.R.; Mei, D. Cu-N-C Assisted MnO Nanorods as Bifunctional Electrocatalysts for Superior Long-Cycle Zn-Air Batteries. *J. Alloys Compd.* 2023, 934, 167781, doi:10.1016/j.jallcom.2022.167781.
- [59] Weng, Z.; Li, J.; Weng, Y.; Feng, M.; Zhuang, Z.; Yu, Y. Surfactant-Free Porous Nano-Mn₃O₄ as a Recyclable Fenton-like Reagent That Can Rapidly Scavenge Phenolics without H₂O₂. *J. Mater. Chem. A* 2017, 5, 15650–15660, doi:10.1039/c7ta04042c.
- [60] Huang, Z.; Wang, H.; Wang, X.; Ma, X.; Ren, J.; Wang, R. Heterostructured Mn Clusters/N-Doped Carbon Foams Enhancing the Polysulfides Immobilization and Catalytic Conversion. *J. Alloys Compd.* 2022, 924, 166514, doi:10.1016/j.jallcom.2022.166514.
- [61] Zhou, C.; Liang, Y.; Xia, W.; Almatrafi, E.; Song, B.; Wang, Z.; Zeng, Y.; Yang, Y.; Shang, Y.; Wang, C.; et al. Single Atom Mn Anchored on N-Doped Porous Carbon Derived from Spirulina for Catalyzed Peroxymonosulfate to Degradation of Emerging Organic Pollutants. *J. Hazard. Mater.* 2023, 441, 129871, doi:10.1016/j.jhazmat.2022.129871.
- [62] Song, S.; Wang, Y.; Tian, P.; Zang, J. One-Step Complexation and Self-Template Strategy to Synthesis Bimetal Fe/Mn–N Doped Interconnected Hierarchical Porous Carbon for Enhancing Catalytic Oxygen Reduction Reaction. *Int. J. Hydrogen Energy* 2022, 47, 24728–24737, doi:10.1016/j.ijhydene.2022.05.218.

- [63] Gao, H.; Wang, Y.; Li, W.; Zhou, S.; Song, S.; Tian, X.; Yuan, Y.; Zhou, Y.; Zang, J. One-Step Carbonization of ZIF-8 in Mn-Containing Ambience to Prepare Mn, N Co-Doped Porous Carbon as Efficient Oxygen Reduction Reaction Electrocatalyst. *Int. J. Hydrogen Energy* 2021, 46, 36742–36752, doi:10.1016/j.ijhydene.2021.08.220.
- [64] Moreno-Castilla, C.; López-Ramón, M. V.; Carrasco-Marín, F. Changes in Surface Chemistry of Activated Carbons by Wet Oxidation. *Carbon N. Y.* 2000, 38, 1995–2001, doi:10.1016/S0008-6223(00)00048-8.
- [65] Xie, Z.; Lyu, Z.; Wang, J.; Li, A.; François-Xavier Corvini, P. Ultrafine-Mn₂O₃@N-Doped Porous Carbon Hybrids Derived from Mn-MOFs: Dual-Reaction Centre Catalyst with Singlet Oxygen-Dominant Oxidation Process. *Chem. Eng. J.* 2022, 429, 132299, doi:10.1016/j.cej.2021.132299.
- [66] Zhou, H.; Yang, J.; Cao, W.; Chen, C.; Jiang, C.; Wang, Y. Hollow Meso-Crystalline Mn-Doped Fe₃O₄ Fenton-like Catalysis for Ciprofloxacin Degradation: Applications in Water Purification on Wide PH Range. *Appl. Surf. Sci.* 2022, 590, 153120, doi:10.1016/j.apsusc.2022.153120.
- [67] Wirecka, R.; Lachowicz, D.; Berent, K.; Marzec, M.M.; Bernasik, A. Ion Distribution in Iron Oxide, Zinc and Manganese Ferrite Nanoparticles Studied by XPS Combined with Argon Gas Cluster Ion Beam Sputtering. *Surfaces and Interfaces* 2022, 30, 101865, doi:10.1016/j.surfin.2022.101865.
- [68] Chen, J.; Li, J.; Zeng, Q.; Li, H.; Chen, F.; Hou, H.; Lan, J. Efficient Removal of Tetracycline from Aqueous Solution by Mn-N-Doped Carbon Aerogels: Performance and Mechanism. *J. Mol. Liq.* 2022, 358, doi:10.1016/j.molliq.2022.119153.
- [69] Gong, Z.; Wang, B.; Chen, W.; Ma, S.; Jiang, W.; Jiang, X. Waste Straw

- Derived Mn-Doped Carbon/Mesoporous Silica Catalyst for Enhanced Low-Temperature SCR of NO. *Waste Manag.* 2021, 136, 28–35, doi:10.1016/j.wasman.2021.09.035.
- [70] Cen, H.; Wu, C.; Chen, Z. N, S Co-Doped Carbon Coated MnS/MnO/Mn Nanoparticles as a Novel Corrosion Inhibitor for Carbon Steel in CO₂-Saturated NaCl Solution. *Colloids Surfaces A Physicochem. Eng. Asp.* 2021, 630, 127528, doi:10.1016/j.colsurfa.2021.127528.
- [71] Tang, F.; Zhao, Y.W.; Ge, Y.; Sun, Y.G.; Zhang, Y.; Yang, X.L.; Cao, A.M.; Qiu, J.H.; Lin, X.J. Synergistic Effect of Mn Doping and Hollow Structure Boosting Mn-CoP/Co₂P Nanotubes as Efficient Bifunctional Electrocatalyst for Overall Water Splitting. *J. Colloid Interface Sci.* 2022, 628, 524–533, doi:10.1016/j.jcis.2022.08.037.
- [72] Xu, B.; Wu, F.; Chen, R.; Cao, G.; Chen, S.; Zhou, Z.; Yang, Y. Highly Mesoporous and High Surface Area Carbon: A High Capacitance Electrode Material for EDLCs with Various Electrolytes. *Electrochem. commun.* 2008, 10, 795–797, doi:10.1016/j.elecom.2008.02.033.
- [73] Kuznetsov, D.A.; Han, B.; Yu, Y.; Rao, R.R.; Hwang, J.; Román-Leshkov, Y.; Shao-Horn, Y. Tuning Redox Transitions via Inductive Effect in Metal Oxides and Complexes, and Implications in Oxygen Electrocatalysis. *Joule* 2018, 2, 225–244, doi:10.1016/j.joule.2017.11.014.
- [74] Elmouwahidi, A.; Bailón-García, E.; Pérez-Cadenas, A.F.; Castelo-Quibén, J.; Carrasco-Marín, F. Carbon-Vanadium Composites as Non-Precious Catalysts for Electro-Reduction of Oxygen. *Carbon N. Y.* 2019, 144, 289–300, doi:10.1016/j.carbon.2018.12.038.
- [75] Xiao, F.; Wang, Z.; Fan, J.; Majima, T.; Zhao, H.; Zhao, G. Selective

Electrocatalytic Reduction of Oxygen to Hydroxyl Radicals via 3-Electron Pathway with FeCo Alloy Encapsulated Carbon Aerogel for Fast and Complete Removing Pollutants. *Angew. Chemie - Int. Ed.* 2021, 60, 10375–10383, doi:10.1002/anie.202101804.

- [76] Li, N.; Huang, C.; Wang, X.; Feng, Y.; An, J. Electrosynthesis of Hydrogen Peroxide via Two-Electron Oxygen Reduction Reaction: A Critical Review Focus on Hydrophilicity/Hydrophobicity of Carbonaceous Electrode. *Chem. Eng. J.* 2022, 450, 138246, doi:10.1016/j.cej.2022.138246.

CHAPTER VIII: CONCLUSIONES GENERALES

En la presente tesis doctoral se han sintetizado diferentes materiales basados en carbono, los cuales fueron obtenidos mediante reacciones de policondensación mediante emulsión inversa (xerogeles), carbonización y activación química (carbones activados) y síntesis solvotermal (eco-grafeno). Además, se han realizado proceso de funcionalización de los carbones activados con diversos heteroátomos (N, O, S, B), mediante procesos solvotermales e hidrotermales, así como, el dopado con óxidos de manganeso con impregnación directa. Por otra parte, se sintetizó magnetita mediante coprecipitación química, la cual fue recubierta con xerogeles de carbono y empleada como catalizador tipo Fenton.

Los materiales obtenidos fueron empleados como catalizadores para las reacciones ORR y Fenton para la degradación de tetraciclina según correspondiera, obteniéndose resultados muy interesantes comparables, e incluso mejores, a los obtenidos con otros materiales basados en carbono reportados en la literatura (degradación >70%) .

Se evidencio que el dopaje de estos materiales carbonosos dio como resultado una mejora en las propiedades electroquímicas de los catalizadores. Los materiales carbonosos dopados podrían suplir la necesidad de usar dos catalizadores diferentes en las reacciones de ORR y Fenton, por medio de la ruta ORR de 3 electrones, ya que, mediante el uso de un único catalizador, se generaría directamente el radical hidroxilo, dando como resultado una actividad bifuncional, es decir, generación directa de $\text{OH}\cdot$ o indirecta mediante la producción/activación de H_2O_2 .

De manera más específica, es posible la obtención de tintas de catalizadores libres de metales, con excelentes propiedades electroquímicas ($J_K = 14.59 \text{ mA cm}^{-2}$, $n = 2.03$ y $E_{\text{onset}} = -0.25 \text{ V}$). Estas tintas se pudieron depositar sobre el soporte

(grafito) sin necesidad de aglutinantes, mediante la aplicación directa con pincel, con lo cual, se consigue cierta microrrugosidad adecuada en el cátodo favoreciendo su uso como catalizador ORR $2e^-$.

El dopaje con heteroátomos como el N, S, B y P mejora considerablemente la densidad de corriente del bio-carbón (desde 5.57 a 10.38 mA cm⁻²). El dopaje con nitrógeno y azufre mejora la actividad catalítica tipo bifuncional, logrando porcentajes de degradación de tetraciclina cercanos al 70 %, aproximadamente un 20% más que el bio-carbón sin dopar. Estas mejoras se atribuyeron a la presencia de N-grafítico y N-piridinico, los cuales pueden generar y activar el H₂O₂ a OH•.

El dopaje con nitrógeno mejora considerablemente las propiedades electroquímicas de los materiales de carbono (xerogeles y carbón activado). Sin embargo, en los xerogeles, el tamaño de la esfera final es un factor clave en la degradación de tetraciclina debido a que con esferas de escala micrométrica el dopaje resulta en niveles de remoción más bajos que en las muestras no dopadas. Esto sucede de manera inversa en esferas nanométricas, posiblemente asociado a que los átomos de N dopados en la superficie del catalizador pueden cambiar la carga de los átomos de carbono (cambio en la fuerza de atracción entre el sitio de anclaje y dopante), siendo más notorio este efecto en superficies más pequeñas, debido a que los sitios dopados pueden estar más cerca uno del otro, dando como resultado un grupo funcional de nitrógeno diferente.

Se puede obtener catalizadores para la ORR mediante la síntesis hidrotérmica de xerogeles de carbono dopados con manganeso, donde se evidenció que, aunque el Mn disminuye el área superficial, aumenta la selectividad hacia la ruta de 4 electrones, reduciendo la generación de H₂O₂. Sin embargo, es necesario realizar el

dopaje con una cantidad adecuada de Mn (20 %), puesto que un exceso disminuye la densidad de corriente, lo que desfavorece la actividad catalítica del material. A partir de estos resultados, se determina que, mediante una correcta sintonización de la cantidad del Mn se pueden obtener catalizadores específicos para aplicaciones de remediación ambiental (electro-Fenton) o almacenamiento de energía (micro celdas de combustible).

Mediante la activación del alperujo, se obtuvieron carbones activados con elevada área superficial que se han dopados con óxido de manganeso. Los resultados muestran que el ciclo redox $\text{Mn}^{3+}/\text{Mn}^{2+}$, presente en el óxido de manganeso (Mn_3O_4), puede mejorar significativamente las propiedades electroquímicas ($J_k = 11.37 \text{ mA cm}^{-2}$, $3 < n < 4$) de los materiales de carbono. Se determinó que, un correcto dopaje (cantidad y dispersión) puede generar una actividad catalítica bifuncional al ser usado como un agente dopante de bio-carbones. Esto podría estar dando lugar a una reacción ORR, por la vía de 3 electrones y/o la generación de H_2O_2 (ORR $2e^-$), seguido de su activación a $\text{OH}\cdot$ por la reacción con el Mn^{2+} , lo que quedó en evidencia al alcanzar el mayor porcentaje de degradación de tetraciclina (70 %) con la muestra CK2-Mn-1-10 (capítulo 7), la cual tenía el mayor contenido de Mn^{2+} (8.42).

Con los resultados obtenidos en esta tesis doctoral, se puede incursionar en el desarrollo de nuevos catalizadores bifuncionales para procesos electro Fenton, aplicados a remediación ambiental, más específicamente en la degradación de fármacos presentes en agua (tetraciclina), con resultados muy prometedores.

